Development of spinal circuits for swimming in Zebrafish (*Danio rerio*) larvae

Emphasizing on the rhythm generation mechanism

Yann Roussel

Supervisor: Dr. Tuan Bui

Examiners: Dr. Emily Standen, Dr. John Lewis and Dr. Michael Hildebrand

External examiner: Dr. Joe Fetcho

A thesis submitted in partial fulfillment of the requirements for the
Doctorate in Philosophy degree in Biology

Department of Biology
Faculty of Science
University of Ottawa

uOttawa

Table of content

LIST OF TABLES

LIST OF FIGURES

LEGEND

5-HT : serotonin

CaP : caudal primary

CBX : carbenoxolone

CEN : commissural excitatory neuron

CiA : circumferential ascending

CiD : circumferential descending

CIN : commissural inhibitory neuron

CNS : central nervous system

CoBL : commissural bifurcating longitudinal

CoLA : commissural longitudinal ascending

CoLo : commissural local

CoPA : commissural primary ascending

CPG : central pattern generator

CoSA : commissural secondary ascending

DA : dopamine

Dpf : days-post-fertilization

FFT : fast Fourier transform

Glu : glutamate/ glutamatergic

Gly : glycine/ glycinergic

Hpf : hours-post-fertilization

IC : ipsilateral caudal

IED : ipsilateral excitatory descending

IIA : ipsilateral inhibitory ascending

IN : interneuron

MCoD : multipolar commissural descending

MiP : middle primary

MN : motoneuron

Mtz : metronidazole

PF : pattern formation

PM : pacemaker

pMN : primary motoneuron

RG : rhythm generation

Rilu : riluzole

RoP : rostral primary

SGDR : Strongly glycine dependent rhythm

sMN : secondary motoneuron

Str : strychnine

UCoD : unipolar commissural descending

VeLD : ventral longitudinal descending

WGDR : Weakly glycine dependent rhythm

ABSTRACT

It has long been established that the spinal cord is able to produce locomotor activity on its own. Despite extensive research identifying and describing the involvement of multiple spinal neuron populations that are part of the spinal locomotor circuit, the manner in which these different components act together to precisely control the rhythm and the pattern of activation of muscles during locomotion remains largely undetermined. We sought to shed light on how the components of spinal locomotor circuits interact to produce robust locomotion using a developmental approach in zebrafish larvae. We used electrophysiological techniques to observe how the rhythm generation mechanism developed while the fish was transitioning from an early form of swimming to a more mature swimming behaviour. In the process we were able to highlight fundamental changes in the organization of spinal locomotor circuits as its operation moves from a pacemaker-based architecture relying on intrinsic properties of neurons to a network oscillator-based architecture relying on synaptic connectivity to generate proper rhythm driving the fish tail beats. Additionally, we revealed that this transition occurred at different times along the spinal cord progressing in a caudorostral direction. By combining these experimental observations with already published insights we were able to propose models of spinal locomotor circuits reproducing the successive locomotor behaviours encountered through development. By incrementing supplementing the circuit model in a manner that reflected biological processes by which the nervous system maturates (neurogenesis, synaptic connectivity refinement and maturation of intrinsic properties) we mirrored the natural development of the spinal locomotor circuit. This series of successively constructed models permitted us to pinpoint possible roles of specific neural populations for swimming behaviour as well as eventual targets and mechanism

of actions of neuromodulators (serotonin and dopamine). In the process, I further provided testable hypotheses for future inquiries. Overall, the experimental findings in combination with the modelling work are an important step forward in fully understanding how the spinal cord generates swimming movements in zebrafish.

RESUMÉ

Il est communément accepté que la moelle épinière isolée est capable de produire une activité locomotrice. Malgré des recherches approfondies identifiant et décrivant l'implication de multiples populations de neurones spinaux faisant partie des circuits locomoteur spinaux, la façon dont ces différents composants agissent ensemble pour contrôler précisément le rythme et le mode d'activation des muscles pendant la locomotion reste largement indéterminée. en utilisant une approche développementale, nous avons tenté d'élucider les manières selon lesquelles les composants des circuits locomoteurs spinaux interagissent pour produire une locomotion robuste chez les larves de poisson zèbre. Nous avons utilisé des techniques électrophysiologiques pour observer le développement du mécanisme de génération de rythme durant le processus de maturation des movement de la nage dans la larve. Nous avons ainsi pu mettre en évidence des changements fondamentaux dans l'organisation des circuits locomoteurs spinaux, passant d'une architecture basée sur des neurones pacemakers reposant sur les propriétés intrinsèques de ces neurones à une architecture basée sur la connectivité synaptique pour former des réseaux oscillant responsable de la génération du rythme approprié pour les battements de queue. De plus, nous avons révélé que cette transition s'est produite à différents moments le long de la moelle épinière progressant dans une direction caudal-rostrale. En combinant ces observations expérimentales avec des connaissances déjà publiées, nous avons pu proposer des modèles de circuits locomoteurs spinaux reproduisant les comportements locomoteurs successifs rencontrés lors du développement du poisson zèbre. En incrémentant le modèle du circuit de manière à refléter les processus biologiques qui provoquent la maturation du système nerveux (neurogenèse, raffinement de la connectivité synaptique et maturation des propriétés

intrinsèques), nous avons émulé le développement naturel des circuits locomoteur spinaux. Cette série de modèles construits de manière itérative a permis d'identifier les rôles possibles de populations neuronales spécifiques pour le comportement de nage ainsi que les cibles et les mécanismes d'action des neuromodulateurs (sérotonine et dopamine). Dans le processus, nous avons également fourni des hypothèses vérifiables pour de futures études. Dans l'ensemble, les résultats expérimentaux en combinaison avec le travail de modélisation sont des progrès importants vers la pleine compréhension de la genèse des mouvements de nage dans la moelle épinière du poisson zèbre.

PREFACE

The candidate contributed largely to Roussel et al. (currently under review in Journal of Neuroscience, Chapter 2). The candidate designed and performed all experiments either partially or completely. Melissa Paradis increased the number of trials for the study of the differential effect of strychnine along the rostro-caudal axis (Chapter 2, Fig. 2.4). The candidate and Dr. Tuan Bui (Supervisor) contributed equally to the writing.

Experiments and modelling in Chapters 3 and 4, respectively were designed and performed fully by the candidate. Writing was fulfilled in collaboration with Dr. Tuan Bui (Supervisor).

The candidate contribution to Pena et al. (2017, Appendix 2) consisted of all tectal recordings, analysis of recordings and writing the Methods paragraph explaining the electrophysiological procedure and data analysis of electrophysiological recordings.

The candidate contribution to Johnstone et al. (currently under review in the journal Brain, Appendix 3) consisted of all tectal recordings, analysis of recordings and writing the Methods paragraph explaining the electrophysiological procedure and data analysis of electrophysiological recordings.

This research was supported by a NSERC Discovery Grant (RGPIN-2015–06403).

ACKNOWLEDGMENTS

I would like to sincerely thank the following people who tremendously supported my work through this adventure:

Dr Tuan Bui, my supervisor for his continuous support, selfless time and great knowledge during my Ph.D. His optimism, composure and style kept me focused (obsessed?) for pursuing my research through thrilling as well as more challenging situations.

Dr. Emily Standen, Dr. Michael Hildebrand and Dr. John Lewis, my advisory committee for their constructive comments about my research project during both formal validation steps and less formal conversations.

Dr. Pierre Drapeau for welcoming me in his lab and taking the time to share his electrophysiology techniques and insightful knowledge. Without his precious trainings it would not have been possible to conduct this research.

Dr. Mark Ekker for providing fish strains and for technical guidance.

Dr. Frédéric Bretzner, Dr. Rob Brownstone, Dr. Abdel El Manira, Dr. Gareth Miles, and Dr. Ken Rose for their comments and critical discussions about the first chapter of this thesis.

All the past and present members of the Bui lab and particularly: Carl Farah for the warm welcome during my first months in Canada and fun inside and outside the lab; Melissa Paradis for her valuable help gathering precious data; and Jonathan Tea, Dominique Dionne and Gerry Huynh for their technical assistance in my research.

Vishal Saxena, Christine Archer and Bill Fletcher for their help with animal care.

I am grateful to Isabella Peña and Devon Johnston for inviting me to be part of their research.

Sur une note plus personnelle, j'aimerais remercier mes proches: mes parents, mes frères et leurs familles pour leur soutien inébranlable durant ces quatre années malgré l'éloignement. My friends from the EM3 and abroad for keeping me entertained all year long. Enfin je remercie profondément Léa pour m'avoir accompagné tout au long de cette expérience et m'avoir supporté durant les derniers mois d'écriture.

Thank you all !

INTRODUCTION

Motor control and the spinal cord

Control of motor activity is one of the very basic tasks executed by the Central Nervous System (CNS); however, it requires strong coordination of various sets of muscles. Two kinds of motor activity are often distinguished: voluntary (or conscious) movements, and automated rhythmic movements (Kandel et al., 2013). The former require conscious attention to the execution of movement, and often involve the higher brain areas such as the motor cortex, basal ganglia and cerebellum. They are best exemplified by complex motor tasks such as playing the piano or drawing. Rhythmic movements such as breathing, chewing or walking, can also be controlled voluntarily but most of the time they are executed in an unconscious and automatic way without strong intervention of the brain. However, both sets of movements still require the proper muscles to be activated at the proper time. This highly coordinated muscle activity is mainly driven by a finely organized neural circuit within the spinal cord that integrates both the motor commands of the brain and sensory feedback from the periphery (Goulding, 2009).

Using terms borrowed from computer engineering, the basic scheme of motor control is that the brain, via pathways through the brainstem, sends a motor command as high-level information, which is then translated within the spinal cord into a more "low-level language" that is converted into coordinated muscle activity. The spinal cord also continually integrates sensory feedback to ensure proper execution of the high-level commands.

More specifically, this low-level language appears to be the result of the inter-communication between different classes of interneurons (INs) organized in precise circuits in

the spinal cord (Kiehn, 2011). While, the outputs of these circuits are concretized by the motoneurons (MN), whose activity is directly responsible for muscle contraction through their innervation of muscles, motoneurons are not believed to play a large role in organizing motor activity. For example, motoneurons do not set the rhythm of locomotion nor are they involved in left-right alternation (Bui and Brownstone, 2015). Consequently, the low-level language (e.g. the rhythm generation for locomotion) seems to be implemented upstream of motoneurons in the spinal cord by spinal interneurons, and it is these spinal interneurons which are responsible for generating the proper spinal cord activity to implement motor goals (Brownstone and Wilson, 2008).

Locomotion

The spinal cord translates high-level motor commands into low-level muscle activity. Indeed, locomotion is characterized by strongly rhythmic activity with a repetitive pattern of muscle contraction and as mentioned above, locomotion is part of the more rhythmic and unconscious movements that require little intervention from the brain. The brain can activate and tune these circuits via descending pathways (Kozlov et al., 2014). For instance in zebrafish, a visual stimulus can elicit locomotion if treatment of the stimuli by the brain via the visual system in the optic tectum triggers locomotion by recruiting brainstem centres that activate spinal circuits (Severi et al., 2014). However, indubitable evidences show that both the rhythm and the pattern of activation underlying locomotor activity are encoded by neural circuits of INs within the spinal cord (Grillner, 2003). This idea is clearly validated by numerous experiments in vertebrates showing that locomotion can be produced by the spinal cord even when isolated from

the rest of the CNS (Jankowska et al., 1967a; Forssberg and Grillner, 1973; McDearmid and Drapeau, 2006). For instance, in their 2006 paper, McDearmid and Drapeau used zebrafish larvae to record locomotor activity in isolated spinal cords where the brain was completely removed from the preparation. Spinal cords were placed in a bath of artificial cerebrospinal fluid and using extracellular recordings of motor roots, the authors showed that simple addition of NMDA, a glutamate receptor agonist, was sufficient to elicit locomotor activity in the spinal cord. This neural activity consisted of rhythmic bursts of activity propagating from the rostral end towards the caudal end of the spinal cord on both the right and left sides of it. The left and right sides were coordinated in opposition of phase allowing the flexor/extensor coordination necessary for the propagation of the contractile wave along the body associated with fish propulsion.

The above study exemplifies something that has been demonstrated across vertebrates, that spinal locomotor circuits are capable of independently generating a rhythm that drives locomotion and they are capable of coordinating the left and the right side of the body such that they act in anti-phase. The coordination of both sides of the body has been found to involve commissural spinal neurons whose axons crosses the midline to innervate targets on the other side of the body. Rhythmogenic spinal circuits, on the other hand, have not been identified as well.

It is widely accepted that there are two main mechanisms of rhythmogenesis in the spinal cord (Harris-Warrick, 2010). The first mechanism relies on intrinsic properties of specific types of neurons named pacemaker (PM) neurons. Membrane properties of PM neurons (i.e. channel expression, typically persistent sodium current, $I_{Na,P}$) allow them to generate endogenous

rhythmic bursting activity at a precise timing (Fig. 1.1*A*). Thus, PM neurons exhibit a resonant frequency corresponding to their natural bursting rhythm and are thought to be the internal clock of the locomotor circuit, thus playing an important role in driving circuit rhythmicity. For instance, the mechanism generating respiratory rhythm in the pre-Bötzinger complex is believed rely on pacemaker neurons expressing I_{NaP} in cadmium insensitive neurons or the calcium activated non selective current I_{CAN} in cadmium sensitive neurons (Ramirez et al., 2012). In locomotion, exploring how the rhythmic behaviours of spinal locomotor circuit are influenced by the intrinsic resonance frequencies of the neurons that make up the circuit has been poorly investigated. Such pacemaker neurons have been recently uncovered in the zebrafish located very rostrally in the spinal cord at the rostral border shared with the hindbrain (Tong and McDearmid, 2012). They express $I_{Na,P}$ endowing them endogenous bursting activity and have been shown to be coactive with MNs and muscle cells during locomotor events. These characteristics make them good candidates to rhythmically drive the circuit during locomotion. However their relatively low number as well as their very rostral location suggest other redundant mechanisms for generating the rhythm of locomotion since isolated caudal sections of the spinal cord (i.e. presumably without IC neurons) are able to generate rhythmic activity (McDearmid and Drapeau, 2006; Wiggin et al., 2012).

In contrast to pacemaker neurons, large numbers of spinal locomotor circuits across vertebrates have been proposed to rely on network oscillators based on reciprocal inhibition between non-rhythmogenic modules. A famous model is the “half-centre pattern generator” (Brown, 1914; Jankowska et al., 1967b). According to this model, locomotor

rhythmic activity comes from reciprocal inhibition between two populations of INs (Fig. 1.1*B*). Each half-centre population rhythmically excites a specific pool of motoneurons (e.g. flexors) while inhibiting the antagonist half-centre population that drives the antagonist (e.g. extensors) motoneurons pool (Jankowska et al., 1967b). This model could be considered as more efficient because both the rhythm and the pattern of motoneuron activation are controlled by the same network. Some models of mammalian locomotor circuits suggest instead a bilayer organization with one layer in charge of "rhythm generation" (RG) and one layer responsible for "pattern formation" (PF) (Rybak et al., 2006). The former generates a constant rhythm governing locomotor output and establishes the duration of flexor/extensor phases. Rhythmogenesis by the RG layer has been proposed to be due to particular patterns of synaptic connections. The NMDA subtype of glutamate receptors seems to be sufficient to elicit locomotion in many vertebrates and could be at the core of RG kernels in many spinal locomotor circuits. The PF layer is composed of spinal interneuron populations driving specific subsets of motoneuron pools (e.g. knee, ankle and hip flexors) and every PF IN populations are interconnected via inhibitory connections. This configuration allows activation of the PF IN population at different phases of the rhythm set by the RG. Thus, this results in various pattern of activation of motoneuron pools within the same agonist or antagonist half-centre, since for example, knee, ankle, and hip flexors are not all active at the same time within the swing phase.

However, global and complex activation patterns of muscles distributed across many joints or along the length of the body may be unable to rely on one single CPG. Grillner proposed that complex activity patterns arise from reciprocal interactions between multiple CPG units found within the spinal cord (Grillner, 2006). And within the larger CPG level, different

motoneuron pools can be controlled by multiple coupled Burst Unit Generators (UBGs) allowing various motoneuron recruitment patterns (Grillner, 2011). For swimming behaviours, Grillner proposes that multiple unit CPGs can be organized in a chain along the body with mutual excitatory connection with nearest neighbours. Activity starts from the CPG unit of highest excitability in the chain (theorized to be rostrally located in fish) and propagates like a wave (i.e. with a phase lag) to other CPGs in the chain (Grillner, 2006).

Whether particular spinal locomotor circuits are governed by pacemaker neurons or by network oscillators is still not determined in most spinal locomotor circuits. One complicating factor is the role of neuromodulators in facilitating rhythmic output in spinal locomotor circuits. In mice, serotonin, noradrenaline, and dopamine have been shown to facilitate rhythmic output (Cowley and Schmidt, 1994; Talpalar, 2010). Similarly in amphibians and fish, neuromodulators such as dopamine and serotonin can tune swimming activity by either increasing or decreasing the rhythm, or the duration of swimming or quiescent periods, for example (Sillar et al., 1998; Brustein et al., 2003; Gabriel et al., 2009). For instance, Brustein et al. (2003) showed that serotonin (5HT) modulates the activity of the neuronal circuit underlying locomotion in the zebrafish larva by regulating the duration of quiescent intervals between activity periods. However, in adult zebrafish, serotonin seems to increase inhibition and slow down depolarizations of MNs resulting in a decrease of swimming rhythm (Gabriel et al., 2009).

The diverging effects of the same neuromodulator on locomotor output are a consequence of their mode of action. Neuromodulators activate G-protein coupled receptors that trigger intracellular pathways that can have a range of effects including but not limited to endocytosis of specific ion channels and/or expression of other ion channels (Kandel et al., 2013), and

modulation of the activation or inactivation of targeted ion channels. These mechanisms result in changes in intrinsic properties of the targeted neurons but neuromodulators could also act on synapses (increasing or decreasing their weight), resulting in changes in the strength of neuronal interconnections and therefore, changes in the activity of the network (Lee et al., 2018; Mokhtari et al., 2018). Changing intrinsic properties of neurons could convert tonic firing neurons into pacemaker neurons. Alternatively, tuning the weight of synaptic connections could lead to the formation of network oscillators. So far, the neuron populations targeted by neuromodulators to tune the locomotor circuit activity remain largely undetermined but their ability to facilitate locomotor output is unquestioned.

The self-sufficiency of spinal locomotor circuits for generating a very specific pattern of muscle activation driven by a neural rhythm makes it a very good candidate for studying motor control at the level of the spinal cord. The consistency of locomotor activity (over time and across individuals) in isolated spinal cord preparations underscores the robustness of spinal locomotor circuits to operate in absence of supraspinal input and sensory feedback. The high reproducibility of these evoked locomotor behaviours in in-vitro settings makes them more tractable to study and has clearly enabled many insights into their operation across vertebrates. Despite the number of models put forward to explain how spinal locomotor circuits operate, we still lack a true understanding of how they operate, let alone their architecture. This highlights the complexity of the spinal circuits that underlie movements and motivates investigations of simpler forms of locomotion.

Swimming in zebrafish and its development

Of the different types of locomotor movements that could be studied, swimming is one of the simplest ones considering that, in theory, swimming just needs rhythmic left/right coordination between two different groups of muscles on opposite sides of the body working in opposition of phase. Therefore, it should be a simpler and more tractable problem to elucidate the spinal control of swimming. Over the past two decades, there has been considerable progress in terms of studying how the spinal cord controls swimming movements. A number of populations of spinal neurons have been identified based upon their morphology (Fig. 1.2; Myers et al., 1986; Hale et al., 2001; Drapeau et al., 2002). Many of these populations have been shown to be active during swimming. In addition to the IC discussed above, glutamatergic circumferential descending (CiD) interneurons are key components of the zebrafish locomotor circuit. Their axons extend over multiple muscle segments (over 10 somites) (Hale et al., 2001) and are thought to convey the main excitatory drive within the circuit. Indeed Ljuggren et al., (2014) demonstrated that exciting solely CiDs was sufficient to trigger swimming activity in adult zebrafish. Glycinergic populations are also required for proper locomotion notably Left/Right alternation. Commisural bifuracating longitudinal (CoBL) and Commissural secondary ascending (CoSA) neurons project contralaterally over multiple somites and are recruited during swimming (Liao and Fetcho, 2008). A more mature form of swimming (i.e. slow swimming) involves multipolar commissural descending (MCoD) neurons that are glutamatergic and project contralaterally and caudally over multiple somites (McLean et al., 2007). Finally, glycinergic Circumferential ascending (CiA) neurons are recruited during swimming and may be involved in burst termination (Higashijima et al., 2004). They project ipsilaterally and caudally over several somites.

Despite the considerable progress made in identifying these spinal neurons involved in swimming and the specific contributions of some of these neurons to swimming, we still lack a complete understanding of how spinal locomotor circuits operate. The main obstacle towards understanding how swimming is generated by the spinal cord is a global comprehension of how these circuit components work together to robustly produce locomotor output. Despite its relative simplicity compared to other forms of locomotion, spinal locomotor circuits are proving to still hold a certain degree of complexity, as exemplified by the large number of different populations of spinal neurons already identified.

In order to shed light on spinal swimming circuits, we propose to use an approach based on studying the maturation of swimming in zebrafish. As outlined below, during their development, zebrafish undergo a series of transitions in swimming movements. At the same time there are waves of neurogenesis generating different populations of spinal neurons (Myers et al., 1986; Kimmel et al., 1995; Drapeau et al., 2002; Lewis and Eisen, 2003), which are believed to progressively integrate into existing spinal circuits or to form new circuits for swimming. Similarly, intrinsic properties of spinal neurons can also undergo modifications during development (Sun and Dale, 1998; Currie and Sillar, 2018). Understanding how swimming matures from one form to another through specific changes in spinal circuitry or in operation will unravel the complexity of spinal swimming circuits and provide a greater understanding of how spinal circuits operate.

Before swimming in zebrafish reaches its final mature form, locomotor behaviour in zebrafish goes through an incremental maturation process during development (Drapeau et al., 2002). The first locomotor behaviour, coiling, appears during the first day of development. It is

characterized by one strong body bend on one side of the fish. It is quickly followed by a transiting behaviour named double coiling to finally exhibit burst swimming at 2-3 days post-fertilization (dpf) as spontaneous second-long, infrequent episodes of multiple tail beats of smaller amplitude. At 4 dpf, swimming behaviour further mature from burst swimming to beat-and-glide swimming exhibit trains of shorter (~200ms) but more frequent bursts of activity (Buss and Drapeau, 2001; Drapeau et al., 2002).

This rapid succession of swimming movements in developing zebrafish arises from the maturation process of spinal locomotor circuits. Three of the main developmental mechanisms that can reshape the network output include 1) The addition or deletion of populations of neurons through neurogenesis or apoptosis, 2) the refinement of synaptic connectivity and 3) the changes in intrinsic properties.

Neurogenesis in zebrafish larvae spinal cord

The timelines of neurogenesis in the zebrafish spinal cord have been well established and spinal neurogenesis during development of embryonic and larval zebrafish occurs in two successive waves, the first around 16-17 hours-post fertilization (hpf) and the second after 24 hpf (Myers et al., 1986; Kimmel et al., 1995; Drapeau et al., 2002; Lewis and Eisen, 2003). A rostrocaudal developmental gradient also exist as rostral somites are the first to develop whereas caudal ones are newer (Kimmel et al., 1991; Lewis and Eisen, 2003). Apart from the primary MNs, other neurons of interest from the first neurogenic wave include ipsilateral caudal (IC) interneurons thought to play an essential role in early locomotor behaviour due to their endogenous bursting activity via expression of $I_{Na,P}$, possibly rhythmically driving spinal locomotor circuits (Tong and

McDearmid, 2012). Also, a population of contralateral glycinergic interneurons from the first neurogenesis wave, possibly early CoBL (Commissural bifurcating longitudinal) neurons, is involved in early coiling by inhibiting the contralateral side (Liao and Fetcho, 2008; Ikenaga et al., 2011). These early neurons are later joined during the second neurogenic wave by excitatory glutamatergic V2a (or CiDs) that are thought to be important for swimming activity since exciting specifically this population is sufficient to trigger locomotion (Ljunggren et al., 2014). Other populations of glycinergic interneurons that are either commissural such as commissural secondary ascending (CoSA) or ipsilateral such as circumferential ascending (CiA or V1; Higashijima et al., 2004; Batista et al., 2008) join the spinal locomotor circuit later in development. CiA are much later born (Higashijima et al., 2004) and are contacted by sensory neurons while projecting to ipsilateral MNs. They are thought to be involved in sensory feedback and possibly burst termination (Higashijima et al., 2004). Glutamatergic multipolar commissural descending (MCoD) neurons are involved in more mature forms of swimming later in development (i.e. slow swimming) (McLean et al., 2008).

Changes in spinal circuitry during early development of zebrafish

Several features of synaptic connectivity for developing zebrafish have already been previously established. Early locomotor behaviour (i.e. coiling) relies solely on gap junction connectivity (Saint-Amant and Drapeau, 2001). Excitatory waves propagate through MNs along the rostrocaudal axis via gap junctions in the form of Periodic depolarization event (PDs) driving an ipsilateral coil. Simultaneously, contralateral MNs receive glycinergic inputs as synaptic bursts (SBs) from a population of commissural interneurons triggered by PDs. This first electrical

scaffold will then integrate chemical synapses (glutamatergic in addition to glycinergic) to support double coiling transitioning behaviour (Knogler et al., 2014). Now, traces from MNs exhibit new mixed events in addition to PDs and SBs. These mixed event are actually composed of a PD and a SB (or vice versa), one right after the other. The PD events drive the ipsilateral coiling while the SB results from the contralateral coil ending in a double coiling event. SBs are thought to prevent simultaneous contractions of both sides of the body. Yet, at the onset of burst swimming, glycinergic transmission seems to still be dispensable for rhythm generation (McDearmid and Drapeau, 2006) and is more likely involved in Left/Right alternation only (Buss and Drapeau, 2001). While neuromodulator involvement in shaping locomotor input is minor very early in development (1-2 dpf), their importance becomes quickly of significance. In addition to the role of serotonin described above, dopamine is essential for transitioning from the early burst swimming to the more mature beat-and-glide swimming. Lambert et al. (2012) showed that partially ablating dopaminergic populations in the zebrafish CNS or blocking dopamine receptor 4 (D_4R) preclude the transition to beat-and-glide swimming. Thus, this results suggest that dopamine involvement in the circuit maturation process perhaps through restructuring the circuit architecture via changes in synaptic weights as well as in the intrinsic properties of spinal neurons. Once the transition to beat-and-glide swimming is settled, ablating supraspinal dopaminergic neurons reduces motor output by changing episode occurrence frequency without changing episode duration nor tail beat frequency (Jay et al., 2015). These results suggest that once transitioned, the spinal locomotor circuit does not require dopaminergic inputs to conserve beat-and-glide phenotype. Thus, the function of core mechanisms such as rhythm generation in the spinal locomotor circuit does not fundamentally rely on

neuromodulators in zebrafish larvae but must be based on either intrinsic or network properties.

We propose to explore the development of the spinal locomotor circuit of the zebrafish with a particular interest on rhythm generation. We investigated whether the mechanisms underlying rhythm generation were robust across different developmental stages when zebrafish undergo transitions in motor movements. In the course of our studies, we demonstrate that the generation of rhythmic output by spinal swimming circuits of developing zebrafish actually changes. In modelling how these changes occur, we pinpoint specific spinal circuits or changes in intrinsic properties that may be critical to these transitions, and thus provide insights into the roles of particular spinal circuits or neurons in the control of locomotor activity.

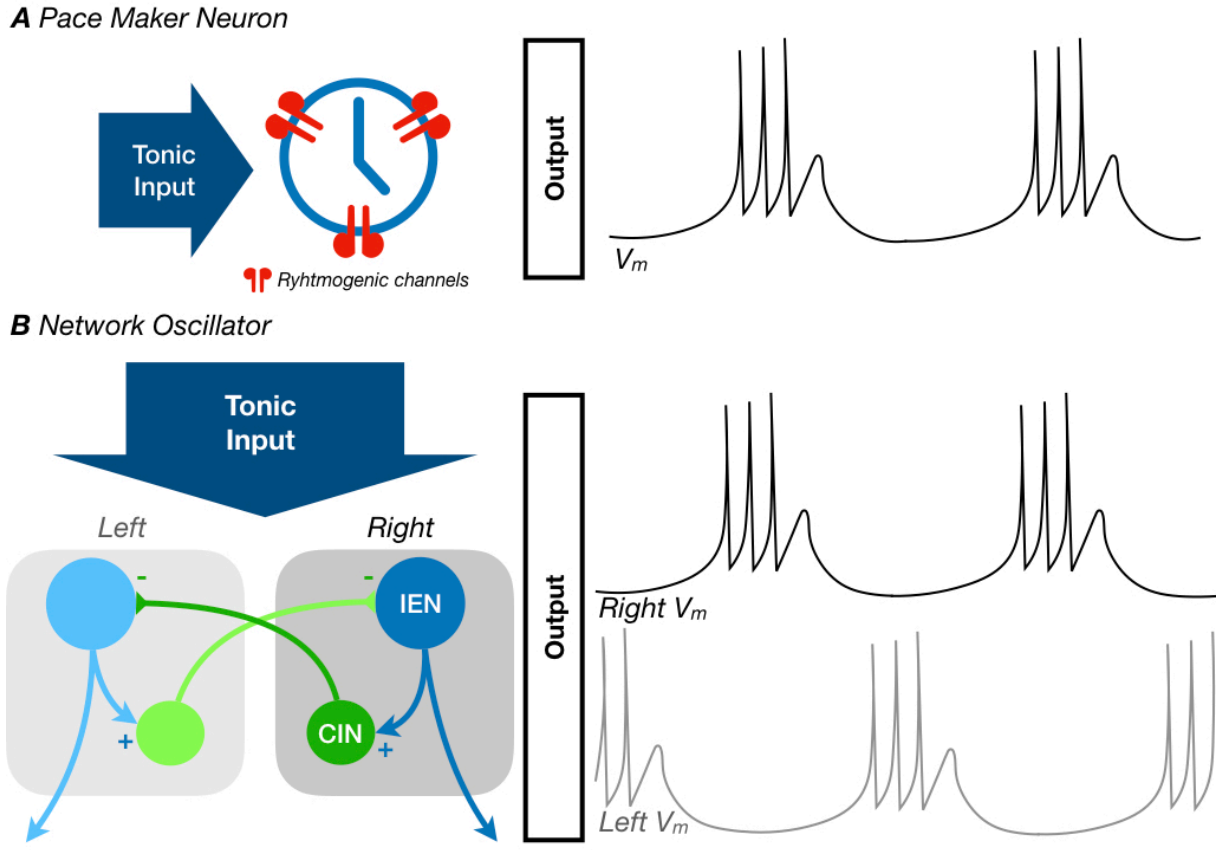

Figure 1.1. Schematic of the two general mechanisms for rhythm generation in the spinal cord.

A, Pacemaker neurons can transform a constant tonic input into rhythmic bursts via expression of rhythmogenic channels (in red), thus rhythmically driving the rest of the circuit. ***B,*** Network oscillators rely on network properties to produce rhythmic output. The half-centre oscillator example proposed here is composed of 2 half-centres (Left and Right). Each centre includes an ipsilateral excitatory neuron (IEN) and a commissural inhibitory neuron (CIN). CINs mutually inhibit the contralateral centre so that when the network oscillator is fed with tonic input, the output from each IEN is rhythmic and out of phase. V_m stands for membrane potential of the pacemaker neuron in *A* or of the left and right IEDs in *B*.

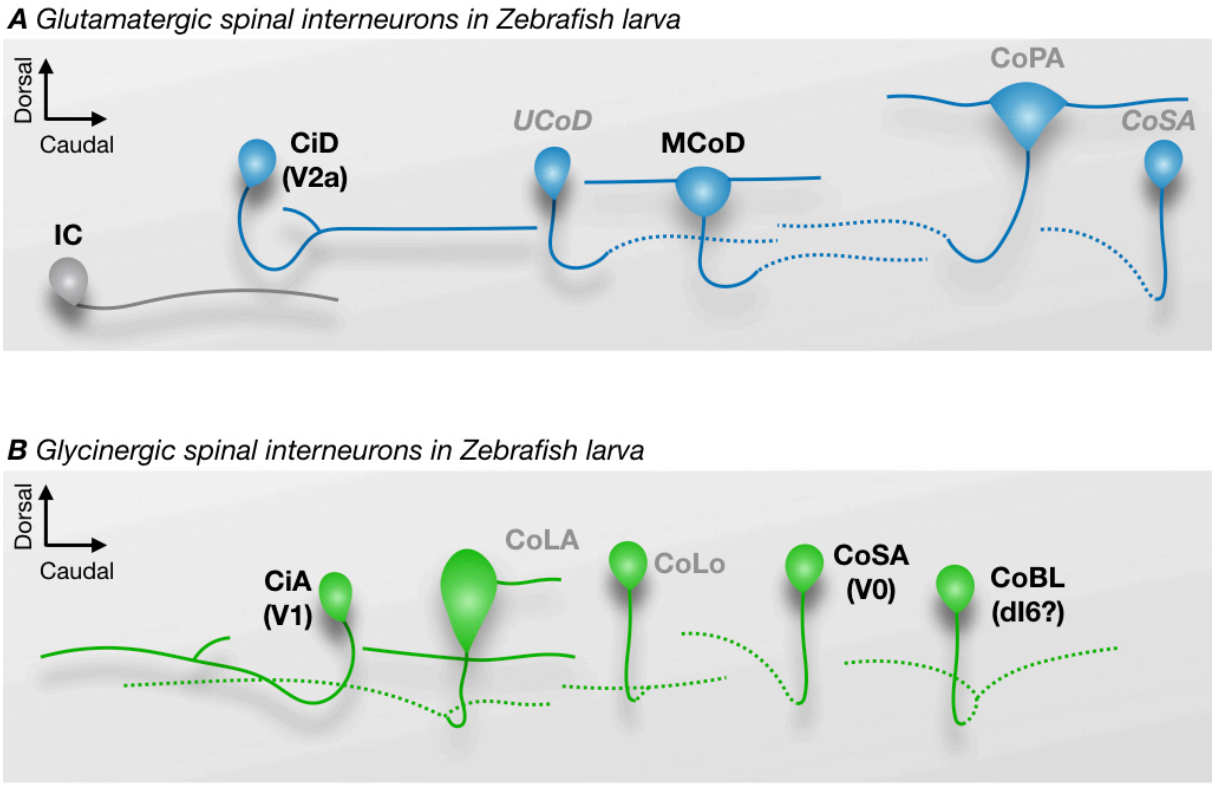

Figure 1.2. Main types of spinal interneurons involved in motor control according to their morphological classification in the Zebrafish larva.

A, Main glutamatergic neurons: Circumferential Descending (CiD), Unipolar Commissural Descending (UCoD), Multipolar Commissural Descending (MCoD), Commissural Primary Ascending (CoPA), and Commissural Secondary Ascending (CoSA). Ipsilateral Caudal (IC) neurons are shaded in grey because their main neurotransmitter type is not elucidated yet. ***B,*** Main glycinergic neurons: Circumferential Ascending (CiA), Commissural Longitudinal Ascending (CoLA), Commissural Local (CoLo), Commissural Secondary Ascending (CoSA), and Commissural Bifurcating Longitudinal (CoBL). Dotted lines represent contralateral axon extensions. Black labels are for neurons involved or active during swimming. Correspondence with genetically identified populations is indicated within parentheses when known. Grey labels

are for neurons not involved in swimming but still involved in other motor behaviours (e.g. escape, struggle) except for UCoD and glutamatergic CoSA (Italic labels in figure) whom involvement is not fully elucidated yet. Adapted in part from McLean and Fetcho (2008) and Liao and Fetcho (2008).

CHAPTER 1: A DEVELOPMENTAL SWITCH IN THE OPERATION OF LARVAL ZEBRAFISH SPINAL LOCOMOTOR CIRCUITS

Roussel, Yann; Paradis, Melissa; and Bui, Tuan Vu

N.B.: This chapter has been submitted in manuscript form for revisions to the Journal of Neuroscience. It is currently under review as of submission of this thesis.

ABSTRACT

Significant maturation of swimming in zebrafish (*Danio rerio)* occurs within the first few days of life when fish transition from coiling movements to burst swimming and then to beat-and-glide swimming. This maturation occurs against a backdrop of numerous developmental changes - neurogenesis, transition from predominantly electrical to chemical-based neurotransmission, and refinement of intrinsic properties. We provide evidence that spinal locomotor circuits undergo fundamental changes as the zebrafish transitions from burst to beat-and-glide swimming. By analyzing the role of glycinergic neurotransmission in the generation of the rhythm of tail beats, we uncover a transition where the operation of spinal locomotor circuits becomes increasingly reliant upon glycinergic neurotransmission for rhythmogenesis. When we examined whether this transition occurred at a uniform pace across the length of the spinal cord, we found that this transition occurred earlier at caudal segments than at rostral segments of the zebrafish spinal cord. These results suggest that as the control of swimming undergoes maturation, the operation of spinal locomotor circuits transitions from putatively relying on pacemakers driving circuits based upon electrical synapses to network oscillators that are gradually set in place in the spinal cord in a caudorostral temporal sequence.

Significance Statement

The neural circuits controlling movements must adapt to the development of the body to enable more refined and complex movements. Our results reveal that the mechanisms for generating the rhythm driving tail beats in developing zebrafish shift from relying upon pacemaker properties to network connectivity involving both excitatory and inhibitory synaptic transmission. Surprisingly, this transition occurs at different developmental time points along the length of the spinal cord, in a direction opposite to the direction of growth of the body. Our findings emphasize that the maturation of motor control by the nervous system results from fundamental changes in the operation of the spinal circuits that underlie these movements and these changes occur at different times across the nervous system.

Introduction

Motor control by the nervous system gradually matures during development as organisms acquire new movements and refine existing ones. This maturation of motor control occurs at a time when the nervous system is still developing; the number of neurons present changes through neurogenesis and apoptosis, new neural circuits are formed, and intrinsic properties are modified (Favero et al., 2014) to support novel and refined network function.

Zebrafish exhibit a rapid series of changes in swimming movements. Large single tail bends (coils) are first seen at 1 day post fertilization (dpf) and then transition to multiple coils later during the first day of development. Coiling movements are then replaced by swimming movements first seen as long (a few seconds in duration) but infrequent episodes of smaller tail bends that emerge at 2-3 dpf (burst swimming) to be replaced around 4-5 dpf by more frequent trains of shorter (hundreds of ms) swimming episodes regularly interspersed with silent "gliding periods" (beat-and-glide swimming; Buss and Drapeau, 2001; Drapeau et al., 2002). How the serial transitioning between these different swimming forms is generated through the continued refinement of neural circuits in the zebrafish is not completely understood.

Early embryonic locomotor activity is generated by spinal locomotor circuits interconnected by electrical synapses (Saint-Amant and Drapeau, 2001) that have been suggested to be rhythmically driven by a small kernel of rostrally-located pacemakers, the previously described Ipsilateral Caudal (IC) spinal interneurons (Tong and McDearmid, 2012). IC neurons display endogenous bursting via persistent sodium currents that could be sufficient to control the rhythm of coiling movements. However, it is not clear whether a network relying upon electrical synapses and driven by a small pacemaker kernel is sufficient to accommodate later more

complex locomotor behaviours produced by the growing body of the larval zebrafish (Kimmel et al., 1995). While gap junctions would lend themselves to rapid and synchronous activation of a small number of motoneurons that would facilitate coiling, a transition towards chemical synapses would facilitate a more refined spatial and temporal control of neural activity of a larger spinal circuit (Bernhardt et al., 1990) for sustained repeated tail beats. In support of this line of reasoning, this first electrical network has been shown to quickly evolve during the first day of development into a hybrid electrochemical network involving both gap junctions and chemical synapses that is capable of generating more complex motor behaviour (multiple-coiling) (Knogler et al., 2014).

Additional spinal circuitry may be necessary for driving more mature swimming (McLean and Fetcho, 2009). These new circuits could continue to be driven by pacemaker kernels. Alternatively, rhythmic activity at later stages could be driven by emerging network-based oscillators whose rhythm results from network connectivity as opposed to a small pool of endogeneous bursters. One of the predictions about the formation of network-based oscillators would be that synaptic excitation and inhibition would then play prominent roles in the swimming activity of larval zebrafish. At the onset of burst swimming, McDearmid and Drapeau (2006) showed that glycinergic neurotransmission, the main inhibitory neurotransmission of the zebrafish spinal cord (Buss and Drapeau, 2001; McDearmid and Drapeau, 2006) is dispensable for rhythm. However, with further maturation of swimming from burst to beat-and-glide swimming, we hypothesize that network-based oscillators become more prominent and predict a transition from a weakly glycine-dependent rhythm (WGDR) to a strongly glycine-dependent rhythm (SGDR) driving spinal locomotor circuits.

To study the maturation of spinal locomotor circuits in the developing zebrafish we tested for possible network-based oscillators by using strychnine to see whether there was a SGDR. In the process, we determined that spinal locomotor circuits seem to switch from a WGDR putatively driven by a small kernel of pacemaker neurons to a SGDR driven by network oscillators. This transition from a WGDR to a SGDR does not occur simultaneously across the length of the fish, but rather progresses in a caudorostral direction, occurring first in newer caudal segments of the developing fish.

Materials and Methods

Animal Care

Adult wild-type zebrafish were maintained according to standard procedures (Westerfield, 2000). All experiments were performed in accordance with the protocol approved by the University of Ottawa animal care committee (BL-2038). Light cycle in the zebrafish room was designed as follow: 14hr light/10hr dark, lights-on at 9:00AM and lights-off at 11:00PM. Water conditions of the fish system were controlled and maintained in the following ranges: 29–30°C, pH 7.5–8.0, conductivity (EC) 690–710. Zebrafish embryos were collected right after breeding and transferred in 10 cm diameter plastic petri dishes. Petri dishes were placed in an incubator maintained at 28.5°C in E3 embryo media. Their density was limited to a maximum of 50 individuals per dish.

Video recording and analysis

The heads of 4 dpf fish were embedded in 1.2% agarose gel so that the rest of the body was free to move. High-speed (500 fps) video recordings of spontaneous swimming were conducted with a Basler acA640-750 μm camera using infrared light. Frame per frame analysis was performed using ImageJ (http://rsbweb.nih.gov/ij/index.html) embedded functions. A custom macro based upon previous work from Fontaine et al. (2008) was developed as follows: A region of interest (ROI) was drawn to span the area bound by the pectoral fins and the tail. Then, a threshold was applied to convert the frame to a binary picture (black and white). Each pixel was extended to smooth the edge of the body of the fish. Any blank space within the reconstructed fish was filled in. Next, the ImageJ « skeletonize » function was executed to extract the midline of the body and

X-Y coordinates of the midline were extracted. The X-Y coordinates were then transferred into a custom Python program that segmented the body in 30 segments from the caudal to the rostral end. Position of the body has been normalized so the extreme caudal segment is 0.0 and the extreme rostral segment is 1.0. For every frame, the program computed the angles between each segment using the arctangent of the derivative and compared to rest position (given the relatively small angles of body curvature for swimming episodes, there was no issue related to arctangent definition). Finally, a Fourier transform of each body segment was performed using the FFT algorithm from the numpy Python library.

Animal preparation for electrophysiology

3 to 5 dpf fish were anaesthetized in 0.02% tricaine solution and pinned down through the notochord in a Sylgard (Dow Corning, Midland, MI, USA) coated dish, one pin above the swim bladder and a second one caudal to the anus. 0.01 mm tungsten wires were used as pins. A skin flap was performed near one of the pins to remove the rest of the skin between the two pins using very fine forceps. The fish was then bathed in aCSF (134 mM NaCl, 2.9 mM KCl, 1.2 mM MgCl2, 2.1 mM CaCl2, 10 mM dextrose, 10 mM HEPES) containing 1mg/mL collagenase solution for 20 minutes. Muscles were removed over 5-9 somites by applying suction through a 15 µm glass micropipette. Tg(*dat:CFP-NTR*) fish line were kindly provided by the lab of Marc Ekker (Godoy et al., 2015).

Chemogenetic ablation of DA neurons

We followed the same protocol described by Godoy and colleagues (Godoy et al., 2015). Briefly, homozygous Tg(*dat:CFP-NTR*) embryos were dechorionated manually. Embryos were treated with 5 mM metronidazole (MTZ; MilliporeSigma, Oakville, ON, Canada) dissolved in 0.1% dimethylsulfoxide in E3 embryo medium (Westerfield, 2000) from 1 day post-fertilization (dpf) to 2 dpf, and then the concentration of MTZ was increased to 7.5 mM. MTZ solution was replaced every day until larvae reached 4 dpf. Embryos were kept in 10 cm dishes with 1 fish per mL of solution and at 28.5°C in complete darkness. At 4 dpf, fish were rinsed in E3 media at least three times and transferred to a clean dish with fresh embryo media for an additional day during which experiments were performed.

Extracellular recordings

10 µm borosilicate glass microelectrodes were backfilled with 2M NaCl solution. We approached the spinal cord targeting a zone just dorsal to a ventral root and a very light suction was applied to seal the ventral root and a part of the spinal cord. Electrical activity was recorded in current clamp mode, amplified and filtered at 1 kHz with a Multiclamp 700B from Axon Instruments (Molecular Devices, Sunnyvale, CA, USA) and finally digitized with a Digidata 1550 (Molecular Devices) to be stored on a computer. Light pulses were occasionally applied to increase occurrence of swimming events. Both spontaneous and light evoked swimming events were merged together since no significant difference in duration and tail beats frequency was observed (Buss and Drapeau, 2001). Somites were numbered from 1 to 9, somite 1 being the sixth somite rostral to the anus and somite 9 being the third somite caudal to the anus. Data from somite 4 to 6 were compiled together for Fig. 2.3*D* and Fig. 2.7*B*.

Intracellular recordings

After muscle removal, 10 MΩ borosilicate glass microelectrodes were backfilled with intracellular recording solution (16mM KCl, 116mM K-gluconate, 4mM MgCl2, 10 mM HEPES, 10 mM EGTA) and targeted motoneurons (MNs) were approached while applying a light positive pressure. Just before entering the spinal cord the electrode was briefly stopped in order to break the dura with positive pressure only. Then, the electrode was introduced in the spinal cord and positive pressure was slightly decreased to finalize the approach. After ensuring that no tissue was present between the micropipette tip and the targeted MN, pressure was released allowing formation of a GΩ seal in most cases. In some cases, very light suction was applied in order to form a seal. A holding potential of -65 mV was then applied and after capacitance compensation, the seal was broken with a series of light suction pulses.

Fluorescent imaging and cell counts

Tg(*isl1*:GFP) (Uemura et al., 2005; ZFIN ID: ZDB-ALT-061222-8) and Tg(*chx10*:GFP) (Kimura, 2006; ZFIN ID: ZDB-ALT-061204-2) 3 dpf larvae were anaesthetized in 0.02% tricaine, pinned down through the notochord in a Sylgard coated dish and imaged with a Zeiss Examiner.D1 microscope equipped with Axiocam 506 mono Zeiss camera and a X-Cite 120 LEDmini light excitation source for fluorescence. 100 µm deep Z-stacks were performed using Zen pro software and cell counts was performed manually. Four independent counts were performed for each Z-stack and means were computed over three different fish.

Data Analysis

Autocorrelation and Peak20-40 detection

In order to quantify the effect of strychnine on rhythmic motor activity, and of different holding potentials on IPSCs, we developed a simple peak detection algorithm to detect the presence of a peak between 20 and 40 Hz in the autocorrelation function of each swimming episode trace (Peak20-40). Raw traces were first band-pass filtered between 1 and 200Hz. Ten 200 ms epochs were extracted during swimming episodes. Because the fictive swimming behaviour matures from a few long episodes (several seconds) at 3 dpf to multiple shorter (few hundreds of ms) episodes at 5 dpf, we chose 200 ms epochs from recordings at all ages to keep the analysis consistent. Autocorrelation functions were computed for each epoch using Clampfit. Then the Autocorrelation function was fitted as a second order polynomial function (in Clampfit).

$$Autocorr_{fit}(\tau) = a_0 + a_1 \bullet \tau + a_2 \bullet \tau^2$$

The fit was performed between 25 and 50 ms time delay (x-axis of the autocorrelation function) corresponding to the targeted range of frequency for tail beats (20-40 Hz) (Fig. 2.2*C*). Finally, the following conditions were applied on the fitting parameters:

$$25ms < \frac{-a_1}{2a_2} < 50ms \qquad \text{and} \qquad a_2 < 0$$

Only if all conditions were respected was a peak considered to be detected. Using the above conditions for all our experiments gave us an average $Peak_{20\text{-}40}$ detection rate above 80% under control conditions. Animals where the $Peak_{20\text{-}40}$ score of recorded swimming episodes in the absence of any pharmacological interventions were all smaller than 60% (meaning that a peak in

the autocorrelation was detected between 25 and 50 ms less than 60% of the time) were considered as arrhythmic and their recordings were discarded.

Short-Time Fourier Transform

The frequency components of swimming under different conditions were computed using the Short-Time Fourier Transform algorithm in Python. 30 s long recordings were band-pass filtered between 1 and 200 Hz, then a Fourier transform was performed on every 375 ms epochs of the recording. Finally, all Fourier transforms were plotted as heat maps in Python.

Modeling

The reductive mathematical model consisted of two coupled oscillators coded in Python: A classical harmonic oscillator with a natural frequency ω_0 of 20 Hz, driving a damped oscillator with the same natural frequency ω_0 and a damping coefficient ζ. The damping oscillator receives an input from the harmonic oscillator characterized as:

$$F_0(t) = F_0 sin(\omega_0 t) \quad \text{with } F_0 \text{ the coupling coefficient}$$

In addition, both oscillators receive a « go signal » from higher centers (i.e. a tonic excitation) $F_1(t)$ defined as a step function:

$$F_1(t) = \begin{cases} F_1 & if \quad t_1 \leq t \leq t_2 \\ 0 & else \end{cases}$$

F_1 is a constant and t_1 and t_2 are the time interval limits during which the step signal is emitted. Thus, the harmonic oscillator (representing the pacemaker IC neurons) is only active during the time interval $\Delta t = t_2 - t_1$. The damped oscillator (representing a half-centre unit oscillator)

receives the input $F_0(t) = F_0 sin(\omega_0 t)$ only for the same interval Δt. The output of the network, read at the output of the damped oscillator, is a solution of a simple ODE:

$$\frac{d^2x}{dt^2} + 2\zeta\omega_0\frac{dx}{dt} + \omega_0^2 = F_0 sin(\omega_0 t) + F_1(t)$$

where x is our oscillating variable from the damped oscillator (homologous to the membrane potential of MNs in our case). ζ represents the strength of reciprocal inhibition in a half-centre rhythm generation mechanism and consequently it represents the application or absence of strychnine. A high ζ models the application of strychnine preventing our half-centre from oscillating. F_0 represents the coupling coefficient between the two oscillators. A high F_0 representing a strong coupling between the harmonic and the damped oscillator, and a low F_0 a weak coupling, such as in the presence of a gap-junction blocker or due to the integration of new neurons into spinal half-centre units that are not directly connected to the IC pacemaker neurons.

We solved the ODE in Python using different parameters: Strong coupling $F_0 = 0.5$, weak coupling $F_0 = 0.01$, strong reciprocal inhibition $\zeta = 0.1$ and weak reciprocal inhibition $\zeta = 0.5$. We finally computed and plotted the autocorrelation function from the output.

Results

Increasingly stronger effect of strychnine on rhythmogenesis from 3 to 5 dpf

To identify the rhythmogenic mechanism underlying tail beats in 3-5 dpf larval zebrafish, we identified the main frequency components of body bends during swimming activity recorded using high-speed video recordings made at 4 dpf (Fig. 2.1*A*). As reported previously (Muller, 2004; McLean et al., 2007; Fontaine et al., 2008), we observed that the maximum tail bend amplitudes were located very caudally (Fig. 2.1*B,C*) and that body oscillations were at a frequency between 20 to 40 Hz (Fig. 2.1*D*). Thus, we focused on this frequency range to conduct our analysis of rhythm generating mechanisms responsible for larval swimming.

We hypothesized that since reciprocal inhibition is a central mechanism of network-based oscillators such as half-centre oscillators (Lundberg, 1981), and glycine is thought to be the main inhibitory neurotransmitter in zebrafish spinal cord (Drapeau et al., 2002), rhythmogenesis would become increasingly reliant upon glycinergic neurotransmission as larval zebrafish develop (i.e. transition from a WGDR to a SGDR). Thus, we tested the role of glycine by blocking glycinergic neurotransmission using 4 μM of strychnine, a glycine antagonist, during swimming episodes recorded between 3-5 dpf. Typical control traces are shown in Fig. 2.2 with spectral analysis of frequency components of recorded swimming episodes (Fig. 2.2*A,B*). 20 to 40 Hz oscillations are easily noticeable in control recordings at 3, 4 and 5 dpf as confirmed by the spectral analysis. After strychnine application, oscillations in the 20-40 Hz range were attenuated at all ages tested (Fig. 2.2*A,B*). However, we could still see typical oscillations in more than half of the fictive swimming events at 3 dpf (Fig. 2.2*B*), consistent with previous observations (McDearmid and Drapeau, 2006). This is in contrast to 5 dpf when strychnine application ablated oscillations

within the 20-40 Hz range more consistently (Fig. 2.2*Avi*). To quantify the effects of strychnine between 3-5 dpf, we plotted autocorrelation functions of 200 ms epochs of electrophysiologically recorded swimming activity both under control and strychnine conditions (Fig. 2.2*C*). We developed a peak detection algorithm and plotted the probability of peak detection in the 20-40 Hz range of the autocorrelation function across age ($Peak_{20\text{-}40}$; Fig. 2.2*D*). At all three developmental stages, the $Peak_{20\text{-}40}$ detection score was reduced by strychnine (Fig. 2.2*D*, left). However, the attenuation of the $Peak_{20\text{-}40}$ detection score by strychnine at 5 dpf was significantly greater than at 3 and 4 dpf (Fig. 2.2*D*, right), suggesting that the importance of glycinergic neurotransmission to the rhythm driving tail beats changes over time, and a transition occurs between a WGDR to a SGDR around 4 to 5 dpf.

To control for potential contributions from supraspinal centres, we performed recordings on acutely spinalized larvae at 3 and 5 dpf (Fig. 2.3*A*). Fictive swimming was induced by applying NMDA to the bath (1-1.5 mM). When strychnine was applied, fictive swimming completely stopped in 5 dpf preparations (Fig. 2.3*C*) but persisted in 3 dpf spinalized preparations (Fig. 2.3*B*) reinforcing observations made in the whole animal preparation. Together, the experiments from whole and acutely spinalized animals suggest that swimming in developing zebrafish transition from a WGDR to a SGDR between 3 and 5 dpf, possibly due to the emergence of network oscillators.

Differential effect of strychnine along the rostrocaudal axis

The development of many parts of the zebrafish occurs along an anterior-posterior gradient (Kimmel et al., 1995) and since the zebrafish body is still developing at 3-5 dpf, we asked

whether there could also be a spatial gradient in the transition from a WGDR to a SGDR within the spinal cord. To test this, we analyzed recordings at three spinal segments underlying the following somites: the sixth somite rostral to the anus (referred to as somite 1), the third somite rostral to the anus (referred to as somite 4) and the third somite caudal to the anus (referred to as somite 9) (Fig. 2.4*A*). Results show a significant effect of strychnine decreasing $Peak_{20\text{-}40}$ detection score for somites 1, 4 and 9, at 4 and 5 dpf (Fig. 2.4*B*). However, when we compared the effect of strychnine on $Peak_{20\text{-}40}$ detection at 3 dpf, strychnine had a significant effect for the caudally located somite 9 but not for somites 1 and 4 ($P = 0.05$). This suggests that the caudal somite 9 already operated by a SGDR at 3 dpf, and that somites 1 and 4 transitioned from a WGDR to a SGDR at later ages. This point is further supported when we compare the attenuation of the Peak20-40 detection score by strychnine across the 3-5 dpf developmental time window for each somite examined (Fig. 2.4*C*). The attenuation is significantly increased between 3 and 5 dpf for somites 1 and 4 but not for somite 9. In addition, we performed a few dual extracellular recordings at 3 dpf and 4 dpf with one electrode situated at the spinal segment underlying somite 1, and another at the spinal segment underlying somite 9, and found examples where strychnine had negligible effects on the 20-40 Hz rhythm at somite 1 but had a significant effect on the 20-40 Hz rhythm at somite 9 (Fig. 2.4*D*). No dual extracellular recordings at 5 dpf showed contrasting effects of strychnine on the rhythms recorded at somite 1 versus somite 9. The sum of these experiments suggests that network oscillators may first emerge at caudal regions of the spinal cord where new neurons are integrated into the spinal locomotor circuits to control the newer parts of the tail.

Secondary motoneurons preferentially generated caudally at 3 dpf

To investigate whether the caudorostral gradient in the transition from a WGDR to a SGDR is accompanied by local density variations of particular populations of spinal neurons along the rostrocaudal axis, we imaged the expression of a reporter GFP protein along the spinal cord in Tg(*isl1:GFP*) and Tg(*chx10:GFP*) fish. *isl1* is thought to be mainly expressed in secondary motoneurons (sMNs) whereas *chx10* expression marks V2a (CiD) interneurons that play a central role in rhythmogenesis for locomotion (Ampatzis et al., 2013; Ljunggren et al., 2014; Stil and Drapeau, 2016). sMNs are younger than primary motoneurons (pMNs) and are primarily involved in swimming as opposed to the latter that are involved in faster, coiling-like movements (Liu and Waesterfield, 1988; Ampatzis et al., 2013). Cell counts performed on a rostral location (centred on the 7th somite rostral to the anus) and caudal location (centred on the 4th somite caudal to the anus) show significant variations for the Tg(*isl1:GFP*) fish only (Fig. 2.5*A,B*). On average, less sMNs were seen rostrally (76.4 ± 7.6; n = 3 fish) as compared to caudally (90.1 ± 3.9; n = 3 fish) in Tg(*isl1:GFP*) fish whereas there were no differences in V2a interneurons found rostrally (68.2 ± 3.9; n = 3 fish) compared to the caudal site (66 ± 6.4; n = 3 fish) in Tg(*Chx10:GFP*) fish (Fig. 2.5*C*). These results suggest that the earlier WGDR to SGDR transition occurring in caudal segments of the spinal cord may be associated with greater neurogenesis of secondary motoneurons, which are associated with slower, more mature forms of swimming, in caudal segments.

Arrhythmic synaptic inhibition to motoneurons becomes rhythmic at 3 dpf

We reasoned that a transition from a WGDR to a SGDR might be reflected through an increase in rhythmicity of glycinergic inputs to motoneurons (Saint-Amant and Drapeau, 2000; Liao and Fetcho, 2008). We proceeded to do patch-clamp recordings in whole-cell configuration of secondary sMNs in the spinal cord. In voltage-clamp recordings, we first recorded currents at -65 mV, near resting potential to assess the rhythmicity of both glutamatergic and glycinergic inputs as the latter have a reversal potential that is depolarized to -65 mV in developing zebrafish (Fig. 2.6*Ai, Aiii, Av*). We then recorded currents at the cation reversal potential (0-5 mV) to isolate outward currents thought to be glycinergic (Buss and Drapeau, 2001). Glycinergic events seemed to be arrhythmic at 3 dpf (Fig. 2.6*Ai*), consistent with previous observations (Buss and Drapeau, 2001). However, after this stage, glycinergic events became rhythmic (Fig. 2.6*Aiii,Av*) as supported by the $Peak_{20\text{-}40}$ detection analysis of the autocorrelation functions (Fig. *2.6C*). It is interesting to note that all recordings performed between 72 hours post-fertilization (hpf) and 78 hpf showed arrhythmic glycinergic events. On the other hand, glycinergic events to motoneurons that were recorded between the stages of 80 hpf and 84 hpf showed rhythmicity. This switch in the properties of glycinergic currents thus seems to occur within a short time window between the 3rd and 4th day of development and could reflect the WGDR to SGDR switch putatively due to the emergence of network oscillators.

Chemical ablation of dopaminergic neurons does not preclude a WGDR to SGDR transition

Since the WGDR to SGDR transition seems to be concomitant with the transition from burst swimming to beat-and-glide swimming, we asked whether the WGDR to SDGR transition was

necessary for the transition in swimming form. In order to test this, we sought to prevent the transition from burst swimming to beat-and-glide swimming that normally occurs at around 4-5 dpf. Dopamine signaling through D4 receptors during early zebrafish development has been shown to be important in reducing the duration of swimming episodes while increasing the frequency of swim episodes, as seen in the transition from burst to beat-and-glide swimming (Lambert et al., 2012). Therefore we employed a chemogenetic strategy where dopaminergic neurons were chemically ablated by application of the pro-drug metronidazole (MTZ) which was converted by nitroreductase (NTR) into a cytotoxic compound in a transgenic line of zebrafish Tg(*dat:CFP-NTR*) (Godoy et al., 2015). The conditional expression of the fusion protein CFP-NTR by dopamine transporter (dat) cis-regulatory elements ensured selective ablation of dopaminergic cells when these fish were treated with MTZ, though it is important to note that not all dopaminergic neurons are ablated using this strategy (about 45-67% decrease according to Godoy et al. 2015).

As previously described (Lambert et al., 2012; Godoy et al., 2015), MTZ application led to longer swimming episodes in 5 dpf Tg(*dat:CFP-NTR*) larvae (Fig. 2.7*A*), more akin to the burst-swimming phenotype of 3 dpf zebrafish. We reasoned that if the WGDR to SGDR transition is important for the transition from burst swimming to beat-and-glide swimming, then blocking glycinergic neurostransmission would have weak effects on the swimming rhythm in 5 dpf MTZ-treated fish since these fish still exhibited burst-swimming-like activity. Instead we found that strychnine had a significant effect on rhythm generation in MTZ-treated fish (Fig. 2.7*Bi*) and this effect was comparable to 5 dpf WT fish as there was no significant difference between attenuation of $Peak_{20\text{-}40}$ detection for 5 dpf WT and 5 dpf MTZ-treated Tg(*dat:CFP-*

NTR) fish (Fig. 2.7*Bii*). On the contrary, we observed a significant difference with the attenuation of $Peak_{20\text{-}40}$ detection for 3 dpf WT (Fig. 2.7*Bii*). These results suggest that dopaminergic signalling shapes the maturation of the swimming pattern (from long infrequent swimming episodes to frequent short episodes) but not the mechanism for rhythm generation within each episode. Consistent with this conclusion, we found that in patch-clamp recordings IPSPs to motoneurons were rhythmic in 5 dpf MTZ-treated fish (Fig. 2.7*C*). These results suggest that the emergence of rhythmic IPSPs was also not involved in transitioning from burst swimming to beat-and-glide swimming. This is further supported by the fact that when we sorted our recordings according to swimming phenotype (burst versus beat-and-glide) instead of age in our strychnine experiments with non-MTZ treated fish (data from Figs. 2.2, 2.4 and 2.7), we observed no significant differences in $Peak_{20\text{-}40}$ detection scores between the two phenotypes (data not shown), suggesting that swimming phenotype is not linked to a WGDR to SGDR transition.

Modelling the maturation of zebrafish swimming with two coupled oscillators

The nascent importance of glycine in rhythmogenesis at later stages of development of zebrafish suggests that the control scheme of swimming is changing in the time it takes for burst-swimming to switch to beat-and-glide swimming. A SGDR may be present if later swimming is generated by network oscillators rather than a pacemaker driven network. In other words, before 3 dpf, tail beats may be generated by a pacemaker kernel (represented by PM blue squares in our model, Fig. 2.8*A,C*) that generates swimming episodes due to endogenous bursting properties. These rhythms are propagated along the length of the fish by a hybrid network involving

chemical and electrical synapses (Knogler et al., 2014). In contrast, our data suggests that tail beats at 4-5 dpf is the result of propagating waves generated by network oscillators (represented as a network oscillator unit in the model, Fig. 2.8*A,C*), requiring glycinergic inhibition. The emergence of rhythmic glycinergic inputs in the 20-40 Hz frequency range observed in MNs (Fig. 2.6) supports the idea of developing network oscillators relying on rhythmic synaptic inhibition.

To test the idea that a switch from a pacemaker-driven electrical network to a network oscillator-based spinal locomotor circuit could lead to a WGDR-to-SGDR transition, we developed a reductive mathematical model consisting of coupled oscillators in which the pacemaker-based rhythmogenic mechanism is modelled by a harmonic oscillator and the network-based rhythmogenic mechanism (e.g. half-centre network oscillator) is modelled by a damped oscillator (Fig. 2.8*A*). The damping coefficient ζ allows us to model the impact of decreasing synaptic inhibition, such as following the application of strychnine, which is modelled by an increasing ζ. The two oscillators have the same natural frequency ω_0 of 20 Hz. In addition, the two oscillators are coupled by a coupling coefficient F_0 (see Materials and Methods). We sought to examine whether we could reproduce the WGDR to SGDR transition as resulting from the emergence of a network-based mechanism (i.e. the half-centre network oscillator) over a pacemaker-based mechanism. We modelled the reduced influence of the pacemaker-based mechanism as a decrease in the coupling coefficient F_0. We simulated the application of strychnine at two developmental stages by simulating the network at two different values of ζ (to model the presence or absence of strychnine) and at two different values of F_0 (high F_0 representing 3 dpf fish, low F_0 representing 4-5 dpf). Autocorrelation functions from

the network output in our simulations (Fig. 2.8*B*) reproduced well our experimental data (in Fig. 2.2*C*) under control and strychnine conditions. Therefore, our coupled oscillator model was able to replicate the WGDR to SGDR transition observed experimentally, thus supporting a transition from a pacemaker kernel to network oscillators in spinal locomotor circuits of developing zebrafish.

Discussion

Zebrafish display movements within hours of fertilization, however their nervous system continues to develop their motor control. Developing zebrafish pass through a remarkably rapid transition between sharp abrupt single coils to more refined rhythmic tail beats within days. Our results reveal that as swimming movements are refined in larval zebrafish, so too are spinal locomotor circuits. We observed a shift in the role of glycinergic neurotransmission to rhythmogenesis and argue that the increased involvement of glycinergic neurotransmission is indicative of the emergence of network oscillators in the developing zebrafish.

In many vertebrate locomotor circuits, glycinergic transmission seems to be dispensable for locomotor activity (Li et al., 2010; though see Moult et al., 2013; Messina et al., 2017). So why does a WGDR to SGDR transition suggest a shift in the operation of the neural circuits responsible for swimming in the developing zebrafish? Two general mechanisms of rhythmogenesis in neural circuits have been described (Harris-Warrick, 2010). The first one is based upon pacemaker neurons capable of endogenously bursting when driven by tonic excitation that drive the network according to their intrinsic oscillating rhythm (Tseng and Nadim, 2010). The second proposed mechanism of rhythmogenesis relies on a network's connectivity pattern. A classic example of network rhythmogenesis is the theoretical half-centre oscillator where reciprocal inhibition of two antagonistic half-centres establishes an alternating activation of the half-centres, thus generating a rhythm (Brown, 1914; Lundberg, 1981). While synaptic inhibition is not a prerequisite to the operation of network-based oscillators, it can be intimately linked to rhythmogenesis as would be the case in a half-centre oscillator. On the other

hand, the involvement of synaptic inhibition in rhythmogenesis would not be a feature of pacemaker-driven oscillators where intrinsic properties are sufficient for rhythmic activity.

Glycinergic currents have the particularity of being inward (i.e. depolarizing) at resting potential in developing zebrafish (Saint-Amant and Drapeau, 2000, 2001), however, the proximity of its reversal potential to the resting potential would lead glycinergic neurotransmission to act as a shunting inhibition (Ben-Ari, 2002; Drapeau et al., 2002; Knogler et al., 2014). Therefore, we suggest that glycinergic inhibition at early developmental stages is still a viable means of implementing reciprocal inhibition between half-centres in the developing zebrafish and the WGDR to SGDR transition indicates a transition away from a pacemaker to a network oscillator mechanism of rhythmogenesis. Whether the reciprocal inhibition between half-centres is actually contralateral or ipsilateral has yet to be determined though each type of synaptic inhibition could play separate roles in coordinating left-right alternation and rhythmogenesis (Gabriel et al., 2008).

Proposed maturation of the neural control of swimming in developing zebrafish

Previous work suggests that glycinergic neurotransmission is dispensable for rhythmic swimming in the early stages of motor control in the zebrafish (Saint-Amant and Drapeau, 2000, 2001). When burst swimming first succeeds single and multiple coils, glycinergic neurotransmission is only needed for left-right alternation (McDearmid and Drapeau, 2006). Pharmacologically blocking gap junctions arrests swimming activity indicating that an early electrical synapse framework is key to the maintenance of swimming at that stage (Buss and Drapeau, 2001). Recently, the rostral spinal IC neurons have been identified as putative

pacemakers for swimming at this developmental stage due to their endogenous bursting driven by persistent sodium currents and their electrical connections to motoneurons (Tong and McDearmid, 2012).

The primacy of this initial pacemaker-driven electrical network to rhythmogenesis may be superseded as the nervous system accommodates a growing body requiring coordination of more body segments to generate increasingly refined forms of movements. Around 4 dpf, swimming behaviour is further refined through a transition from burst to beat-and-glide swimming (Buss and Drapeau, 2001). During this transition, new neurons are potentially integrated to the spinal locomotor circuits such as sMNs (Fig. 2.5) thought to be recruited mostly during slow swimming events (Menelaou and McLean, 2012). Our results show that at this age, glycinergic neurotransmission becomes a key component of rhythm generation for tail beats. Strychnine application was more likely to disrupt swimming at later stages and we also observed a switch from arrhythmic to rhythmic IPSCs to motoneurons within a time span of 6 hours at around 80 hpf. Our simulations of a pair of coupled oscillators, one representing a pacemaker-mechanism of rhythmogenesis, the other representing network oscillators involving synaptic inhibition for rhythmogenesis, also suggest that a relatively decreasing drive from pacemakers to spinal locomotor circuits during development, putatively due to the addition of new spinal circuitry, could lead to locomotor activity that relies more strongly on glycinergic transmission. Thus, our findings indicate that early spinal locomotor circuits relying upon electrical synapses are replaced or supplemented by a single or by multiple network oscillators, which underlie the slow swimming activity observed first as burst swimming and then beat-and-glide swimming.

The presence of multiple longitudinally distributed network oscillators rather than a single oscillator at 5 dpf is suggested by experimental studies where very short 5 dpf spinal cords segments have been shown to be able to generate rhythmic activity (McDearmid and Drapeau, 2006; Wiggin et al., 2012). As well, we found that the WGDR to SGDR occurred earlier at a caudal somite when compared to more rostral somites, suggesting an early establishment of a network oscillator at more caudal spinal segments. In developing zebrafish, growth occurs at different rates along the rostrocaudal axis of the body (Kimmel et al., 1995). More caudal somites are much smaller earlier in development than their rostral counterparts, and it stands to reason that the neural circuits involved in the control of caudal somites may develop at different rates than rostrally located circuits. Our cell counts of sMNs, associated with slower swimming, reveal a greater number of sMNs in caudal segments at the studied ages. Considering that pMNs and sMNs are primarily dedicated to swimming movements of different speeds (Liu and Waesterfield, 1988), it is possible that nascent swimming networks at the caudal end of the growing fish first establish local network oscillators controlling primarily sMNs as opposed to pMNs.

Over time, there is a possibility that two overlapping networks arise: an electrical network linking pacemaker neurons and pMNs used for faster swimming movements such as coils and perhaps escape responses, and a network based upon longitudinally distributed half-centre network oscillators linking sMNs to neural circuits dedicated to slower forms of swimming. It is however likely that both electrical and chemical synapses are concomitantly involved during some swimming activity, as suggested by the presence of both types of synapses in the V2a-motoneuron circuit (Song et al., 2016). Similarly, a hybrid pacemaker-network

oscillator has been proposed to underlie different speeds of locomotion in mammalian locomotor circuits (Brocard et al., 2010).

Role of dopaminergic neurons in pattern generation

The WGDR to SGDR transition becomes important to the rhythm of tail beats during the transition from burst swimming to beat-and-glide swimming patterns. However, the coincidence of these two transitions does not mean that they are causally related. Previous studies have suggested that dopamine through D4 receptor signalling is essential for the maturation to beat-and-glide swimming (Lambert et al., 2012). While our observed phenotype was closer to burst swimming at 5 dpf when dopaminergic neurons were partially ablated, strychnine effectively disrupted the tail beat rhythm and we also observed rhythmic IPSPs in motoneurons. In addition, we noticed typical beat-and glide phenotype for spinalized 5 dpf non-MTZ treated larvae in the presence of NMDA in a preparation where descending dopaminergic inputs would be presumably absent (Fig. 2.3). The latter suggests that while dopamine undoubtedly plays a critical role for the developmental establishment of beat-and-glide swimming, its involvement does not extend to the maintenance of tail beat rhythm. While we cannot definitely conclude that the transition from a SGDR to a WGDR is completely disconnected from the swimming phenotype transition from burst to beat-and-glide swimming, other mechanisms would be required to explain this maturation such as perhaps the modulation of an ultraslow hyperpolarization (Zhang et al., 2015).

Future directions

Our findings could relate to the development of motor circuits in other vertebrates. For instance, it seems that an early electrical scaffold is a necessary first step in the development of mice spinal locomotor circuits (Tresch and Kiehn, 2000). Whether an electrical network acts as monolithic block from which locomotor circuits will later be sculpted and refined via new chemical connections to accommodate more precisely defined locomotor movement needs to be determined across vertebrates. Our results suggest that the circuits involved in rhythmogenesis operate as network oscillators, an important finding considering the continued failure to identify pacemakers solely responsible for driving locomotor activity in many well characterized vertebrate spinal locomotor circuits (Ziskind-Conhaim and Hochman, 2017).

In closing, it is interesting to note that glycine is also very important for neurogenesis and cell fate in the zebrafish spinal cord (McDearmid and Drapeau, 2006; Côté and Drapeau, 2012). This opens up the intriguing possibility that the role of glycine in the maturation of spinal locomotor circuits is not restricted to its emerging mechanistic contribution to rhythmogenesis but perhaps to the development of populations that make up the network oscillators.

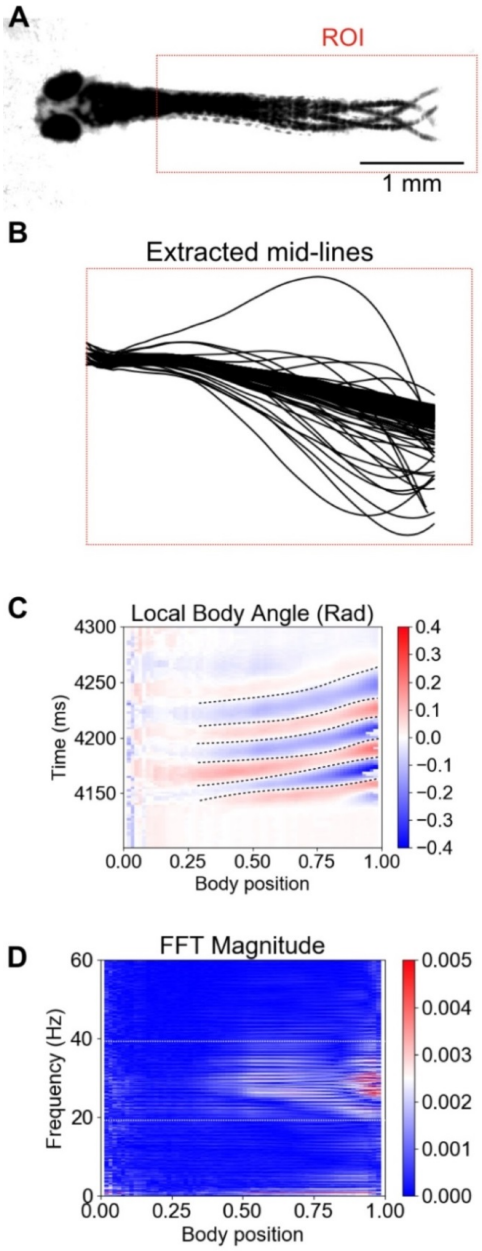

Figure 2.1. Larval zebrafish tail beat frequency during swimming is mainly between 20 and 40 Hz.

A, 4 superposed frames recorded during a single swimming episode of a 4 dpf larval fish. The red dotted box is the region of interest (ROI) in which the frame by frame analysis was performed. B, Examples of extracted midlines of fish body over a swimming episode. C, Heat

map of the local body angle amplitude. The fish body was divided in thirty segments from the caudal to the rostral end. Position of the body has been normalized such that the extreme caudal segment is 1.0 and the extreme rostral segment is 0.0. Every frame, the angle of each segment was computed and compared to resting position. The resulting amplitude was assigned a color, blue for negative angles and red for positive angles. D, For each body segment, a Fast Fourier Transform (FFT) was applied on a swimming episode and the result plotted as a heat map. Note that FFT outputs only positive values. The white dotted box highlights the 20 to 40 Hz range where the frequencies of tail beats seem to reside.

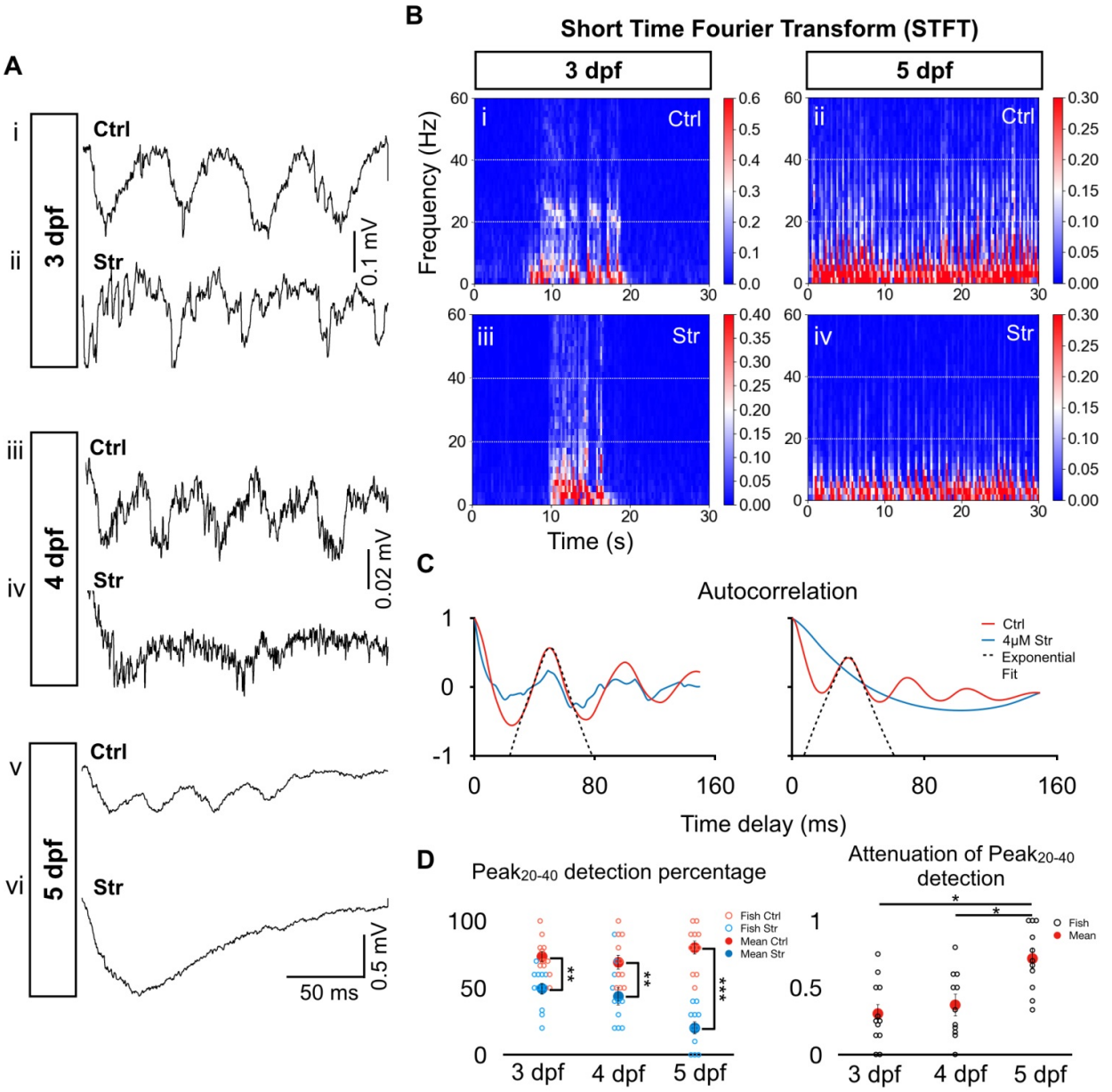

Figure 2.2. Greater effect of strychnine on tail beat rhythmicity at 5 dpf than at 3 and 4 dpf.

***A*,** Typical extracellular recordings of fictive swimming activity under control (Ctrl) and 4 μM strychnine (Str) conditions at 3 dpf (*Ai*, *Aii*), 4 dpf (*Aiii*, *Aiv*) and 5 dpf (*Av*, *Avi*). ***B*,** Short Time Fourier Transform (STFT) of a 30 s long recording of spinal cord activity under control and 4 μM strychnine conditions at 3 dpf (*Bi*, *Bii*) and 5 dpf (*Biii*, *Biv*). White dotted lines mark the

20-40 Hz frequency range. We can see local maxima in the 20-40 Hz range for both 3 dpf plots and the control 5 dpf plot but not for the strychnine positive 5 dpf plot. ***C,*** Example of autocorrelation function of typical 3 dpf and 5 dpf traces (left and right panel, respectively) under control condition (blue) and strychnine (red). A polynomial fit (dashed line) was performed on the 25-50 ms time delay range (dotted box) corresponding to the 20-40 Hz frequency range to detect a peak in this range (see Methods). ***D,*** Left, results from $Peak_{20\text{-}40}$ detection algorithm in the 25-50 ms time delay range for autocorrelation functions under control (blue) and strychnine (red) conditions. Right, attenuation of $Peak_{20\text{-}40}$ detection computed as 1 – ($Peak_{20\text{-}40}$Strychnine / $Peak_{20\text{-}40}$Ctrl). Open circles represent scores of each individual. Solid circles are the averages for every age and condition. N= 120 episodes (10 per fish, 12 fish) at 3 dpf, and N= 110 episodes (10 per fish, 11 fish) at each of 4 dpf and 5 dpf. Left, two-tailed Student's t-test, ** means $p<0.01$ and *** means $p<0.001$. Right, one-way ANOVA followed by Bonferroni's post hoc test, *$p < 0.017$. Top horizontal bars display result of tests between the two groups at each ends of the bars. Error bars display SE.

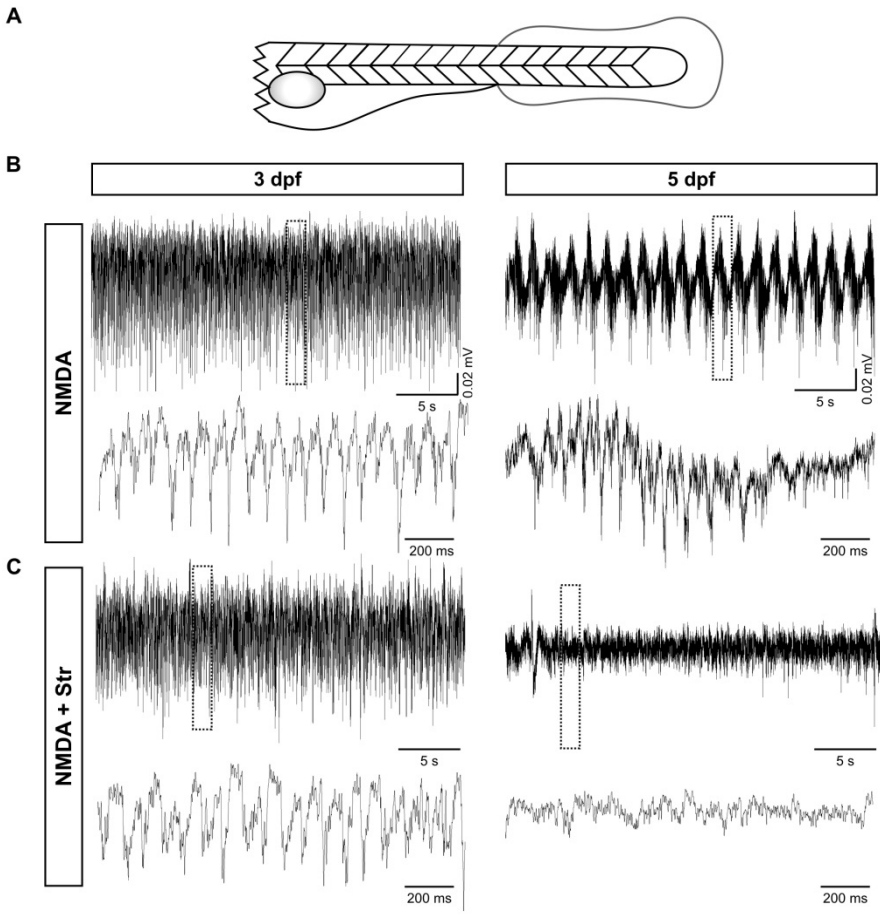

Figure 2.3. Effect of strychnine on fictive swimming in spinalized fish at 3 dpf and 5 dpf.

A, Diagram of the acutely spinalized preparation. Fish were decapitated before transferring to the recording chamber. ***B***, Traces of NMDA (1.2-1.5 mM) induced swimming in spinalized fish at 3 and 5 dpf. Bottom traces are expanded time-scale representation of area within dotted boxes in top traces. ***C***, Traces from the same preparations after addition of 4 μM strychnine, which is present throughout the illustrated recordings.

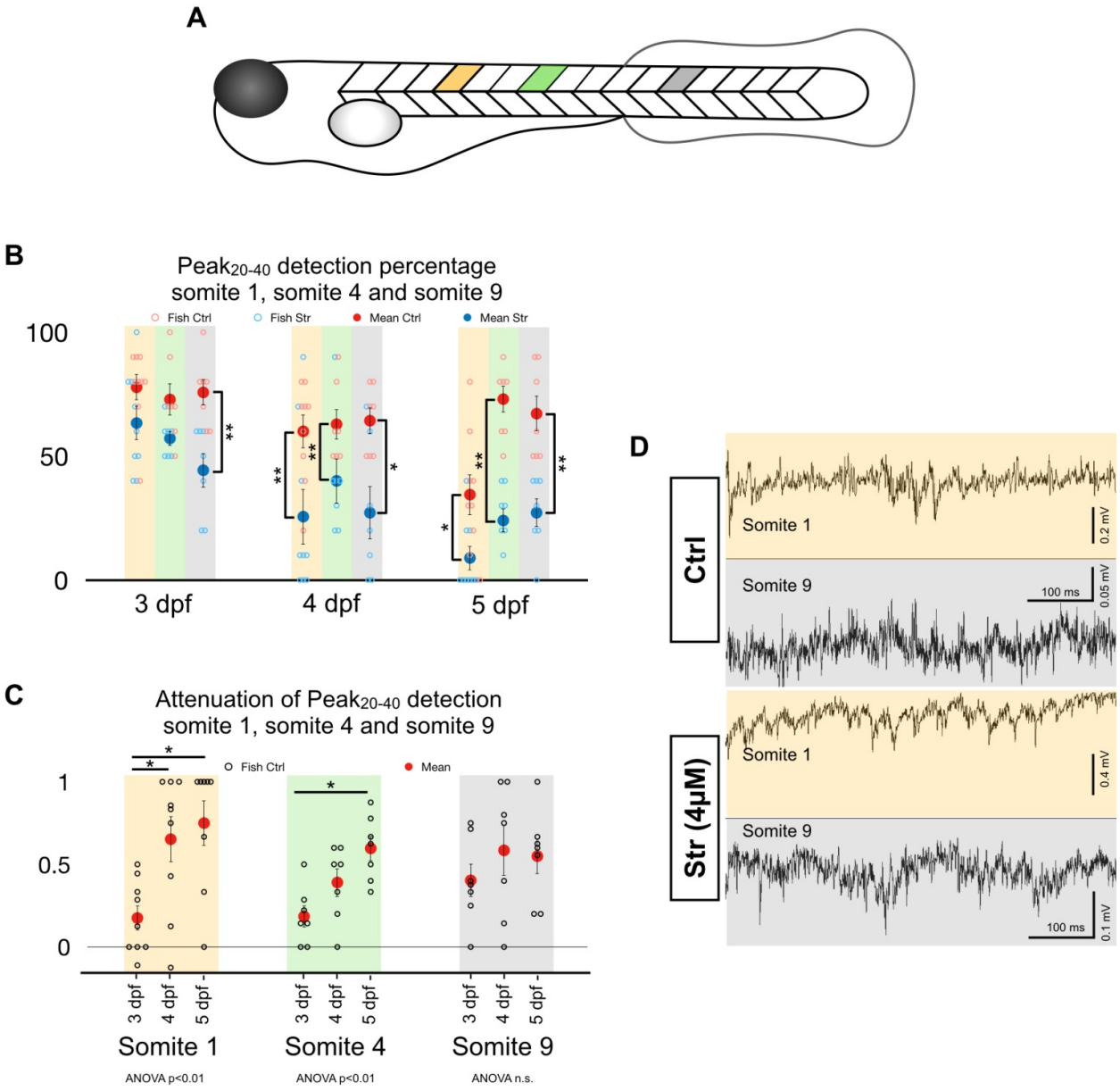

Figure 2.4. Differential effect of strychnine along the rostrocaudal axis of the zebrafish.

***A*,** Schematic of the position at which extracellular recordings were taken: somite 1 (gold), somite 4 (green) and somite 9 (gray). Somites were numbered from 1 to 9 such that that somite 1 was the sixth somite rostral to the anus and somite 9 the third one caudal to the anus. ***B*,** Results from $Peak_{20\text{-}40}$ detection algorithm in the 25-50 ms time delay range for autocorrelation functions under control (blue) and strychnine (red) conditions for somites 1, 4 and 9. N= 10 episodes per

fish in 9 fishes at every age for somites 1, 4 and 9. ***C*,** Attenuation of $Peak_{20\text{-}40}$ detection computed as 1 - ($Peak_{20\text{-}40}$Strychnine / $Peak_{20\text{-}40}$Ctrl) for somites 1, 4 and 9. Open circles represent scores of each individual. Filled circles are the averages for every age and condition. ***D*,** Typical traces of dual recordings from somites 1 and 9 from the same fish (3 dpf) before and after strychnine application. *B*, two-tailed Student's t-test, * means $p<0.05$ and ** means $p<0.01$. *C*, one-way ANOVA followed by Bonferroni's post hoc test, *$p < 0.017$. Top horizontal bars display result of tests between the two groups at each ends of the bars. Error bars display SE.

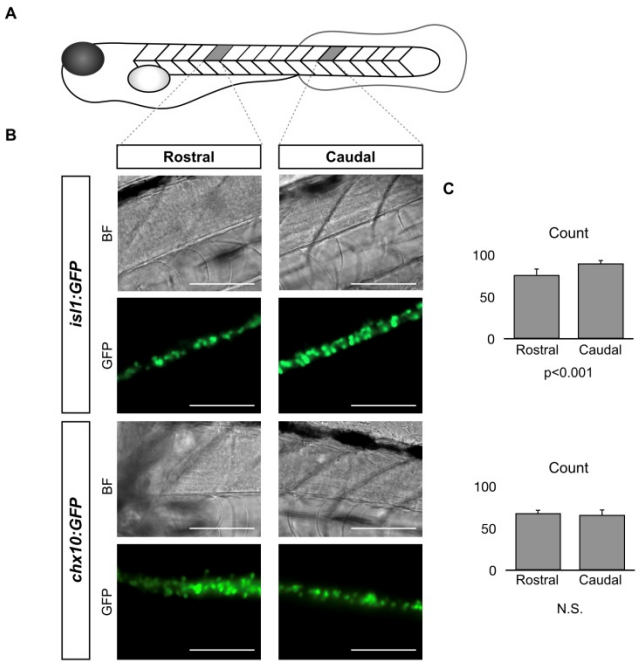

Figure 2.5. Cell count of secondary motoneurons and Chx10^{+} spinal neurons.

***A*,** Schematic of the position at which Z-stacks were imaged. Counting was performed over three somites as camera field of view allowed clear imaging of three somites at 40x. ***B*,** Typical pictures of targeted rostral and caudal section, in brightfield (BF) and fluorescent (GFP) conditions for a *isl1:GFP* and a *chx10:GFP* fish. ***C*,** Average cell count for the rostral and caudal section for the *isl1:GFP* (top) and *chx10:GFP* (bottom) fish. Average was computed from 4 independent counts of 3 fish for each configuration (Rostral/Caudal/*isl1:GFP*/*chx10:GFP)*). Two-tailed Student's t-test. Error bar represents SD.

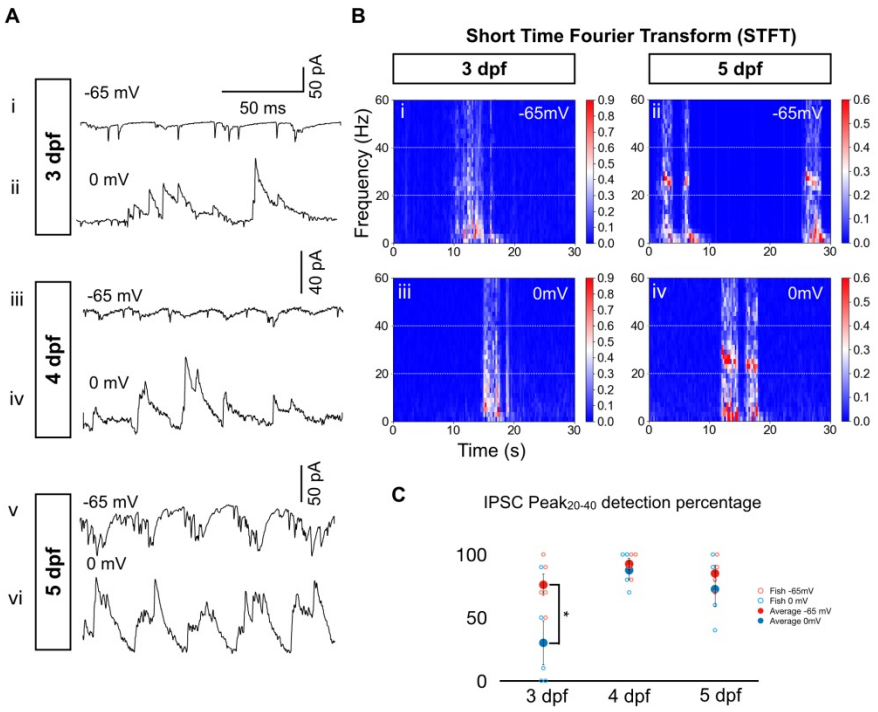

Figure 2.6. IPSCs mature from arrhythmic at 3 dpf to rhythmic with a frequency close to that of tail beats at 5 dpf during swimming episodes.

A*,** Typical voltage-clamp recordings of MNs during swimming activity at resting (-65mV) and cation reversal potentials (0mV) for 3 dpf (*Ai*, *Aii*), 4 dpf (*Aiii*, *Aiv*) and 5 dpf fish (*Av*, *Avi*). ***B, Short Time Fourier Transform (STFT) of a 30 s long recording of spinal cord activity under control and strychnine conditions at 3 dpf (*Bi*, *Bii*) and 5 dpf (*Biii*, *Biv*). White dotted lines mark the 20-40 Hz frequency range. We can observe local maxima in the 20-40 Hz range for both 5 dpf plots but not for the 0 mV 3 dpf plot. ***C***, Results from $Peak_{20\text{-}40}$ detection algorithm in the 25-50 ms time delay range for autocorrelation functions of each traces at 3, 4 and 5 dpf at -65 mV (blue) and 0mV (red) holding potentials. N = 10 episodes per sMN in 5 sMN at 3 dpf, in 4 sMN at 4 dpf and 4 sMN at 5 dpf. Error bars display SE. Two-tailed Student's t-test, * means $p<0.05$.

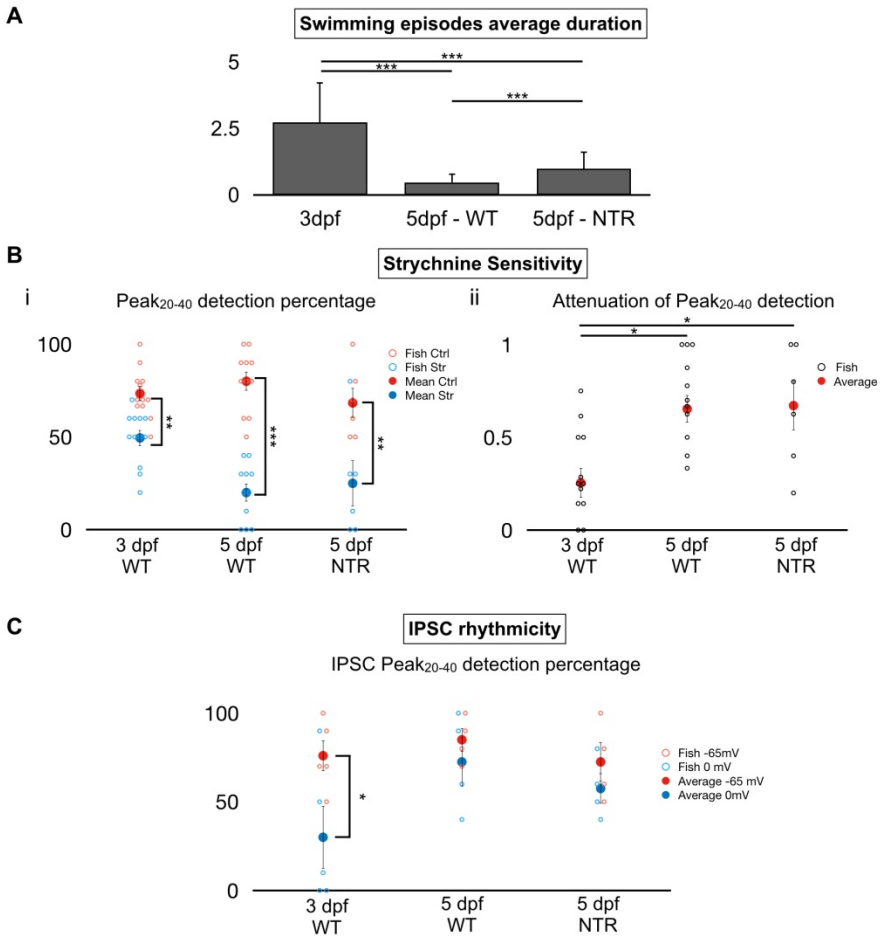

Figure 2.7. Metronidazole-treated Tg(*dat:NTR-CFP*) fish exhibit a development profile closer to 5 dpf rather than 3 dpf.

***A*,** Average swimming episode duration (in seconds) calculated for 50 episodes (10 per fish for 5 fishes) at 3 dpf and 5 dpf for WT fish and at 5 dpf only for metronidazole-treated Tg(*dat*:*NTR-CFP*) fish (NTR). ***B*,** Results from $Peak_{20\text{-}40}$ detection algorithm in the 25-50 ms time delay range for autocorrelation functions of each extracellular recording at 3 and 5 dpf for WT and at 5 dpf for metronidazole-treated Tg(*dat*:*NTR-CFP*) fish under control (blue) and strychnine (red) conditions (*Bi*). Attenuation of $Peak_{20\text{-}40}$ detection computed as 1 - ($Peak_{20\text{-}40}$Strychnine / $Peak_{20\text{-}40}$Ctrl) for each fish. N= 60 episodes (10 per fish for 6 fish) for 5 dpf Tg(*dat*:*NTR-CFP*)

fish (*Bii*). ***C,*** Results from $Peak_{20\text{-}40}$ detection algorithm in the 25-50 ms time delay range for autocorrelation functions of each patch recordings at 3 and 5 dpf for WT and 5 dpf for metronidazole-treated Tg(*dat*:*NTR*-*CFP*) fish at -65 mV (blue) and 0mV (red) holding potentials . N= 50 episodes (5 fish) for 5 dpf Tg(*dat*:*NTR*-*CFP*) fish. Open circles represent scores of each individual. Solid circles are the averages for every age and condition. *Bi* and *C*, two-tailed Student's t-test, * means $p<0.05$, ** means $p<0.01$, and *** means $p<0.001$. *Bii*, one-way ANOVA followed by Bonferroni's post hoc test, $*p < 0.017$. Top horizontal bars display result of tests between the two groups at each ends of the bars. Error bars display SD for *A*, SE for *B* and *C*.

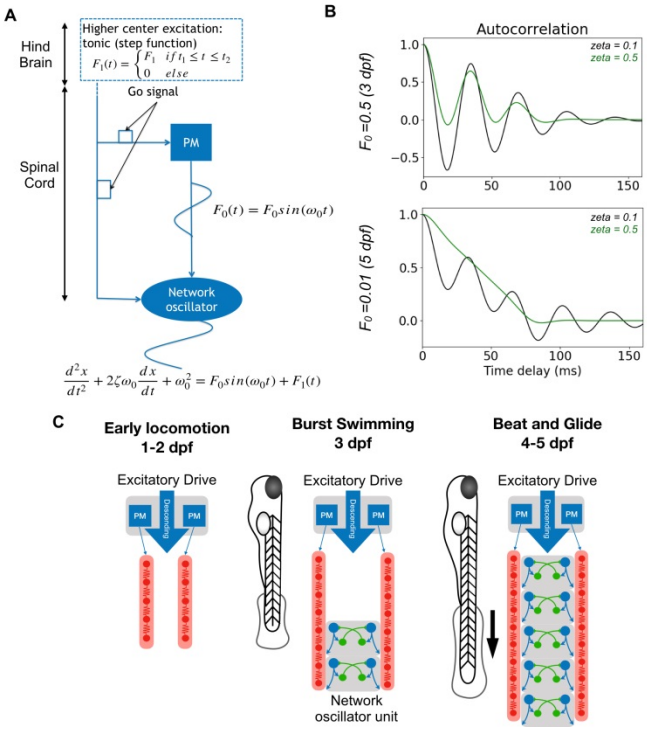

Figure 2.8. Coupled oscillator model of architectural change from pacemaker to network oscillator-based spinal locomotor circuits of developing zebrafish.

***A*,** Schematic of coupled oscillators model. Two coupled oscillators: a harmonic oscillator representing a pacemaker (PM) kernel and a damped oscillator representing a half-centre network oscillator. The coupling coefficient F_0 represents either the developmental stage or the presence (or absence) of gap-junctions. The damping coefficient models the application or absence of strychnine. The output of the network is read at the output of the half-centre. ***B*,** Autocorrelation analysis of model output. ***C*,** Schematics of the development of spinal locomotor circuits from 3 to 5 dpf. Before 3 dpf, a kernel of IC drives, via gap junctions, two contralateral chains of electrically coupled MNs distributed along the body. Reciprocal inhibition between both sides, which is not illustrated, exists but is not responsible for rhythm generation. After 3

dpf, network oscillators are assembled, first at caudal end of the spinal cord and then across the length of the spinal cord.

CHAPTER 2: TESTING MECHANISMS OF RHYTHMOGENESIS IN SPINAL LOCOMOTOR CIRCUITS OF THE DEVELOPING ZEBRAFISH SPINAL CORD

Roussel, Yann; and Bui, Tuan Vu

ABSTRACT

Rhythm generation is a key feature of many central pattern generator networks. Two general mechanisms have been proposed to enable rhythm generation in neural circuits. While the first mechanism is based on pacemaker neurons (PM) intrinsic properties to produce neural circuits rhythmic oscillation, the other mechanism is based on particular synaptic connections patterns to create a network oscillator. Our previous work suggests a transition in the mode of operation for rhythmogenesis in spinal locomotor circuits of the zebrafish showing that it becomes increasingly reliant upon glycinergic neurotransmission. Thus, this results suggest a transition from rostral PM kernels of IC neurons to network oscillators to generate tail beats rhythm. Here we investigate the potential redundancy of the rhythm generating mechanism in the Zebrafish spinal cord during its development. We first tested for presence of other PM neurons more caudally located using ZAP patch-clamp recordings. Then, we disrupted rhythmogenic properties of known IC PM neurons using riluzole or carbenoxolone while looking at the rhythmicity of the locomotor output through extracellular recordings. We finally further characterized the synaptic drive of the putative network oscillators using dual patch recordings of secondary motoneurons. We found no convincing candidate for caudal PM neurons and we also observed that the effect of riluzole on rhythmogenesis was decreasing over the studied developmental period between (3-5 days-post-fertilization). These results strengthen previous findings suggesting a progressive disengagement of PM neurons supplanted by network oscillators.

Introduction

Rhythm generation is a key feature of many central pattern generator networks. Two general mechanisms have been proposed to enable rhythm generation in neural circuits. The first mechanism is based on intrinsic properties enabling some neurons, the so-called pacemaker neurons (PM), to exhibit endogenous bursting activity when excited. The other mechanism is based on network properties, in particular patterns of synaptic connections, which facilitate oscillations in populations of neurons that are not inherently rhythmic, hence creating a network oscillator (Harris-Warrick, 2010). Network oscillators often feature reciprocal inhibition between two antagonistic units (or half-centres) that oscillate out of phase. A good example of a network oscillator architecture is the half-centre model in which two "centers" reciprocally inhibit each other to ensure that when one half-centre is active, the other half-centre is silent. This architecture is capable of converting a tonic drive into rhythmic activity with alternations between each half-centre.

Locomotor activity is an ideal neural output for studying mechanisms for rhythm generation. This robust and stereotypical behaviour encoded in spinal circuits has been proposed to be based either on PM neurons or network oscillators across different neural locomotor circuits (Harris-Warrick, 2002; Brownstone and Wilson, 2008; Grillner and Jessell, 2009; Brocard et al., 2010; Li, 2011). In the zebrafish, swimming is characterized by successive contractile waves leading to left/right body bend alternations propagating along the rostrocaudal axis of the body (McDearmid and Drapeau, 2006). However, before swimming in zebrafish reaches its final mature form, locomotor behaviour in zebrafish goes through an incremental

maturation process during development. The maturation of swimming starts early after the first day post-fertilization (1 dpf) when the first observable locomotor behaviour appears characterized by a strong coil on one side of the body before coming back to resting position. It is quickly followed by double-coiling (i.e. two successive coils on each side of the body) before maturing to swimming after 2 dpf. From here, two successive forms of swimming follow, the early form is characterized by second-long, infrequent bursts of activity (referred as burst swimming), while the later form consists of trains of shorter (~200 ms long), more frequent bursts of activity interspaced by short quiescent periods (referred as beat-and-glide) appearing at 4 dpf.

Our recent work suggests that the refinement of swimming involves transitions in how the rhythm driving tail beats during swimming episodes is generated. Early in development when fish exhibit coiling or burst swimming, the mechanism of tail beat rhythm generation is putatively supported by kernels of a small number of rostral PM neurons rhythmically driving motoneurons (MNs) via gap-junctions (Saint-Amant and Drapeau, 2001). These PM neurons, identified as Ipsilateral caudal (IC) neurons, express persistent sodium current ($I_{Na,P}$) granting them pacemaking properties (Tong and McDearmid, 2012). Later in development as fish transition from burst to beat-and-glide swimming, network oscillators may play a more prominent role in rhythm generation as evidenced by our most recent work (Chapter 2).

Therefore, several rhythmogenic circuits may be operating in the developing zebrafish spinal cord. We first asked whether there are additional rhythmogenic circuits in the spinal cord beyond those that we have described. Here we tested the hypothesis that new PM population are involved by exploring the potential rhythmogenic intrinsic properties of caudal spinal neurons.

We were unable to reveal additional rhythmogenic circuits or mechanisms. We then asked whether both the IC-based pacemaker kernel and the network oscillators participate equally in generating rhythmic tail beats in developing larval zebrafish. Thus, we tested whether perturbing the rhythmogenic activity of IC neurons by blocking gap junctions as well as persistent sodium current compromised the rhythm of tail beats. Finally, having shown the primacy of network oscillators to the rhythm of tail beats in the larval zebrafish, we further explored the network oscillator hypothesis by performing dual patch experiments of secondary MNs to characterize the precise timing between glutamatergic and glycinergic drive.

Methods

Animal Care

Adult wild-type zebrafish were maintained according to standard procedures (Westerfield, 2000). All experiments were performed in accordance with the protocol approved by the University of Ottawa animal care committee (BL-2038). Light cycle in the zebrafish room was designed as follows: 14hr light/10hr dark, lights-on at 9:00AM and lights-off at 11:00PM. Water conditions of the fish system were controlled and maintained in the following ranges: 29–30°C, pH 7.5–8.0, conductivity (EC) 690–710. Zebrafish embryos were collected right after breeding and transferred in 10 cm diameter plastic petri dishes. Petri dishes were placed in an incubator maintained at 28.5°C.

Animal preparation for electrophysiology

2 to 5 dpf fish were anaesthetized in 0.02% tricaine solution and pinned down through the notochord in a Sylgard (Dow Corning, Midland, MI, USA) coated dish, one pin above the swim bladder and a second one caudal to the anus. 0.01 mm tungsten wires were used as pins. A skin flap was performed near one of the pins to remove the rest of the skin between the two pins using very fine forceps. The fish was then bathed in aCSF (134 mM NaCl, 2.9 mM KCl, 1.2 mM $MgCl_2$, 2.1 mM $CaCl_2$, 10 mM dextrose, 10 mM HEPES) containing 1mg/mL collagenase solution for 20 minutes. Muscles were removed over 5-6 somites by applying suction through a 15 μm glass micropipette.

Extracellular recordings

10 µm borosilicate glass microelectrodes were backfilled with 2M NaCl solution. We approached the spinal cord targeting a zone just dorsal to a ventral root and a very light suction was applied to seal the ventral root and a part of the spinal cord. Electrical activity was recorded in current clamp mode, amplified and filtered at 1 kHz with a Multiclamp 700B from Axon Instruments (Molecular Devices, Sunnyvale, CA, USA) and finally digitized with a Digidata 1550 (Molecular Devices) to be stored on a computer. Light pulses were occasionally applied to increase occurrence of swimming events. Both spontaneous and light evoked swimming events were merged together since no significant difference in duration and tail beat frequency was observed (Buss and Drapeau, 2001).

Intracellular recordings

After muscle removal, 10 MΩ borosilicate glass microelectrodes were backfilled with intracellular recording solution (16mM KCl, 116mM K-gluconate, 4mM $MgCl_2$, 10 mM HEPES, 10 mM EGTA) and targeted neurons were approached while applying a light positive pressure. Just before entering the spinal cord the electrode was briefly stopped in order to break the dura with positive pressure only. Then, the electrode was introduced in the spinal cord and positive pressure was slightly decreased to finalize the approach. After ensuring that no tissue was present between the micropipette tip and the targeted MN, pressure was released allowing formation of a GΩ seal in most cases. In some cases, very light suction was applied in order to form a seal. A holding potential of -65 mV was then applied and after capacitance compensation, the seal was broken with a series of light suction pulses. Sulforhodamine (*Sigma-aldrich*) was present in ICS allowing neuron classification based on morphological features via fluorescence imaging.

ZAP

To perform the resonant frequency analysis of spinal neurons, we used a ZAP (Ulrich, 2014) function to scan all the frequencies from 0.1 to 200 Hz in 60s in current clamp mode:

$$I(t) = I_A + I_0 sin(f_{min}(\frac{f_{Max}}{f_{min}})^{\frac{t}{T}} \bullet 2\pi t)$$

I_A being a constant current injection to hold the cell near desired membrane potential; I_0 chosen to keep the membrane oscillations in a range of 5 mV; f_{min} and f_{max} are the extremum of the frequency range we desire to scan (here 0.1 and 200 Hz respectively) and T the maximum time of the scan (60 s). We applied CNQX (10 µM, *Tocris*) and DL-AP5 (50 µM, *Tocris*) to chemically isolate the cells from rhythmic inputs that could impair the experiment. *r*

Data Analysis

Impedance fitting

Impedance profiles (Z) were computed as the square root ratio of the power spectrum of the membrane potential trace over the injected current trace:

$$Z = \sqrt{\frac{PS(V_m)}{PS(I)}}$$

Then Z profiles were fitted as a sum of two exponentials using Clampfit fitting algorithms.

$$Z_{fit} = \sum_{i=1}^{2} A_i e^{a_i \bullet f} + C$$

Two exponentials were chosen since the first exponential provides the typical low-pass filter information from the classic RC circuit formed by the membrane resistance and membrane capacitance whereas the second exponential provides information on frequency preferences (Hutcheon and Yarom, 2000).

Computation of Z extrema

The fitted expressions were then used to find local extrema representing the frequency at which the cell response was largest (i.e. frequency preference). Null values of the derivative were computed. Two exponential fittings have the advantage to give an analytical response for this problem:

$$\frac{dZ_{fit}}{df} = 0 \Leftrightarrow f_{max} = -\frac{ln(a_0 A_0) + ln(a_1 A_1)}{a_0 + a_1}$$

Given $a_0 \bullet A_0 > 0$; $a_1 \bullet A_1 > 0$ and $a_0 + a_1 \neq 0$ which is respected in most fits. Otherwise if f_{max} was undefined or if the expression gave us negative values for f_{max}, we then recorded $f_{max} = 0$.

Autocorrelation and Peak$_{20\text{-}40}$ detection

In order to quantify the effect of strychnine on rhythmic motor activity, and of different holding potentials on IPSCs, we developed a simple peak detection algorithm to detect the presence of a peak between 20 and 40 Hz in the autocorrelation function of each episode trace (Peak$_{20\text{-}40}$). Raw traces were first band-pass filtered between 1 and 200Hz. Ten 200 ms epochs were extracted during swimming episodes. Because the fictive swimming behaviour evolves from a few long

bursts (several seconds) at 3 dpf to multiple shorter (few hundreds of ms) bursts at 5 dpf, we chose 200 ms epochs from recordings at all ages to keep the analysis consistent. Autocorrelation functions were computed for each time-slice using Clampfit. Then the Autocorrelation function was fitted as a second order polynomial function (in Clampfit).

$$Autocorr_{fit}(\tau) = a_0 + a_1 \bullet \tau + a_2 \bullet \tau^2$$

The fit was performed between 25 and 50 ms time delay (x-axis of the autocorrelation function) corresponding to the targeted range of frequency for tail beats (20-40 Hz). Finally, the following conditions were applied on the fitting parameters:

$$25ms < \frac{-a_1}{2a_2} < 50ms \qquad \text{and} \qquad a_2 < 0$$

Only if all conditions were respected was a peak considered to be detected. Using the above conditions for all our experiments gave us an average $Peak_{20\text{-}40}$ detection rate above 80% under control conditions. Animals where the $Peak_{20\text{-}40}$ score of recorded swimming episodes in the absence of any pharmacological interventions were all smaller than 0.6 (meaning that a peak in the autocorrelation was detected between 25 and 50 ms less than 60% of the time) were considered as arrhythmic and their recordings were discarded.

PCA and k-means clustering

PCA and k-means clustering were performed using Orange v3.3, an open access Python based environment dedicated for data analysis. Neuron parameters were composed of 7 features: the five fitting parameters A_1, τ_1, A_2, τ_2 and C as well as the resting potential V_r and F_{max} the frequency at which the impedance is maximal. The first four principal components of the PCA

captured 92 % of the data variance. K-means clustering was first performed with a target of 4 clusters to try to force differentiation of neurons based on their identified functional class (MNs, V2as, VINs and dINs) or age (2, 3, 4 and 5 dpf). None of the clustering gave satisfactory results. Similarly k-means clustering with 2 clusters to try to differentiate neurons expressing resonant frequencies from the ones that did not was also performed. Resulting cluster could classify resonating neurons from others but the critical frequency was between 1.3 and 1.72 Hz.

Results

Lack of spinal neurons with subthreshold rhythmogenic intrinsic properties

The rhythms of some central pattern generators seem to be driven by the oscillations of individual neurons, i.e. pacemaker neurons (Harris-Warrick, 2010). These pacemaker neurons are endowed with intrinsic properties conferring endogenous bursting properties. Previous work has shown that intrinsic properties can set frequency preferences in individual pacemaker neurons that coincide with the frequency range of network activity (Tseng and Nadim, 2010; Tseng et al., 2014; Hull et al., 2016). In zebrafish, such pacemaker neurons exist. They are located very rostrally in the spinal cord and are thought to drive early locomotor behaviour (Tong and McDearmid, 2012). Considering the increasingly larger size of the spinal cord as zebrafish develop, we hypothesized that other neuron population with PM properties could be found more caudally in the spinal cord. In order to test whether intrinsic properties could be linked to rhythmic generation of tail beats in caudal spinal neurons, we performed an analysis of subthreshold frequency preferences in spinal neurons located in the middle segments of the spinal cord (near the anus) in the larval zebrafish. Subthreshold properties were preferentially tested since suprathreshold properties (i.e. firing activity) seem to be far above the targeted frequency range (80-300 Hz compared to 20-40 Hz) of network oscillations in most identified spinal neurons (Supp. Data; Menelaou and McLean, 2012). In order to do so, recorded spinal neurons were scanned in the frequency domain by applying a 60s long sinusoidal current waveform with gradually increasing frequency (ZAP function) between 0.1 Hz and 200 Hz (Ulrich, 2014). The amplitude of the injected current was adjusted to keep the membrane oscillations within a 5 mV range.

Impedance (Z) profiles were computed as the square root ratio of the power spectrums of the membrane potential trace over the injected current trace and fitted as a sum of two exponential (Fig. 3.1*B*). Z local maxima, indicating preferred frequencies, were extracted as null values of the derivative. The distribution of preferred frequencies clearly shows that most of the 59 tested neurons (19 motoneurons, 34 interneurons and 6 unknown) have none (i.e. maximum is at 0 Hz). While a few cells exhibit a non-null resonant frequency, their resonant frequencies are widely distributed between 2 to 8 Hz never reaching the required minimum of 20 Hz to match tail beat frequencies of larval zebrafish (Fig. 3.1*C*). We weren't able to test IC interneurons that are putative pacemakers in embryonic zebrafish (1 dpf) (Tong and McDearmid, 2012) as they are more difficult to access at later stages of development because of their deep location within the spinal cord (Bernhardt et al., 1990)**.** We conclude from this analysis that intrinsic properties of most spinal neurons do not predispose caudal spinal circuits to drive tail beats within frequencies observed during swimming.

Additionally, some PCA and k-means clustering analysis were performed on fitting parameters as well as other measurements of passive properties of our recorded neurons (7 features in total: five fitting parameters A_1, τ_1, A_2, τ_2 and C as well as the resting potential V_r and F_{max} the frequency at which the impedance is maximal) to investigate whether we could classify spinal neurons according to their impedance profiles. PCA extracts orthogonally-related principal components that capture the greatest variance in the data. Thus, it provides a useful projection of the feature space (e.g. from a 7 dimension features space to a 4 dimensions space after PCA) to

better capture the overall distribution of the data. K-means clustering on the other hand is a classification method that was used to group together recorded neurons sharing similar features. We thus used k-means clustering using the results of the PCA to test whether our recorded neurons could be clustered in a way that reflected their putative functional grouping (MNs, V2as, dINs and VINs) as determined by location within the spinal cord and cell morphology of recorded cells or clustered in a way that reflected the developmental stages at which they were recorded (2, 3, 4 and 5 dpf) were performed using 4 clusters. Unfortunately, this analysis lead to inconclusive results (Fig. 3.1*Di),* as each cluster was composed of neurons from the different functional classes sampled (Fig. 3.1*Ei)* or from the different ages (data not shown). Additional k-means clustering performed while setting the number of clusters to 2 was performed to determine whether the resultant two clusters could differentiate between Z profiles exhibiting resonant frequencies and those which did not. The resulting two clusters managed to segregate neurons having a resonant frequency from those which do not (the dotted line Fig. 3.1*Eii* depicts the critical frequency separating the two clusters). However, classification according to their preference in frequency was not consistent with any functional or morphological classification (Fig. 3.1*Dii, Eii)*. For instance, some CiD (i.e. V2a) or motoneurons (MNs) showed frequency preferences but not most of them. No differentiation could be made according to the developmental stage either (data not shown). Therefore, our analysis suggests that there are few neurons in the developing (3-5 dpf) zebrafish spinal cord that exhibit pacemaker properties, and they don't belong to any particular functional group nor are related to any particular age.

Gap junctions are dispensable to the rhythmic tail beats after 3 dpf

Since we were not able to show that there were other rhythmogenic pacemaker neurons along the length of the spinal cord, we next asked whether the IC pacemaker kernel and the network oscillators that we describe in our previous work (Chapter 2), equally contribute to the rhythm driving tail beats. Early locomotor behaviour between 1-3 dpf, putatively driven by IC neurons, mostly relies on a preliminary electrical scaffold built upon gap junctions (Saint-Amant and Drapeau, 2001). At this age, locomotor activity is more resistant to blocking glycinergic neurotransmission than at 5 dpf when fish exhibit beat-and-glide swimming. To test the idea that the strychnine-resistant rhythm at 3 and 4 dpf could be generated by this electrical circuit, we added 500 μM carbenoxolone (a gap junction blocker) with strychnine and recorded fictive swimming activity at 3 and 4 dpf. With the addition of carbenoxolone to strychnine, traces show that swimming activity is more consistently disrupted compared to experiments with strychnine alone (Fig. 3.2*Ai,ii,* see also chapter 2). From here we used our previously developed peak detection algorithm to quantify the effect of carbenoxolone (See Methods). Briefly, we used autocorrelation functions of fictive swimming episodes to look at the presence of a peak in the tailbeat frequency range (i.e. between 20-40 Hz corresponding to 25-50 ms time delay). The resulting $Peak_{20\text{-}40}$ detection score shows a significant gap between the detection score under control and combined strychnine and carbenoxolone conditions (Fig. 3.2*B*). When carbenoxolone alone is added while recording from 3 dpf fish, we observe a much fainter (comparing the attenuation of peak detection) yet significant difference in peak detection score between control and carbenoxolone alone (Fig. 3.2*C-D*). Conversely, we treated 5 dpf fish with carbenoxolone only (since we had shown that strychnine already had an important effect at 5 dpf, Chapter 2). Typical rhythmic swimming activity is clearly noticeable even after drug application (Fig.

3.2*Aiii,iv*) and the probability of peak detection between carbenoxolone and control does not differ at this later age. Finally, attenuation of peak detections at 3 dpf from experiments using strychnine alone (Chapter 2) is significantly smaller than the attenuation from experiments using a cocktail of strychnine and carbenoxolone. No significant difference is seen at 4 dpf (Fig. 3.2*D*).

To make sure that the brain did not intervene we repeated these experiments but with spinalized preparations. Fictive swimming was evoked using 1 mM NMDA and carbenoxolone was added a few minutes after. Addition of the drug did not disturb the continuous fictive swimming rhythm observed as suggested by typical traces and power spectrums (Fig. 3.2*E,F*). Overall, these results suggest that electrical synapses reinforce but are not entirely necessary for rhythm generation driving tail beats at 3 dpf and that gap junctions are fully dispensable for rhythm generation driving tail beats at 4 and 5 dpf.

Blocking persistent sodium current decreases the rhythm of tail beats in burst swimming fish

We also tried to specifically target the ionic current responsible for pacemaker activity in IC cells, the persistent sodium current $I_{Na,P}$. Riluzole is known to block this current (Urbani and Belluzzi, 2000; Darbon et al., 2004; Tong and McDearmid, 2012), so we therefore recorded swimming activity of the spinal cord with and without riluzole (5µM) at 3, 4 and 5 dpf. The $Peak_{20\text{-}40}$ detection scores show significant effect of riluzole on the rhythm of tail beats at 3 dpf only (Fig. 3.3*A*). As done previously for the study of gap junctions, experiments with riluzole were repeated with spinalized experiments. One out of two experiments on spinalized 3 dpf fish showed persistence of rhythm under riluzole (Fig. 3.3*B,*C), however once both strychnine and

riluzole were added the rhythm completely disappeared as activity was silenced (note however, n = 1 animal).

Whole-cell patch-clamp recordings of MNs in 5 dpf fish show typical trains of short episodes of activity that is a signature of beat-and-glide swimming (Fig. 3.3*Di,* shaded area on typical traces highlight a single episode in one train). In each of these episodes, oscillations believed to drive the tail beats can be observed (Fig. 3.3*Dii, Eii, Fii*). Even though our extracellular recordings suggest that after 3 dpf, riluzole (5 μM) ceased to affect the rhythm driving tail beats (Fig 3.3*A*), our intracellular recordings of MNs suggests that riluzole triggered a two-fold increase in amplitude of episodes from 4.29 ± 1.47 mV (n = 29 episodes) to 8.88 ± 3.02 mV (n = 35 episodes) (Fig. 3.3*Diii, Eiii, Fiii*). The number of episodes per train slightly increased as well from 5.2 ± 1.6 episodes (n = 9 trains of episodes over a 2 min period) per train to 6.5 ± 1.0 episodes (n = 7 trains over a 2 min period) per train. While duration of episodes was similar, from 303 ± 85 ms (n= 47 episodes) under control to 330 ± 78 ms (n = 39 episodes) under riluzole, episode frequency within a train of episodes slightly decreased from 1.97 ± 0.86 Hz to 1.38 ± 0.54 Hz, respectively. These results suggest that $I_{Na,P}$ is present throughout zebrafish development but its involvement in rhythm generation decreases after 3 dpf.

Dual patch-clamp recordings further confirm establishment of network oscillators at 5 dpf

The void in sustaining rhythm generation of tail beats due to the gradual absence of involvement of $I_{Na,P}$ is putatively filled in by network oscillators (Chapter 2). We previously described that glycinergic inputs in secondary MNs (sMNs) in the zebrafish spinal cord transitioned around 80 hpf from arrhythmic to rhythmic. The timing of this transition coincided with the transition from

a weakly glycine-dependent rhythm to a strongly glycine-dependent rhythm that we interpreted as a switch from pacemaker to network oscillator mode of rhythmogenesis. To further investigate the precise timing of these newly rhythmic glycinergic inputs in relation to rhythmic excitatory inputs during swimming we proceeded to dual patch-clamp recordings of sMNs so that we could compare one type of synaptic drive received by one sMN with that received by another during locomotor output. We chose to record sMNs spaced apart by 4 to 6 somites to concurrently investigate the phase delay of the synaptic inputs along the rostrocaudal axis. Pairs of recorded cells were either both held near the reversal potential of glycinergic synapses (-65 mV) to record glutamatergic EPSCs (Fig. 3.4*Ai*), at positive potentials near the reversal potential of glutamatergic synapses (around +10 mV) to record glycinergic IPSCs (Fig. 3.4*Bi*) or in a hybrid configuration (one cell at resting potential and the other at +10 mV) (Fig. 3.4*Ci*). Crosscorrelation of swimming episodes from the rostral versus the caudal sMN were computed for each configuration to estimate the phase-delay of EPSCs and IPSCs arriving at each respective sMN. The first two configurations (both held at resting potential or at positive potential) show a local maximum at 0 ms time delay (Fig. 3.4*Aii, Bii*), suggesting that EPSCs arrive in phase in both MNs and IPSCs also arrive in phase with each other in both MNs. Finally, in the third configuration (hybrid) where we held one cell at resting potential to study the EPSCs received by this cell while the second cell is held at depolarized potentials isolating IPSCs, crosscorrelations functions of swimming episodes showed a local minimum near 0 ms lag (Fig. 3.4*Cii*) suggesting that EPSCs and IPSCs are mostly out of phase. Crosscorrelation in hybrid configuration were performed between the trace at resting potential and the inverse of the trace at positive holding potential so that synaptic currents were of the same sign and crosscorrelation

measures could be more easily interpreted. Alternating EPSPs and IPSPs input is concomitant with a network oscillator organization.

Interestingly, patch-clamp experiments did not allow us to make conclusions on the direction of propagation of the excitatory drive of MNs as averaging crosscorrelations from resting potential traces gave a maximum exactly at 0ms (Fig. 3.4*Aii*) suggesting no phase delay between rostral and caudal MNs. Some episodes gave a positive phase delay while other a negative one. This is in contrast to results obtained with extracellular recording (Fig. 3.4*Di*), where crosscorrelations function of swimming episodes between a rostral somite and a caudal somite 8 segments apart consistently had a maximum at a positive time delay suggesting descending excitatory waves (Fig. 3.4*Dii*). These suggest that, individual ipsilateral motoneurons do not reflect the precise timing of descending inputs suggested by recordings of pools of motoneurons (through extracellular recordings of motor nerves).

Discussion

Early in development, locomotor movements of zebrafish seem to be generated by neural circuits driven by a pacemaker kernel setting the timing of movements. Our recent work has identified the presence of circuits organized as network oscillators that rely more on synaptic connections than on intrinsic properties for rhythmogenesis. There seems therefore to be several circuits that can rhythmically drive swimming movements in zebrafish. We sought to identify additional cells or circuits for rhythmogenesis, and after failing to identify any other pacemaker cells, we sought to determine whether the pacemaker kernel and the network oscillators contribute equally to driving rhythmic tail beats in later stages of development when fish transition from burst to beat-and-glide swimming.

Taken together, our results reinforce the idea that later on in development PM-driven rhythm generation is superseded by network oscillators within the spinal cord. We were unable to find any good PM candidate in caudal spinal neurons when we searched for cells with subthreshold active conductances that would endow them with resonant frequencies. A potential reason for our failure to identify more caudally located pacemaker cells could be due to the high activity dependency of the impedance. Impedance is very dependent on the membrane potential, and we made the choice of scanning over a small range of the subthreshold membrane potential because the firing frequency of most cells seems to be too fast for the rhythm of tail beats (Menelaou and McLean, 2012; *Supp. Data*). However, a more extensive scan in the membrane potential domain to complement our scan of the frequency domain could reveal hidden pacemakers though it is to be noted that membrane potential and oscillations cannot be uncoupled easily due to the non-linear dynamics of many active conductances. Nonetheless, the

search for resonant frequency using the ZAP technique has previously been demonstrated to be useful in revealing typical pacemaker behaviour in the thalamus as well as in the crab stomatogastric ganglion (Nowak et al., 1997; Enomoto et al., 2007; Tseng et al., 2014). We therefore suggest that the negative results of our search for resonant frequencies indicate an absence of PMs in the caudal spinal cord of the developing zebrafish.

In contrast to our failure to reveal any pacemakers in the caudal spinal cord of the larval zebrafish, we observed that EPSPs and IPSPs to sMNs are rhythmic and out of phase with each other. In the classic half-centre architecture of network oscillators, a key feature is the presence of reciprocal inhibition that provides an inhibitory drive out of phase with the excitatory drive in the output neurons. This finding coupled with our previous work (Chapter 2) strongly advocates for a typical half-centre architecture in spinal swimming circuits of the zebrafish underlying more mature swimming movements.

Experiments using carbenoxolone and riluzole further strengthen the idea of a switch from PM based architecture toward network oscillator-based architecture for tail beat rhythm generation. These drugs targeted gap-junctions and the persistent sodium current, $I_{Na,p}$ as they were shown to be important for rhythmogenesis of the embryonic spinal cord and/or of IC neurons, the putative pacemakers of early locomotor behavior in zebrafish.

We showed that the rhythm of tail beats at 3 and 4 dpf is relatively insensitive to blocking glycinergic neurotransmission using strychnine in our previous chapter. However, when we co-applied the gap-junction blocker carbenoxolone in combination with strychnine at these ages, we observed a greater disruption of the rhythm driving tail beats at 3 and 4 dpf. Interestingly, carbenoxolone by itself had little effect on the tail beat rhythm at 3 dpf and and 4dpf suggesting

that at this age where fish swimming activity is still maturing, the rhythm is not fully dependent on either glycinergic neurotransmission nor electrical synapses

The $I_{Na,p}$ antagonist, riluzole, alone also showed a small effect at 3 dpf and negligible effects at 4 and 5 dpf. In fact, spinal motor output seemed to be stronger with riluzole. However, in spinalized 3 dpf fish, a cocktail of strychnine and riluzole seemed to silence NMDA induced activity. However, we note that these two drugs (riluzole and carbenoxolone) can have an impact on other targets than the one aimed in these experiments. Riluzole has been reported to also alter glutamate uptake as well as blocking acetylcholine receptor γ subunit (Azbill et al., 2000; Deflorio et al., 2012). Carbenoxolone might have an effect on chemical synapse (glutamatergic and glycinergic) for high concentrations and long exposure (Tovar et al., 2009). Therefore, analyzing experiments with these compounds requires a bit more caution.

Altogether, the results from this study suggest that the primary electrical scaffold driven by PM neurons do not play an important role in sustaining tail beat rhythm after 3 dpf. While it is most probable that higher centres in the brainstem and the brain become more involved in the control of swimming after 3 dpf, previous studies showing the presence of rhythmic spinal output following transections of the spinal cord suggest that there are spinal circuits that are capable of generating the rhythm necessary for tail beats. However looking for intrinsic properties at latter developmental stage would still be valid as some intrinsic properties in network oscillators can facilitate rhythmogenesis such as post inhibitory rebound firing or adaptive firing (Daun et al., 2009). Our results further reinforce the conclusion from our prior work that this rhythm is not generated by any pacemaker cells but rather by circuits organized as network oscillators.

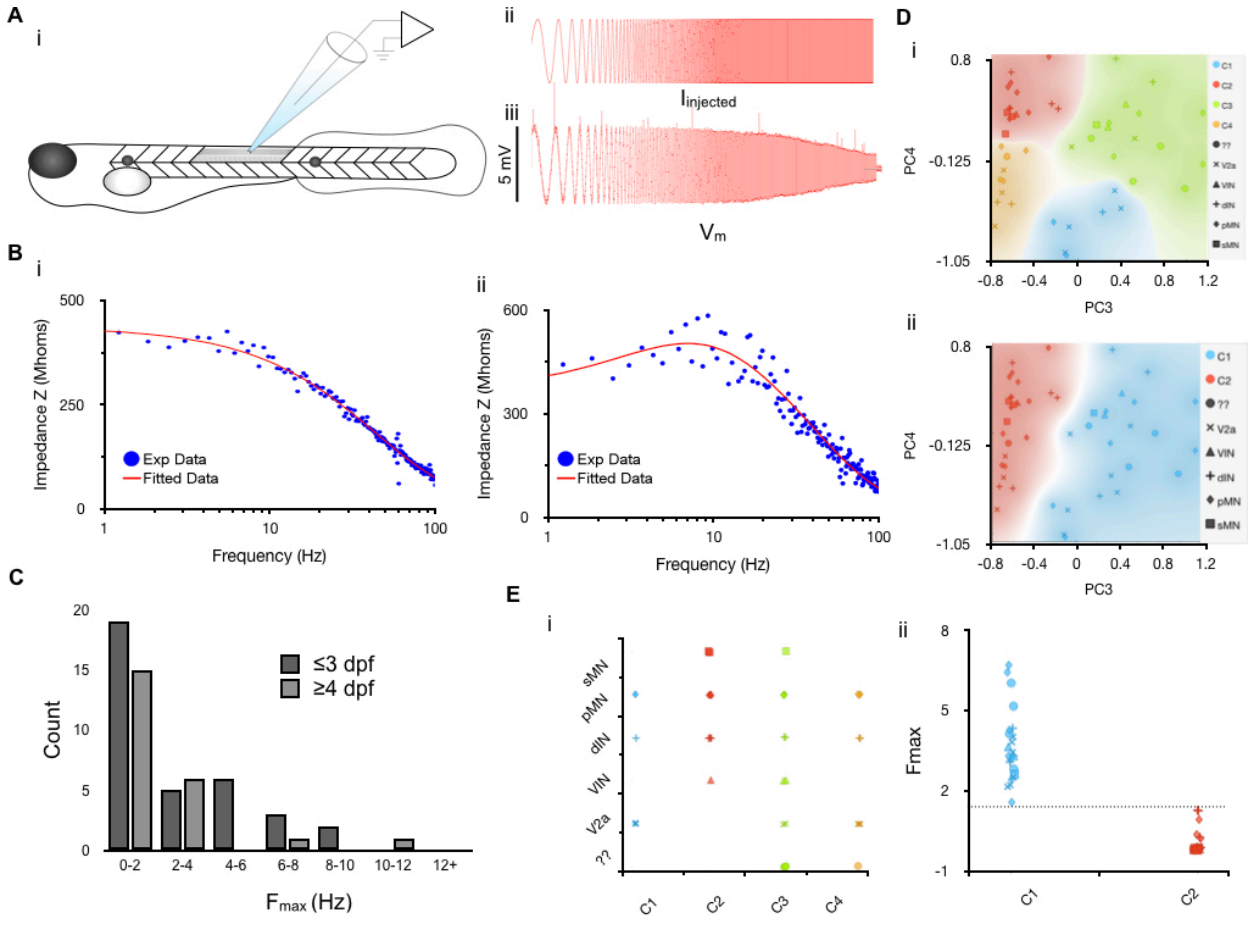

Figure 3.1. Subthreshold frequency preference analysis of caudal spinal neurons fails to identify pacemakers.

A, Experimental setup. Dorsal muscles over 5 segments rostral to the anus were removed to expose the spinal cord in 3-5 dpf fish. Then an electrode was inserted in the spinal cord to patch-clamp spinal neurons (*i*). In current-clamp mode, a time-varying sinusoidal current was injected to the recorded neuron according to a ZAP function to perform a frequency scan (from 0.1 to 200 Hz, duration of 60 s) (*ii*). Membrane potential variation is recorded (*iii*). ***B,*** Example of impedance (Z) profiles extracted from ZAP recordings as square root ratio of V_m power spectrum

over $I_{injected}$ power spectrum. Example of low-pass filter (*i*) and resonating *(*ii*)* Z profiles. ***C,*** Repartition histogram of the tested neurons according to their resonating frequency (frequency where Z is maximum) for neurons from 2-3 dpf fish (dark grey) and 4-5 dpf fish (light grey). ***D,*** Results from PCA and k-means clustering analysis. Projection over PC3 and PC4 for 4 clusters (*i*) and 2 clusters (*ii*). Data points were shaped according to functional population. PC3 and PC4 were chosen over PC1 and PC2 for visual clarity (*Supp. Data)*. ***E,*** Repartition of the different types of neurons in the 4 different clusters (C1-C4) (*i*). Repartition of the tested neurons in the 2 clusters from k-means clustering (C1, C2) according to the resonating frequency (F_{max}). The dotted line represents the critical frequency operating the two clusters (*ii*).

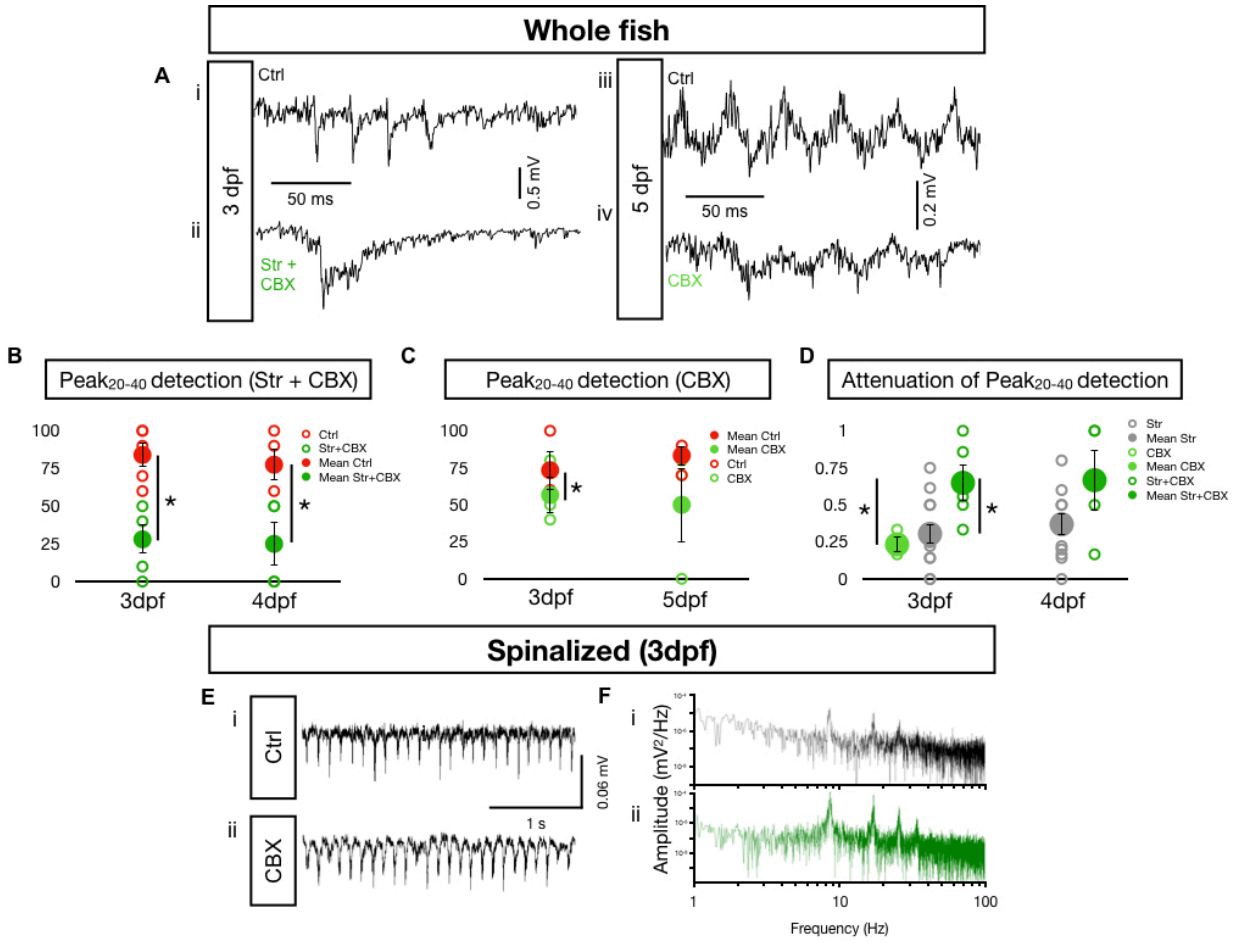

Figure 3.2. Carbenoxolone (CBX) reinforces the effect of strychnine at 3dpf but is dispensable at 4 and 5 dpf.

A, Typical traces from whole fish extracellular recordings of spinal activity during fictive swimming. (*i*) and (*ii*) are recordings from a 3 dpf fish under control and strychnine (4µM) + carbenoxolone (500µM) conditions, respectively. (*iii*) and (*iv*) are recordings from a 5 dpf fish under control and carbenoxolone alone conditions, respectively. ***B,*** $Peak_{20\text{-}40}$ detection scores for fish from 3 and 4 dpf under control (red) and strychnine + carbenoxolone (dark green) conditions. Open circles are results from individual animals, calculated from 10 swimming events. Filled circles are averages (N = 5 fish at 3 dpf; N = 4 fish at 4 dpf. 10 episodes per fish).

C, $Peak_{20\text{-}40}$ detection scores for fish from 3 and 5 dpf under control (red) and carbenoxolone alone (light green) conditions (N = 3 fish at 3 dpf and 5 dpf. 10 episodes per fish). ***D,*** Attenuation of $Peak_{20\text{-}40}$ detection scores, calculated as 1 - ($Peak_{20\text{-}40;\ Drugs}$ / $Peak_{20\text{-}40;\ Ctrl}$), for fish from 3 and 4 dpf under strychnine + carbenoxolone (dark green), carbenoxolone alone (light green), and strychnine alone (grey) conditions (for strychnine, N = 12 fish at 3dpf ; N = 11 fish at 4dpf. 10 episodes per fish). Error bars display SE. * $p < 0.05$ (two tailed T-test). ***E,*** Typical traces from extracellular recordings of spinal activity in spinalized fish during NMDA (1mM) evoked swimming under control (*i*) and carbenoxolone alone (*ii*) conditions. ***F,*** Power spectrums performed over 30s of the recordings in E for control (*i*) and carbenoxolone alone (*ii*) conditions.

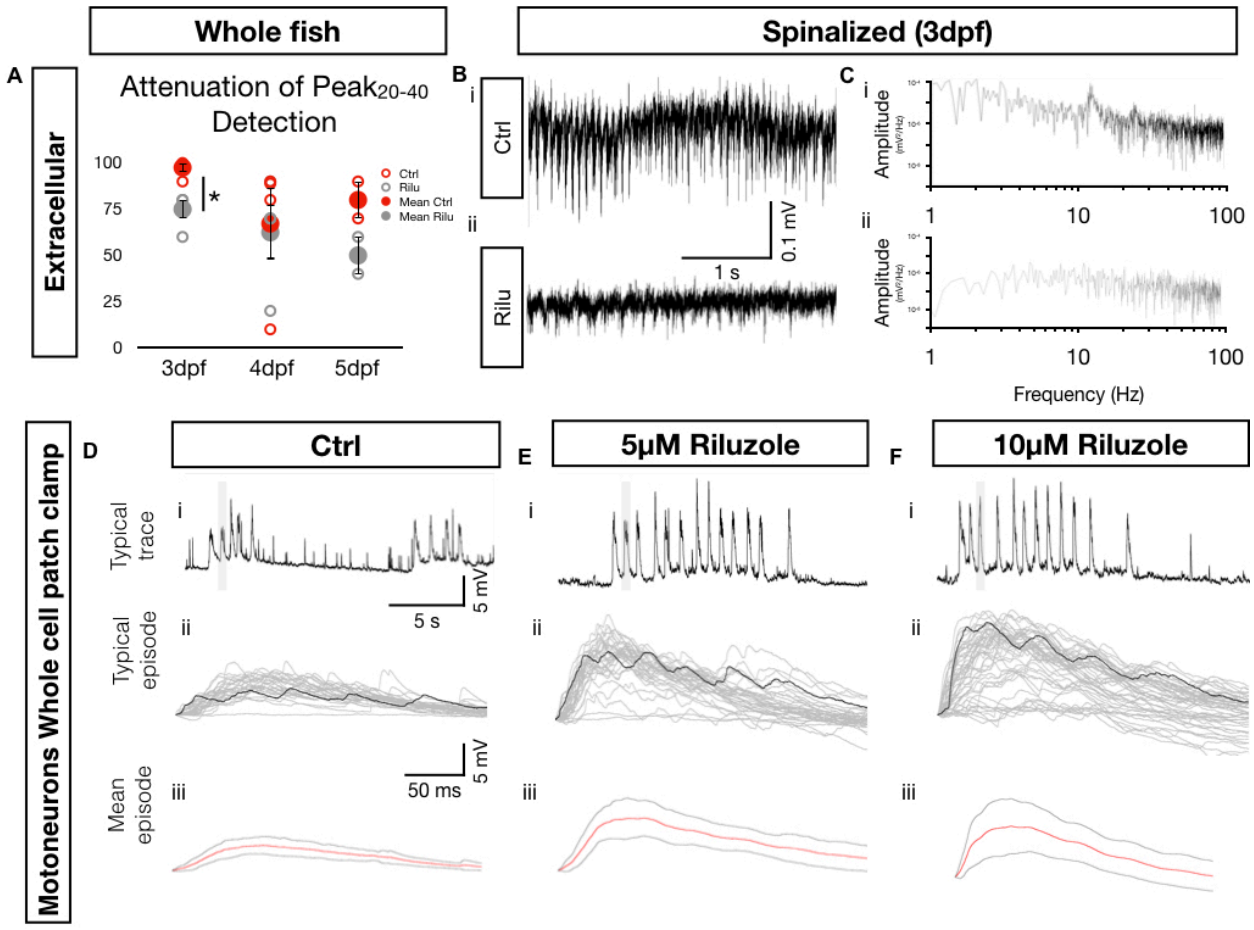

Figure 3.3. Riluzole disturbs rhythm of tail beats but only at 3 dpf.

A, Peak$_{20\text{-}40}$ detection scores for fish from 3 to 5 dpf under control (red) and 5 µM riluzole (grey) conditions. Open circles are results from individual animals, calculated from 10 swimming episodes. Filled circles are averages (N = 4 fish at 3 dpf; N = 4 fish at 4 dpf ; N = 2 fish at 5 dpf. 10 episodes per fish). Error bars display SE. * $p < 0.05$ (two tailed T-test). ***B,*** Typical traces from extracellular recordings of spinal activity in spinalized fish during NMDA (1mM) evoked swimming under control (*i*) and riluzole (*ii*) conditions. ***C,*** Power spectrums performed over 30s of the recordings in B for control (*i*) and riluzole (*ii*) conditions. Note the disappearance of the peak between 10 and 20 Hz under riluzole. ***D,*** *i,* Typical trace from a whole cell patch clamp

recording of a MN, in current-clamp mode, in a 5 dpf fish spinal cord. Shaded area highlights one swimming episode from a train. *ii,* Episodes extracted from the recording in *i* (grey line, 29 episodes). Typical episode in black. *iii,* Mean trace (red) ± SD (grey lines) computed from the extracted episodes in *ii*. ***E-F*** Same as in D but with 5µM and 10 µM riluzole, respectively. N = 35 episodes for E*ii* and N = 51 episodes for F*ii*.

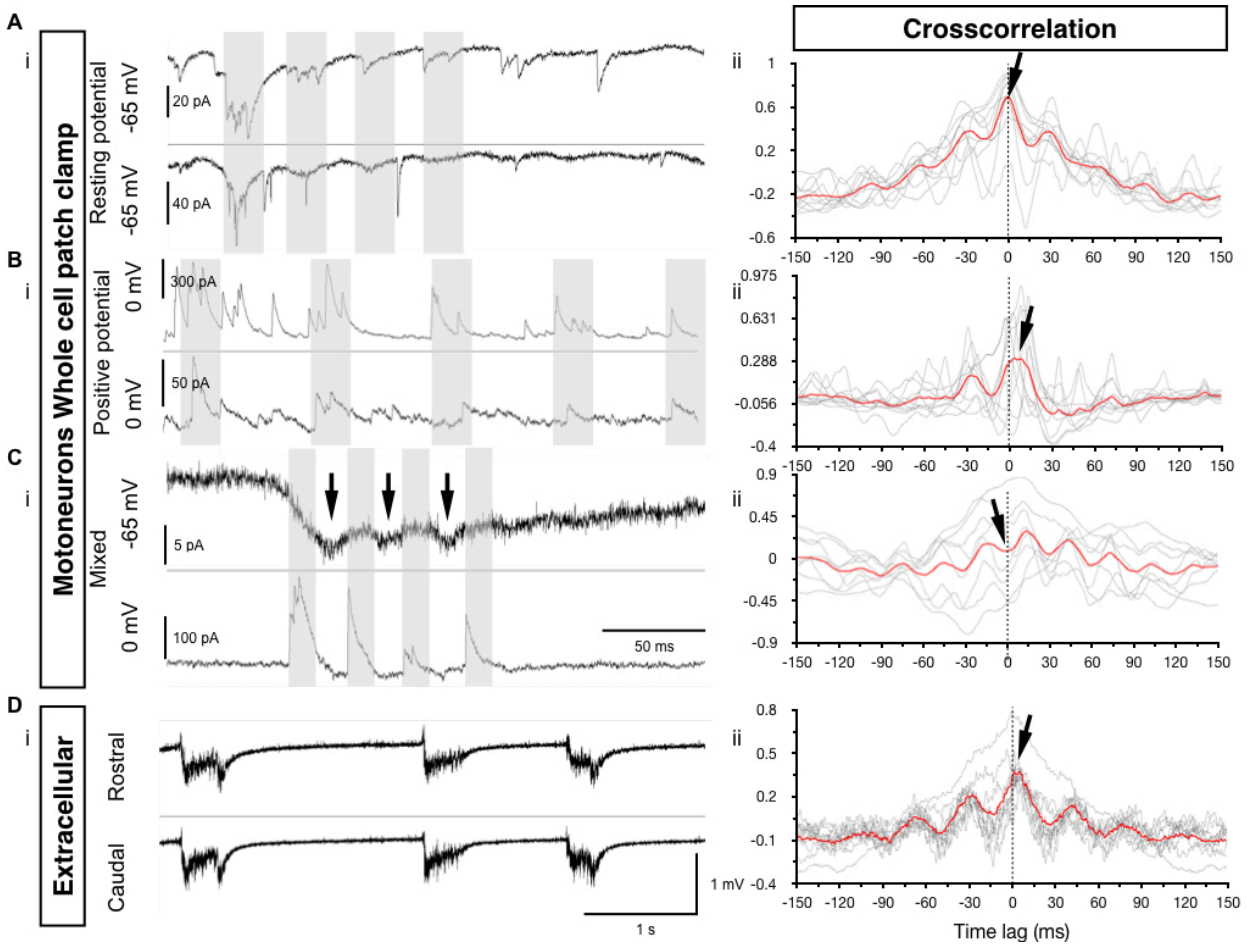

Figure 3.4. Dual recordings in beat-and-glide swimming fish.

A, *i,* Typical recording from a dual patch-clamp (2 MNs) experiment in a 5 dpf whole fish during swimming. Both cells are held near resting potential (-65 mV). Shaded area highlights inward current oscillations. *ii,* Crosscorrelation graph between traces from the two recorded MNs in (*i*) for 10 swimming episodes (grey lines). Average trace in red. The arrow indicates the local maximum near 0 ms time lag. ***B,*** Same as in A when both MNs are held at a positive holding potential (0 mV). *i* Shaded area highlights outward current oscillations. *ii* The arrow indicates the local maximum near 0 ms time lag. ***C*** Same as in A when MNs are held in a mixed configuration (one is at resting potential while the other is at a positive holding potential). *i,* Shaded area indicates outward current oscillations while black arrows show inward current oscillations. *ii,* The arrow feature the local minimum near 0 ms time lag. Autocorrelations were

computed from the trace of the MN at resting potential and the inverse of the trace of the MN at positive holding potential. ***D*** *i,* Dual extracellular recordings from a rostral and a caudal segment (8 somites apart) of the spinal cord in a 5 dpf whole fish during swimming. *ii,* Crosscorrelation graph between traces from the recordings in (*i*) for 10 swimming episodes (grey lines). Average trace in red. The arrow indicates the local maximum above the 0 ms time lag.

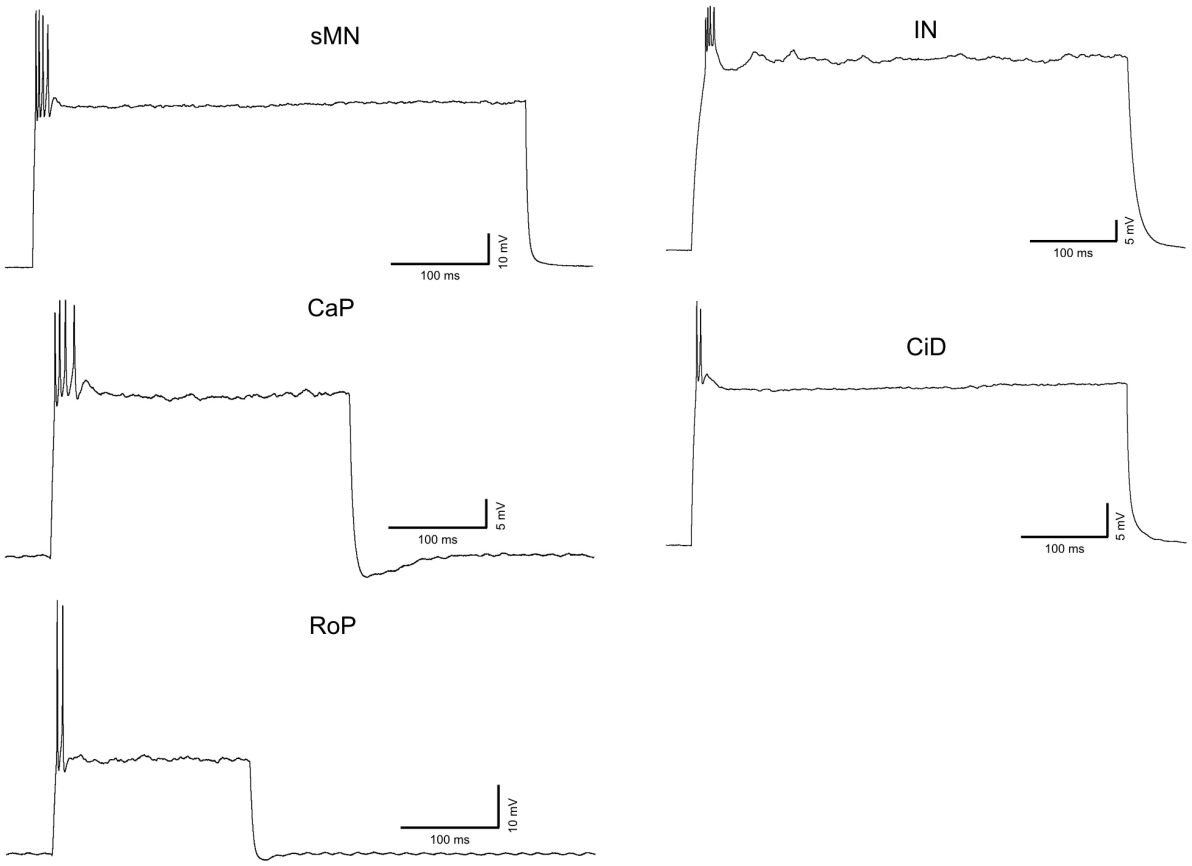

Figure 3.S1. Typical spiking activity of current-clamped spinal motoneurons (MN) and interneurons (IN).

sMN: secondary motoneuron; CaP: Caudal Primary motoneuron; RoP: Rostral Primary motoneuron; CiD: Circumferential Descending interneuron (V2a)

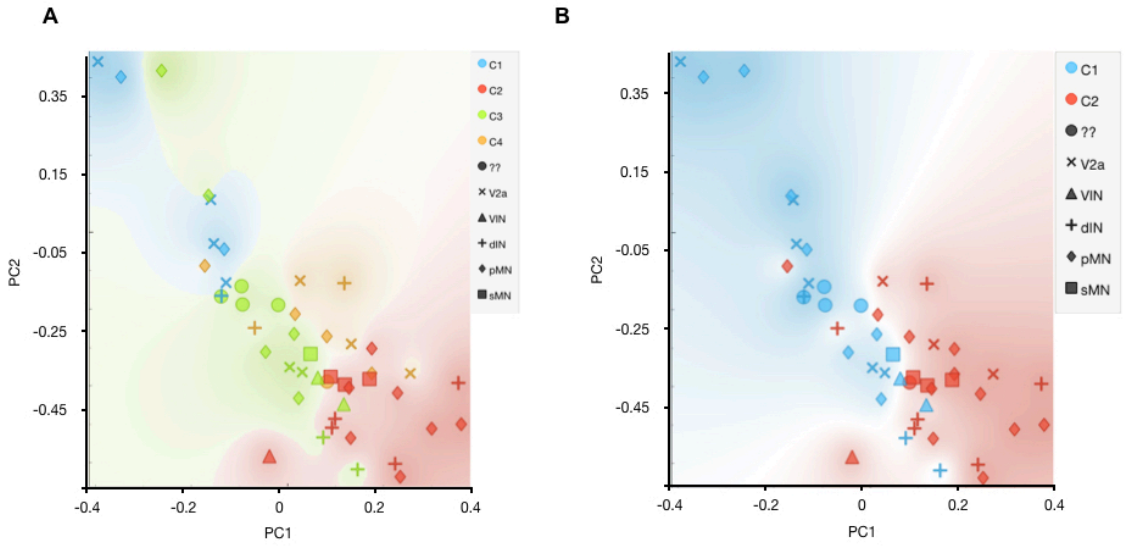

Figure 3.S2. K-mean clustering of impedance profiles features on projection over PC1 and PC2.

A, Projection over PC1 and PC2 for 4 clusters ***B,*** and 2 clusters. Data points were shaped according to functional population.

CHAPTER 3: MODELLING THE MATURATION OF SWIMMING IN ZEBRAFISH (*DANIO RERIO*) THROUGH THE DEVELOPMENT OF SPINAL CIRCUITS

Roussel, Yann; and Bui, Tuan Vu

ABSTRACT

It has long been established that locomotor activity can be produced by isolated spinal cords. However, the spinal circuits controlling locomotion do not come fully formed but rather undergo a maturation process. While extensive knowledge has been gathered on multiple components of the spinal locomotor circuit over different developmental time points, the manner in which these maturing components operate together in order to produce required rhythm and muscle coordination for locomotion remains elusive. By combining our previous experimental observations with already published insights on the zebrafish spinal cord, we propose here several models, each of which is able to reproduce a developmental milestone in the locomotor behaviour development. We incrementally developed the successive models using reflectively previously described developmental processes (i.e. neurogenesis, synaptic refinement and intrinsic properties maturation). The resulting circuit model output was fed into a reductive musculoskeletal model able to emulate the phenotype of the desired motor behaviours. In the process we were able to describe the role of specific populations of neurons in locomotion as well as identify potential targets on broad mechanisms of action of neuromodulators such as dopamine and serotonin).

Introduction

Moving the body is one of the earliest tasks executed by the nervous system and early precocious movements can be critical for the survival of many species. The escape response seen in various fish and amphibians is one such example of a movement produced during early development that is critical for survival. However, the control of movement by the nervous system does not come fully formed but matures as the nervous system develops. This maturation enables a wider repertoire of movements to arise. During this process, new neurons are born and neural circuits are either newly formed or refined, supposedly leading to the emergence of more and more refined movements. Therefore, if we are able to determine how the arrival of new neurons or the formation of new circuits lead to the emergence of new movements, then we could gain important insights into the role of distinct neurons or circuits in the overall scheme of motor control.

Zebrafish are a species where the maturation of swimming has been well described at both the organismal and the neurobiological level (Drapeau et al., 2002; McLean and Fetcho, 2009). Single strong body bends on one side of the body (also known as coils) emerge during the first day of development as the earliest locomotor behaviour. Single coils are quickly followed by double coils (i.e. two successive coils, one for each side of the body). Coiling movements are then replaced by swimming movements involving episodes of repeated tail beats. By the end of the second day post fertilization (dpf) comes the emergence of a form of swimming known as burst swimming that is characterized by long but infrequent episodes (several seconds long) of swimming activity. Locomotor behaviour will further mature around 4 dpf to beat-and-glide

swimming characterized as trains of multiple shorter episodes (hundreds of milliseconds long) interspaced by quiescent (or "gliding") periods.

Many aspects of the development of the nervous system during these stages of motor maturation have been revealed. Neurogenesis in the spinal cord, where many circuits critical for movements are located, occurs in two successive waves, the first around 16-17 hours-post fertilization (hpf) and the second after 24 hpf (Myers et al., 1986; Kimmel et al., 1995; Drapeau et al., 2002; Lewis and Eisen, 2003). Notably, primary motoneurons (MNs) that innervate both red and white muscles at early developmental stages (Buss and Drapeau, 2000) and permit coiling and escape movements to be made arise in the first wave (Kimmel et al., 1995; Saint-Amant and Drapeau, 2000). A number of spinal interneurons are also born alongside primary MNs during the first neurogenic wave that may be important for controlling locomotor activity. These include ipsilateral caudal (IC) interneurons thought to play an essential role in early locomotor behaviour due to their endogenous bursting activity that possibly rhythmically drives spinal locomotor circuits (Tong and McDearmid, 2012), as well as a population of contralateral glycinergic interneurons, CoBL (Commissural bifurcating longitudinal) neurons, that is active during early locomotor behaviours (Liao and Fetcho, 2008; Ikenaga et al., 2011). These early neurons are later joined during the second neurogenic wave by excitatory glutamatergic V2a (or CiDs) that seem to provide an important excitatory drive for swimming activity (Menelaou and McLean, 2012; Ampatzis et al., 2013; Ljunggren et al., 2014) as well as different populations of glycinergic interneurons either ipsilaterally projecting such as V1 (i.e. CiA, Higashijima et al. 2004, Batista et al., 2008) or commissurally projecting such as Commissural Secondary

Ascending (CoSA) or Multipoplar Commissural Descending (MCoD) interneurons (Liao and Fetcho, 2008) whose involvement in swimming have been described but whose exact roles remain to be verified. The integration of these spinal populations into spinal locomotor circuits is believed to underlie the gradual maturation of locomotor behaviour.

We have recently provided evidence that the maturation of swimming in larval zebrafish during which burst swimming is replaced by beat-and-glide swimming is accompanied by an operational switch in how spinal locomotor circuits generate the rhythm underlying tail beats. Specifically, we demonstrated that whereby early coiling and burst swimming movements relied upon pacemaker cells to generate the rhythm of locomotor movements, spinal circuits transitioned towards relying upon network oscillators whose rhythm is driven by excitatory and inhibitory synapses as opposed to endogenous bursting properties of individual pacemakers.

In light of these findings, we sought to generate computational models that could test how transitions between different swimming movements result from either the incorporation of specific spinal populations or maturation of intrinsic properties of populations of neurons already involved in the overall spinal locomotor circuit. While computational modelling has generated invaluable insights into the function and mechanisms of spinal locomotor circuits of a number of different species (Rybak et al., 2006; Kozlov et al., 2014), there is to our knowledge no such model for the developing zebrafish spinal cord. Here, we build the very first developmental model of the zebrafish spinal locomotor circuit that is able to accurately reproduce the locomotor behaviour from each developmental stage starting from single coiling all the way to beat-and-glide swimming. In the process we identify the possible contributions of specific neural circuits

and spinal populations to swimming movements in zebrafish and highlight paths for possible future studies on zebrafish spinal locomotor circuits.

Methods

Modelling environment

Modelling was performed with the Spyder 3.2.5 environment using Python 3.6.3 64bits.

Modelling of single neurons

Neurons were modeled using a single compartment, simple spiking neuron model developed by Izhikievch (2003) where the dynamics of the membrane potential are governed by general differential equations:

$$\begin{cases} V' = 0.04V^2 + 5V + 140 - u + I_{syn} \\ u' = a(bV - u) \end{cases} \quad if \quad V = 30mV, then V \leftarrow c, u \leftarrow u + d \qquad (1)$$

While specific active conductances are not modelled in these models, changes in the parameters *a, b, c* and *d (*which respectively represent the time scale of the recovery variable *u*, the sensitivity of *u* to the sub-threshold variation of *V*, the reset value of *V* after a spike and the reset value of *u),* can be selected to model either bursting (or chattering) pacemaker neurons, tonic spiking neurons (e.g. MNs or V2a), phasic spiking neurons or adaptive spiking neurons (Table 1). I_{syn} represents the sum of the synaptic and gap junctions currents received by the neuron. The Euler method was used for solving ordinary differential equations.

Modelling synapses

Synaptic conductances of chemical synapses were modelled as a sum of two exponential weighted by a synaptic weight based upon the general equation:

$$I_{pre,post} = \begin{cases} (V_{post} - E_{rev})(e^{-\frac{t-t_0}{\tau_r}} - e^{-\frac{t-t_0}{\tau_f}}) \bullet W_{pre,post} & if\ V_{pre} > V_{thr} \\ 0 & else \end{cases} \quad (2)$$

Where $I_{pre,post}$ is the synaptic current received by the postsynaptic neuron from neurotransmitter release by the presynaptic neuron, and considered to be non zero if the presynaptic neuron membrane potential V_{pre} crosses a voltage threshold V_{thr} at the synapse. V_{post} is the membrane potential of the postsynaptic neuron, E_{rev} is the reversal potential, τ_r and τ_f are the rise- and fall-time constants respectively, t_0 is the time at which V_{pre} crossed V_{thr} and $W_{pre,post}$ is the synaptic weight between the presynaptic and postsynaptic neurons (Table 4.3).

Two types of chemical synapses were implemented, glutamatergic and glycinergic synapses. The former differs from the latter by the reversal potential values E_{rev} as well as the time constant values τ_r and τ_f (Table 4.4). All electrical synapses (i.e. gap junctions) in our model were approximated as ideal resistors following Ohm's Law:

$$I_{gap:pre,post} = V_{pre} \bullet G_{pre,post} \quad (3)$$

With $I_{gap:pre,post}$ the synaptic current flowing to the postsynaptic neuron from the presynaptic neuron through gap junctions and $G_{pre,post,}$ the total conductance of gap junctions between the presynaptic and postsynaptic neurons (Table 4.2).

Spatial arrangement of spinal neurons

A key feature of our modelling approach is to assign spatial coordinates *(x, y, z)* to point-like neurons (i.e. neurons have no spatial dimension but they have a position in space) giving the spatial distribution of neurons a central place in our model computing process. The Euclidian distance was used to calculate the distance between each neuron and to approximate axon length,

hence a time delay for each synaptic connection is computed from the distance between neurons. We can therefore rewrite the synaptic current from *eq. (2)* giving an instantaneous synaptic transmission as a delayed synaptic current:

$$I_{delayed:pre,post}(t) = I_{pre,post}(t - \frac{D_{pre,post}}{c}) \qquad (4)$$

With $D_{pre,post}$ the Euclidian distance between the presynaptic and postsynaptic neuron and c the transmission speed. This distance as well as neuron position were also used to apply conditions on synaptic weights of neurons (e.g. limits as to the how far descending neurons projected to).

Spinal locomotor circuits were distributed along two columns, one for each side of the body, giving the network a nearly one-dimensional organization along the rostrocaudal axis. Therefore, we used the x axis as the rostrocaudal axis whereas the y axis was only used to segregate neurons from left and right sides (giving the coordinate $y = 1$ for the right side and $y = -1$ for the left side). The z axis was not used in our model.

Noise in the network

To take into account the inherent stochasticity associated with biological systems we introduced Gaussian noise into the positioning of neurons. The position was randomized by multiplying the given value with a random number picked from a Gaussian distribution of mean $\mu = 1$ and variance σ_{pos} (Table 4.1). Parameters of each neurons were modulated in a similar way. The descending excitatory drive to spinal circuits was also modulated with white noise using a similar process.

Musculoskeletal model

Interpretation of the model's output in terms of body angles and frequency of locomotor movements was done by implementing a musculoskeletal model of the fish body. Each MN output along the fish body was fed into a muscle cell (Fig. 4.1*A,B*) modelled as a simple passive RC circuit (*R* and *C* being the muscle cell membrane resistance and capacitance respectively), described by the following equation:

$$V'_{muscle} = \frac{v}{RC} + \frac{I_{syn}}{C} \qquad (5)$$

One muscle cell represents one somite for one side of the body. The whole body of the fish was modelled as a chain of uncoupled dampened pendulums. Local body angles were thus computed according to the differential activity from the local left and right somites (i.e. muscle cells). The deflection angle θ_i of the ith somite vas computed according to the following differential equation.

$$\theta_i'' + 2\zeta\omega_0\theta_i' + \omega_0^2\theta_i = \alpha(V_{Rmuscle,i} - V_{Lmuscle,i}) \qquad (6)$$

With $V_{Rmuscle,i}$ and $V_{Lmuscle,i}$ being the solution of the equation *(5)* for the right and left muscles from the ith somite respectively (Fig. 4.1*C*). α is the conversion coefficient from electric drive of the muscle cells to mechanic contraction of the same cells. The midline of the body can be computed at any given time as (x,y) coordinates using trigonometric identities from θ_i (Fig 4.1*D*). Thus, heat maps of local body angles (θ_i) variation through time provides comprehensive information about the network output (Fig. 4.1*E*). Fast Fourier Transform of the local body angles were computed to give a map of the local body bend frequencies. Autocorrelation were calculated on traces of given muscle cells.

Results

We aimed to describe how spinal locomotor circuits develop over the first few days of development such that zebrafish undergo a number of changes in swimming movements. Therefore, we built an initial model based upon previously reported experimental observations of spinal circuits to replicate early locomotor movements. We then successively built upon this initial model to replicate successive transitions in zebrafish swimming movements.

Part 1. Early locomotor behaviour, coiling, is encoded by a fully electrical network

Coiling results from unilateral gap-junction coupling

Coiling, which is already observed at 1 dpf, is characterized by one strong tail beat on one side of the body before the body returns to rest position (Saint-Amant and Drapeau, 1998). The occurrence of coiling is rather infrequent, reaching a maximum frequency of occurrences of 1 Hz around 20 hours post fertilization (Saint-Amant and Drapeau, 1998). Left coilings are as likely to happen as right coilings. Previous studies have established that this behaviour is generated by a spinal circuit relying mostly on gap junctions (i.e. electrical synapses) (Saint-Amant and Drapeau, 2001) as the obstruction of glutamatergic and glycinergic transmission does not prevent coiling or rhythmic activity in MNs while heptanol (a gap junction uncoupler) suppressed spinal activity responsible for coiling. It has been proposed that IC pacemaker neurons expressing persistent sodium currents ($I_{Na,P;}$ Tong and McDearmid, 2012) drive periodic depolarizations of ipsilateral MNs via electrical synapses leading to contraction of the muscles (Saint-Amant and Drapeau, 2001; Drapeau et al., 2002). Since glycinergic synaptic bursts are observed in MNs

during contralateral coiling events, a population of contralaterally projecting glycinergic neurons (which we term CINs) must be present in the spinal cord at this developmental stage and must be ipsilaterally coupled to either the ICs, the MNs or most likely both while projecting to contralateral motoneurons to inhibit the other side (Saint-Amant and Drapeau, 2001). Intrinsically generated periodic depolarization of ipsilateral IC neurons due to the activation of $I_{Na,P}$ leads to the depolarization of downstream ipsilateral MNs and CINs. MNs trigger the contraction of the ipsilateral muscles while CINs depolarize contralateral MNs. Blocking glycinergic transmision using strychnine does not disturb the coiling behaviour but will remove the synaptic bursts observed in MNs (Saint-Amant and Drapeau, 2001). Contralateral inhibition might be important to prevent unlikely events as synchronous contractions of both sides of the fish body.

Network description

Based upon the experimental observations reported above, we therefore propose the following architecture for the spinal locomotor circuit responsible for coiling (Fig. 4.2*A*). Two bilaterally located kernels of recurrently connected pacemakers (PMs, five for each kernel) based upon IC interneurons each drive a pair of rostrocaudal chains of electrically coupled neurons via gap junctions. One chain consists of 10 MNs and the other consists of 10 CINs. We simulated a noisy depolarizing step current as the excitatory drive to PMs that eventually lead them to bursting. In addition to their recurrent connections, each PM forms electrical synapses with several rostral MNs and CINs (the first 5 of each ipsilateral chain in our model). The connectivity within the chains is identical for both MNs and CINs chains. Each neuron in a chain forms electrical

synapses with its 3 closest rostral neighbours and its 3 closest caudal neighbours within the same chain. There is also electrical coupling across the two ipsilateral chains as MNs form gap junctions with the 3 closest rostral and 3 closest caudal CINs (and vice-versa). Even though it is not essential for coiling activity we chose to implement commissural inhibitory to reproduce experimental data (Saint-Amant and Drapeau, 2001). CINs form glycinergic synapses with contralateral MNs (as well as with PMs in the case of rostrally located CINs). These synapses were only formed to contralateral MNs within 5 to 6 segments, so that the i^{th} CINs projected to all contralateral MNs between the *i-2* and *i+2* segments. Note that CINs are present in later extensions of the spinal locomotor circuit model and serve to generate the left/right alternation pattern.

Synaptic weights and the extent of the connections were first estimated based upon experimental observations and then finely tuned through multiple simulations. For instance, IC neurons upon which our PM neurons are based project caudally through multiple somites (Bernhardt, 1990) and coupling between early active neurons have been previously determined (Saint-Amant and Drapeau, 1998).

Simulation results

Our simulations show that this model is capable of generating coils characterized by large body bends to one side of the body (Fig. 4.2*B, Supp. Data video 4.S1*). Left and right coils are independent and quite infrequent (1.10 +\- 0.19 Hz, calculated from 20 iterations of 1s long simulations) as observed experimentally (Saint-Amant and Drapeau, 1998). The average phase lag of 1.6 ms between each segment also reproduced experimental observations (McDearmid and Drapeau, 2006). Previously reported whole-cell patch clamp recordings of MNs at this

developmental stage display two typical events (Saint-Amant and Drapeau, 2001): periodic depolarizations (PDs) via electrical synapses putatively driven by upstream PM neurons (i.e. ICs) and synaptic bursts (SBs) from contralateral spinal glycinergic neurons. Both of these events can be observed on MN traces from the model (Fig. 4.2*C*). PDs propagate along the rostrocaudal axis and drive ipsilateral contraction of muscles whereas SB are due to glycinergic input from CINs activated during contralateral contraction (Fig. 4.2*D*). Overall, the model captures well this first locomotor behaviour in zebrafish in terms of the proper spatiotemporal activation of motoneurons and the synaptic events that motoneurons receive. We next built upon this model to try to replicate the next step in the development of swimming: the appearance of double coiling.

Part 2. Double coiling, an intermediate state toward swimming generated by a hybrid spinal circuit

Double coiling is generated by a balance between excitatory and inhibitory commissural neurons

Quickly after single coils appear, a new transitory locomotor behaviour named double coils emerges during the same first day of development, coexisting with the single coiling behaviour (Knogler et al., 2014). It is characterized by two successive coils, one on each side of the body. The previous electrical scaffold for single coils is supplemented with chemical glutamatergic synapses to form a hybrid circuit. Indeed, adding CNQX and APV to block glutamatergic transmission in fish expressing this behaviour prevents double coils and only single coils are present suggesting a necessary role of glutamatergic synapse in promoting the appearance of a second coil (Knogler et al., 2014). In contrast, blocking glycinergic synapses leads to triple or

even quadruple coils. Patch-clamp recordings of MNs at this developmental stage exhibit the same isolated PDs and SBs from earlier developmental stages but also show mixed events in which a PD event directly follows a SB or vice-versa (Knogler et al., 2014). These mixed events are though to underlie double coiling behavior since PDs drive ipsilateral coils and SBs result from the glycinergic drive of contralateral interneurons during contralateral coils.

Network description

To replicate double coils, we reasoned based upon prior experimental results (Knogler et al., 2014) that the single coil model should be supplemented with the addition of commissural excitation such that a second coil would be driven by excitation arising from the side where the first coil is being generated. Therefore, we built upon the model by adding a population of commissural excitatory neurons (CENs, 10 neurons for each sides) electrically coupled to the previous scaffold (i.e. the ipsilateral PM-MN-CIN scaffold) arranged in a rostrally located chain within the spinal cord (Fig. 4.3*A*). Electrical synapses are formed with neighbouring MNs, CINs and CENs (the closest 3 of each type of neuron in both the rostral and the caudal direction). Some ipsilateral PMs are coupled with the most rostral CENs. Glutamatergic synapses from PMs to ipsilateral CENs could have been implemented instead of or in addition to gap junctions between the two populations. However, considering the lack of experimental evidence we chose electrical synapses to reflect the predominant electric nature of spinal circuits at these early developmental stages. To generate the crossing excitation underlying the second coils, all CENs project to the contralateral PM kernel forming glutamatergic synapses with most of the contralateral PM neurons. PMs also receive glycinergic inputs from the previously formed

synapses from contralateral CINs as suggested by experiments in which blockade of glycinergic transmission increases the frequency of double and even triple or quadruple coiling events (Knogler et al., 2014).

Simulation results

MN membrane potential traces from the model exhibit the typical SB, PD and mixed behaviours (Fig. 4.3*Bi-iii*) observed experimentally (Knogler et al., 2014), which were converted to actual double or single coiling behaviour in the musculoskeletal model (Fig. 4.3*Biv, Supp. Data video 4.S2*). When analyzing neural activity of a right/left double coil, we observed a PD propagating along the rostrocaudal axis on the right side first immediately followed by another descending PD on the left side (Fig. 4.3*Bv*, neural activity during event in dashed box Fig. 4.3*Biv*). when a PD was present in MNs of one side, a SB could be observed in MNs of the contralateral side. Double coiling seems to result from competition between contralateral glutamatergic inputs from CENs and contralateral glycinergic inputs from CINs onto PMs. Single coiling occurs if the glycinergic drive is greater than glutamatergic drive and double coiling occurs if glutamatergic drive is strong enough (Fig. 4.3*C*). The proposed network model reproduces reported distributions of single and double-coiling events for control conditions (Fig. 4.3*D*: 80% single coils, 17% double coils and 3% triple coils; calculated from 20 iterations of 1 s simulation). As well, blocking glutamatergic synapses prevents any double-coiling event since it effectively converts the network architecture at this age to the previous coiling architecture seen in single coils whereas blocking glycinergic synapses leads to an increase of multiple coilings of 3 or more coils (Fig. 4.3*D*: 57% single coils, 21% double coils, 18% triple coils and 3% quadruple

coils; calculated from 20 iterations of 1s simulation with blockade of glycinergic synapses) due to unopposed reverberating commissural excitation from CENs that leads to coiling echoes.

Part 3. First step of swimming: Burst swimming

Network oscillators drive episodes of tail beats

Around 2 or 3 dpf, burst swimming characterized by long (1 s long) but infrequent episodes of repeated tail beats emerges during which successive low amplitude tail beats propagate from the rostral toward the caudal end of the fish body. The tail beat rhythm ranges between 20 to 40 Hz and rhythm generation appears to be resistant to blockade of glycinergic neurotransmission at this stage (Chapter 2; McDearmid and Drapeau, 2006). Furthermore, the previously mentioned IC neurons upon which we modelled our PMs have increased their pacemaker frequency and they appear to oscillate in this same 20-40 Hz frequency range at the onset of burst swimming making them ideal candidates for being responsible of for the rhythm generation of tail beats. However, as reported in a previous study (Chapter 2), there may be important differences between rostral and caudal spinal locomotor circuits during this developmental phase. Rhythmogenesis of rostral locomotor circuits seems to be only weakly dependent on glycinergic neurotransmission and thus has been suggested to be driven by PMs. In contrast, caudal spinal locomotor circuits rely more strongly on glycinergic neurotransmission for the rhythm of tail beats. Based upon the latter finding, it has been proposed that the newly generated caudal spinal segments may rely on network oscillators (e.g. half-centre units) to generate the rhythm of tail beats. Across all spinal locomotor circuits, glycinergic transmission is essential for pattern generation (i.e. L/R alternation).

Network description

The previous model for double coiling is expanded to accommodate this new form of swimming. First, to emulate the body growth that occurs at the time that zebrafish transition between coiling behaviours and swimming, we increased the size of the fish from 10 to 15 segments. Chains of MNs and CINs contain now 15 neurons for each side. Rostral rhythm generation is still under the auspices of mature PM (still five for each side) neurons and the pattern generation still relies on rostral CIN and CEN populations. This architecture was supplemented with a new population of ipsilateral excitatory descending neurons (IED, 8 for each side) that could be considered as the model version of V2a neurons (or CiDs). IED neurons are integrated to produce a network oscillator architecture (Fig. 4.4*A*). A source of synaptic inhibition is required since reciprocal inhibition between half-centres is a key mechanism of network oscillators. There is no experimental data available to indicate whether the source is actually ipsilateral or contralateral (though see Moult et al., 2013 for evidence of contralateral inhibition contributing to swimming rhythm in frog tadpoles). An ipsilateral source is possible, however it requires the addition of a new population of ipsilateral inhibitory neurons into spinal locomotor circuits. As for a contralateral source, we could also consider a new population of commissural inhibitory interneurons dedicated to rhythm generation while the function of older CINs would be limited to left-right pattern generation. We chose the parsimonious approach to integrate the already present CIN to form new connections with the new population of IEDs in order to generate the rhythm of tail beats. Thus, IED formed chemical connections with downstream IED as well as CINs and MNs (the i^{th} IED projects to all MNs, IEDs and CINs between the $i+1$ and $i+9$ segment). In turn, CINs connect to contralateral IEDs via new glycinergic synapses with IEDs

within 5 to 6 segments in a similar way that CINs connect to MNs (see coiling section). Therefore, IEDs and CINs formed continuous half-centre like architecture along the rostro-caudal axis in which each half-centres would be formed by one IED and one CIN. We implemented half-centre network oscillators only in the most caudal 8 segments so that 8 ipsilateral IEDs were added starting at segment 5 to segment 12. Finally, rostrally located IEDs (between segment 5 and 8 included) also receive a noisy tonic drive similar to that received by PMs.

Simulation results

This extended spinal locomotor circuit reproduced a key feature of burst swimming, which is sustained episodes of tail beats. The swimming activity from the model lasted for as long as tonic inputs were present. Hence, quiescent periods of the model circuit were solely due to absence of tonic drive. Under control conditions, long burst of continuous activity propagated along the rostrocaudal axis with a robust rhythm contained in the 20 to 40 Hz frequency range and left/right alternation was observed (Fig. 4.4*Bi*, *Ci*, *Di*, *Ei, Supp. Data video 4.S3*). When glycinergic neurotransmission is blocked (Fig. 4.4*Bii*, *Cii*, *Dii*, *Eiii*), pattern generation is strongly disturbed as well as caudal rhythm generation as shown by the autocorrelation (grey and blue traces in Fig. 4.4*Eii*) of the simulated muscle trace from the 12th somite (out of 15) from 10 different simulations. However, the rostral 6th somite still shows rhythmic activity while the pattern is disturbed (yellow and red traces in Fig. 4.4*Eii*). Indeed crosscorrelation between traces from the left and right muscle activity of the 6th somite showed a maximum at 0 ms lag indicating synchronous activation of both sides as opposed to left/right alternation (left/right alternation

would give a local minimum at 0 ms lag delay in the crosscorrelation graph as seen in control condition, see Fig. 4.4*Fi* and 4.4*Fii*).

Part 4. Transitioning to beat-and-glide swimming

Network oscillators completely take over

The last developmental step we sought to investigate was the transition between burst swimming and a more mature form of swimming, named beat-and-glide swimming. Even though the phenotype is well characterized, moving from infrequent second-long bursts of rhythmic tail beats to more frequent hundreds-of-ms long bursts, the mechanism underlying this maturation process is not well understood yet. The transition from PM driven rhythm generation driving the tail beats to spinal locomotor circuits relying on network oscillators does not seem to be also involved in shortening the duration of swimming episodes that characterizes the transition from burst to beat-and-glide swimming (Chapter 2). A pump-driven mechanism could generate silent periods following episodes of locomotor activity however previous experiments using the sodium-potassium pump antagonist ouabain seemed to disqualify this possibility (*See Appendix*). Alternatively, accumulating synaptic inhibition building up during a swimming episode could be envisaged but its contribution would not be critical to reducing episode duration since strychnine application roughly reduce duration of swimming episodes by half (McDearmid and Drapeau, 2006). The observation of a beat-and-glide phenotype in isolated larval zebrafish spinal cord preparations in which fictive swimming was elicited by NMDA application (Chapters 2 and 3; McDearmid and Drapeau, 2006; Lambert et al. 2012) suggests that the more frequent swimming episodes of beat-and-glide is encoded within spinal locomotor circuits at larval stages. Thus,

spinal circuits are sufficient to not only generate the tail beat rhythm but also the much slower episodic rhythm. Finally, we can also eliminate proprioceptive and most other sensory feedback as underlying the beat-and-glide phenotype since this form of swimming can be observed in isolated and paralyzed spinal cord preparations (Chapters 2 and 3; Ampatzis et al., 2014, Buss and Drapeau 2001, Liao and Fetcho 2008, Lambert et al., 2012).

At the cellular scale, further maturation of intrinsic properties of spinal neurons is an intriguing possibility. Adaptive spiking could reduce the duration of swimming episodes (and quiescent episodes if under the control of synaptic inhibition) and intrinsic properties of V2a's and MNs have been shown to generate either tonic firing or adaptive spiking (Ampatzis et al., 2014; Liao and Fetcho 2008). In this case, neurons undergoing a constant tonic drive would adapt to eventually stop firing action potentials for a short time period.

Network description

First, we implemented the transition from weakly glycine dependent rhythm driving tail beats to a strongly glycine dependent rhythm driving tail beats over the whole rostrocaudal extent of the spinal cord (Chapter 2) by increasing the number of IEDs by 4 on each side such that their distribution begins more rostrally at segment 3 (Fig. 4.5A). Furthermore, to model the reduced coupling between the rostral pacemaker kernel and the chain of network oscillators along the length of the spinal cord, we chose to reduce the coupling between PMs and MNs, IEDs, and CINs by artificially reducing the coupling strength by two orders of magnitude rather than increasing the number of the latter three populations by adding neurons not coupled to PMs. This allowed us to model the reduced coupling without having to dramatically increase the computational requirements to run simulations of our model.

Next, we considered a number of possible mechanisms to reduce the duration of swim episodes as well as controlling the quiescent periods between episodes. Mechanisms responsible for the transition from burst swimming to beat-and-glide swimming are not fully elucidated. Yet, we know that neuromodulators such as DA and maybe 5-HT are involved (Lambert et al., 2012; Gabriel et al., 2009). We investigated two mechanisms that could arise from the downstream effects of neuromodulators: cumulative inhibition via recruitment of a new population of inhibitory neurons and changes in intrinsic properties of existing populations (Fig. 4.5*A*).

CUMULATIVE INHIBITION THROUGH ACTIVATION OF IIA (CIA). At the onset of beat-and-glide swimming, a new population of later born inhibitory neurons is integrated to spinal locomotor circuits. Circumferential ascending (CiA) interneurons mature late during development and have been proven to be involved in swimming with a possible role in shaping burst duration (Higashijima et al., 2004). We thus modelled CiAs as a new population of tonic spiking neurons that have ipsilateral ascending glycinergic projections (or IIA in the model). They are a bit less numerous than IEDs (10 versus 12 for per side, respectively) and their distribution starts a bit more caudally around segment 5 because of their ascending projections. Furthermore, IIAs are found all the way down the caudal end. They project ascending ipsilateral glycinergic synapses with rostral IEDs and CINs. Conversely, IEDs form new glutamatergic synapses with caudally located IIA (Fig. 4.5*A*).

CHANGES FROM TONIC TO ADAPTIVE SPIKING. We explored the possibility that changes in intrinsic properties of neurons within spinal locomotor circuits could drive the transition from

burst swimming to beat-and-glide swimming. Specifically, we focused on a conversion from tonic to adaptive spiking (Fig. 4.5B) as a possible mechanism for reducing swim and quiescent episode duration. We focused on three key populations. IEDs that are the network "cornerstone" driving the excitation throughout the network, MNs that represent the network outputs but are also provide feedback on their current state of activity through gap junctions with various other spinal neurons, and the CINs that are essential for both pattern and rhythm generation in our models. While experimental evidence is lacking regarding such a change in V2a spinal neurons, the biological analogs of IEDs (Menelaou and McLean, 2012; Ljunggren et al., 2014), some sMNs exhibit some adaptive spiking behaviour (Menelaou and McLean, 2012). CINs have no well identified biological analogs yet. However, later born commissural bifurcating longitudinal (CoBL) glycinergic neurons are involved in swimming and are recruited during the beginning of the burst only (Liao & Fetcho, 2008). Even though CoBL do not display a purely adaptive spiking profile, they show an adaptive behaviour that can be modelled as adaptive spiking CIN neurons. Excitation of the network was implemented as previously with noisy drive of rostral IEDs and PMs.

Simulation results

First, we added network oscillators along most of the rostrocaudal extent of the spinal cord except for the most rostral segments. Along with reducing the coupling between PMs and the rest of the spinal locomotor circuits, these changes are thought to lead to rhythmic tail beats that are sensitive to inhibition of glycinergic transmission (Chapter 2). However, experimental evidence suggests that expanding network oscillators as well as decreasing the overall coupling between

PMs and the rest of the spinal locomotor circuit does not generate a transition from burst swimming to beat-and-glide swimming (Chapter 2).

Thus, we tested two proposed mechanisms to transition the model from burst swimming to a beat-and-glide swimming. We found that the addition of ipsilateral inhibitory ascending (IIA) interneurons strengthened the generation of rhythmic tail beats but failed to shape the motor output as trains of short swimming episodes, typical of beat-and-glide swimming (Fig. 4.5*C*). Instead, the sole incorporation of IIA interneurons led to long burst swimming-like episodes. On the other hand, we found that we could reduce swim episode duration by changing the dynamics of the neuron models of IED, MN and CINs such that these three targeted populations exhibited an adaptive spiking profile (Fig. 4.5*D-E*). However, bursts were terminated too soon with adaptive IEDs, while adaptive MNs or CINs alone also failed to display beat-and-glide like swimming.

We finally chose an architecture with both adaptive MNs and adaptive CINs while adding IIA neurons. Network output showed trains of shorter bursts (~200 ms) containing typically 4-5 tail beats (Fig. 4.5*F, 3.6A, Supp. Data video 4.S4*) as described experimentally (Buss and Drapeau, 2001; Drapeau et al., 2002). Episodic frequency was typically around 2 Hz. This network architecture was also able to reproduce experimental data describing the effects of strychnine (i.e. blocking glycinergic transmission) on the rhythm of tail beats. Indeed the weak coupling between PMs and the rest of the spinal locomotor circuit and the addition of more network oscillators were sufficient to make the rhythm of tail beats sensitive to blocking glycinergic neurotransmission, therefore reproducing experimental data (Fig. 4.6*A-D*). Blocking glycinergic transmission led to loss of rhythmic tail beats as seen in the measurement of body

angles (Fig. 4.6*A*), and the loss of rhythmic firing in some MNs (Fig. 4.6*B*). The loss of rhythm driving tail beats is further supported by measuring autocorrelation of muscle activity (Fig. 4.6*C*), and the cross correlation between left and right sides (Fig. 4.6*D*).

Interestingly, increasing the parameter b in our single neuron models, which models the sensitivity of the recovery variable u to the subthreshold fluctuations of the membrane potential v (Izhikevich, 2003), increased the motor output by decreasing the quiescent periods (Fig. 4.6*E*) similarly to the effect of 5HT on spinal locomotor circuits during in vivo experiments (Brustein et al., 2003). These simulations suggest that both changes in intrinsic properties of CINs and MNs and the activation of IIA seem necessary to properly emulate beat-and-glide phenotype.

Discussion

We have progressively built models of spinal locomotor circuits representing the successive locomotor behaviours of the developing zebrafish by implementing mechanisms described experimentally. In the process, we identify specific mechanisms by which spinal locomotor circuits generate further and further refined movements through changes in connectivity, integration of new spinal populations, and changes in firing properties.

PM based network for early simple behaviour

The earliest locomotor behaviours in zebrafish, single and multiple coilings, require global recruitments of neurons, especially MNs, to synchronously contract all ipsilateral muscles. Electrical coupling, which lacks the delays inherent with chemical neurotransmission, enables these types of ballistic movements and early locomotor behaviour in zebrafish seems to rely on this architecture as demonstrated by experimental evidence that electric synapses are necessary and chemical transmission is dispensable. The quick and multidirectional current transmission supported by electrical synapses is a perfect solution for global control of a neural circuit (Bennett and Zukin, 2004). However, synchronous activation of an ensemble of neurons does not easily accommodate rhythmic activity unless some neurons possess intrinsic properties that enable bursting activity within these neurons.

Network oscillator for more refined movements

A drawback of the early architecture assembled in embryonic zebrafish is that it does not easily accommodate more refined movements that require more exquisite spatio-temporal patterning of

muscle activity. The establishment of chemical synapses in between older and newly emerging populations of neurons within spinal locomotor circuits allows a more precise and directed control of swimming. The addition of chemical synapses is not the only change that we incorporated in our model of spinal locomotor circuits at this stage. The generation of rhythm driving tail beats was delegated to network oscillators distributed along the length of the spinal cord. The rationale for moving away from pacemakers as source of the rhythm is that relying on a single population of pacemakers leaves spinal locomotor circuits vulnerable to any flaws in the function of a small population of neurons. In addition, there may be multiple local rhythms that control body oscillations along the length of the growing zebrafish. In support of the presence of many rhythm-generating kernels along the length of the spinal cord, locomotor output has proven to be very robust to experimental disturbances of spinal locomotor circuits such as sectioning of large parts of the circuit and that has led to the suggestion that redundant rhythm-generating circuits must be present within the spinal cord (McDearmid and Drapeau, 2006; Wiggin et al., 2014). Experimental evidence from our lab further suggests that the development of local half-centres that occurs progressively from the caudal toward the rostral end of the body. The implementation of this idea in our model of spinal locomotor circuits at this age succeeded in reproducing typical larval swimming behaviours as well as experimental observation such as the differential effect of blocking glycinergic transmission on rhythmogenesis along the rostro-caudal axis (Fig. 4.4).

One limitation of our model is that burst swimming involves long sustained episodes of tail beats without the even longer quiescent periods experimentally observed. In our model, the sustained episodes of tail beats were driven by tonic excitatory drive. We suspect that the long

quiescent periods seen experimentally are due to cessation of excitation of spinal locomotor circuits and that the infrequent swim episodes are generated by brief pulses of excitatory drive, putatively from supra spinal structures. Note though that in our beat-and-glide model, the alternation between swim and quiescent episodes occurred during continual tonic drive. We believe that this response to a tonic drive is due to the additions to the model (IIA and adaptive spiking).

Another limitation is that the model failed to reproduce the transition from arhythmic to rhythmic glycinergic inputs in MNs as network oscillators are implemented (Chapter 2). Glycinergic inputs are always rhythmic in the model (data not shown). Arrhythmic glycinergic inputs in early developing fish may be due to the transmission of several populations of inhibitory neurons presynaptic to MNs. An early population that spikes erratically would therefore produce an arhythmic drive, as opposed to a late population presenting a more consistent spiking profile, thus producing rhythmic drive. Maturation of intrinsic properties of CINs that was not modelled could also change the rhythm of glycinergic inputs to MNs during development.

Competing during a transition period

During the transitioning period of burst swimming at around 3 dpf, we propose that two oscillators driving the rhythm of tail beats coexist. The first oscillator consists of a rhythmogenic layer driven by PMs that is fully separated from a pattern generation layer consisting of the contralateral inhibition generated by CINs and contralateral excitation by CENs. This is in contrast to the second type of oscillator, based on a half-centre architecture, where both rhythm

and pattern generation are merged together through reciprocal inhibition. In our model, this type of inhibition is responsible for both the left-right alternating pattern and rhythm generation though these two facets of swimming behaviour could be controlled by separate populations of spinal neurons.

We propose that these two types of oscillators work together at this developmental stage - the PM based oscillator driving predominantly the rostral part of the fish body whereas the half-centre-like network oscillators drive the caudal end of the body. However the coexistence of both oscillators is not sustained as the PM based oscillator will eventually be superseded due to the integration of new neurons into spinal locomotor circuits, which has the effect of decreasing the coupling coefficient between the PM based oscillator with the rest of the spinal locomotor circuit. This was previously modelled by a reductive mathematical model of two coupled harmonic oscillators and was shown to be sufficient to capture this transition (Chapter 2).

Mechanisms of transition of burst to beat-and-glide swimming

While our experimental data showed that the 20-40 Hz rhythm driving tail beats could emerge from network oscillators replacing the PM-based architecture of early embryonic zebrafish, this transition does not seem to be responsible for the switch from burst to beat-and-glide swimming where swimming episodes become shorter and more frequent (Buss and Drapeau, 2001). In this current study, we tested several possible mechanisms that could underlie this transition but only the change toward adaptive spiking in conjunction with the presence of ipsilateral ascending inhibition could correctly reproduce the beat-and-glide phenotype. Neither the rostrally directed extension of network-oscillator units throughout the spinal cord nor the sole addition of IIA

neurons (corresponding to biological CiAs) could shape the motor output into multiple short swimming bursts driven by a continuous excitation from descending inputs. Both tonic and adaptive spiking profiles for IIA neurons were tested but neither led to the desired sus-mentionned phenotype (i.e. beat-and-glide swimming). However, a combination of tonic IIAs and changes in firing behaviour of either MNs, CINS, or IEDs transformed a steady excitatory drive of the network to alternating periods of swimming activity and quiescence. Interestingly, modelling any of the MNs, CINs and IEDs with adaptive spiking parameters was sufficient to reproduce beat-and glide phenotype. However, experimental evidence (Ampatzis et al., 2014) suggests no such profiles for V2a interneurons (the biological analog of our IED). We therefore modeled adaptive spiking MNs and CINs. While the existence of biological analogs to CINs at the onset of coiling early in development is suggested by the presence of glycinergic synaptic bursts in the contralateral side during coiling events, experimental evidence seems to be lacking to draw any conclusion about their firing behaviour and its putative change during development. MNs on the other hand have been shown to be capable of adaptive spiking (Menelaou and McLean, 2012).

What mechanisms could drive changes in the intrinsic properties of specific populations of neurons during the development of zebrafish? It has previously been reported that blocking D4 dopamine receptors during zebrafish larval development prevented transitioning from burst to beat-and-glide swimming, suggesting that dopamine from supraspinal sources (Lambert et al., 2012) plays a role in shaping the beat-and-glide phenotype. However, in already transitioned fish, isolated spinal cords exhibit typical beat-and-glide pattern with just NMDA application. Since there are relatively few dopaminergic sources in the spinal cord (McLean and Fetcho,

2004; Tay et al., 2011), it suggest that, once transitioned, the spinal locomotor circuit is sufficient to sustain beat-and-glide activity. Thus, dopamine could trigger through D4Rs signalling pathways modifications of intrinsic properties in targeted populations (e.g. CINs) during development. Serotonin might also play a role in tweaking intrinsic properties since experimental results using 5-HT to modify motor output could be reproduced in our model by changing the value of the parameter *b* in CINs, MNs or IEDs. Indeed, increasing the value of parameter *b*, which models the sensitivity of the recovery variable *u* to the subthreshold fluctuations of the membrane potential *v* (Izhikevich, 2003), to generate adaptive spiking MNs and CINs reduced the quiescent period duration between two bursts in similar way that increasing serotonin (5-HT) concentration experimentally produces the same reduction (Brustein et al., 2003). 5-HT might be involved in changing the intrinsic properties of the aforementioned neurons to shape the motor output such as changes in subthreshold properties (biological analog to changes in parameter *b*) due to tweaks in channel sensitivity for instance (Gao and Ziskind-Conhaim, 1998; Spitzer and Ribera, 1998; Sun and Dale, 1998; Perrier and Hounsgaard, 2000; Hsiao et al., 2005). Thus, it might also been involved in the transition in conjunction with DA.

The model is reductive in a sense that it incorporates only a subset of all known population of spinal neurons to identify key mechanisms that underlie the transition between different behaviours in developing zebrafish spinal cord. Further expansions of this model could be to increase biological accuracy in terms of number of neurons per population (e.g. over 100 cells for each), which may enable the implementation of more complex network organizations and locomotor function such as the modular organizations controlling different speeds of locomotion (Ampatzis et al., 2014, Menelaou et al., 2012). Indeed, previous studies in zebrafish

have shown that MNs and V2a neurons are organized in three different modules (slow, medium and fast) that are differentially recruited regarding the swimming speed (Ampatzis et al., 2014). We could therefore differentiate populations of primary and secondary MNs known to be involved in swimming episodes of different speeds (fast and slow respectively, Menelaou and McLean, 2012) and further subdivide secondary MNs as well as V2a populations in mirroring fast, medium and slow modules. The different subpopulations should bemostly similar with slightly different intrinsic properties (parameters) so that each sub population is gradually recruited as the supraspinal drive gradually increases in intensity. More recently, MCoD (Multipolar Comissural Descending) neurons have been described as involved in the modulation of swimming speed (McLean et al., 2008; Björnfors and El Manira, 2016) and could be also implemented in a similar way as V2a neurons.

Another direction to expand our models would be to implement postural changes and turning movements. These could be achieved combining non-uniform distributions of descending inputs along the length of the spinal cord and separation of MNs into two subpopulations of primary, harder to recruit MNs and secondary easily recruited MNs. Network architecture should be based on a similar organization as our model for beat-and-glide swimming such that only sMNs would be recruited by steady, relatively low amplitude descending inputs, therefore generating “slow” swimming. Rostral pMNs would be sporadically recruited via asymmetric pulses (e.g. asymmetry in descending drives to the left side and right side of the spinal cord) in descending inputs. Therefore, transient recruitment of rostral ipsilateral pMNs curves the body in the rostral region correcting the position of the head and changing the

direction of swimming. Hence, around the 2/3 of the fish body starting from the caudal end would act as the propeller whereas the rostral part of the fish would act as the rudder.

Our modelling work provides clearly defined roadmaps for new investigations. Many of these changes may be driven by neuromodulators such as dopamine and serotonin and our model suggests further experiments to elucidate the mechanism in which neuromodulators are directly responsible for transitioning and controlling motor output. This model could be used to predict the exact roles of various populations of spinal neurons, as well as to predict how diverse types of movements such as turns and escapes, can be produced by motor commands from different reticulospinal inputs to spinal locomotor circuits. Even though refinements and more research is needed to further complete our understanding of development of neural activity encoding locomotion in zebrafish spinal cord, this model serves as a valuable base for further investigations in zebrafish as well as in other species as several neural mechanisms described in zebrafish have been demonstrated to be present in other mammalian systems (Goulding, 2009). By iteratively building upon our model to simulate the different developmental milestones of the zebrafish locomotor behaviour, we highlight the value of our approach in being able to identify how the incorporation of specific populations of neurons and the subsequent creation of new spinal circuits, in addition to changes in firing behaviour of identified spinal neurons, contribute to the maturation of locomotion. This ultimately allows us to make better sense of a complex circuit for motor control.

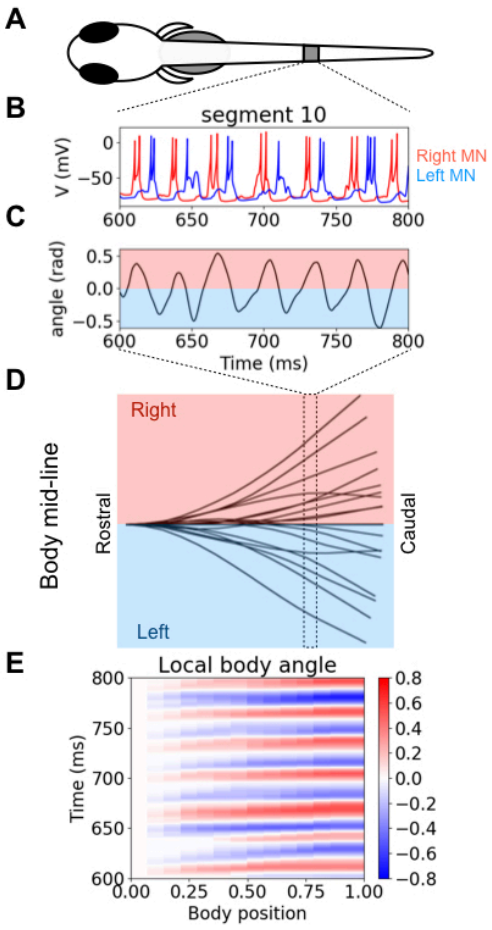

Figure 4.1. Musculo-skeletal model helps to read network output.

A, Schematic of a fish body (Top view). ***B,*** Motoneuron (MNs) output of the 10th segment spinal segment from the simulated spinal circuit (red traces for the right MN and blue trace for the left MN) is used to calculate body angle variation. ***C,*** of this segment via a simple musculoskeletal model (See Methods). ***D,*** 20 body midlines extracted from a simulated burst swimming. Body midline is computed by compiling all the calculated local body angles along the simulated fish body. ***E,*** Heat-map of local body angle variation across the total body length and through time. Red is for right curvatures while blue labels left curvatures. Body position on the abscissa, 0 is the rostral extremum wile 1.00 is the caudal extremum.

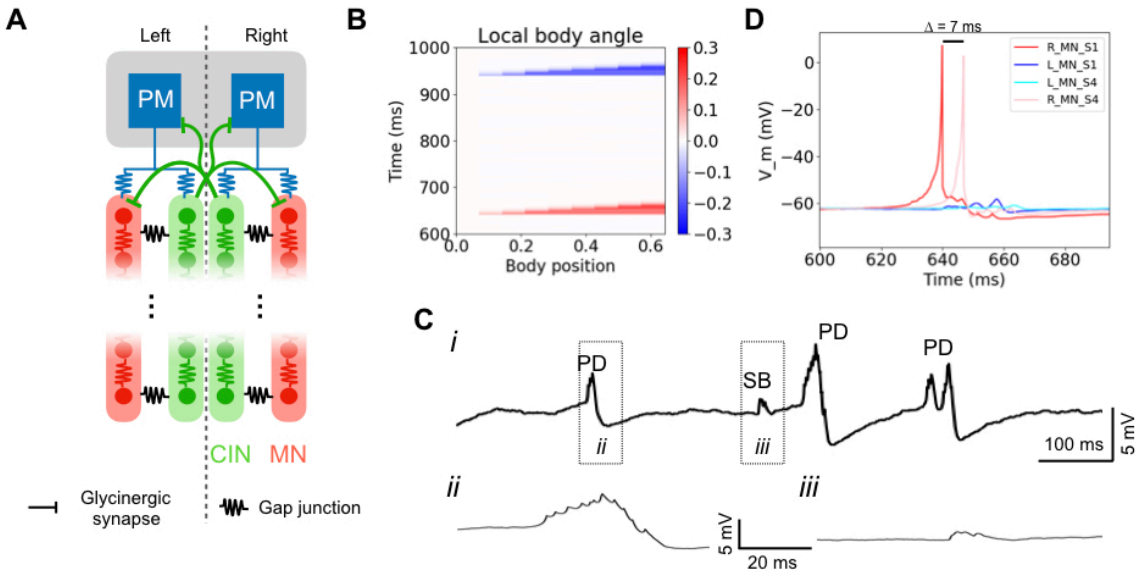

Figure 4.2. Single coiling model relies on a fully electrical network driven by pacemaker neurons.

A, Schematic of the model architecture underlying coiling. Rostral kernels of PM neurons drive chains of MNs (red) and commissural inhibitory neurons (CINs in green) through electrical synapses. The chains span over 10 spinal segments. MNs project to muscles while CIN project to contralateral MNs and PMs forming glycinergic synapses. ***B,*** Heat-map of local body angle variation through time in a simulation. Right coiling in red, left coiling in blue. ***C,*** *i,* Typical trace of a MN membrane potential from a simulation. Two different events can be observed: Periodic depolarization (PD) - *ii,* zoom from the dotted box in *i* - and synaptic bursts (SB) - *iii,* zoom from the dotted box in *i*. ***D,*** Membrane potentials from four different MNs during a right coiling event. Red trace is for right MN from segment 1, blue trace is for left MN from segment 1, pink trace is for right MN from segment 4, cyan trace is for left MN from segment 4.

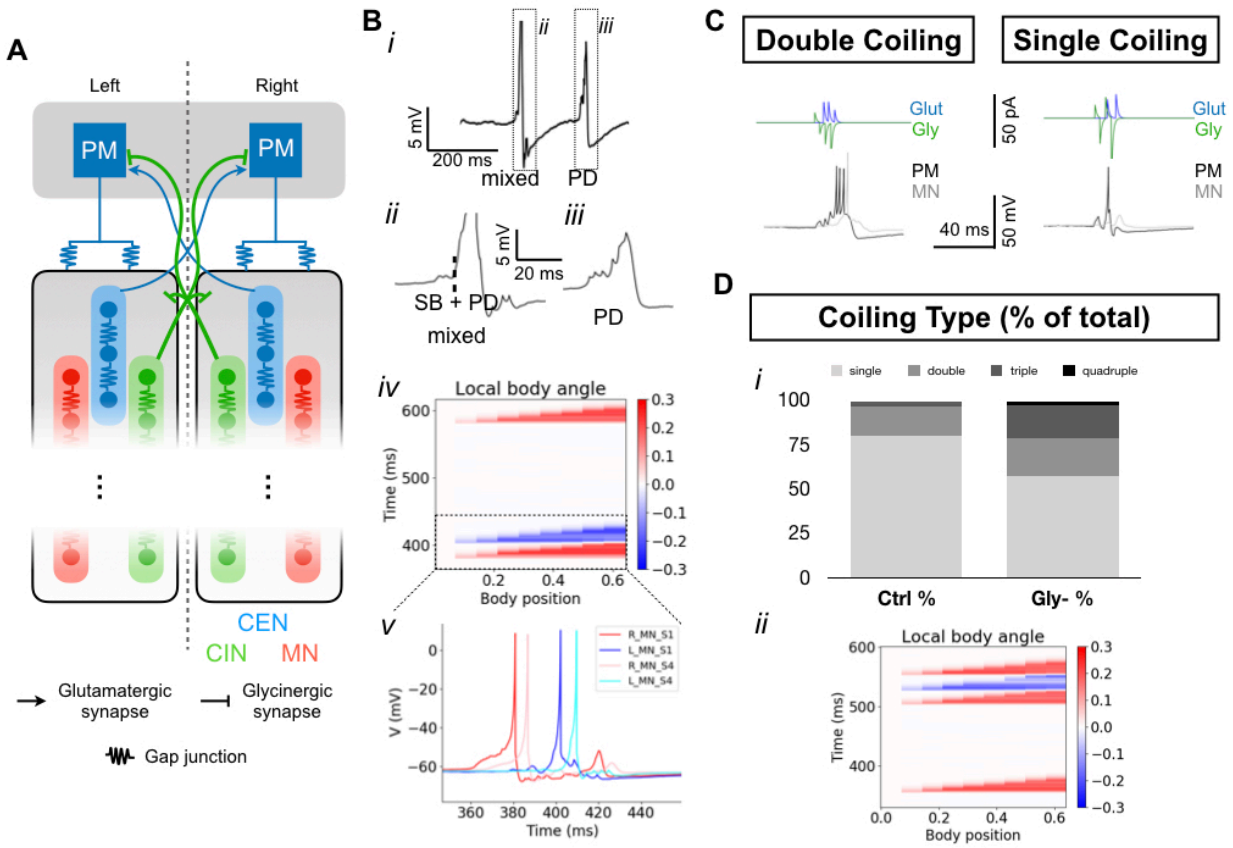

Figure 4.3. Double coiling model relies on a hybrid network of electrical and chemical synapses.

A, Schematic of the model architecture underlying double coiling. From the single coiling model we added a new population of commissural excitatory neurons (CEN) projecting to contralateral PMs forming glycinergic synapses. ***B,*** *i,* Typical trace of a MN membrane potential from a simulation. A new kind of event coexisting with the previous PD and SB can be observed: mixed events in which a PD directly followed by a SB or vice-versa - *ii,* zoom from the dotted box in *i* - *iii,* zoom from the doted box in *i*. *iv* Heat-map of local body angle variations through time. The dotted box highlight a double coiling. *v* Membrane potentials from four different MNs during the double coiling event from the dotted box. Red trace is for right MN from segment 1, blue trace is for left MN from segment 1, pink trace is for right MN from segment 4, cyan trace is for left MN from segment 4. ***C,*** Example of glutamatergic (blue) current and glycinergic current (green) received by a PM neuron (black) during a double coiling (left) or single coiling (right) event. Grey line represents the membrane potential of a downstream ipsilateral MN. ***D,*** *i,*

Proportions of single, double, triple and quadruple coiling events under control conditions and while blocking glycinergic synapses (gly$^-$). *ii,* Heat map of local body angles variatio showing a single and a triple coiling during a simulation.

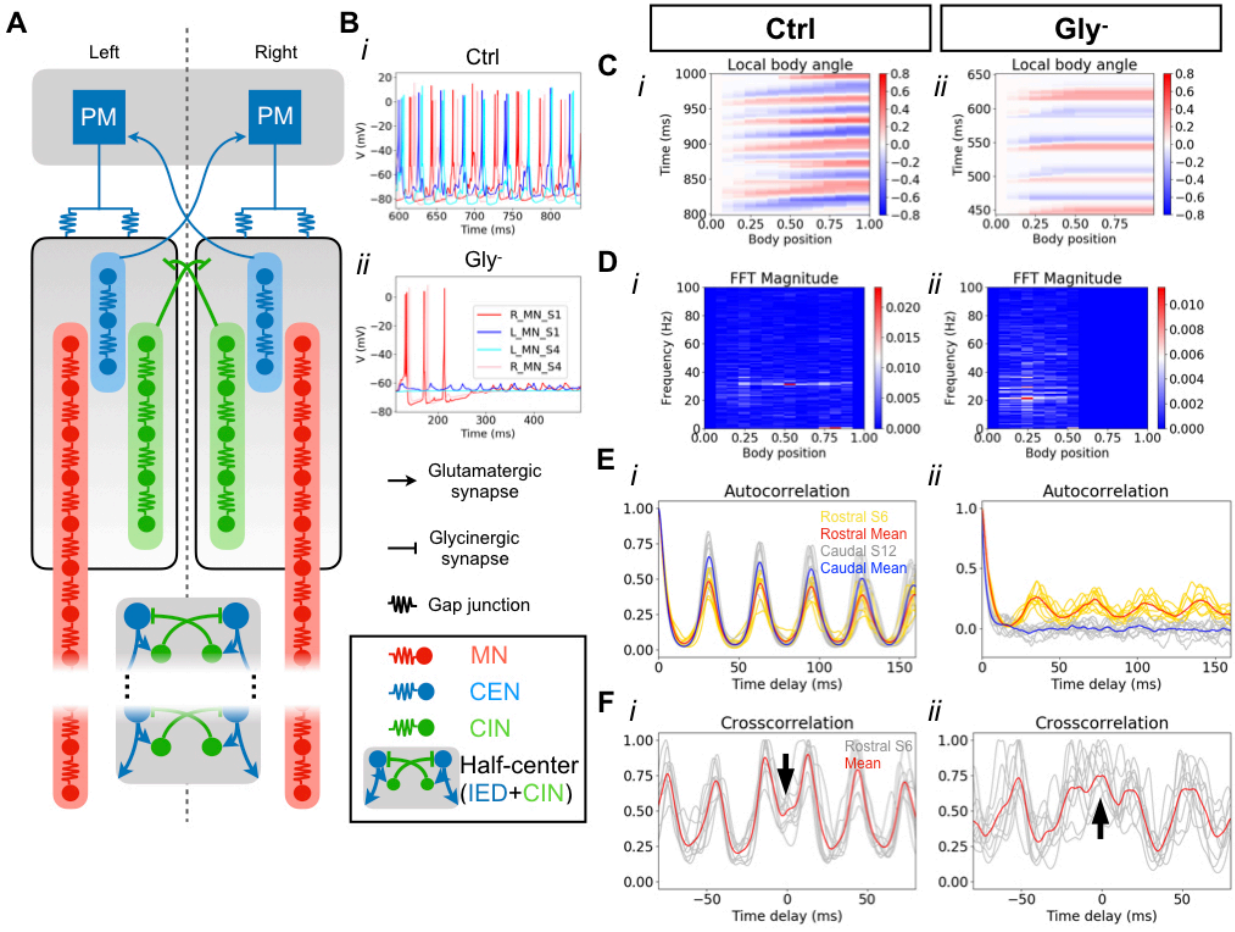

Figure 4.4. Emergence of half-centre oscillators during burst swimming.

A, Schematic of the model architecture underlying burst swimming. From the double coiling model we added a new population of Ipsilateral excitatory descending neurons (IED) forming half-centre oscillators with the caudal CINs. IEDs drive downstream MNs. The number of spinal segment is increased to 15 to take into account the growth of the fish body. ***B,*** Traces of four MNs (left and right, segment 1; left and right, segment 4). ***C,*** Heat map of local body angle variation from a typical simulation. ***D,*** A fast Fourier transform (FFT) is applied on each body segment during a simulated burst swimming event. ***E,*** Autocorrelation of left muscle cell activity from the 6th segment over 10 runs (yellow traces, average in red) and the 12th segment (grey traces, average in blue). ***F,*** Crosscorrelations of left versus right muscle activity of the 6th somite for 10 simulations (grey traces, average in red). Note the local minimum (*i*,

black arrow) and maximum (*ii*, black arrow) at the 0 ms time delay. ***B-F*** control conditions (*i*) and while blocking glycinergic synapses (*ii*).

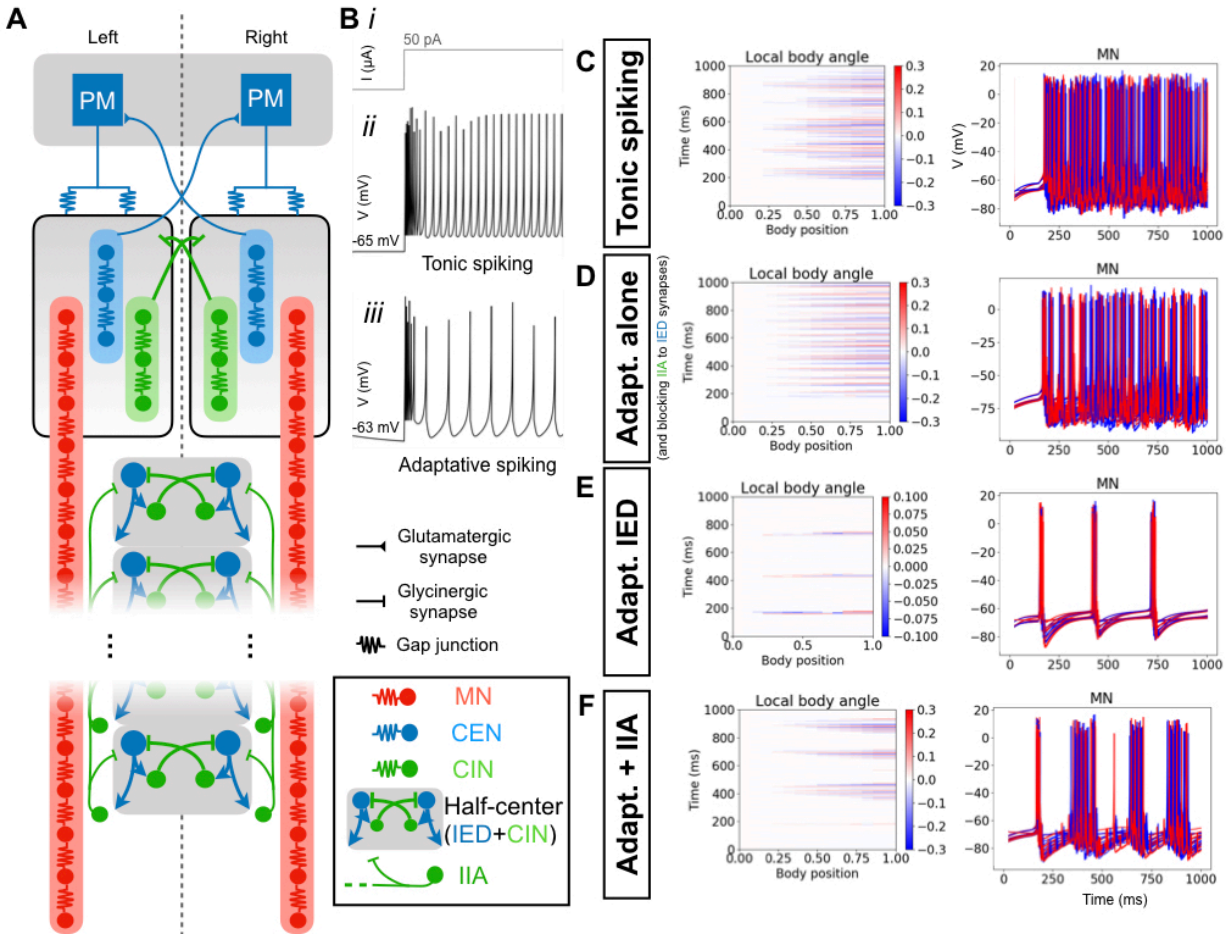

Figure 4.5. Beat-and-glide swimming model requires both the implementation of a new population of neurons and maturation of intrinsic properties of existing neurons.

A, Schematic of the model architecture underlying beat-and-glide swimming. From the burst swimming model, half centers are expended rostrally and a new population of Ipsilateral inhibitory ascending neurons (IIA) is added. IIA forms glycinergic synapses with upstream IEDs and MNs. ***B,*** example of a current step used for stimulating a single neuron model (*i*). Changing parameters of a neuron model changes spiking phenotype from tonic spiking (*ii*) to adaptive spiking (*iii*). ***C,*** Output example from a beat-and-glide network that includes IIA and all neurons exhibit tonic spiking phenotype. ***D,*** Output example from a beat-and-glide model network with adaptive CINs and MNs but does not include IIAs. ***E,*** Output example from a beat-and-glide network with adaptive IEDs only and without IIAs. ***F,*** Output

example from a beat-and-glide model network with adaptive CINs and MNs and with implementation of IIAs (tonic). ***C-F*** Left - heat-map of local body angles. Right - membrane potential traces of all MNs of the network. Left MNs in blue and right MNs in red.

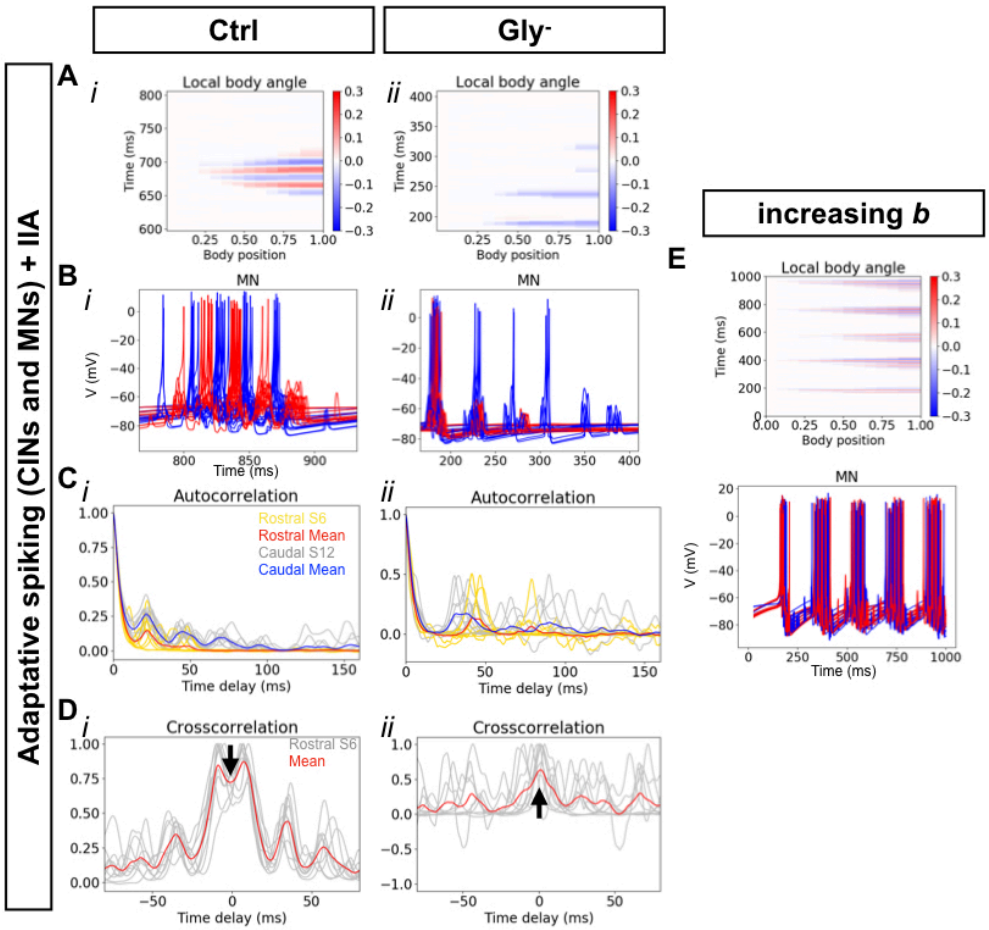

Figure 4.6. Beat-and-glide model network with adaptive CINs and MNs and tonic IIAs reproduces experimental observations of tail beat rhythm generation.

A, Heat map of local body angle variation from a typical simulation. ***B,*** Membrane potential traces of all MNs of the network. Left MNs in blue and right MNs in red. ***C,*** Autocorrelation of left muscle cell activity from the 6th segment over 10 runs (yellow traces, average in red) and the 12th segment (grey traces, average in blue). ***D,*** Crosscorrelations of left versus right muscle cells activities of the 6th somite for 10 simulations (grey traces, average in red). Note the local minimum (*i*, black arrow) and maximum (*ii*, black arrow) at the 0 ms time delay. ***A-D,*** control conditions (*i*) and while blocking glycinergic synapses (*ii*). ***E,*** Up - Heat map of local body angle variation from a typical simulation with an increased

value of *b* parameter in adaptive spiking CINs and MNs. Down - Membrane potential traces of all MNs of the network from the same simulation.

Table 4.1. *Parameter values of simple spiking neuron models of all populations involved in the modelling process*

population	Existing candidate	Izhikievich parameters											
		a	σ_a	b	σ_b	c	σ_c	d	σ_d	x position [a, b]	σ_{pos}	I_{drive}	σ_I
MN	pMN, sMN	0.02	0.001	0.2	0.001	-53	0.001	6.0	0.001	5.0 +1.6*n*r	0.01		0.25
PM	IC	0.02	0.001	0.25	0.001	-50	0.001	2.0	0.001	1.0	0.3	7.5-10	0.25
CIN	CoBL, CoSA	0.02	0.001	0.2	0.001	-53	0.001	6.0	0.001	5.0 +1.6*n*r	0.01		
CEN	??	0.02	0.001	0.2	0.001	-53	0.001	6.0	0.001	5.1 +1.6*n*r	0.01		
IED	CiD(V2a)	0.02	0.001	0.2	0.001	-53	0.001	6.0	0.001	5.1 +1.6*n*r	0.01	1.9 - 2.1	0.25
IIA	CiA (V1)	0.02	0.001	0.2	0.001	-53	0.001	6.0	0.001	10.1 +1.6*n*r	0.01		

[a] *n value is the number of the neurons in the population, from 0 to N-1, N being the total number of neurons in that given population.*

[b] *r is a random variable introduced to add noise in the neuron positioning along the rostrocaudal (x) axis. For each neuron, an r value was picked from a Gaussian probability distribution of mean* $\mu = 1$ *and variance* σ_{pos}

Table 4.2. *Electrical synapse (gap junctions) weights used for modelling.*

population	MN	PM	CIN	CEN	IED	IIA
MN	0.04	-	-	-	-	-
PM	0.03	0.01	-	-	-	-
CIN	0.05	0.05	0.05	-	-	-
CEN	0.05	0.06	0	0.05	-	-
IED	0.001	0.05	0	0	0.005	-
IIA	0	0	0	0	0	0

Table 4.3. *Chemical synapses (glutamatergic in white and glycinergic in grey) weights used for modelling. Pre-synaptic neurons are in columns. Post-synaptic neurons in rows.*

population	MN	PM	CIN	CEN	IED	IIA
MN	0	0	0.25	0	0.4	0.005
PM	0	0	0.05	0.02	0	0
CIN	0	0	0	0	0.05	0
CEN	0	0	0	0	0	0
IED	0	0	0.2	0	0.005	0.005
IIA	0	0	0	0	0.005	0

Table 4.4. *Glutamatergic (white) and glycinergic (grey) reversal potential and time constants used to model respective synapses.*

Chemical Synapse	E_{rev}	τ_r	τ_f	V_{thr}
Glutamatergic	0	0.5	1.0	-15
Glycinergic	-42	0.5	1.0	-15

Video 4.S1 Single coiling model behavior

https://www.dropbox.com/home/Supplementary_Videos

Video 4.S2 Double coiling model behavior

https://www.dropbox.com/home/Supplementary_Videos

Video 4.S3 Burst swimming model behavior

https://www.dropbox.com/home/Supplementary_Videos

Video 4.S4 Beat-and-glide swimming model behavior

https://www.dropbox.com/home/Supplementary_Videos

CONCLUSION

It is common knowledge that the spinal cord is able to generate locomotor activity on its own. Spinal locomotor circuits in vertebrates have been extensively studied, and as a result, many of the properties of neural populations that make up these circuits have been described. However, we still lack a full understanding of how these components operate together within the spinal locomotor circuit in order to produce rhythmic output and muscle coordination. We sought to unravel this intricate neural machinery by studying the development of the zebrafish spinal locomotor circuits, in particular the rhythm generation mechanism thought to drive the rest of the circuit. In the process, we were able to provide evidence that spinal locomotor circuits undergo fundamental changes as the zebrafish transitions from early locomotor behaviour to more mature form of swimming. The early pacemaker (PM) based architecture is superseded by a network-oscillator architecture. By combing these finding with previously published insights we were able to propose models reflecting the maturation process of the spinal locomotor circuit of the zebrafish from the first observable motor behaviour (coiling) to an advanced form of swimming (beat-and-glide).

Identification of mechanisms for rhythm generation in developing zebrafish larvae

We tested different potential mechanisms for rhythm generation in the zebrafish spinal locomotor circuits of developing zebrafish. Since there are two general mechanisms for rhythm generation, one based on intrinsic properties and the other on network properties, we tested for the presence

of both of them. Our search for potential PM neurons in the caudal sections of the spinal cord using a ZAP approach to detect intrinsic properties conducive to endogenous rhythmogenesis failed to yield any cell population that could supplement IC neurons in being PMs. On the other hand, focusing on the presence of network-based rhythmogenesis by testing the effects of blocking synaptic inhibition (i.e. glycinergic synapse) allowed us to reveal that mechanisms for tail beat rhythm generation transitioned from weakly glycinergic dependent to strongly glycinergic dependent. We argue that the differential effect of strychnine on tail beat rhythm generation is due to an organizational switch in the spinal locomotor network from a pacemaker-based architecture toward a network-oscillators based architecture. However, we showed that this transition is not sufficient for explaining the phenotype change from burst swimming to beat-and-glide swimming later supported by our modelling approach. We also tested other candidate mechanisms to explain this phenotype transition by investigating the role of neuromodulators (DA) and the ATP-ase Na+/K+ pump. While experiments testing the involvement of the pump were inconclusive, we confirmed prior studies showing that DA plays an important role in maturation and especially in the development of the beat-and-glide phenotype (Lambert et al., 2012). Indeed, blocking D4receptors during development maintains the burst swimming phenotype. However, once transitioned, DA is not necessary to maintain the beat-and-glide phenotype suggesting other changes in network structure (connectivity) and/or intrinsic properties of targeted neurons. Serotonin might also be involved in transitioning from burst to beat-and-glide swimming as it has been shown to shape the duration of quiescent periods between swim episodes in beat-and-glide swimming without changing neither episode duration nor tail beats frequency (Brustein et al., 2003).

However, we cannot fully reject the hypothesis of the potential presence of caudal PM neurons in the spinal cord as ZAP experiment does not necessarily give definitive answer on this question. First of all, there is the non-negligible possibility that we simply missed potential PM neurons. Our whole fish preparation for whole cell patch-clamp recordings of spinal neurons biases our sample towards more easily accessed laterally located cells (right under the spinal dura) than those located more medially. Thus, if potential caudal PM neurons are sparse and located deeply in the spinal cord, we might not have patched any in our 58 tested neurons. In addition, potential caudal PM neurons might only express their endogenous bursting properties under neuromodulation (i.e. presence of DA or 5-HT), meaning that the experiment might give different outcomes if performed with 5-HT and DA in bath. However, the absence of effect of 5-HT on tail-beat rhythm in larval zebrafish as well as the ability of the isolated spinal locomotor circuits to produce consistent motor output whiteout dopaminergic input does not support this idea (Jay et al., 2015; Brustein et al., 2003).

Nevertheless, the ZAP approach might not be the best suited experiment for PM detection and other ways to explore this hypothesis should be studied. For instance, using a transgenic line expressing the fast calcium indicator GCaMP6f could enable the monitoring of the activity of multiple neurons at a time in frequency ranges close to that of swimming (i.e. 20 Hz; Chen et al., 2013). Blocking synaptic transmission with kynurenic acid while increasing neurons excitability by increasing potassium concentration in aCSF would help detect neurons exhibiting endogenous bursting profiles closer to swimming frequency

Finally, we cannot exclude that the residual rhythm at 3 dpf is produced by a network oscillator relying on gap junctions and glutamatergic synapses only. This configuration would

require a depressing mechanism for glutamatergic synapses with a bistable recovery process. Thus, the synaptic weight would increase while the neuron remains inactive but once the neuron fires a few action potentials, the synapse is depressed silencing the neuron. Such mechanism provides a rhythmic output when the neuron is fed with tonic inputs.

We were able to combine our experimental findings with previously published insights into the development of swimming in zebrafish to generate computational models of the developing spinal locomotor network in zebrafish larva. By iteratively building upon the model in ways that reflected mechanisms by which the nervous system matures - neurogenesis, refinement of synaptic connectivity and changes in intrinsic properties, I was able to capture the different swimming movements that occur along the way during the maturation of zebrafish locomotion. The model predicted the transition from burst to beat-and-glide could occur only if both a new source of ipsilateral inhibition and some changes in intrinsic properties were implemented. Both mechanisms have good biological candidates that can be targets for further experiments. The new source of inhibition is based on the previously described biological CiA neurons whereas changes of intrinsic properties of MNs and commissural inhibitory neurons could be downstream results of dopaminergic signalling pathways in targeted cells. It finally allowed us to predict that 5-HT could shape the quiescent period's duration via tweaking intrinsic properties of either MNs, or analog neurons of CiDs or CoBLs.

While being an excellent proof of concept for development of tail beats rhythm generation, the proposed model is reductive in the number of simulated neurons and is not able

to catch the complex intricacies of multiple populations of neurons organized in sub-circuits (See Future directions Below).

Future directions

Switch in intrinsic properties

Even though, the proposed model suggests that the transition from burst to beat-and-glide swimming is partially due to changes in spiking phenotype of some population of neurons involved in the locomotor circuit, the exact transition mechanism remains unclear and further research is needed to fully characterize them. Neuromodulators such as DA or 5-HT are able to modulate changes in the level of expression as well as regulating the activation/deactivation dynamic of particular ionic channels resulting in changes in intrinsic properties, and thus spiking phenotype (Gao and Ziskind-Conhaim, 1998; Spitzer and Ribera, 1998; Sun and Dale, 1999; Perrier and Hounsgaard, 2000; Hsiao et al., 2005). We suggested that DA is involved in this transition, however, there is no known example of a change from tonic to adaptive spiking phenotype solely due to DA neuromodulation. More subtle tweaks in intrinsic properties via 5-HT could be responsible for reduced synaptic inhibition during quiescent periods, hence decreasing their duration resulting in increased motor outputs. Again, exact mechanisms by which this modulation is implemented are not known let alone the targeted neuron populations. Our model proposes candidate spinal neuron population that could be targets for 5-HT neuromodulation, thus giving an entry point to further characterize these mechanisms.

Identify sources of synaptic inhibition during swimming

One of the populations potentially targeted by neuromodulation proposed in our model is a class of commissural inhibitory neurons (CINs) that does not have a clear biological homolog. A clear identification of this source of commissural inhibition is key to fully comprehend the spinal circuit for locomotion in the zebrafish larvae. Numerous candidate populations already exists and are active during locomotor behaviours. Contralateral bifurcating longitudinal (CoBL), Commisural and secondary ascending (CoSA) and Comissural local (CoLo) could be considered as good candidates (Liao and Fetcho, 2008). However, the extensive study from Liao and Fetcho characterizing the activity of spinal glycinergic interneurons during motor movements tells us that we can easily eliminate CoLA and CoLo as they are not active in swimming. CoSA and CoBL on the other hand, are involved in all type of locomotor movements including swimming. Thus, they are good candidates for studying changes in intrinsic properties during development in particular in response to D4R signalling based upon the work of Lambert and colleagues (2012). Keeping track of these populations of neurons through development can be challenging however, as well exemplified by a population of glycinergic ventrally longitudinal descending (VeLDs) spinal interneurons that are well observed in 1-2 dpf fish but seems to disappear later in development (McLean and Fetcho, 2008).

Future maturation mechanism to integrate turns and slow/fast swimming modules

Our model included only a subset of all spinal population of neurons limiting the incorporation of those that were believed to be essential to different swim behaviours studied and the transition between them. This also reduced the computational requirements of the model. Generalizing this model to include the full complement of spinal neurons would allow us to implement more

complex mechanisms involving modular organization within populations. One such modular mechanism has been proposed to underlie the control of different speeds of locomotion. In some motor systems, increases in speed, which is likely due to increased in force production, has been proposed to be generated by the MN size principle where increasingly stronger motor drive will lead to the progressive recruitment of larger and larger MNs that have increasingly smaller input resistance, and are therefore considered less excitable (Henneman et al., 1965; Henneman, 1985; Mendell, 2005; McLean and Dougherty, 2015). However, findings in the zebrafish larval spinal cord suggests that variation in speed does not lead to the recruitment of spinal interneurons in the same manner as motoneurons would if the size principle were to be applied. On the contrary, McLean et al. (2008), suggest that fast and slow swimming in larval zebrafish are supported by distinct populations of interneurons. While, MCoDs (Multipolar Commissural Descending) are recruited for slow swimming, they appeared to be silenced for fast swimming whereas different populations of CiDs are recruited during slow and fast swimming. The recruitment of different populations of spinal neurons during different swimming speeds is opposed to the size principle, which predicts that an increasing number of neurons within a population of spinal neurons would be progressively recruited (McLean and Dougherty, 2015). As well, multiple studies in zebrafish have shown that MNs and V2a neurons are organized in three different modules (slow, medium and fast) that are differentially recruited following a dorsoventral pattern regarding the swimming speed (McLean et al., 2008; Ampatzis et al., 2012). This within population module differentiation is reflected in the topological organization of the spinal cord as earlier-born MNs and INs encoding faster swimming end up being more dorsally located in the spinal cord while slower swimming is supported by later born neurons that end up being more ventrally located

(MacLean and Fetcho, 2009). Differentiation between populations of primary and secondary MNs known to be involved in swimming episodes of different speeds (fast and slow respectively, (Liu and Waesterfield, 1988; Ampatzis et al., 2013) should be implemented in our models as well as further subdividing secondary MNs and V2a populations in mirroring fast, medium and slow modules. The different subpopulations should have similar yet slightly different intrinsic properties or differences in synaptic weight from descending drive so that each subpopulation is gradually recruited as the supraspinal drive gradually increases in intensity.

These implementation are necessary to fully reflect the speed variation of zebrafish swimming as well as full 3D motion (Left/right, forward/backward, up/down; Bagnall and McLean, 2014) and will more accurately emulate the output of the established spinal circuits for locomotion (i.e. adult swimming) which also relies on modular organisation of the network (Fontaine et al., 2008; Ampatzis et al., 2013). More recently, MCoDs neurons has been described as being divided into subpopulation encoding swimming speed variation too (Björnfors and El Manira, 2016) in adult zebrafish and could be also implemented in a similar way

Incorporate sensory feedback in model

To further complete the model, sensory feedback such as proprioceptive or tactile should be implemented. CiAs are a good first entry point to sensorimotor integration at the level of the spinal cord since they have shown to be contacted by sensory neurons while projecting to MNs and thought to be involve in relaying sensory inputs to shape motor outputs (Higashijima et al., 2004). Recently studied Cerebral spinal fluid contacting neurons (CSF-CNs) as well as Rohon-Beard neurons could be a valuable addition to the model (Hubbard et al., 2016; Knafo and Wyart,

2018). Wyart and colleagues suggested that RB and CSF-CNs could modulate swimming speed through excitation of CiDs (or V2a) or inhibition of MCoDs (V0v) respectively (Knafo and Wyart, 2018 for a review). To implement the latter would require modelling of CSF flow during body movements.

Incorporate supraspinal centers in model

Previous research on hindbrain component of the locomotor circuit could help us to complete the model incorporating circuit elements form these higher centers. The reticulospinal (RS) system is the major source of input from the hindbrain to the spinal locomotor circuits in simpler vertebrates such as zebrafish. It integrates sensory information from various centers to start, modulate or terminate locomotor behaviour (Drew and Rossignol, 1990; Svoboda and Fetcho, 1996; Viana Di Prisco et al., 1997; Deliagina et al., 2000; Sirota et al., 2000; Fagerstedt et al., 2001; Gahtan et al., 2002; Orger et al., 2008; Severi et al., 2014; Haesemeyer et al., 2018). An increase in the input intensity from RS neurons will directly be translated into an increase of the motor output from the spinal cord through more episodes composed of more frequent tail beats of higher amplitude. Previous work done in the lamprey (Grillner et al., 1995; Grillner, 2006; Kozlov et al., 2014) gives us invaluable guidelines on how to implement RS inputs. Two populations of RS neurons should be to integrated to the model, one population of tonic spiking neurons and on population of phasic spiking neurons. Such spiking profiles have been observed in the zebrafish hindbrain respectively in the Ro3 and Ro2 populations of neurons that are associated with locomotor behaviour (Chong and Drapeau, 2007). These neurons should project caudally in the spinal cord forming excitatory synapses with PM (i.e. IC) and IED (i.e. V2a).

Neurons from this population would be gradually recruited as the motor command intensity increases augmenting the drive to downstream spinal neurons.

The hindbrain is further involved in other motor movements such as escape responses largely due to activation of Mauthner cells. The Mauthner cell axon crosses to the contralateral side and project down to the spinal cord. A single discharge from a Mauthner cell directly or indirectly triggers multiple neuron populations, primary and secondary motoneurons provoking ipsilateral muscle contraction but also inhibitory interneurons that silence the contralateral side (Eaton et al., 1977; Liu and Fetcho, 1999; Takahashi et al., 2017). In addition, laser ablation experiments done on RoV3-MiV1-MiV2 region abolished turning behaviour in those fish (Orger et al., 2008) suggesting a role of these neurons in the decision making of escape responses. Later work from Engert and colleagues suggest that input from discrete set of neurons in the nucleus of medial longitudinal fascicles (nMLF) to the spinal locomotor circuit are responsible for controlling bout duration as well as tail beat frequency (Severi et al., 2014). Incorporating these features could help build an extensive model of motor control circuit in the zebrafish larvae.

Comparison with other animal models

The debate as to whether network oscillators or pacemaker neurons underlie rhythm generation is longstanding. Graham Brown proposed his hypothesis of half-centre (i.e. network oscillators) early in the twentieth century (Brown, 1914) spurring the research for rhythm generation in spinal locomotor circuits. However in the 1980s, the pacemaker (PM) neurons hypothesis became predominant in vertebrates suggested by the persistence of a rhythm after pharmacological blockade of the key component of network oscillator: reciprocal inhibition

(Soffe, 1989 for the *Xenopus* tadpole; Droge and Tao for the mouse, 1993; Rioult-Pedotti, 1997 for the frog). In the zebrafish, the presence of PM IC neurons (Tong and McDearmid, 2012) as well as the strychnine resistant rhythm early in development (McDearmid and Drapeau, 2006) suggests a PM organization for this vertebrate. However our data suggest that both PM and network oscillators coexists in the zebrafish and furthermore that network oscillators are prominent in rhythm generation later in development. Evidence for network oscillator-based rhythm generation can be found in other vertebrates. For instance, in the Xenopus tadpole dIN neurons in the caudal hindbrain drive locomotion in the spinal cord and their rhythmic firing relies on reciprocal inhibition and noisy excitation (Roberts et al., 2014; Borisyuk et al., 2017). However, a rhythm resistant to pharmacological blockade of reciprocal inhibition could be observed in tadpoles as well as in dINs during NMDA induced swimming (Soffe, 1989). Li suggested that the activation of NMDAR lead to intrinsic oscillations in the membrane potential of dINs responsible for producing swimming-like rhythms in what is essentially a reduced dINs-MNs only network (2011). These oscillations could be blocked with Cd2+ suggesting a further role of Ca2+.

In mice, mutual inhibition between half-centres is believed to only be dedicated to pattern generation while rhythm generation is reserved to hypothetical pacemakers (Brocard et al., 2010; Li, 2011). This is partly based upon experiments where locomotor bursts could be observed in the presence of strychnine, the so-called disinhibited bursting. During this type of locomotor activity, left-right coordination is synchronous as opposed to alternating, and the rhythm of locomotor output is much more variable than observed during fictive locomotion, suggesting inhibition may still play a role in rhythmogenesis. Furthermore, the continued failure to identify

pacemakers solely responsible for driving locomotor activity (Ziskind-Conhaim and Hochman, 2017) might give weight to reconsidering the network oscillator hypothesis for rhythm generation in mammalian locomotion.

Overall, my experimental findings in combination with the modelling work are an important step forward in fully understanding how the nervous system controls swimming movements in zebrafish. I shed light on a developmental switch in the fundamental mode of operation of spinal swimming circuits. To my knowledge, this is the first demonstration of how motor maturation can involve a transition in the manner that rhythm generation is produced. This transition may be necessary for the nervous system to accommodate a larger body as well as a larger repertoire of movements as fish grow into adults. By modelling transitions in swimming through changes in spinal circuitry and/or intrinsic properties of spinal neurons, I identify the possible roles of specific spinal circuits, spinal neurons, and firing behaviour in various aspects of fish swimming. My modelling work also identifies many promising hypotheses to test with regards to the operation of spinal circuits for swimming and their modifications by neuromodulation during development. I suggest that combining modelling studies and experimental verification via in vivo neural manipulation, using for example optogenetic techniques that are ideally suited for use in zebrafish larvae, will lead to further insights into the neural control of movements in zebrafish but also in vertebrates in general.

Appendix 1

Ouabain does not perturbed rhythm generation nor episode duration

It has previously been reported that a Na+/K+-ATPase pump could be involved in slow locomotor rhythm generation mechanism such as observed in tadpole swimming (Zhang and Sillar, 2012). By driving the extrusion of sodium out of the cell and transporting K+ into cells against their concentration gradients during prolonged firing of action potentials, Na+/K+-ATPase pumps hyperpolarize membrane potentials and prolong quiescent periods following bursts of activity. Thus, they would be a perfect candidate to allow long swimming episodes in 3 dpf zebrafish (i.e. fish expressing burst swimming behaviour). A gradual down regulation of this pump would decrease the hyper polarization of the membrane potential during the quiescent period following swimming episodes, which could underlie the shortening of quiescent episodes that is seen in beat-and-glide swimming.

To test if this pump plays a role in the frequencies of tail beats or of swim episodes we recorded extracellular spinal activity during fictive swimming episodes in fish expressing burst swimming or beat-and-glide swimming without and with ouabain (known to inhibit Na+/K+-ATPase activity). Autocorrelation of 10 second-long segments from recorded traces showed presence of peaks in the 20-40 Hz tail-beat frequency range (blue shaded area in the 25-50 ms time delay corresponding to 20-40 Hz, Fig. Appendix.1*C*) at 3 dpf as well as peaks in the 0.66 - 2 Hz swim episode frequency range (grey shaded area in the 0.5 - 1.5 s time delay corresponding

to 0.66 - 2 Hz , Fig. Appendix.1*D*) in beat-and-glide swimming fish. Swim episode duration and frequency did not significantly change from control to ouabain conditions. At 3 dpf, average durations under control and ouabain conditions were 3.69 ± 3.55 s (n = 21 episodes) and 3.68 ± 3.87 s (n = 23 episodes), respectively, while swim episode frequencies were 0.26 ± 0.11 Hz (n = 20) and 0.33 ± 0.15 Hz (n = 22), respectively. At 5 dpf swim episode durations were 274 ± 116 ms (n = 29) for control and 222 ± 40 ms (n = 30) for riluzole condition, while episode frequencies were 1.57 ± 0.9 Hz (n = 28) and 1.50 ± 0.37 Hz (n = 29) respectively. Together, these results suggest that a Na+/K+-ATPase pump is not involved in shaping locomotor activity in zebrafish at these developmental stages.

Discussion

These transition from PMs driven to network oscillators driven rhythm is concomitant to transition from burst to beat-and-glide swimming but the former does not imply the latter (Chapter 2). Other mechanisms must be involved in this swimming phenotype transition. It has been previously reported that dopamine might play a role in this transition (Lambert et al., 2012) as blocking D4R or ablating dopaminergic neurons during development prevents the swimming phenotype transition. However, our previous results suggest that dopamine plays a role in the transition but may not be necessary to sustain the phenotype (Chapter 2). Therefore, dopamine may help to shape the spinal locomotor circuit to transition from burst to beat-and-glide swimming but once the transition is settled the network is able to maintained the beat-and-glide output on its own. Thus, the mechanism responsible for shortening but increasing the frequency of swim episodes must not involve dopamine.

One could argue a pump such as Na+/K+-ATPase might be implied in this transitioning. If active early on development, the pump could help sustain long bursts of swimming activity that would shorten as its impact would be decreased via network maturation. However, our experiment using ouabain in transitioned fish expressing beat-and-glide swimming seems to dismiss the presence of such a pump. More research is definitively needed to dissect mechanisms responsible for this swimming phenotype transition. In conclusion, these additional experiments further confirm the transition from a PM based to a network oscillator based architecture of the zebrafish spinal locomotor circuits during development. It also disqualifies the involvement of Na+/K+-ATPase as a potential mechanism for burst to beat-and-glide swimming transition

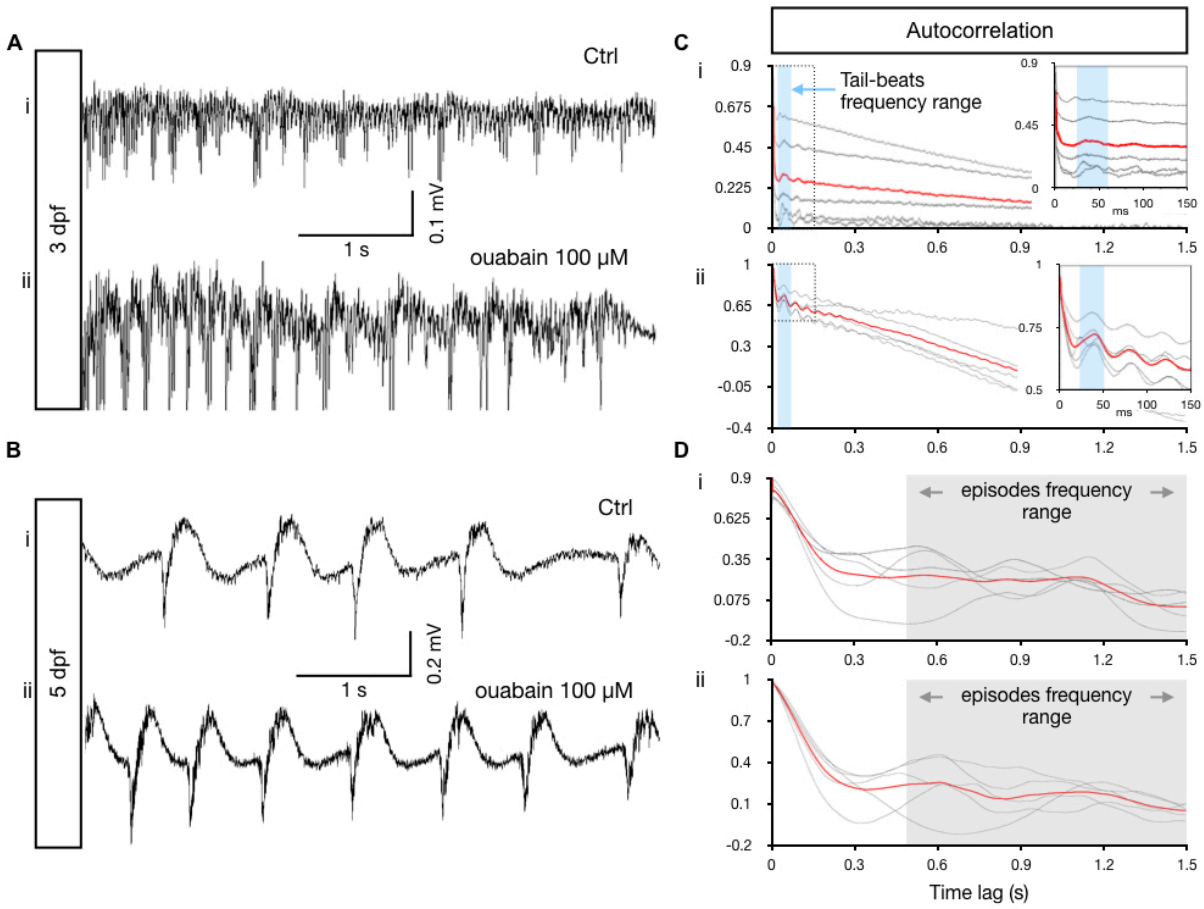

Figure Appendix.1. Ouabain has little to no effect on tail beats rhythm or episode rhythm.

A, Extracellular recordings from a 3 dpf whole fish spinal cord during fictive swimming activity under control (i) and 100 µM ouabain (ii) conditions. ***B,*** Same as in A but for a 5 dpf fish. ***C,*** Autocorrelations from 10s long epochs from the recordings in A for control (i) and ouabain (ii) conditions. Five epochs (grey lines); average in red. Blue shaded area highlights the tail beat frequency range (corresponding to the 25-50 ms time lag range). Subplots are magnified versions from the dotted box. ***D,*** Same as in C for traces from B. Grey shaded area highlights the episodes frequency range (corresponding to the 0.5-1.5 s time lag range).

Appendix 2

Pyridoxine-dependent epilepsy in zebrafish caused by aldh7a1 deficiency

The candidate contribution to Pena et al. (2017) consisted of all tectal recordings, analysis of recordings and writing the Methods paragraph explaining the electrophysiological procedure and data analysis of electrophysiological recordings.

Appendix 3

Insights into the genotypic/phenotypic spectrum and the pathophysiology of PLPBP-deficiency from novel B6-responsive clinical features, cellular, yeast and zebrafish models

The candidate contribution to Johnstone et al. (currently under review in the journal Brain) consisted of all tectal recordings, analysis of recordings and writing the Methods paragraph explaining the electrophysiological procedure and data analysis of electrophysiological recordings.

Bibliography

Ampatzis K, Song J, Ausborn J, El Manira A (2013) Pattern of Innervation and Recruitment of Different Classes of Motoneurons in Adult Zebrafish. J Neurosci 33:10875–10886 Available at: http://www.jneurosci.org/cgi/doi/10.1523/JNEUROSCI.0896-13.2013.

Azbill RD, Mu X, Springer JE (2000) Riluzole increases high-affinity glutamate uptake in rat spinal cord synaptosomes. Brain Res 871:175–180.

Bagnall MW, McLean DL (2014) Modular organization of axial microcircuits in zebrafish. Science (80-) 343:197–200.

Batista MF, Jacobstein J, Lewis KE (2008) Zebrafish V2 cells develop into excitatory CiD and Notch signalling dependent inhibitory VeLD interneurons. Dev Biol 322:263–275.

Ben-Ari Y (2002) Excitatory actions of GABA during development: The nature of the nurture. Nat Rev Neurosci 3:728–739.

Bennett MVL, Zukin RS (2004) Electrical Coupling and Neuronal Synchronization in the Mammalian Brain. Neuron 41:495–511.

Bernhardt RR, Chltnis AB, Lindamer L, Kuwada JY (1990) Identification of Spinal Neurons i n the Embryonic and Larval Zebrafish. J Comp Neurol 302:603–616 Available at: http://www.ncbi.nlm.nih.gov/pubmed/1702120.

Björnfors ER, El Manira A (2016) Functional diversity of excitatory commissural interneurons in adult zebrafish. Elife 5.

Borisyuk R, Merrison-Hort R, Soffe SR, Koutsikou S, Li WC (2017) To swim or not to swim: A population-level model of Xenopus tadpole decision making and locomotor

behaviour. BioSystems 161:3–14.

Brocard F, Tazerart S, Vinay L (2010) Do pacemakers drive the central pattern generator for locomotion in mammals? Neuroscientist 16:139–155.

Brown TG (1914) On the nature of the fundamental activity of the nervous centres; together with an analysis of the conditioning of rhythmic activity in progression, and a theory of the evolution of function in the nervous system. J Physiol.

Brownstone RM, Wilson JM (2008) Strategies for delineating spinal locomotor rhythm-generating networks and the possible role of Hb9 interneurones in rhythmogenesis. Brain Res Rev 57:64–76.

Brustein E, Chong M, Holmqvist B, Drapeau P (2003) Serotonin Patterns Locomotor Network Activity in the Developing Zebrafish by Modulating Quiescent Periods. J Neurobiol 57:303–322.

Bui T V., Brownstone RM (2015) Sensory-evoked perturbations of locomotor activity by sparse sensory input: a computational study. J Neurophysiol 113:2824–2839 Available at: http://jn.physiology.org/lookup/doi/10.1152/jn.00866.2014.

Buss RR, Drapeau P (2000) Physiological properties of zebrafish embryonic red and white muscle fibers during early development. J Neurophysiol 84:1545–1557.

Buss RR, Drapeau P (2001) Synaptic drive to motoneurons during fictive swimming in the developing zebrafish. J Neurophysiol 86:197–210 Available at: http://www.ncbi.nlm.nih.gov/pubmed/11431502.

Chen T-W, Wardill TJ, Sun Y, Pulver SR, Renninger SL, Baohan A, Schreiter ER, Kerr RA, Orger MB, Jayaraman V, Looger LL, Svoboda K, Kim DS (2013) Ultrasensitive fluorescent proteins for imaging neuronal activity. Nature 499:295–300 Available at:

http://www.nature.com/doifinder/10.1038/nature12354.

Chong M, Drapeau P (2007) Interaction between hindbrain and spinal networks during the development of locomotion in zebrafish. Dev Neurobiol.

Côté S, Drapeau P (2012) Regulation of spinal interneuron differentiation by the paracrine action of glycine. Dev Neurobiol 72:208–214.

Cowley KC, Schmidt BJ (1994) A comparison of motor patterns induced by N-methyl-d-aspartate, acetylcholine and serotonin in the in vitro neonatal rat spinal cord. Neurosci Lett 171:147–150.

Currie SP, Sillar KT (2018) Developmental changes in spinal neuronal properties, motor network configuration, and neuromodulation at free-swimming stages of *Xenopus* tadpoles. J Neurophysiol 119:786–795 Available at: http://www.physiology.org/doi/10.1152/jn.00219.2017.

Darbon P, Yvon C, Legrand JC, Streit J (2004) INaP underlies intrinsic spiking and rhythm generation in networks of cultured rat spinal neurons. Eur J Neurosci 20:976–988.

Daun S, Rubin JE, Rybak IA (2009) Control of oscillation periods and phase durations in half-center central pattern generators: A comparative mechanistic analysis. J Comput Neurosci 27:3–36.

Deflorio C, Palma E, Conti L, Roseti C, Manteca A, Giacomelli E, Catalano M, Limatola C, Inghilleri M, Grassi F (2012) Riluzole blocks human muscle acetylcholine receptors. J Physiol 590:2519–2528.

Deliagina TG, Zelenin P V, Fagerstedt P, Grillner S, Orlovsky GN (2000) Activity of reticulospinal neurons during locomotion in the freely behaving lamprey. J

Neurophysiol 83:853–863.

Drapeau P, Saint-Amant L, Buss RR, Chong M, McDearmid JR, Brustein E (2002) Development of the locomotor network in zebrafish. Prog Neurobiol 68:85–111.

Drew T, Rossignol S (1990) Functional organization within the medullary reticular formation of intact unanesthetized cat. II. Electromyographic activity evoked by microstimulation. J Neurophysiol 64:782–795.

Droge MH, Tao Y (1993) Glycine effects on in vitro motor pattern generation in mouse spinal cord. Neurosci Lett 158:139–142.

Eaton RC, Farley RD, Kimmel CB, Schabtach E (1977) Functional development in the mauthner cell system of embryos and larvae of the zebra fish. J Neurobiol 8:151–172.

Enomoto A, Han JM, Hsiao C, Chandler SH (2007) Sodium Currents in Mesencephalic Trigeminal Neurons From Na v 1 . 6 Null Mice. J Neurophysiol:710–719.

Fagerstedt P, Orlovsky GN, Deliagina TG, Grillner S, Ullén F (2001) Lateral turns in the Lamprey. II. Activity of reticulospinal neurons during the generation of fictive turns. J Neurophysiol 86:2257–2265 Available at: http://www.ncbi.nlm.nih.gov/pubmed/11698516%5Cnhttp://jn.physiology.org/content/86/5/2257.short.

Favero M, Cangiano A, Busetto G (2014) The timing of activity is a regulatory signal during development of neural connections. J Mol Neurosci.

Fontaine E, Lentink D, Kranenbarg S, Muller UK, van Leeuwen JL, Barr AH, Burdick JW (2008) Automated visual tracking for studying the ontogeny of zebrafish swimming. J Exp Biol 211:1305–1316 Available at: http://jeb.biologists.org/cgi/doi/10.1242/jeb.010272.

Forssberg H, Grillner S (1973) The locomotion of the acute spinal cat injected with clonidine i.v. Brain Res 50:184–186.

Gabriel JP, Mahmood R, Kyriakatos A, Söll I, Hauptmann G, Calabrese RL, El Manira A (2009) Serotonergic modulation of locomotion in zebrafish: endogenous release and synaptic mechanisms. J Neurosci 29:10387–10395 Available at: http://www.jneurosci.org/cgi/doi/10.1523/JNEUROSCI.1978-09.2009%5Cnhttp://www.ncbi.nlm.nih.gov/pubmed/19692613.

Gabriel JP, Mahmood R, Walter AM, Kyriakatos A, Hauptmann G, Calabrese RL, El Manira A (2008) Locomotor pattern in the adult zebrafish spinal cord in vitro. J Neurophysiol 99:37–48.

Gahtan E, Sankrithi N, Campos JB, O'Malley DM (2002) Evidence for a Widespread Brain Stem Escape Network in Larval Zebrafish. J Neurophysiol 87:608–614 Available at: http://www.physiology.org/doi/10.1152/jn.00596.2001.

Gao BX, Ziskind-Conhaim L (1998) Development of ionic currents underlying changes in action potential waveforms in rat spinal motoneurons. J Neurophysiol 80:3047–3061.

Godoy R, Noble S, Yoon K, Anisman H, Ekker M (2015) Chemogenetic ablation of dopaminergic neurons leads to transient locomotor impairments in zebrafish larvae. J Neurochem 135:249–260.

Goulding M (2009) Circuits controlling vertebrate locomotion: Moving in a new direction. Nat Rev Neurosci 10:507–518.

Grillner S (2003) The motor infrastructure: From ion channels to neuronal networks. Nat Rev Neurosci 4:573–586.

Grillner S (2006) Biological Pattern Generation: The Cellular and Computational Logic of Networks in Motion. Neuron 52:751–766.

Grillner S (2011) Control of Locomotion in Bipeds, Tetrapods, and Fish. In: Comprehensive Physiology Available at: http://doi.wiley.com/10.1002/cphy.cp010226.

Grillner S, Deliagina T, El Manira A, Hill RH, Orlovsky GN, Wallén P, Ekeberg Ö, Lansner A (1995) Neural networks that co-ordinate locomotion and body orientation in lamprey. Trends Neurosci 18:270–279.

Grillner S, Jessell TM (2009) Measured motion: searching for simplicity in spinal locomotor networks. Curr Opin Neurobiol 19:572–586.

Haesemeyer M, Robson DN, Li JM, Schier AF, Engert F (2018) A Brain-wide Circuit Model of Heat-Evoked Swimming Behavior in Larval Zebrafish. Neuron 98:817–831.e6.

Hale ME, Ritter DA, Fetcho JR (2001) A confocal study of spinal interneurons in living larval zebrafish. J Comp Neurol 437:1–16.

Harris-Warrick RM (2002) Voltage-sensitive ion channels in rhythmic motor systems. Curr Opin Neurobiol 12:646–651.

Harris-Warrick RM (2010) NIH Public Access. Brain Res Rev:213–222.

Henneman E (1985) The size-principle: a deterministic output emerges from a set of probabilistic connections. J Exp Biol 115:105–112 Available at: http://jeb.biologists.org/content/115/1/105%5Cnhttp://jeb.biologists.org/content/115/1/105.full.pdf%5Cnhttp://jeb.biologists.org/content/115/1/105.short.

Henneman E, Somjen G, Carpenter DO (1965) Functional Significance of Cell Size in

Spinal Motoneurons. J Neurophysiol 28:560–580.

Higashijima SI, Schaefer M, Fetcho JR (2004) Neurotransmitter properties of spinal interneurons in embryonic and larval zebrafish. J Comp Neurol 480:19–37.

Hsiao C-F, Wu N, Chandler SH (2005) Voltage-dependent calcium currents in trigeminal motoneurons of early postnatal rats: modulation by 5-HT receptors. J Neurophysiol 94:2063–2072.

Hubbard JM, Böhm UL, Prendergast A, Tseng PEB, Newman M, Stokes C, Wyart C (2016) Intraspinal Sensory Neurons Provide Powerful Inhibition to Motor Circuits Ensuring Postural Control during Locomotion. Curr Biol 26:2841–2853.

Hull MJ, Soffe SR, Willshaw DJ, Roberts A (2016) Modelling Feedback Excitation, Pacemaker Properties and Sensory Switching of Electrically Coupled Brainstem Neurons Controlling Rhythmic Activity. PLoS Comput Biol 12:1–19.

Hutcheon B, Yarom Y (2000) Resonance, oscillation and the intrinsic frequency preferences of neurons. Trends Neurosci 23:216–222.

Ikenaga T, Urban JM, Gebhart N, Hatta K, Kawakami K, Ono F (2011) Formation of the spinal network in zebrafish determined by domain-specific pax genes. J Comp Neurol 519:1562–1579.

Izhikevich EM, Izhikevich EM (2003) Simple model of spiking neurons. IEEE Trans Neural Netw 14:1569–1572 Available at: http://www.ncbi.nlm.nih.gov/pubmed/18244602.

Jankowska E, Jukes MGM, Lund S, Lundberg A (1967a) The Effect of DOPA on the Spinal Cord 5. Reciprocal organization of pathways transmitting excitatory action to alpha motoneurones of flexors and extensors. Acta Physiol Scand 70:369–388.

Jankowska E, Jukes MGM, Lund S, Lundberg A (1967b) The Effect of DOPA on the Spinal Cord 6. Half−centre organization of interneurones transmitting effects from the flexor reflex afferents. Acta Physiol Scand 70:389–402.

Jay M, De Faveri F, McDearmid JR (2015) Firing dynamics and modulatory actions of supraspinal dopaminergic neurons during zebrafish locomotor behavior. Curr Biol 25:435–444.

Kandel E, Schwartz J, Jessel T, Siegelbaum S, Hudspeth A (2013) Principles of Neural science. Available at: https://books.google.com.co/books/about/Principles_of_Neural_Science_Fifth_Editi.html?id=s64z-LdAIsEC&redir_esc=y.

Kiehn O (2011) Development and functional organization of spinal locomotor circuits. Curr Opin Neurobiol 21:100–109.

Kimmel CB, Ballard WW, Kimmel SR, Ullmann B, Schilling TF (1995) Stages of embryonic development of the zebrafish. Dev Dyn an Off public 203:253–310.

Kimmel CB, Schilling TF, Hatta K (1991) Patterning of Body Segments of the Zebrafish Embryo. Curr Top Dev Biol 25:77–110.

Knafo S, Wyart C (2018) Active mechanosensory feedback during locomotion in the zebrafish spinal cord. Curr Opin Neurobiol 52:48–53.

Knogler LD, Ryan J, Saint-Amant L, Drapeau P (2014) A Hybrid Electrical/Chemical Circuit in the Spinal Cord Generates a Transient Embryonic Motor Behavior. J Neurosci 34:9644–9655 Available at: http://www.jneurosci.org/cgi/doi/10.1523/JNEUROSCI.1225-14.2014.

Kozlov AK, Kardamakis AA, Hellgren Kotaleski J, Grillner S (2014) Gating of steering signals through phasic modulation of reticulospinal neurons during locomotion.

Proc Natl Acad Sci 111:3591–3596 Available at: http://www.pnas.org/lookup/doi/10.1073/pnas.1401459111.

Lambert AM, Bonkowsky JL, Masino MA (2012) The Conserved Dopaminergic Diencephalospinal Tract Mediates Vertebrate Locomotor Development in Zebrafish Larvae. J Neurosci 32:13488–13500 Available at: http://www.jneurosci.org/cgi/doi/10.1523/JNEUROSCI.1638-12.2012.

Lee KKY, Soutar CN, Dringenberg HC (2018) Gating of long-term potentiation (LTP) in the thalamocortical auditory system of rats by serotonergic (5-HT) receptors. Brain Res 1683:1–11.

Lewis KE, Eisen JS (2003) From cells to circuits: Development of the zebrafish spinal cord. Prog Neurobiol 69:419–449.

Li W, Roberts A, Soffe S (2010) Specific brainstem neurons switch each other into pacemaker mode to drive movement by activating NMDA receptors. J Neurosci 30:16609–16620.

Li WC (2011) Generation of locomotion rhythms without inhibition in vertebrates: The search for pacemaker neurons. In: Integrative and Comparative Biology, pp 879–889.

Liao JC, Fetcho JR (2008) Shared versus Specialized Glycinergic Spinal Interneurons in Axial Motor Circuits of Larval Zebrafish. J Neurosci 28:12982–12992 Available at: http://www.jneurosci.org/cgi/doi/10.1523/JNEUROSCI.3330-08.2008.

Liu DW, Waesterfield M (1988) Function of identified motoneurones and co-ordination of primary and secondary motor systems during zebra fish swimming. J Physiol 403:73–89 Available at: https://physoc.onlinelibrary.wiley.com/doi/abs/10.1113/

jphysiol.1988.sp017239.

Liu KS, Fetcho JR (1999) Laser ablations reveal functional relationships of segmental hindbrain neurons in zebrafish. Neuron 23:325–335.

Ljunggren EE, Haupt S, Ausborn J, Ampatzis K, El Manira A (2014) Optogenetic Activation of Excitatory Premotor Interneurons Is Sufficient to Generate Coordinated Locomotor Activity in Larval Zebrafish. J Neurosci 34:134–139 Available at: http://www.jneurosci.org/cgi/doi/10.1523/JNEUROSCI.4087-13.2014.

Lundberg A (1981) Half-centres revisited. Regul Funct CNS Motion Organ Princ:155–167.

McDearmid JR, Drapeau P (2006) Rhythmic motor activity evoked by NMDA in the spinal zebrafish larva. J Neurophysiol 95:401–417 Available at: http://apps.webofknowledge.com/full_record.do?product=WOS&search_mode=GeneralSearch&qid=5&SID=3Ar2S6AZrp5j13B5kcB&page=1&doc=6 [Accessed September 28, 2016].

McLean DL, Dougherty KJ (2015) Peeling back the layers of locomotor control in the spinal cord. Curr Opin Neurobiol 33:63–70.

McLean DL, Fan J, Higashijima SI, Hale ME, Fetcho JR (2007) A topographic map of recruitment in spinal cord. Nature 446:71–75.

McLean DL, Fetcho JR (2004) Ontogeny and innervation patterns of dopaminergic, noradrenergic, and serotonergic neurons in larval zebrafish. J Comp Neurol.

McLean DL, Fetcho JR (2009) Spinal Interneurons Differentiate Sequentially from Those Driving the Fastest Swimming Movements in Larval Zebrafish to Those Driving the Slowest Ones. J Neurosci 29:13566–13577 Available at: http://

www.jneurosci.org/cgi/doi/10.1523/JNEUROSCI.3277-09.2009.

McLean DL, Masino MA, Koh IYY, Lindquist WB, Fetcho JR (2008) Continuous shifts in the active set of spinal interneurons during changes in locomotor speed. Nat Neurosci 11:1419–1429.

Mendell LM (2005) The size principle: a rule describing the recruitment of motoneurons. J Neurophysiol 93:3024–3026.

Menelaou E, McLean DL (2012) A Gradient in Endogenous Rhythmicity and Oscillatory Drive Matches Recruitment Order in an Axial Motor Pool. J Neurosci 32:10925–10939 Available at: http://www.jneurosci.org/cgi/doi/10.1523/JNEUROSCI.1809-12.2012.

Messina JA, St. Paul A, Hargis S, Thompson WE, McClellan AD (2017) Elimination of Left-Right Reciprocal Coupling in the Adult Lamprey Spinal Cord Abolishes the Generation of Locomotor Activity. Front Neural Circuits 11:89 Available at: http://journal.frontiersin.org/article/10.3389/fncir.2017.00089/full.

Mokhtari EB, Lawrence JJ, Stone EF (2018) Effect of Neuromodulation of Short-Term Plasticity on Information Processing in Hippocampal Interneuron Synapses. J Math Neurosc Available at: http://arxiv.org/abs/1804.02115.

Moult PR, Cottrell GA, Li WC (2013) Fast Silencing Reveals a Lost Role for Reciprocal Inhibition in Locomotion. Neuron 77:129–140 Available at: http://dx.doi.org/10.1016/j.neuron.2012.10.040.

Muller UK (2004) Swimming of larval zebrafish: ontogeny of body waves and implications for locomotory development. J Exp Biol 207:853–868 Available at: http://jeb.biologists.org/cgi/doi/10.1242/jeb.00821.

Myers PZ, Eisen JS, Westerfield M (1986) Development and axonal outgrowth of identified motoneurons in the zebrafish. J Neurosci 6:2278–2289 Available at: http://www.ncbi.nlm.nih.gov/pubmed/3746410.

Nowak LG, Sanchez-Vives M V., McCormick DA (1997) Influence of low and high frequency inputs on spike timing in visual cortical neurons. Cereb Cortex 7:487–501.

Orger MB, Kampff AR, Severi KE, Bollmann JH, Engert F (2008) Control of visually guided behavior by distinct populations of spinal projection neurons. Nat Neurosci 11:327–333.

Perrier JF, Hounsgaard J (2000) Development and regulation of response properties in spinal cord motoneurons. Brain Res Bull 53:529–535.

Ramirez JM, Doi A, Garcia AJ, Elsen FP, Koch H, Wei AD (2012) The Cellular Building Blocks of Breathing. In: Comprehensive Physiology Available at: http://doi.wiley.com/10.1002/cphy.c110033.

Rioult-Pedotti MS (1997) Intrinsic NMDA-induced oscillations in motoneurons of an adult vertebrate spinal cord are masked by inhibition. J Neurophysiol 77:717–730 Available at: http://www.ncbi.nlm.nih.gov/pubmed/9065844.

Roberts A, Conte D, Hull M, Merrison-Hort R, al Azad AK, Buhl E, Borisyuk R, Soffe SR (2014) Can Simple Rules Control Development of a Pioneer Vertebrate Neuronal Network Generating Behavior? J Neurosci 34:608–621 Available at: http://www.jneurosci.org/cgi/doi/10.1523/JNEUROSCI.3248-13.2014.

Rybak IA, Stecina K, Shevtsova NA, McCrea DA (2006) Modelling spinal circuitry involved in locomotor pattern generation: Insights from the effects of afferent

stimulation. J Physiol 577:641–658.

Saint-Amant L, Drapeau P (1998) Time course of the development of motor behaviors in the zebrafish embryo. J Neurobiol 37:622–632 Available at: http://www.ncbi.nlm.nih.gov/pubmed/9858263.

Saint-Amant L, Drapeau P (2000) Motoneuron Activity Patterns Related to the Earliest Behavior of the Zebrafish Embryo. J Neurosci 20:3964–3972 Available at: http://www.jneurosci.org/content/20/11/3964.long.

Saint-Amant L, Drapeau P (2001) Synchronization of an embryonic network of identified spinal interneurons solely by electrical coupling. Neuron 31:1035–1046.

Severi KE, Portugues R, Marques JC, O'Malley DM, Orger MB, Engert F (2014) Neural Control and Modulation of Swimming Speed in the Larval Zebrafish. Neuron 83:692–707.

Sillar KT, Reith CA, McDearmid JR (1998) Development and aminergic neuromodulation of a spinal locomotor network controlling swimming in xenopus larvae. In: Annals of the New York Academy of Sciences, pp 318–332.

Sirota MG, Di Prisco GV, Dubuc R (2000) Stimulation of the mesencephalic locomotor region elicits controlled swimming in semi-intact lampreys. Eur J Neurosci 12:4081–4092.

Soffe SR (1989) Roles of Glycinergic Inhibition and N−Methyl−D−Aspartate Receptor Mediated Excitation in the Locomotor Rhythmicity of One Half of the Xenopus Embryo Central Nervous System. Eur J Neurosci 1:561–571.

Song J, Ampatzis K, Björnfors ER, El Manira A (2016) Motor neurons control locomotor circuit function retrogradely via gap junctions. Nature 529:399–402.

Spitzer NC, Ribera AB (1998) Development of electrical excitability in embryonic neurons: Mechanisms and roles. J Neurobiol 37:190–197.

Stil A, Drapeau P (2016) Neuronal labeling patterns in the spinal cord of adult transgenic Zebrafish. Dev Neurobiol 76:642–660.

Sun QQ, Dale N (1998) Developmental changes in expression of ion currents accompany maturation of locomotor pattern in frog tadpoles. J Physiol 507:257–264.

Sun QQ, Dale N (1999) G-proteins are involved in 5-HT receptor-mediated modulation of N- and P/Q- but not T-type Ca2+ channels. J Neurosci 19:890–899.

Svoboda KR, Fetcho JR (1996) Interactions swimming between the neural networks for escape and swimming in goldfish. J Neurosci 16:843–852.

Takahashi M, Inoue M, Tanimoto M, Kohashi T, Oda Y (2017) Short-term desensitization of fast escape behavior associated with suppression of Mauthner cell activity in larval zebrafish. Neurosci Res 121:29–36.

Talpalar (2010) Glutamatergic mechanisms for speed control and network operation in the rodent locomotor CPG. Front Neural Circuits Available at: http://journal.frontiersin.org/article/10.3389/fncir.2010.00019/abstract.

Tay TL, Ronneberger O, Ryu S, Nitschke R, Driever W (2011) Comprehensive catecholaminergic projectome analysis reveals single-neuron integration of zebrafish ascending and descending dopaminergic systems. Nat Commun 2.

Tong H, McDearmid JR (2012) Pacemaker and plateau potentials shape output of a developing locomotor network. Curr Biol 22:2285–2293 Available at: http://dx.doi.org/10.1016/j.cub.2012.10.025.

Tovar KR, Maher BJ, Westbrook GL (2009) Direct Actions of Carbenoxolone on Synaptic Transmission and Neuronal Membrane Properties. J Neurophysiol 102:974–978 Available at: http://jn.physiology.org/cgi/doi/10.1152/jn.00060.2009.

Tresch MC, Kiehn O (2000) Motor coordination without action potentials in the mammalian spinal cord. Nat Neurosci.

Tseng H -a., Martinez D, Nadim F (2014) The Frequency Preference of Neurons and Synapses in a Recurrent Oscillatory Network. J Neurosci.

Tseng H -a., Nadim F (2010) The Membrane Potential Waveform of Bursting Pacemaker Neurons Is a Predictor of Their Preferred Frequency and the Network Cycle Frequency. J Neurosci.

Ulrich D (2014) Subthreshold delta-frequency resonance in thalamic reticular neurons. Eur J Neurosci 40:2600–2607.

Urbani A, Belluzzi O (2000) Riluzole inhibits the persistent sodium current in mammalian CNS neurons. Eur J Neurosci 12:3567–3574.

Viana Di Prisco G, Pearlstein E, Robitaille R, Dubuc R (1997) Role of sensory-evoked NMDA plateau potentials in the initiation of locomotion. Science (80-) 278:1122–1125.

Westerfield M (2000) The Zebrafish Book. A Guide for the Laboratory Use of Zebrafish (Danio rerio), 4th Edition.

Wiggin TD, Anderson TM, Eian J, Peck JH, Masino MA (2012) Episodic swimming in the larval zebrafish is generated by a spatially distributed spinal network with modular functional organization. J Neurophysiol 108:925–934 Available at: http://jn.physiology.org/cgi/doi/10.1152/jn.00233.2012.

Wiggin TD, Peck JH, Masino MA (2014) Coordination of fictive motor activity in the larval zebrafish is generated by non-segmental mechanisms. PLoS One 9.

Zhang HY, Picton L, Li WC, Sillar KT (2015) Mechanisms underlying the activity-dependent regulation of locomotor network performance by the Na+ pump. Sci Rep 5:1–14 Available at: http://dx.doi.org/10.1038/srep16188.

Zhang HY, Sillar KT (2012) Short-term memory of motor network performance via activity-dependent potentiation of Na +/K + pump function. Curr Biol 22:526–531 Available at: http://dx.doi.org/10.1016/j.cub.2012.01.058.

Ziskind-Conhaim L, Hochman S (2017) Diversity of molecularly-defined spinal interneurons engaged in mammalian locomotor pattern generation. J Neurophysiol:jn.00322.2017 Available at: http://jn.physiology.org/lookup/doi/10.1152/jn.00322.2017.

Pyridoxine-Dependent Epilepsy in Zebrafish Caused by Aldh7a1 Deficiency

Izabella A. Pena,*,†,‡,1 Yann Roussel,‡ Kate Daniel,* Kevin Mongeon,*,† Devon Johnstone,*,† Hellen Weinschutz Mendes,‡ Marjolein Bosma,§ Vishal Saxena,‡ Nathalie Lepage,* Pranesh Chakraborty,* David A. Dyment,*,† Clara D. M. van Karnebeek,§, Nanda Verhoeven-Duif,†† Tuan Vu Bui,‡ Kym M. Boycott,*,† Marc Ekker,‡,2 and Alex MacKenzie*,†,2**

*Children's Hospital of Eastern Ontario Research Institute and †Department of Pediatrics, Faculty of Medicine, University of Ottawa, Ontario K1H 8L1, Canada, ‡Department of Biology, University of Ottawa, Ontario K1N 6N5, Canada, §Departments of Pediatrics and Clinical Genetics, Academic Medical Centre, 1105 AZ Amsterdam, The Netherlands, **Department of Pediatrics, Centre for Molecular Medicine and Therapeutics, University of British Columbia, Vancouver V5Z 4H4, British Columbia, Canada, and ††Department of Genetics, Center for Molecular Medicine, University Medical Center (UMC), 3584 EA Utrecht, The Netherlands

ORCID IDs: 0000-0001-5242-3724 (I.A.P.); 0000-0003-3352-5631 (C.D.M.v.K.); 0000-0003-0024-1544 (T.V.B.); 0000-0003-4186-8052 (K.M.B.)

ABSTRACT Pyridoxine-dependent epilepsy (PDE) is a rare disease characterized by mutations in the lysine degradation gene *ALDH7A1* leading to recurrent neonatal seizures, which are uniquely alleviated by high doses of pyridoxine or pyridoxal 5′-phosphate (vitamin B6 vitamers). Despite treatment, neurodevelopmental disabilities are still observed in most PDE patients underlining the need for adjunct therapies. Over 60 years after the initial description of PDE, we report the first animal model for this disease: an aldh7a1-null zebrafish (*Danio rerio*) displaying deficient lysine metabolism and spontaneous and recurrent seizures in the larval stage (10 days postfertilization). Epileptiform electrographic activity was observed uniquely in mutants as a series of population bursts in tectal recordings. Remarkably, as is the case in human PDE, the seizures show an almost immediate sensitivity to pyridoxine and pyridoxal 5′-phosphate, with a resulting extension of the life span. Lysine supplementation aggravates the phenotype, inducing earlier seizure onset and death. By using mass spectrometry techniques, we further explored the metabolic effect of *aldh7a1* knockout. Impaired lysine degradation with accumulation of PDE biomarkers, B6 deficiency, and low γ-aminobutyric acid levels were observed in the *aldh7a1*$^{-/-}$ larvae, which may play a significant role in the seizure phenotype and PDE pathogenesis. This novel model provides valuable insights into PDE pathophysiology; further research may offer new opportunities for drug discovery to control seizure activity and improve neurodevelopmental outcomes for PDE.

KEYWORDS pyridoxine-dependent epilepsy; aldh7a1; zebrafish model; lysine metabolism; metabolic epilepsy

PYROXIDINE-DEPENDENT epilepsy (PDE, MIM #266100) is a rare autosomal recessively inherited metabolic disease (Gospe 2017) in which intractable and recurrent neonatal or infantile seizures are alleviated uniquely by high doses of pyridoxine (Pyr, vitamin B6) or pyridoxal 5′-phosphate (PLP) (Baxter 2001; Mills *et al.* 2006; Stockler *et al.* 2011). When untreated, PDE can lead to death, usually of status epilepticus (Gospe 2017). This condition is caused by mutations in the lysine degradation gene *ALDH7A1* (Mills *et al.* 2006) that encodes α-aminoadipic-semialdehyde-dehydrogenase, which is also known as "Antiquitin" (Lee *et al.* 1994) due to its remarkable level of conservation through evolution (Supplemental Material, Figure S1). Loss of ALDH7A1 enzyme function leads to the pathogenic accumulation of the lysine intermediates aminoadipate semialdehyde (AASA) and its cyclic equilibrium form piperideine 6-carboxylate (P6C) in tissues including the central nervous system (CNS) [4] (Figure 1). P6C has been shown to react with and inactivate PLP (the active form of vitamin B6), a cofactor for over 140 enzymes including those

doi: https://doi.org/10.1534/genetics.117.300137
Manuscript received August 11, 2017; accepted for publication October 4, 2017; published Early Online October 10, 2017.
Available freely online through the author-supported open access option.
Supplemental material is available online at www.genetics.org/lookup/suppl/doi:10.1534/genetics.117.300137/-/DC1.
[1]Corresponding author: Children's Hospital of Eastern Ontario Research Institute, University of Ottawa, 401 Smyth Rd., Ottawa, ON K1H 8L1, Canada. E-mail: ipena2@uottawa.ca
[2]These authors contributed equally to this work.

involved in neurotransmission (Percudani and Peracchi 2003). It is thus hypothesized that the local or global depletion of PLP results in the Pyr-dependent seizures (Clayton 2006), possibly via disturbance of the PLP-dependent biosynthesis of γ-aminobutyric acid (GABA), the main cerebral inhibitory neurotransmitter. So far, clinical data from cerebrospinal fluid (CSF) measurements of these compounds were inconclusive and the pathophysiology of PDE remains to be fully elucidated.

While PDE seizures are responsive to pharmacological dosages of Pyr, lifelong supplementation fails to prevent the neurodevelopmental disabilities observed in > 75% of PDE patients (Baxter 2001; Stockler *et al.* 2011; van Karnebeek *et al.* 2016). These include mild to severe developmental and cognitive disabilities including disorders of expressive language (van Karnebeek *et al.* 2016). This observation underscores the need for further studies on the pathophysiology of PDE and the development of novel therapies. Consequently, in addition to Pyr, adjunct treatment strategies of lysine restriction (van Karnebeek *et al.* 2012) and arginine supplementation (Mercimek-Mahmutoglu *et al.* 2014), separately or in combination ["triple therapy" (Coughlin *et al.* 2015)], have been recently introduced as attempts to both improve seizure control and moderate the long-term neurodevelopmental impact of PDE [for reviews see Pena *et al.* (2016), van Karnebeek *et al.* (2016), and Gospe (2017)].

Although the PDE disease gene has been known for more than a decade (Mills *et al.* 2006), there has been a dearth of genetically engineered animals modeling the disease. Zebrafish (*Danio rerio*) is a simple vertebrate species easily amenable to genetic manipulation, which has emerged as a successful model in epilepsy research (Baraban *et al.* 2005, 2013; Hortopan *et al.* 2010; Teng *et al.* 2011; Grone *et al.* 2016; Sourbron *et al.* 2016; Griffin *et al.* 2017). Here, we report the use of clustered regularly interspaced short palindromic repeat (CRISPR)/Cas9 gene editing to generate an *aldh7a1*-null zebrafish model that recapitulates the clinical and biochemical features of PDE. Aldh7a1 loss-of-function led to the accumulation of the toxic PDE biomarkers, spontaneous, recurrent seizures from 10 days postfertilization (dpf), and premature death (by 14 dpf). As with PDE, Pyr or PLP treatment halts zebrafish seizures; moreover, it also prolongs the survival of the mutant fish. Mass spectrometry (MS) studies of untreated fish identified several alterations in amino acid levels, most remarkably in the lysine metabolism pathway. Importantly, low B6 vitamers and GABA levels were observed, which may suggest that PDE is, at least in part, a disorder of GABA homeostasis.

Materials and Methods

Zebrafish maintenance

Adult wild-type (WT) zebrafish were maintained according to standard procedures (Westerfield 2000). All experiments were carried out in accordance with animal care guidelines provided by the Canadian Council on Animal Care and the University of Ottawa animal care committees approved this study under the protocol number BL-2678. The zebrafish room was maintained on a 14 hr light: 10 hr dark cycle, with lights-on at 9:00 AM and lights-off at 11:00 PM. Fish system water conditions were maintained in the following ranges by automated feedback controls: 29–30°, pH 7.5–8.0, and conductivity (EC) 690–710. Embryos were bleached 24 hr postfertilization. Zebrafish embryos and larvae were raised in plastic petri dishes (10-cm diameter) in an incubator maintained at 28.5° until 7 dpf in E3 embryo media. Their housing density was limited to a maximum of 60 individuals per dish until 6 dpf, when the larvae were split in groups of 20 or fewer individuals in 750 ml static tanks containing rotifer solution in 200 ml system water. Rotifers (*Brachionus plicatilis*) were obtained from Reed Mariculture and were fed RGComplete (APBreed). Larvae were fed with ∼15 mg of Gemma 75 per day and 50 ml of fresh water was added every day. Food quantity was gradually increased as the larvae grew. Juveniles and adults were grown in 3-liter tanks and fed on Gemma 150 and Gemma 300, respectively. Survival experiments were performed usually with a minimum of five or six fish per experimental group. Pyr and PLP (Sigma [Sigma Chemical, St. Louis, MO]) was dissolved in the system water; larvae were exposed to treatment for 30 min daily. Lysine treatment was performed with 48 hr of exposure. We considered our replicates as biological replicates as each sample was a different individual larva.

Morpholino gene knockdown in zebrafish

Translation-blocking (TB) or splice-blocking (SB) morpholino oligonucleotides (MO) (Gene Tools, LLC, Philomath, OR) were diluted in H_2O to 1 mM stock solution. The working solution was prepared in 1× *Danio* Buffer for the microinjections in embryos at the single-cell stage. The TB morpholino sequence was obtained from Babcock *et al.* (2014) 5′-TCGGACACTCGGCAACAGTTTATGC-3′ (referred in their paper as "*aldh7a1*-MO1"), targeting the first coding exon of the zebrafish gene. We used injections of 7.5 ng of MO to replicate the procedure described in Babcock *et al.* (2014) as well as testing a lower dose (3.5 ng). The control MO (5′-CCTCTTACCTCAGTTACAATTTATA-3′) and SB morpholino designed to target the intron 4–exon 5 splice junction "*aldh7a1*-SBMO-1" (5-GACACCTACGCATAGCAAACTCCTG-3′) were also obtained from Gene Tools, and 2.5 ng was similarly injected at the single-cell stage.

Western blot

Total soluble proteins were extracted from single larvae in RIPA buffer containing protease inhibitors (Sigma). Whole-larval lysates were obtained by sonication in 100 μl RIPA buffer using a Bioruptor Pico (Diagenode), 10 cycles of 10 sec on and 30 sec off. Proteins were quantified by bicinchoninic acid assay (BCA) assay; 30 μg of protein of each sample were separated by SDS-PAGE (10%). Antibodies raised in rabbit against ALDH7A1 and c-Fos were obtained from Sigma (code A9860) and Santa Cruz biosciences (code sc-166940 X) and used at dilutions 1:2500 and 1:100, respectively, in 3% BSA. Anti-rabbit IgG, HRP-linked antibody was used in a dilution of 1:2000. The Clarity ECL Western

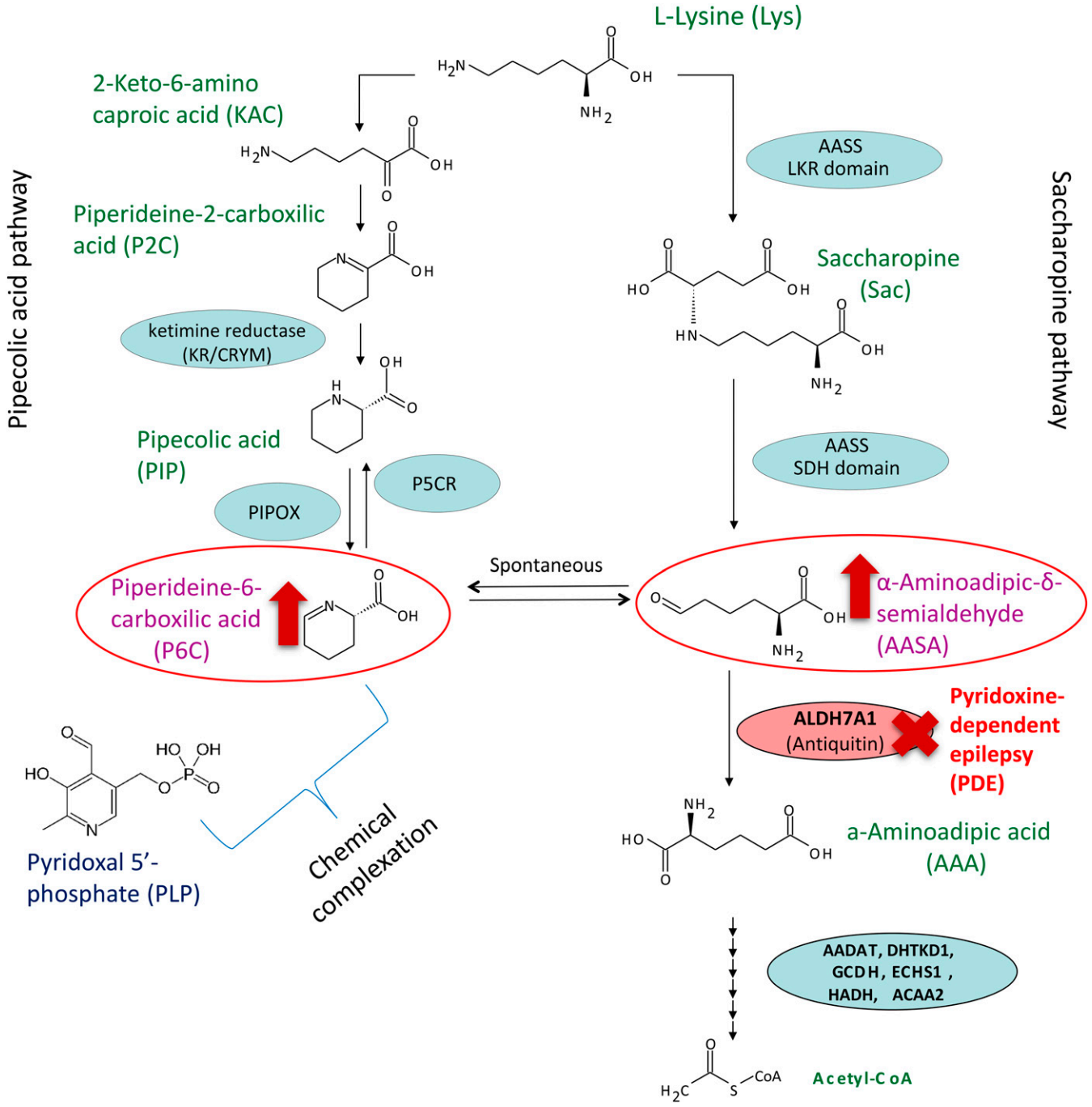

Figure 1 Pipecolic acid (left) and saccharopine (right) pathways for L-lysine catabolism in animals. The L-pipecolic acid pathway. LKR (lysine-ketoglutarate reductase) domain and SDH (saccharopine dehydrogenase) domain of the bifunctional AASS (aminoadipic semialdehyde synthase) enzyme. Antiquitin (encoded by the gene *ALDH7A1*) is deficient in pyridoxine-dependent epilepsy (red) leading to accumulation of AASA and P6C (red arrows). PIPOX (pipecolic acid oxidase). P5CR (piperideine-5-carboxilic reductase), encoded by the gene *PYCR1*. Further enzymatic steps convert AAA to Acetyl-CoA.

Blot Substrate kit (Bio-Rad, Hercules, CA) was used for chemiluminescent protein detection. Images were obtained and processed using the ChemiDoc Touch Imaging System (Bio-Rad).

Establishing mutant lines

CRISPR/Cas9 mutations were generated in WT zebrafish as described elsewhere (Hwang *et al.* 2013). The *aldh7a1*-targeting single-guide RNA (sgRNA) template plasmid was generated by annealing oligonucleotides and ligation of the double-stranded DNA in the plasmid DR274 (Addgene, code 42250). The CRISPR target sequence (5′-GGACTTAAAGAGGACAATGA-3′) and oligonucleotide design were performed using ZiFit software (Sander *et al.* 2010). To avoid off-target effects, we chose a target site with the lowest number of potential mutagenesis off-targets and with a minimum of three mismatches with such off-target sites. Plasmid sequences were checked by Sanger sequencing (ABI 3730).

The sgRNAs were transcribed from linearized template plasmids (Ambion MEGAscript T7/SP6) and purified (Promega, Madison, WI; Wizard SV Gel and PCR Clean-Up kit). The Cas9 protein was obtained from New England Biolabs (Beverly, MA). Fertilized one-cell-stage zebrafish eggs were injected with a mix containing ~300 ng/μl Cas9 protein and 15 ng/μl sgRNA. Embryos were raised and a portion of them (five pools of five embryos) were genotyped by heteroduplex melting assay (HMA) as described in Zhu *et al.* (2014). Briefly, primers flanking the CRISPR target site (forward sequence: "Gen1_FW," 5′-ATGATGCAGCGCGTGCT GAC-3′, reverse sequence: "Gen2_RV," 5′-CCCTTTGAACCTC ACAGGAGTT-3′) were used to amplify a segment of 434 bp. The PCR product was denatured and annealed. It was expected to contain a mixture of insertion/deletion mutations and WT alleles, which can form heteroduplex and homoduplex DNA. These can be easily identified by PAGE. The remaining embryos were raised to adulthood (F_0 generation) and backcrossed with WT fish. DNA was extracted from F_1 embryos to check for F_0 founders carrying specific mutations by HMA-PAGE. F_1 fish were raised to adulthood and heterozygous mutants were identified by fin clipping, followed by DNA extraction and HMA-PAGE. Potential mutants were sequenced allowing the identification of specific mutations (Figure S4). Populations of heterozygous F_1 fish carrying the same mutation were identified; the most common was a 5-nt insertion leading to a premature stop codon. F_1 heterozygous fish were backcrossed to WT fish to further eliminate potential off-target effects generated by the Cas9 nuclease. For the experiments described in this paper, we used crossings of F_2 heterozygous fish obtaining F_3 offspring containing a homozygous 5-nt deletion in the gene *aldh7a1*. The newly generated mutant allele was designated *aldh7a1*^{ot100} using the University of Ottawa designation and in accordance with the Zebrafish Information Network guidelines.

Larval fin clipping and multiplex PCR for genotyping

For genotyping of larvae to identify and distinguish the 5-nt insertion from the WT allele, we extracted genomic DNA from larval fins at 3–5 dpf and raised the corresponding larvae. Larval fin clipping was performed as an adaptation of a previously described protocol (Wilkinson *et al.* 2013). This method allowed genotyping and subsequent fin regeneration in a few days. Briefly, 3-dpf larvae were anesthetized in Tricaine, and then a microscalpel was used to section and obtain a microscopic caudal fin slice under a stereomicroscope (Nikon SMZ1500). The section was made by applying steady downward pressure to incise within the pigment gap site of the caudal fin, distal to the limit of the blood circulation. The fin was then placed in a small piece of filter paper, which was then submerged in 30 μl of Chelex 5% solution in 96-well PCR plates. For tissue lysis, the samples were heated in a thermocycler at 95° for 15 min, then cooled to 4° for 10 min. The samples were centrifuged to pellet the Chelex beads leaving DNA in suspension. A 1.5 μl volume of the DNA supernatant was used in each PCR reaction. This method allowed efficient recovery of DNA in 97% of the larvae on average. A multiplex PCR reaction was used to precisely genotype WT and/or mutant alleles enabling the identification of fishes homozygous, heterozygous, or null for the 5-nt insertion mutation. This strategy is summarized in Figure S5, using the primers "Gen1_FW": 5′-ATGATGCAGCGCGTGCT GAC-3′, "Gen2_RV": 5′-CCCTTTGAACCTCACAGGAGTT-3′, "5 nt-ins-specific_FW": 5′-TGTTTTC**AACGG**TTCAACGG-3′, and "WT-specific_RV": 5′-TCCCTGTCCTCCCCA**AG**AAC-3′. Three bands are expected using these four primers in a multiplex reaction: an ~430-bp amplicon resulted from amplification using Gen1_FW and Gen1_RV for both alleles, a 293-bp band specifically for the mutant allele, and a 195-bp band specifically for the WT allele (Figure S5). Samples were then run in an agarose 1% gel, stained with GelRed, and visualized under UV light, allowing discrimination of the different amplicons. We observed that the caudal fin regenerated in a few days (Figure S5, F and G) and normal development proceeded, as reported previously in Wilkinson *et al.* (2013).

RNA extraction and real-time PCR

Total RNA was extracted from three pools of five WT or *aldh7a1*$^{-/-}$ larvae using the reagent QIAzol (QIAGEN, Valencia, CA) (each pool considered one biological replicate). First-strand-complementary DNA was synthesized from 1 μg total RNA using the iScript kit (Bio-Rad). Quantitative real-time PCR was conducted using the following primer pairs: *gapdh* (5′-TGTTCCAGTACGACTCCACC-3′ and 5′-ACCTGCATCACCCC ACTTAA-3′), *aldh7a1* (5′-TGTTCGACAGATTGGAGAGGC-3′ and 5′-GGCTGTGATGATTCCTACCAAG-C-3′), gad1 (5′-AACTCAGGCGATTGTTGCAT-3′ and 5′-CCAGCATCCTGAGG ACATTT-3′), and *gad2* (5′-AGCTGCTCTTGGA-ATCGGTA-3′ and 5′-GCTGACAAAGAACGGCACGT-3′), with iQ SYBR Green Supermix (Bio-Rad). Relative mRNA levels were normalized to glyceraldehyde-3-phosphate dehydrogenase mRNA levels using the ΔΔCT method. The PCR amplification was performed in three technical replicates. The Student's *t*-test was used to evaluate the statistical significance of the differential mRNA levels between the three biological replicates of WT and *aldh7a1*$^{-/-}$ siblings.

Morphological phenotyping

Larvae were photographed using a stereomicroscope (Nikon, Garden City; SMZ1500). Standard lengths (distance from the anterior tip of head to the base of the caudal fin) were measured manually using imageJ software.

Behavioral phenotyping

For locomotion tracking, 8 dpf and younger zebrafish larvae were placed in individual wells of a 96-well flat-bottomed culture dish (Corning); a 48-well flat-bottomed culture dish was used otherwise. For 96-well plates, each well contained 200 μl of embryo medium, and 500 μl for 48-well plates. Behavior was monitored at 28.5° using a ZebraBox system (ViewPoint Behavior Technology) consisting of a sound proof chamber with an infrared camera; analyses were performed

using Zebralab locomotion tracking software (ViewPoint Behavior Technology). Larvae were allowed to acclimate to the plate and ZebraBox environment for 10 min. Five minutes of baseline were recorded followed by 5 min recording with light stimulus [five cycles of 10 sec on (100% light) and 50 sec off]. Using ZebraLab software, we calculated the distance traveled, duration, and number of high-speed [$>$ 20 mm/sec (Afrikanova *et al.* 2013)], intermediate (8–20 mm/sec), and slow movements ($<$ 8 mm/sec) for the 5-min baseline and 5 min light stimulus recordings. Larvae were plated each experiment in a randomized position to avoid bias. Videos were also analyzed blindly for the classification of seizure scores based on Baraban *et al.* (2005). GraphPad Prism was used to conduct ANOVA tests to compare the experimental groups.

Metabolite extraction and MS

For analysis of polar amino acids, each biological replicate consisted of pools of five deep-frozen 11-dpf larvae, which were sonicated in 150 μl methanol and 75 μl chloroform in 10 cycles (10 sec on, 30 sec off) using a Bioruptor Pico (Diagenode). Then, 112 μl of chloroform and 112 μl of H_2O were added to the lysate, vortexed, and centrifuged at 20000 $\times$ *g* for 20 min at 4°, allowing phase separation. The supernatant containing polar metabolites was collected and dried under nitrogen. The metabolite extract was resuspended in HPLC-grade H_2O (Sigma) and used for liquid chromatography-MS analysis (LC-MSMS). P6C and pipecolic acid were measured using previously described methods (Struys *et al.* 2012a). AASA was measured using published methods (Mills *et al.* 2006). All analytes described in Figure S10 as part of the targeted amino acid panel were measured using LC-MSMS in the Newborn Screening Ontario-Inherited Metabolic Disease laboratory, using a method adapted from a published procedure (Waterval *et al.* 2009). For quantification of B6 vitamers, 300 μl ice-cold trichloroacetic acid (TCA) solution (50 g/liter) was added to a pool of six deep-frozen zebrafish at 11 dpf. A small amount of zirconium oxide beads was added to the solution and put into a bullet blender for 5 min at level 8. Hereafter, the samples were centrifuged for 5 min at 13,000 rpm. The supernatant was prepared for the analysis of vitamin B6 vitamers using a published method (van der Ham *et al.* 2012), except that an 80-μl volume of sample was used instead of 60 μl [internal standard ratio (1:1)] and concentrations of the calibration solutions were 10 times lower than in the publication.

Electrophysiology

Electrophysiological recordings were obtained using methods described in the literature (Baraban *et al.* 2005). Specifically, 11-dpf zebrafish larvae were embedded in a 1.2% agarose gel prepared by dissolving low-melting temperature agarose in artificial CSF (aCSF) (NaCl 134 mM, KCl 2.9 mM, $MgCl_2$ 1.2 mM, $CaCl_2$ 2.1 mM, Glucose 10 mM, and HEPES 10 mM). Larvae were placed dorsal-up to give easy access to the brain. A waiting time of 15–20 min was allowed for the zebrafish to become acclimated to the embedding. The bath volume was adjusted to 5 ml, and excess aCSF and gel were carefully removed to expose the top of the head. After transferring the larva to a chamber placed under a BX51WI Olympus microscope, a glass microelectrode was placed under visual guidance in the optic tectum of the fish. The glass microelectrode tip openings were ~2 μm and were backfilled with 2 M NaCl. Electrical activity of the brain was amplified and low-pass filtered at 1 kHz with a MultiClamp 700B (Axon Instruments, Foster City, CA), digitized with a Digidata 1550 (Axon Instruments), and stored on a computer for later analysis. Traces were band-pass filtered (0.2–1 kHz). A detection threshold of three times background noise was applied to extract the events on a 5-min-long window. Detected events were manually sorted; those presenting two or more consecutive spikes were considered as seizure-like. Times and duration of each event were extracted. To test if movement artifacts were present, the neuromuscular blocker d-tubocurarine (15 μM, Sigma) was used to paralyze larvae, added directly to the bathing medium (Figure S8).

Immunofluorescence

Fish larvae were sacrificed at 10 or 11 dpf and fixed in 4% PFA/PBS overnight at 4°. The samples were washed the following day with PBS three times, and equilibrated with a solution of 30% sucrose in PBS overnight at 4°. The samples were then incubated in a 1:2 30% sucrose: optimum cutting temperature (OCT) Compound (Tissue-Tek) solution for 30 min, frozen in cryomolds using liquid nitrogen, and then stocked at −20° for further sectioning. Transverse cryosections of 14–16 μm of the whole head were obtained with a CM3050S cryostat (Leica, Concord, ON) and collected on microscope slides. All antibodies for the immunohistochemistry assay were previously validated. Sections were first rehydrated in PBS solution, and blocked in 10% calf serum in PBS-T (PBS plus 0.1% Tween 20) for 2 hr at room temperature. The primary rabbit anti-calretinin antibody (1:500, Swant7697) was incubated overnight at 4° in a 1% calf serum in PBS-T solution. Slides containing sections were then washed for 15 min 3 times with PBS-T, and incubated with the secondary antibody Alexa Fluor 488 goat anti-rabbit (1:1000, Invitrogen, Carlsbad, CA) protected from light for 2 hr at room temperature. Sections on slides were washed again three times with PBS-T and sealed and mounted with Vectashield mounting media (Vector Laboratories, Burlingame, CA) containing DAPI for nuclei staining. For each larval sample, every transverse section from the head was subjected to immunohistochemistry and visualized with a Zeiss ([Carl Zeiss], Thornwood, NY) AxioPhot fluorescence microscope, and images were acquired. Cells labeled with fluorescence were manually counted and the counts were crossed with an estimate number of cells using ImageJ.

Statistics

For multiple comparisons, one-way ANOVA with Tukey's test, or Kruskal–Wallis ANOVA with Dunn's *post hoc* test, were

used as appropriate. For pairwise comparisons, the Student's *t*-test was used. Significance testing and graphing was performed with GraphPad Prism 7 software. Processing of the chromatograms obtained by LC-MSMS was done using TargetLynx (Waters Associates, Milford, MA), including peak detection, peak integration, and concentration estimation based on calibration curves. For analysis of the MS amino acid panel, we used Metaboanalyst v3 (Xia *et al.* 2015), statistical analysis module for one-way ANOVA with Tukey's *post hoc* test, and the heatmap module to produce the heatmap representation (Figure S11) using Euclidean distance measure and Ward clustering algorithm.

Data availability

Sequences, plasmids, and the zebrafish line aldh7a1^{ot100} used in this study are available upon request. Figure legends and video descriptions for the supplemental material are contained in File S4. The authors state that all data necessary for confirming the conclusions presented in the article are represented fully within the article.

Results

Morpholino-based aldh7a1 knockdown in zebrafish

The phenotypic impact of MO-based downregulation of *aldh7a1* in zebrafish was initially assessed; an MO molecule targeting the intron 4–exon 5 splice junction site (designated *aldh7a1*-SBMO-1) was designed to induce splice defects and therefore *aldh7a1* knockdown (Figure S2). First, 2.5 ng of either *aldh7a1*-SBMO-1 or control MO were injected in to one-cell-stage embryos and larvae collected at 4 dpf. Although the Aldh7a1 protein levels were knocked down to ~13% using the *aldh7a1*-SBMO-1 (Figure S3A), the morphant larvae displayed grossly normal morphology (Figure S3B) and did not differ in length, hatching time, or swimming behavior compared to controls. A second morpholino molecule (*aldh7a1*-MO1), used previously by Babcock *et al.* (2014), was also assessed. Although, as previously reported, a series of deformations were observed in the morphant larvae, western blot analysis failed to reveal any protein knockdown by this MO (Figure S3, F and G), indicating that these reported abnormalities are probably independent of *aldh7a1* function. In contrast, the successful knockdown of Aldh7a1 protein using the *aldh7a1*-SBMO-1 (Figure S3A) did not result in the phenotypes reported in Babcock *et al.* (2014), such as skeletal abnormalities and eye deformities (data not shown).

In an attempt to elicit a phenotype, *aldh7a1*-SBMO-1-injected larvae were exposed to lysine (20 mM) for 24 hr. We observed a significant increase in Aldh7a1 protein levels, partially overriding the inhibition caused by the morpholino (Figure S3C). However, the morphants did not accumulate the toxic PDE metabolite P6C in either control conditions or in the presence of lysine overload (Figure S3D). This suggests that low Aldh7a1 levels are sufficient for effective lysine metabolism, consistent with the known high catalytic efficiency of this enzyme (Brocker *et al.* 2010; Kiyota *et al.* 2015). Therefore, we concluded that a complete loss-of-function of *aldh7a1* would be required to induce the AASA/P6C accumulation phenotype and thus PDE.

The aldh7a1^{ot100} allele leads to complete loss of functional Aldh7a1

By injecting single-cell zebrafish embryos with Cas9 protein and an *aldh7a1*-specific sgRNA, germline mutations were introduced in the first coding exon of the *Aldh7a1* gene. We identified and crossed F_0 founders with WT fish to generate F_1 zebrafish heterozygous for mutations in the *aldh7a1* gene. Identification of mutations was performed by a heteroduplex melting assay using PAGE gels. Sequencing of the CRISPR target region in the F_1 fish revealed the presence of several insertions or deletions in the *aldh7a1* gene (Figure S4).

We chose an F_1 heterozygous population carrying a 5-nt insertion mutation to generate F_2 fish by backcrossing with WT fish. Heterozygous F_2 fish were bred to generate homozygous mutants. The 5-nt insertion allele was easily detected by a multiplex PCR method allowing discrimination between WT, heterozygous, and *aldh7a1*$^{-/-}$ (mutant) genotypes (Figure S5). F_3 offspring were sequenced to confirm the presence of homozygous mutants for the 5-nt insertion mutation in the *aldh7a1* gene (Figure 2, A and B). The insertion caused a frameshift in the primary *aldh7a1* transcript (GenBank: NM_212724), leading to a premature stop codon at position 50 of the translated protein sequence. This novel mutant was given the line designation *aldh7a1*^{ot100}. Fin clipping of randomly sorted F_3 larvae at 7 dpf was performed to extract DNA, and the whole larva was used to extract protein from the same animal. Western blotting showed successful Aldh7a1 protein knock-out in these fish (Figure 2C, lanes 1, 5, 6, and 9). As expected, heterozygous fish had approximately half of the normal Aldh7a1 protein levels compared to WT (Figure 2C). Multiplex PCR using the DNA samples extracted from the fins of the same fish confirmed each genotype (Figure 2D). The *aldh7a1* transcript in the mutants was 9% of that observed in the WT larvae, likely a result of nonsense-mediated mRNA decay (Figure S6).

Starting at 10 dpf, the mutants exhibited a hyperactive behavior characterized by fast swimming and convulsion-like activities, which intensified with time; these larvae all died by 14 dpf (Figure 2E). We tested two larval feeding protocols: one involving rotifer feeding from 6 dpf and one solely with the formulated zebrafish feed Gemma-75. Both elicited the same death phenotype (data not shown) and we chose to continue the experiments using the rotifer protocol. Although the morphology of the mutants from 0 to 10 dpf was indistinguishable from that of controls (WT and heterozygous), by the time of death, the mutants often displayed a ventrally-curved body phenotype (Figure 2F). As expected, the ablation of functional Aldh7a1 protein disrupted lysine degradation leading to the accumulation of AASA/P6C in the mutants. A representative LC-MSMS chromatogram of a control [WT or Het (Figure 2, G–H, top)] and a mutant larva

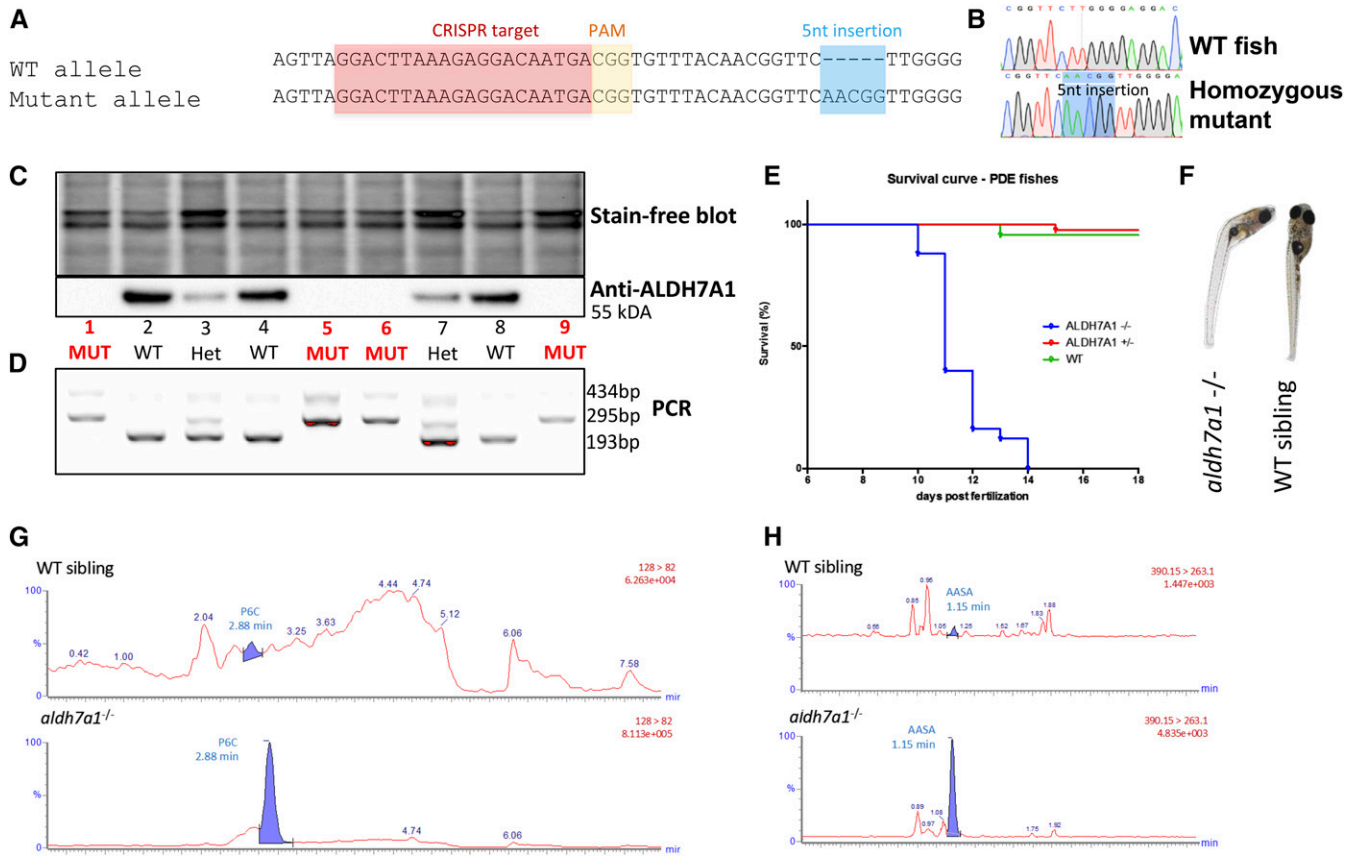

Figure 2 Development of an *aldh7a1*$^{-/-}$ zebrafish model by CRISPR/Cas9. The allele *aldh7a1*^{ot100} contains a 5-nt insertion mutation (A), which leads to a premature stop codon and an N-terminal-truncated Aldh7a1 protein product. Sequencing chromatograms from F_3 larvae show the WT and homozygous mutant (B) patterns. Western blot detected the Aldh7a1 protein in WTs, with ~50% reduction and complete loss of expression in heterozygous and in the homozygous mutants, respectively (C). PCR-based genotyping (D) using DNA extracted from the fins of the larvae shown in (C) were consistent with the western findings. Kaplan–Meier survival plot showing early death in the homozygous mutants (11–14 dpf), n = 12 *aldh7a1*$^{-/-}$, n = 18 *aldh7a1*$^{+/-}$, n = 10 *aldh7a1*$^{+/+}$ (E). Curved body phenotype observed at 11–14 dpf in the mutants after seizure onset (F). Representative liquid chromatography-mass spectrometry analysis of 7 dpf single larva (n = 6 per genotype); polar metabolite extracts revealed detection and accumulation of the PDE biomarkers P6C and AASA exclusively in the mutants (G and H bottom). No P6C or AASA signal was obtained in the extracts from WT or heterozygous siblings (G and H top). AASA, aminoadipate semialdehyde; CRISPR, clustered regularly interspaced short palindromic repeat; dpf, days postfertilization; HET, heterozygote; MUT, mutant; P6C, piperideine 6-carboxylate; PAM, protospacer adjacent motif; PDE, pyridoxine-dependent epilepsy; WT, wild-type.

(Figure 2, G–H, bottom) shows P6C and AASA detection in the micromolar range in the mutant larva. Heterozygous fish were indistinguishable from control WT fish and had normal lysine metabolism (data not shown), consistent with the hypothesis that this phenotype requires *aldh7a1* loss-of-function as seen in human patients with PDE.

Spontaneous seizure activity in aldh7a1 mutant zebrafish

Epilepsy models in zebrafish larvae are characterized by seizure-like behavior ranging from episodes of excessive locomotor activity, sustained rhythmical jerking (clonus), and stiffening (tonus) to tonic–clonic seizures (Baraban *et al.* 2005, 2013; Hortopan *et al.* 2010; Teng *et al.* 2010). Normal movement behavior can be characterized as little (stage 0) or some swimming activity (stage 1), whereas seizure behavior is characterized as rapid "whirlpool-like" circling swimming (stage 2) and a series of whole-body convulsions culminating in loss of posture (stage 3) (Baraban *et al.* 2005). Therefore, we monitored *aldh7a1* mutants for evidence of seizure-like behavior from video recordings. Larvae were genotyped by larval fin clipping at 3 dpf, fed on a rotifer diet from 6 dpf, and monitored using a high-speed infrared video tracking system (ZebraBox, ViewPoint Behavior Technology) in multi-well plates. Baseline and light stimulus recordings were performed daily from 7 to 14 dpf. There was no evidence of seizure-like behavior in fish of any genotype before 10 dpf. Video recordings starting in the evening of 10 dpf or in the morning of 11 dpf consistently showed signs of hyperactivity, with rapid "whirlpool-like" circular swimming (stage 2) and whole body-convulsions leading to loss of posture (stage 3) (Figure 3, A–D). We observed that hyperactivity/seizure-like behavior was immediately induced upon light stimulus in the *aldh7a1*$^{-/-}$ fish, which spent more time (Figure 3A) and traveled greater distances (Figure 3B) in high-speed movements [traces shown in red in Figure 3C)] than WT and

heterozygous siblings. This was consistently observed in several batches of fish. No significant difference in quantified movement behavior was observed in 5-min baseline recordings analysis in either ambient light or darkness prior to the light stimulus, although spontaneous and sporadic convulsive behavior was consistently observed over > 10 batches of null-mutants. It is possible that the light induced convulsions in a more frequent and simultaneous fashion and thus facilitated the detection and quantification of the abnormal behavior. Examples of normal behavior in WT siblings and seizure-like behavior observed under microscope light in the mutant larvae are shown in File S1 and File S2, respectively. Blinded analysis of video recordings resulted in the identification of stages 2 and 3 of seizure behavior exclusively in the mutant fish (Figure 3D). Healthy larvae would only display stages 0 and 1, consistent with what is described in the literature (Baraban *et al.* 2005). The curved phenotype observed after seizure onset may be related to muscle stiffness, potentially derived from recurrent and uncontrolled tonic–clonic seizures.

We next tested whether the seizure-like behavior in *aldh7a1*$^{-/-}$ mutants was associated with an electrographic component. Tectal field potential recordings from agar-immobilized 11-dpf larvae revealed spontaneous seizure-like events exclusively in *aldh7a1* mutants ($n = 5$) (Figure 3F). In contrast, WT or heterozygous siblings ($n = 5$) showed only normal electric activity (Figure 3E). In all mutants tested, we observed a high number of bursts of abnormal electrical discharge with long duration and high amplitude (Figure 3F), resembling the ictal-like activity described in other zebrafish and mammalian seizure models (Figure 3F, ii). In addition, short and low-amplitude bursts of interictal activity were also present (Figure 3F, iii). Representative recordings from additional *aldh7a1*$^{-/-}$ mutants, negative control recordings from electrodes inserted into agar mounting medium, and movement artifacts not considered as spikes are illustrated in Figure S7. We also obtained traces after paralyzing mutant larvae with d-tubocurarine, demonstrating the same features shown by the data in the absence of paralyzing agent, with no significant differences in the number and duration of events ($n = 3$ mutant larvae) (Figure S8). This further excludes the possibility of movement artifacts in our analysis. In summary, the seizure-like behavior, abnormal electrographic activity, and the early death phenotype are all consistent with an epilepsy phenotype in the *aldh7a1*$^{-/-}$ larvae.

Pyr-dependent seizures in aldh7a1$^{-/-}$ *larvae*

In humans, PDE manifests as intractable recurrent seizures that are significantly lessened by pharmacological doses of Pyr or PLP (Mills *et al.* 2006). We tested whether the *aldh7a1*$^{-/-}$ larval epilepsy phenotypes described above responded to treatment with either compound. We observed a dose-dependent extension of the life span of the mutants with both PLP (Figure 4A) and Pyr (Figure 4B) at high doses. The median survival of 12 dpf for untreated mutants was increased up to 22 dpf with the PLP 500 μM treatment. With daily treatment with millimolar doses of Pyr (5 and 10 mM), mutants survived until late juvenile stages (40 dpf), when the experiment was stopped. Therefore, high doses of either PLP or Pyr promote long-term survival of *aldh7a1*-null mutant fish. We chose to continue investigating Pyr (10 mM) responsiveness as it appeared to have a greater effect on life span, as well as being more stable, soluble, and less toxic than PLP. We observed that withdrawal of Pyr daily treatments would result in the appearance of the seizure behavior within 2–6 days and subsequent death (data not shown), highlighting the Pyr-dependency of the *aldh7a1*-null model.

We observed that the seizure-like behavior was prevented by Pyr treatment. Movement traces obtained from treated mutants under baseline (data not shown) and light stimulus conditions were indistinguishable from WT and Pyr-treated WT (Figure 4C). The duration and distance traveled in high-speed movements showed no statistical difference compared to WT and Pyr-treated WT, and all were significantly lower than in untreated mutants (Figure 4, D and E) ($P = 0.0009$ and 0.0019, ANOVA with Tukey's *post hoc* tests for pairwise comparisons). Blinded analysis of video recordings revealed that *aldh7a1*$^{-/-}$ fish treated with Pyr did not display S2 and S3 stages of seizure behavior, hyperactivity, or high-speed movements, whether at baseline or under light stimulus (Figure 4, F and G). Additionally, the treated mutants did not display the curved body phenotype (Figure S9). Taken together, these results indicate the alleviation of the manifestations associated with the epilepsy phenotype with Pyr treatment. Video recordings showing the typical behavior of untreated and treated mutants can be seen in File S2 and File S3.

The electrophysiological burst characteristics were also compared between untreated ($n = 5$) and Pyr-treated mutants ($n = 9$; Figure 4, H–J). A statistically significant suppression of burst activity, measured as total event duration ($P = 0.0207$, Figure 4H) and number of events ($P = 0.0348$, Figure 4I) in a window of 5 min, was observed, suggesting Pyr-mediated amelioration of the spontaneous seizure phenotype (Kruskal–Wallis ANOVA with a Dunn's *post hoc* test). Given the time-consuming nature of this experiment and our ability to analyze only 4–5 larvae per day, four batches of larvae were analyzed, with consistent results. All untreated *aldh7a1*-null mutants displayed seizure-like bursts of electrical activity, whereas this was true for only 55% of the Pyr-treated mutants (5/9). Still, in the five Pyr-treated mutant fish displaying burst activity, it consisted of a lower number of events, as shown in Figure 4, H and I. Representative recordings of four Pyr-treated mutants are shown in Figure 4J. One Pyr-treated mutant displayed a high number of spikes (Figure 4J, third trace from top to bottom). These analyses were performed in ambient light and so we also tested whether light stimuli would further induce seizure-like activity in the untreated and treated mutants. Although the behavior of treated mutants was indistinguishable from WT siblings even after light stimuli, electrographic seizure events could be induced in the Pyr-treated mutants (Figure S9) and the burst activity was significantly higher than that recorded in ambient light.

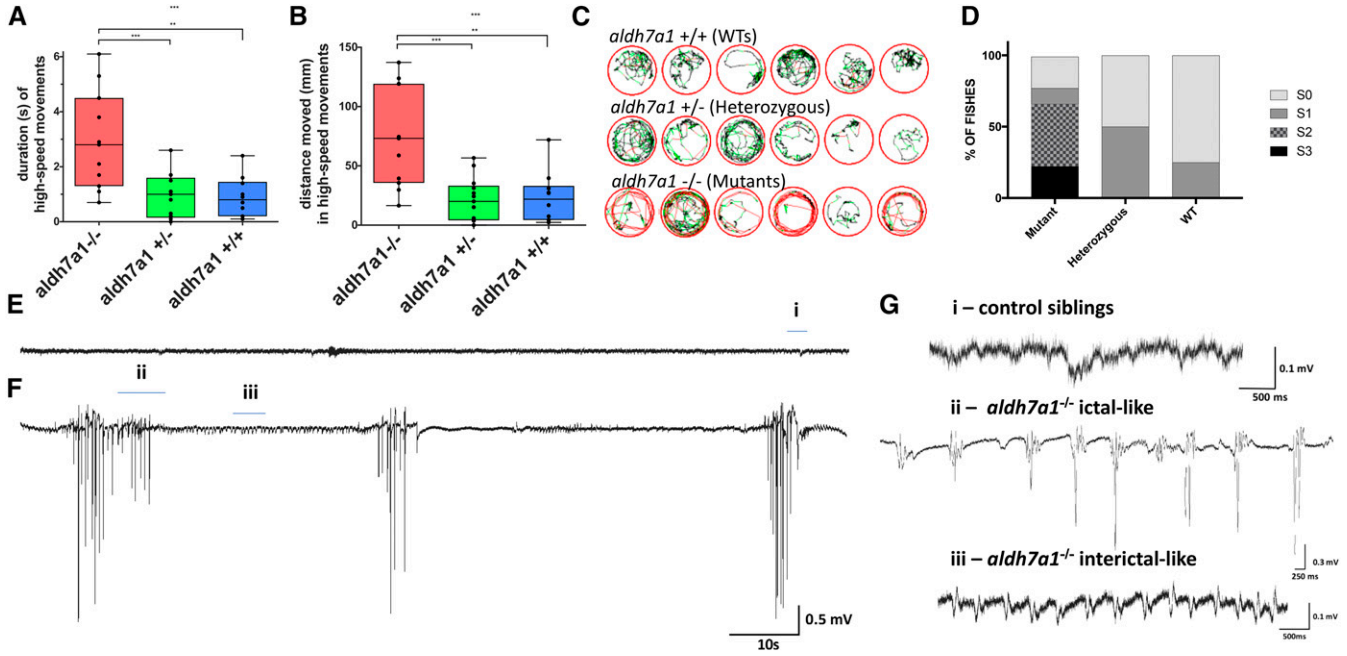

Figure 3 Seizure phenotype in *aldh7a1*$^{-/-}$ 11-dpf larvae. Video recordings (n = 12 larvae per genotype) were analyzed for high-speed movement in the presence of light stimulus; the calculated duration (A) and distance traveled (B) are shown. Movement traces shown in red, green, and black represent high-speed, intermediate, and slow movements, respectively (C). Blinded classification of seizure scores from video recordings of mutants, heterozygous, and WT larvae (n = 12 larvae per genotype). S0 characterizes normal swimming behavior, S1 reflects increased activity, S2 indicates rapid circular swimming activity, and S3 represents whole-body convulsions. Tectal field recordings of representative 11-dpf WT sibling (E) and *aldh7a1*$^{-/-}$ (F) showing spontaneous epileptiform-like electrographic activity in the mutants. Amplified view (G) of regions of the traces shown in (E and F): "i" normal activity as seen in WT and heterozygous siblings, "ii" ictal-like, and "iii" interictal-like epileptiform discharge observed in the mutants. Asterisks indicate statistical significance (* $P < 0.05$, ** $P < 0.01$, and *** $P < 0.001$) according to one-way ANOVA test on top of the graphics (in (A) $P = 0.0003$ and in (B) $P = 0.0002$) with Tukey's *post hoc* pairwise tests. Error bars represent ± SD. All experiments were performed comparing *aldh7a1*$^{-/-}$ and its heterozygous or WT siblings. dpf, days postfertilization; WT, wild-type

In mammalian models, it is well established that almost all types of seizures cause dynamic alterations of immediate early genes, such as *c-fos*, in neurons located in seizure-initiation sites (Kiessling and Gass 1993). This has also been observed in zebrafish models of epilepsy (Baraban *et al.* 2005; Teng *et al.* 2011). We observed, by western blot analysis (Figure 4K), that *aldh7a1*$^{-/-}$ larvae collected at 11 dpf displayed higher expression of *c-fos* compared to WT siblings and that this expression was normalized with Pyr treatment. Protein extracts from WT larvae treated with 15 mM of pentylenetetrazole for 2 hr were used as positive controls for *c-fos* upregulation (Baraban *et al.* 2005) (Figure 4K, first two lanes). Therefore, we provide consistent evidence for Pyr responsiveness (survival, behavior, electrophysiology and *c-fos* expression) of the epileptic phenotype of *aldh7a1* mutants.

Lysine supplementation induces an earlier seizure phenotype

We next hypothesized that, since P6C accumulation leads to PLP inactivation and seizure occurrence, lysine supplementation would induce a more severe phenotype due to increased P6C production, quickly reaching a threshold necessary for PLP inactivation. The effects of lysine supplementation on mutant larvae before the onset (10 dpf) of the seizure-like behavior were assessed. We observed that mutants invariably died within 48 hr of exposure to 20 mM lysine; Lys enrichment initiated at 6, 7, and 8 dpf in mutants lead to death of all larvae by 8, 9, and 10 dpf, respectively (Figure 5A). WT siblings, in contrast, were unaffected by lysine supplementation.

We then assessed whether the toxicity of AASA/P6C or the Pyr deficiency itself leads to persistent seizures and death. This was explored by assessing the impact of combining lysine overload with Pyr treatment. Mutants and WT siblings were supplemented at 8 dpf with lysine 20 mM and seizure-like behavior was monitored at 24 hr after the treatment (at 9 dpf). Two out of eight Lys-exposed mutants died after 24 hr of exposure, whereas the remaining six larvae clearly displayed seizure-like behavior (Figure 5) and died after 48 hr of exposure (Figure 5B). Pyr-untreated mutants died by 14 dpf as consistently observed previously. However, mutants treated with Pyr alone or in combination with Lys all survived until the end of this experiment (20 dpf), suggesting that it is the Pyr-deficiency, and not an unrelated AASA/P6C toxicity or other nonlysine-related *aldh7a1* loss-of-function, that underlies the seizure/death phenotype.

Early lysine-elicited seizure behavior was next quantified as outlined above. Lys-supplemented mutants (24 hr of exposure) displayed more high-speed movements at 9 dpf (Figure 5, C and D), whereas untreated, Pyr-treated, and Lys + Pyr-treated mutants of the same age did not display any evidence of

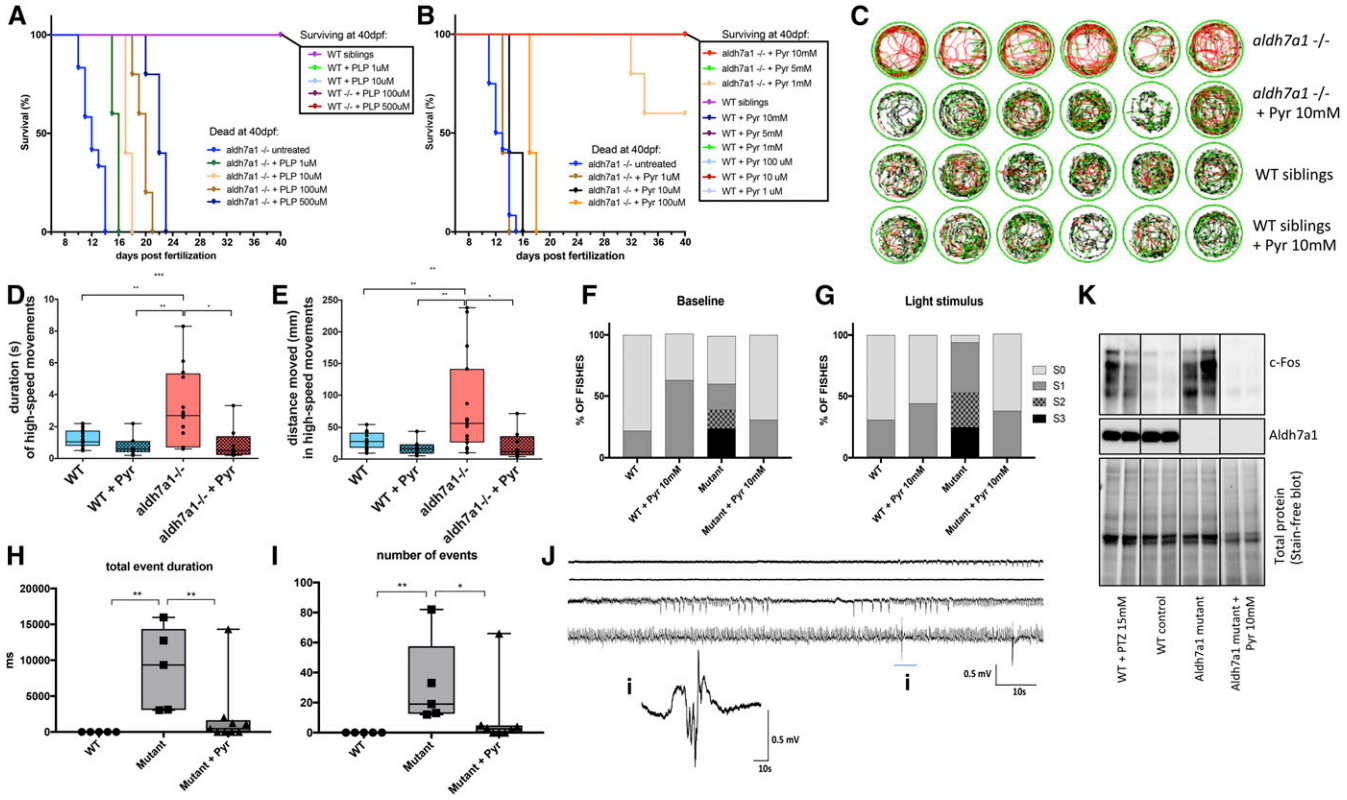

Figure 4 Pyridoxine (Pyr)-dependent epilepsy in *aldh7a1*$^{-/-}$ larvae. Pyridoxal 5′-phosphate (PLP) treatment promoted dose-dependent increase in survival of mutant larvae (A). Pyr treatment also led to prolonged life span of the null-mutants, with 100% survival until juvenile stage (5 and 10 mM daily) (B). In both cases, experiments were terminated at 40 days postfertilization (dpf) and consisted of $n = 5$ individuals per group except for untreated *aldh7a1*$^{-/-}$ ($n = 12$). Representative movement traces obtained from Zebralab software showing in red, high-speed, green, intermediate, and black, slow movements for mutants and their wild-type (WT) siblings, untreated and treated with Pyr 10 mM (C). Movement analysis using Zebralab showing duration (D) and distance traveled in high-speed movements (E). Blinded analysis of baseline (F) and light stimulus (G) video recordings classified the behavior in seizure scores as described previously. $N = 16$ *aldh7a1*$^{-/-}$ untreated, $n = 8$ *aldh7a1*$^{-/-}$ + Pyr 10 mM, $n = 16$ WT untreated, and $n = 8$ WT + Pyr 10 mM (D–G). Total event duration of the electrographic seizure-like bursts (H) and total number of such events (I) observed in a window of 5 min for $n = 5$ WT siblings, $n = 5$ untreated *aldh7a1*$^{-/-}$, and $n = 9$ *aldh7a1*$^{-/-}$ treated with Pyr 10 mM. Examples of traces of treated mutants showing magnification of one burst are shown in "i" (J). Western blot probing with anti-c-Fos and anti-ALDH7A1 antibodies (K); each lane corresponds to protein extracts of a single larva. Asterisks indicate statistical significance (* $P < 0.05$, ** $P < 0.01$, and *** $P < 0.001$) based on ANOVA test with Tukey's *post hoc* pairwise tests. Error bars represent ± SD. All experiments were performed comparing *aldh7a1*$^{-/-}$ and its WT siblings. Electrophysiology measurements were performed using four different batches of larvae.

seizure-like behavior. Time-course analysis suggested that the seizure onset occurred ~20 hr after addition of lysine (data not shown). This early seizure induction could also be seen in the movement diagrams obtained from Zebralab (Figure 5E) and was identified by blind video analysis, as all Lys-exposed mutants were classified as stages 2 or 3 (Figure 5F). These observations suggest the existence of a critical "seizure-inducing" AASA/P6C level, which is more rapidly attained with lysine supplementation.

Impairment of lysine metabolism in aldh7a1$^{-/-}$ *larvae leading to low B6 vitamers and reduced GABA synthesis*

LC-MSMS was next used to quantify lysine metabolites in polar extracts from mutant larvae and compare them with WT and heterozygous siblings. Several analytes could be detected and quantified in the extracts obtained from pools of five 11 dpf larvae using a targeted LC-MSMS amino acid panel (Figure S11). MetaboAnalyst 3.0 (Xia and Wishart 2002; Xia *et al.* 2015) was used to study two different batches of *aldh7a1*-null mutants (Mut1 and Mut2) compared with their respective batches of WT siblings (WT1 and WT2). Results of relative quantification (fold change) are shown in Figure S11 as a clustered heatmap visualization distinguishing WT and mutant samples based on patterns of cooccurrence of metabolites. One-way ANOVA and Tukey's *post hoc* analysis of the four sample groups indicated 11 metabolites with statistical difference (Figure 6A). Four analytes showed consistently low levels in the two batches of *aldh7a1*$^{-/-}$ larvae compared to the two batches of WT larvae (Figure 6B): GABA, 2-aminobutyric acid, taurine, and methionine. The opposite pattern, high levels in mutants compared to WT, was found for seven compounds: P6C, saccharopine (SAC), pipecolate (PIP), tyrosine, β-alanine, serine, and citrulline.

Patients affected with PDE accumulate the toxic ALDH7A1 substrates AASA and P6C (Figure 1), which constitute both the main disease biomarkers and pathogenic drivers. Mutants

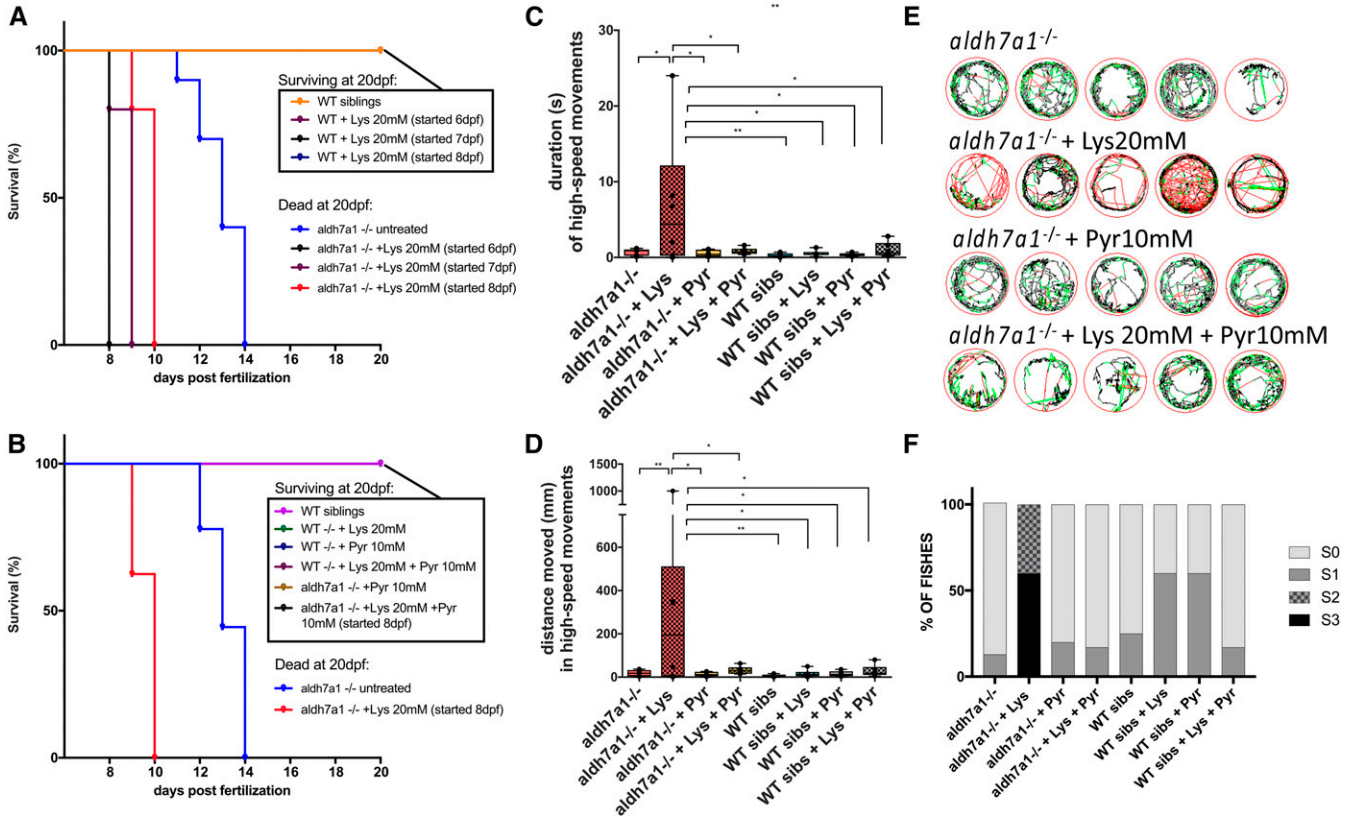

Figure 5 Early seizure onset and death following Lysine (Lys) treatment. Survival of *aldh7a1*$^{-/-}$ and wild-type (WT) siblings after 48 hr of exposure with Lysine 20 mM (A) started at days 6, 7, or 8 days postfertilization (dpf). Survival of *aldh7a1*$^{-/-}$ and WT siblings after 48 hr of treatment with Lys with or without daily Pyridoxine 10 mM (Pyr) treatments (B). Survival experiments were terminated at 20 dpf. Video analysis of 9-dpf larvae after 24 hr of treatment with Lys 20 mM, Pyr 10 mM, or both, showing significant increase in duration (C) and distance moved (D) in high-speed movements after light stimulus. Representative movement traces obtained from the Zebralab software at 9 dpf (24 hr after Lys treatment) showing the presence of larvae with hyperactivity and high-speed movements (red) (E). Blinded analysis of the same videos analyzed in (C–E) showing classification of each fish by seizure scores (S0, S1, S2, and S3), $n = 8$ larvae per group, except for mutant + Lys 20 mM where two fish died during the first 24 hr of treatment (F). Asterisks on top of the graph indicate statistical significance according to one-way ANOVA test [$P = 0.0081$ in (C) and $P = 0.0060$ in (D)] and asterisks comparing each pair of samples reflect Tukey's *post hoc* pairwise tests (* $P < 0.05$ and ** $P < 0.01$). Error bars represent ± SD.

accumulated AASA and P6C in the micromolar range in contrast to healthy heterozygous and WT larvae, in which this compound was undetectable (Figure 2 and Figure 6). Another lysine metabolite found elevated in a number of PDE patients is PIP (Plecko *et al.* 2005; Dalazen *et al.* 2014), possibly formed directly from the excess of P6C via the enzyme piperideine-5-carboxilic reductase (Figure 1) (Struys and Jakobs 2010; Neshich *et al.* 2013; Pena *et al.* 2017). PIP was also found to be elevated in mutant fish compared to controls (Figure 6B). To date, no publications have described the levels of SAC in PDE patients; SAC is the metabolite immediately upstream of AASA and P6C in the lysine degradation pathway. Here, we found 10-fold greater SAC levels (Figure 6B) in mutant larvae compared to controls. Elevated P6C levels could have reduced the catabolic flow via the SAC dehydrogenase domain of the aminoadipic semialdehyde synthase enzyme (Figure 1). It is possible that SAC can be used as a potential novel biomarker for PDE diagnostics and/or monitoring of lysine degradation.

The amino acids shown in Figure 6B and that are not directly involved with the lysine degradation pathway are potentially related to PLP-dependent enzymes for their synthesis or catabolism (Mills *et al.* 2011). Serine, for example, was found to be increased in the plasma of pyridoxamine 5′-phosphate oxidase (PNPO)-deficient patients [another disease leading to B6 deficiency (Mills *et al.* 2014)], and one hypothesis for its increase could be due reduced catabolism via serine dehydratase, a PLP-dependent enzyme (Mills *et al.* 2011). In addition, the diet provided to the zebrafish larvae might play an important role in the amino acid levels and patterns observed. Thus, rotifers (*B. plicatilis*) are rich in most amino acids (Srivastava *et al.* 2006) except for methionine, tryptophan, GABA, and citrulline. The amino acids obtained from their diet could have affected their metabolism through local or systemic B6 deficiency.

The conjugation of the accumulated P6C to PLP has been suggested to lead to the depletion of the latter, causing PLP deficiency (Mills *et al.* 2006). Therefore, we investigated if untreated mutants at 11 dpf would display lower systemic levels of PLP, as well as other vitamin B6 vitamers. We observed no significant changes in the levels of pyridoxine (Pyr),

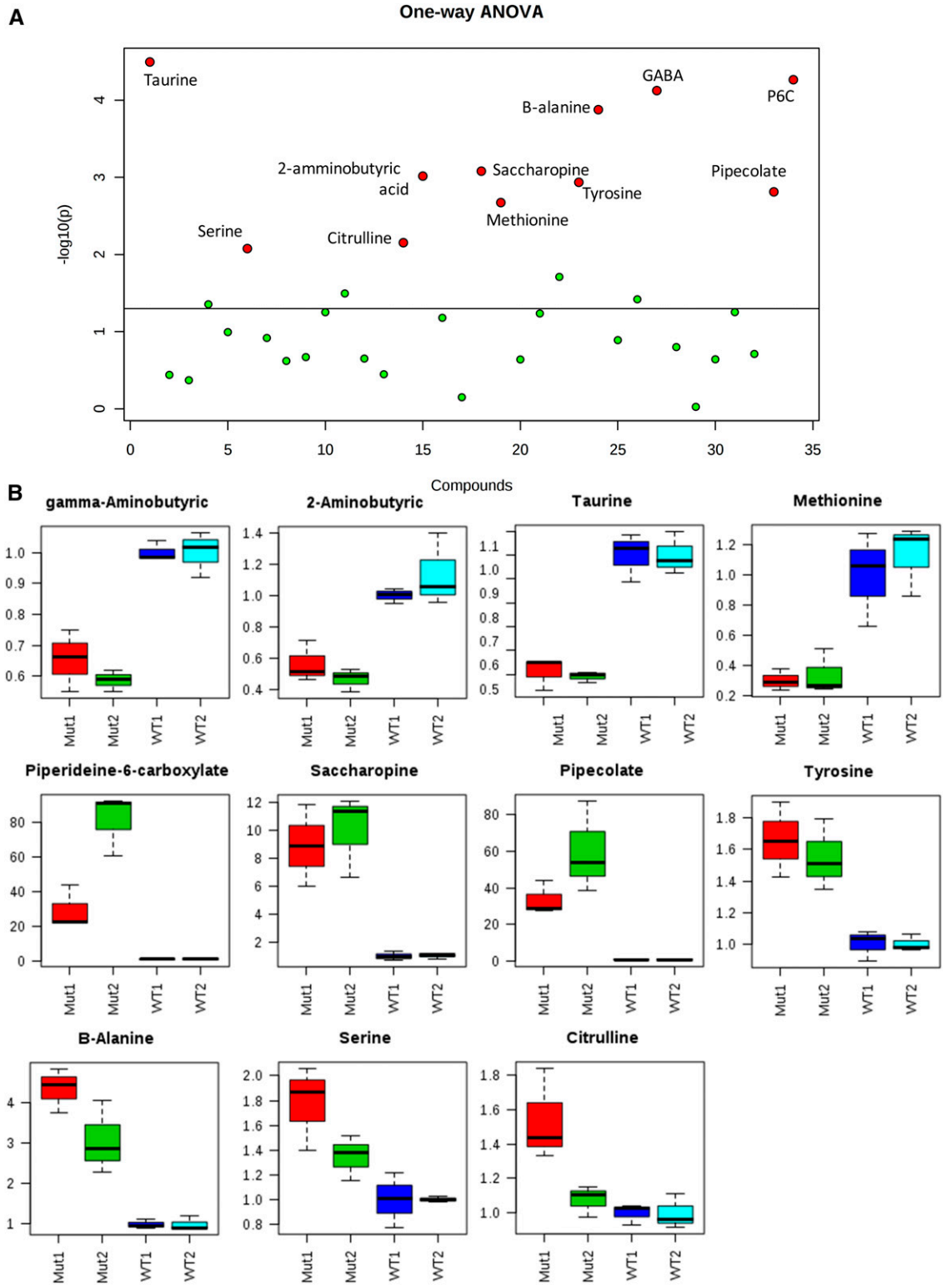

Figure 6 Targeted mass spectrometry allowed the identification of several amino acid perturbations when comparing two different batches of *aldh7a1*-null mutants (Mut1 and Mut2) and their WT siblings (WT1 and WT2). (A) Graphical summary of one-way ANOVA analysis comparing the four groups of samples, using *P*-value cutoff of 0.05. Metabolites identified with statistically significant changes are shown in red and labeled. (B) box and whisker plots summarize the normalized values (mean fold change ± SD) for the metabolites shown in red in (B) significantly different between the two batches of WT and Mut. For this experiment, polar metabolite extracts of three pools (five 11-days postfertilization larvae each) were used for each group. GABA, γ-aminobutyric acid; P6C, piperideine 6-carboxylate; WT, wild-type.

pyridoxamine (PM), 4-pyridoxic acid, and Pyr 5′-phosphate (data not shown), but the null-mutants showed a statistically significant reduction in the levels of pyridoxal (PL, $P = 0.0094$, Figure 7A) and pyridoxamine 5′-phosphate (PMP, $P = 0.0013$, Figure 7B), and a reduction of PLP that almost reached statistical significance ($P = 0.0628$ Figure 7C) based on a Student's *t*-test. P6C is known to react with PLP and we expected to see mainly low PLP levels. Therefore, the large reductions of PMP and PL were unexpected. A possible condensation reaction between P6C or AASA and PMP or PLP has not been previously suggested. It is possible that reduced PL and PMP levels are due to a higher metabolic flux through the enzymes pyridoxal kinase and PNPO to replenish PLP. Since PL and PMP are direct precursors of PLP, transient PLP deficiency or local cerebral deficiency might possibly be occurring, despite its systemic levels appearing to be reduced by only ~30%.

Vitamin B6 deficiency is believed to be the main cause of seizures in PDE, as they are readily alleviated by Pyr treatment. One possible biological interpretation is based on the fact that PLP is the cofactor for glutamate decarboxylase (GAD), the enzyme responsible for synthesis of the central inhibitory neurotransmitter GABA (Figure 7D). Given that a sustained decrease in GABA levels can lead to seizures (Treiman 2001), it may be that a PLP-dependent reduction in the levels of active GAD (GAD^{PLP}) and thus in GABA levels, either locally in the brain or systemically, may underlie this key clinical feature of PDE (Figure 7D). In keeping with this, a previous study using skin fibroblasts isolated from PDE patients has suggested that these cells have impaired GABA synthesis compared to cells from healthy individuals (Gospe *et al.* 1994). We observed a reduction of ~50% of the levels of GABA in the 11-dpf *aldh7a1*-null mutants compared to controls in two different batches, as shown in Figure 6B. Therefore, assessed mutant larvae systemic GABA levels with or without Pyr treatment during the period that seizures are observed (*i.e.*, 11 dpf). As shown in Figure 8A, untreated *aldh7a1*$^{-/-}$ larvae displayed a twofold reduction in systemic GABA levels relative to controls, and these levels were normalized under Pyr treatment.

We also observed that Pyr treatment did not significantly change the lysine degradation metabolite levels (PIP and SAC), but that P6C levels were reduced not normalized (Figure 8, B–D). Lysine levels were not significantly changed (ANOVA, data not shown). We also observed a strong correlation between P6C and lysine (Pearson's $r = 0.8442$, $P < 0.0001$), P6C and SAC ($r = 0.8941$, $P < 0.0001$), and P6C and PIP ($r = 0.874$, $P < 0.0001$) over measurements in two sets of mutant fish (data not shown). These results demonstrate a clear disruption of the lysine metabolic flow in the *aldh7a1*$^{-/-}$ larvae, which is not rescued by Pyr treatment, reflecting what is seen in PDE patients.

We also investigated if there would be fewer GABAergic neurons in the larval brain at 11 dpf, given that such cells would likely be affected by persistent seizures, as previously reported in several models of other types of epilepsy (Tóth *et al.* 2010; Tóth and Maglóczky 2014). We did not observe a significant difference in the number and organization of calretinin-positive cells in the telencephalon, diencephalon, mesencephalon, or rhombencephalon (Figure S12). Other GABA interneuron subpopulations might still be changed and this will be further investigated. It is possible that the strong regenerative capacity of the zebrafish brain may preclude the observation of slight decreases. Additionally, we did not observe a statistically significant difference between mRNA levels of *gad1b* and *gad2* by quantitative PCR when comparing WT and null-mutant larvae at 11 dpf (data not shown). These results may suggest that reduced PLP (or its precursors) leads to reduced GABA synthesis in the *aldh7a1*$^{-/-}$ brain due to lowered GAD activity, rather than reduced GABA synthesis secondary to a loss of GABAergic neurons (here investigating the calretinin-positive population) or low GAD expression.

Discussion

PDE was initially described over 60 years ago (Hunt *et al.* 1954); we now present the first animal model of PDE, a zebrafish null for *aldh7a1*, manifesting dysregulated lysine metabolism with spontaneous seizure activity and premature death in the larval stage. The epileptic phenotype was responsive to Pyr and PLP treatments, which prolonged life span. The mutant fish accumulated the Aldh7a1 substrates AASA and P6C (Figure 1 and Figure 2) (the main PDE biomarkers); in contrast, morpholino-based knockdown of Aldh7a1 resulting in ~13% of normal protein levels did not result in either the accumulation of AASA/P6C (Figure S3) or any discernible larval phenotype. Thus, approximately one-tenth of normal Aldh7a1 activity may catalyze sufficient oxidation of AASA/P6C, preventing their accumulation to the toxic threshold that triggers PDE. In keeping with this observation, measurement of several heterologously-expressed missense-mutated Aldh7a1 proteins (pathogenic variants) in *Escherichia coli* were associated with < 3% of activity (Coulter-Mackie *et al.* 2012). For example, the E399Q mutation, which accounts for > 30% of the published human disease alleles (Plecko *et al.* 2007; Bennett *et al.* 2009; Mills *et al.* 2010), was reported to result in null Aldh7a1 enzymatic activity in overexpression assays using Chinese Hamster Ovary cells (Mills *et al.* 2006). These observations demonstrate the necessity of an *aldh7a1*-null model to study the pathogenesis of this rare condition in both the untreated and treated state.

Untreated *aldh7a1*$^{-/-}$ mutant fish consistently displayed spontaneous seizures with convulsive behavior starting at 10 dpf and early death by 14 dpf. The reason why the seizure onset is consistently at 10 dpf remains unknown but some scenarios can be proposed. The maturation of the blood–brain barrier (BBB) has been demonstrated to occur in zebrafish from 3 to 10 dpf (Fleming *et al.* 2013). It is possible that the trapping of cerebrally-produced AASA and/or P6C (if impermeable to the BBB) after complete BBB maturation at 10 dpf could lead to seizure onset. A second possible scenario

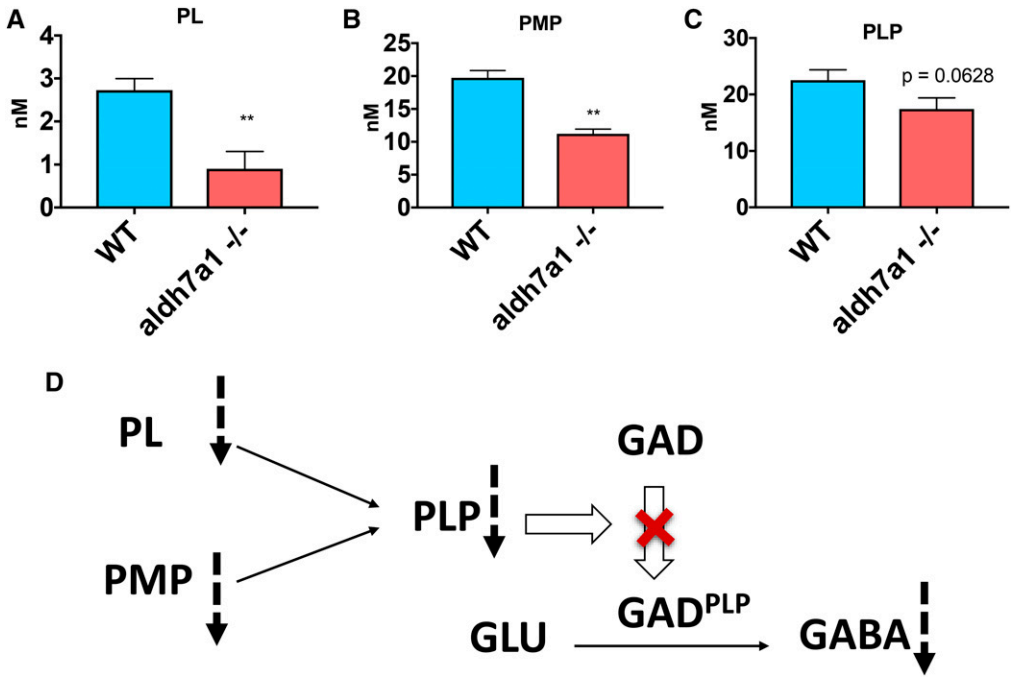

Figure 7 B6 vitamers are changed in *aldh7a1*$^{-/-}$ larvae compared to WT siblings. Lower levels of PL (A), PMP (B), and PLP (C) were observed in the null-mutants compared to WT according to liquid chromatography-mass spectrometry analysis using polar metabolite extracts (three replicates of six larvae pools). Asterisks indicate statistical significance according to Student's *t*-test (* $P < 0.05$ and ** $P < 0.01$). Error bars represent ± SD. Possible mechanism for low GABA levels observed in the mutant larvae correlating with lower B6 vitamer levels (D), with potential reduction in the conversion levels of the inactive apo-form of GAD (and other PLP-dependent enzymes) to their catalytically active holo-form (GAD^{PLP}) by the covalent attachment of PLP. GABA, γ-aminobutyric acid; GAD, glutamate decarboxylase; PL, pyridoxal; PMP, pyridoxamine 5′-phosphate; PLP, pyridoxal 5′-phosphate; WT, wild-type.

could be that certain specific neuronal populations, more prone to seizures, might develop ∼10 dpf. A third scenario could be that excess vitamin B6 that is maternally inherited and deposited in the yolk sac is depleted by PLP–P6C conjugation until 10 dpf. Finally, it may be that the seizure onset ∼10 dpf simply occurs due to the fish obtaining lysine from their diet and thus reaching a threshold of AASA/P6C levels needed for PLP depletion [similar to what is hypothesized to occur in hyperprolinemia Type II (Farrant *et al.* 2001)]. Support for the threshold hypothesis comes from our observation that lysine supplementation accelerates seizure behavior and death (Figure 5). Pyr cotreatment was sufficient to rescue the larvae from seizures and mortality, in keeping with seizures that are indeed triggered by accelerated Pyr deficiency.

In our genetic model, tectal recordings revealed a complex electrographic seizure pattern resembling what is observed in mammalian models and in previously reported zebrafish epilepsy models (Baraban *et al.* 2013; Zhang *et al.* 2015; Grone *et al.* 2016; Sourbron *et al.* 2016). The observed electroencephalogram (EEG) profile in the *aldh7a1*$^{-/-}$ larvae consisted of frequent/brief interictal-like bursts and spontaneous ictal-like events with large-amplitude (minimum threefold higher than interictal-like) and long-duration spikes of electrical activity (hundreds of milliseconds), similar to seizure activity that is induced by the convulsing agent pentylenetetrazol (PTZ) (Baraban *et al.* 2005). Both electrographic spontaneous seizures and the convulsive-like behavior halted with Pyr (Figure 4), and the expression of c-Fos, an indicator of high neuronal activity and a gene highly expressed during seizures (Dragunow and Robertson 1987; Baraban *et al.* 2005; Teng *et al.* 2011), normalized. Withdrawal of Pyr treatment in fish larvae led to convulsive behavior and death within a week; seizure recurrence occurs between 1 and 51 days after withdrawal in PDE patients (Plecko *et al.* 2005; Mills *et al.* 2010; Yang *et al.* 2014). Interestingly, we observed the rapid intensification of larval convulsive behavior by light in untreated fish, and bursts of spikes without associated convulsive behavior could be induced even in treated fish (Figure S10). Photosensitive seizures have been observed in three molecularly-confirmed PDE patients based on clinical history, but photic stimulation via EEG studies has not yet been performed (personal communication, CDMvK). Families have also reported photosensitivity and/or light-triggered seizures in PDE patients (especially after exposure to flashes and intense light) despite Pyr treatment (personal communication with the Pyridoxine Dependent Epilepsy parent support group). In addition, several EEG abnormalities have been reported in PDE patients, which may remain despite B6 treatment (Mikati *et al.* 1991; Naasan *et al.* 2009; Bok *et al.* 2010; Schmitt *et al.* 2010; van Karnebeek and Jaggumantri 2015). More than three-quarters of individuals with PDE have or develop neurodevelopmental disabilities; whether this is a result of persistent subclinical EEG abnormalities, some other toxic effect of the elevated P6C, or some non-lysine-related function of ALDH7A1 remains to be determined. It may be that long-term behavioral and EEG phenotyping of our Pyr-treated mutant fish as they reach adulthood could shed light on this question.

In PDE, it is proposed that the accumulated levels of P6C undergo spontaneous Knoevenagel condensation with PLP, forming an inactive complex (P6C–PLP) that reduces the

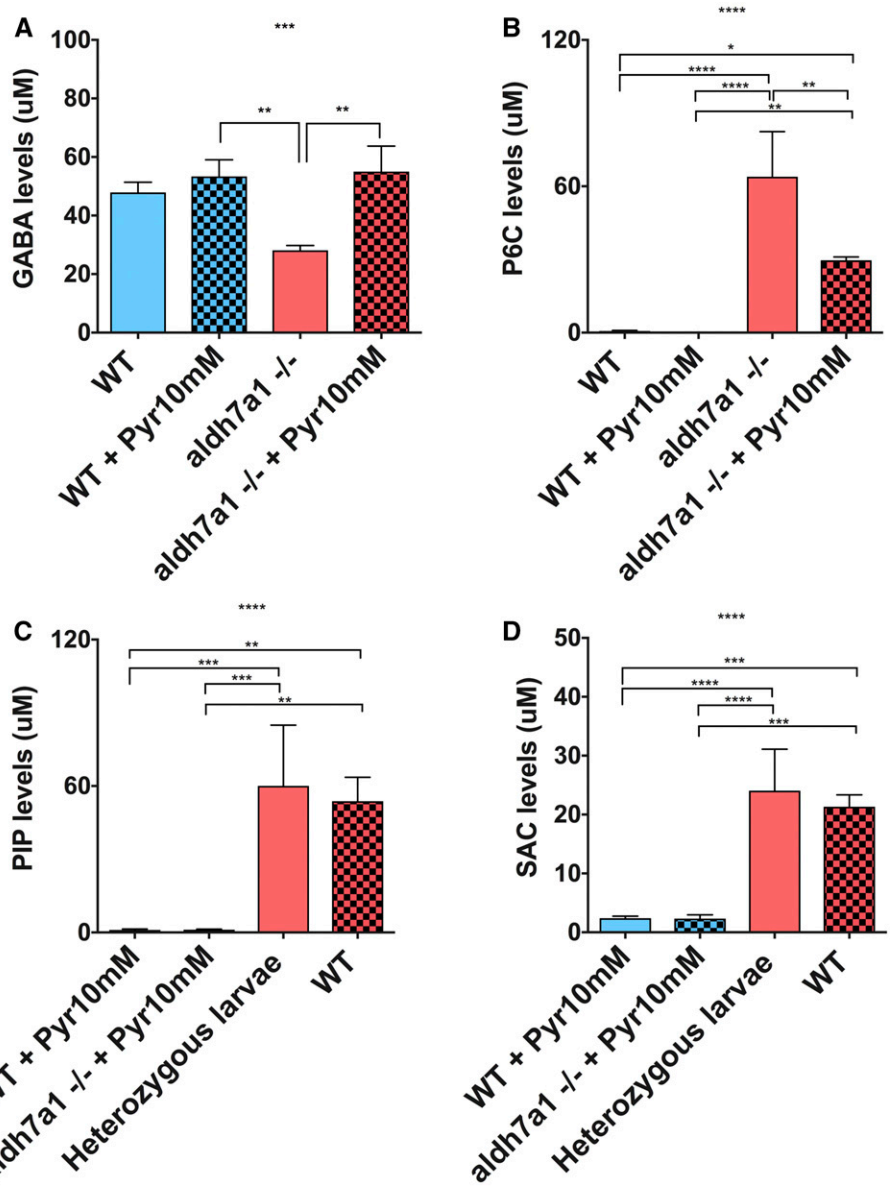

Figure 8 GABA levels are normalized by Pyr treatment but lysine metabolites are mostly unaffected in *aldh7a1*$^{-/-}$ larvae. Mass spectrometry analysis of lysine metabolites in polar metabolite extracts was obtained from three pools of 11-days postfertilization larvae (six individuals each pool) per experimental condition; GABA (A), P6C (B), SAC (C), and PIP (D). Asterisks indicate statistical significance according to one-way ANOVA Tukey's *post hoc* tests (* $P < 0.05$, ** $P < 0.01$, *** $P < 0.001$, **** $P < 0.0001$). Error bars represent ± SD. GABA, γ-aminobutyric acid; P6C, piperideine-6-carboxylate; PIP, pipecolic acid; Pyr, pyridoxine; SAC, saccharopine; WT, wild-type.

available PLP (Mills *et al.* 2006) in the CNS, and possibly systemically. PLP acts as a cofactor for over 140 enzymes, several of which are involved in amino acid and neurotransmitter metabolism (Percudani and Peracchi 2003; Clayton 2006); thus, it is not surprising that the neurodevelopmental and functional impact is significant. A similar impact is seen in children with Pyr-responsive epilepsy secondary to *PNPO* (MIM #610090) deficiency (Mills *et al.* 2005) or proline synthetase cotranscribed homolog (*PROSC*, MIM #617290) gene mutations (Darin *et al.* 2016). In both cases, it is believed that reduced PLP availability underlies the pathogenesis; specifically, due to reduced PLP synthesis in PNPO deficiency (Mills *et al.* 2005), and likely impaired cellular PLP homeostasis for PROSC deficiency (Darin *et al.* 2016). In hyperprolinemia type II (MIM #239510), a similar PLP (and likely other B6 vitamers) condensation with 1-pyrroline-5-carboxylate (structurally related to P6C) is observed, leading to low plasma PLP levels and infantile seizures (Farrant *et al.* 2001). These disorders effectively capture the detrimental effects of functional PLP depletion. Correspondingly, we have observed a series of perturbations in amino acid levels, which might be related to low activity of PLP-dependent enzymes or deficient lysine metabolism (Figure 6).

It has been hypothesized that PLP deficiency leads to seizures secondary to its impact on a particularly important PLP-dependent enzyme, GAD, which is responsible for the biosynthesis of GABA, the main cerebral inhibitory neurotransmitter. Indeed, low GABA production due to PLP deficiency was proposed as the underlying mechanism for Pyr-dependent seizures long before the discovery of the genetic causes of PDE (Kurlemann *et al.* 1992; Gospe *et al.* 1994; Goto *et al.* 2001). However, measurement of GABA and PLP levels in PDE patients have yielded inconsistent results: low CSF/cerebral levels found in two studies (Lott *et al.* 1978;

Mills *et al.* 2011) and normal CSF, plasma, and urine levels reported by others (Goto *et al.* 2001; Footitt *et al.* 2013). One possible limitation in the investigation of PLP and GABA levels in patients is that the ongoing B6 treatment and B6 administration regimen may mask persistent depletions. In addition, PLP and GABA depletion in PDE may be localized to specific brain compartments and intracellular changes may not necessarily be captured using CSF measurements. By studying untreated *aldh7a1*$^{-/-}$ fish, we observed a reduction of B6 vitamers (PLP, PMP, and PL) (Figure 7), and an approximate halving of systemic GABA levels relative to WT siblings (Figure 6 and Figure 8). Furthermore, the unanticipated observation of low PMP and PL levels (~1.8-fold and threefold reduction, respectively) might indicate the novel possibility of AASA and/or P6C reacting with these B6 vitamers leading to their inactivation. Another possibility might be that PL and PMP are being rapidly metabolized by the enzymes pyridoxal kinase and PNPO in the body's homeostatic attempt to replenish PLP and thus have reduced levels. Not surprisingly, several other amino acids also showed significant change, and it is possible that many other metabolic pathways are disturbed in Aldh7a1 deficiency. Ultimately, GABA levels in the mutants normalized remarkably under Pyr treatment (Figure 8)and the seizure phenotype was halted (Figure 4).

There are no other reports of animal models for *aldh7a1*-deficiency or PDE in the literature, but other genetic or pharmacological models displaying Pyr-responsive seizures (PRS) have been described. For example, Ginkotoxin acts as an inhibitor of PLP synthesis and ginkotoxin-phosphate as a competitive inhibitor for PLP (Lee *et al.* 2012). Zebrafish larvae (5–7 dpf) treated with ginkotoxin develop seizure-like behavior that is reversed by PLP and/or GABA treatment, further supporting a role of PLP and GABA deficiency in seizure pathogenesis (Lee *et al.* 2012). The PLP ecto-phosphatase activity of the enzyme TNSALP (tissue-nonspecific alkaline phosphatase, OMIM #171760) is likely related to the PRS observed in *TNSALP* deficiency (Weiss *et al.* 1988). Mice deficient for TNSALP display seizures and early death by 2 weeks of age, with low PLP and GABA levels (50% reduction) detected in the brain as the potential epilepsy-triggering mechanism (Waymire *et al.* 1995). Imbalance in GABA levels could be possibly related to the seizure phenotype in these diseases, in PDE, and in our zebrafish model. It is also possible that other metabolites altered as a consequence of Aldh7a1 deficiency and/or PLP deficiency can also play a role in seizures, and this will be studied in the future. Additional studies investigating levels of other neurotransmitters and other AASA/P6C toxicity effects could also provide alternative and/or complementary explanations for the mechanisms underlying seizure occurrence.

In conclusion, the *aldh7a1*$^{-/-}$ fish constitute a faithful model for PDE and thus represent an important tool for an improved understanding of PDE pathogenesis. Given the Pyr dependency of the animals, there will be opportunities to study the pathogenesis and biochemistry of this disease, not only in larvae but in juvenile and adult stages as well. One unique advantage is the "drug inducibility" of our model, *i.e.*, the ability to withdraw Pyr treatment at any given time and study the dynamics of PDE pathogenesis. Although our analysis strongly suggests that the primary driver of PDE pathogenesis arises from AASA/P6C accumulation due to Aldh7a1 ablation, impairment in other functions of this enzyme [*e.g.*, involvement in oxidative stress (Brocker *et al.* 2011), osmotic stress (Brocker *et al.* 2010), and cell growth/DNA protection (Chan *et al.* 2011)] may also play a role. Our results also give further support to the theory that lysine, in excess, is toxic for PDE patients. Finally, our model can now be used for drug screening and testing of new therapies, to potentially identify drugs that can add to the pyridoxine treatment to further control seizure activity and improve the neurodevelopmental outcomes for these children.

Acknowledgments

The authors would like to thank the patients and families living with pyridoxine-dependent epilepsy who give this work meaning. They also thank Willian Fletcher and Christine Archer for the support with zebrafish care and helpful discussions, Sandra Noble for sharing CRISPR/Cas9 protocols and reagents, and Sarah Schock for critically reviewing this manuscript. The authors thank the Rare Disease Models and Mechanism Network [funded by the Canadian Institutes of Health Research (CIHR) and Genome Canada] and the Care4Rare Canada Consortium (funded by Genome Canada, CIHR, Ontario Genomics, Ontario Research Fund, and the Children's Hospital of Eastern Ontario Foundation) for financially supporting this research. I.A.P. is supported by a CIHR postdoctoral fellowship award.

Literature Cited

Afrikanova, T., A.-S. K. Serruys, O. E. M. Buenafe, R. Clinckers, I. Smolders *et al.*, 2013 Validation of the zebrafish pentylenetetrazol seizure model: locomotor versus electrographic responses to antiepileptic drugs. PLoS One 8: e54166.

Babcock, H. E., S. Dutta, R. P. Alur, C. Brocker, V. Vasiliou *et al.*, 2014 aldh7a1 regulates eye and limb development in zebrafish. PLoS One 9: e101782.

Baraban, S. C., M. R. Taylor, P. A. Castro, and H. Baier, 2005 Pentylenetetrazole induced changes in zebrafish behavior, neural activity and c-fos expression. Neuroscience 131: 759–768.

Baraban, S. C., M. T. Dinday, and G. A. Hortopan, 2013 Drug screening in Scn1a zebrafish mutant identifies clemizole as a potential Dravet syndrome treatment. Nat. Commun. 4: 2410.

Baxter, P., 2001 Pyridoxine-dependent and pyridoxine- responsive seizures. Dev. Med. Child Neurol. 43: 416–420.

Bennett, C. L., Y. Chen, S. Hahn, I. A. Glass, and S. M. J. Gospe, 2009 Prevalence of ALDH7A1 mutations in 18 North American pyridoxine-dependent seizure (PDS) patients. Epilepsia 50: 1167–1175.

Bok, L. A., N. M. Maurits, M. A. Willemsen, C. Jakobs, L. K. Teune *et al.*, 2010 The EEG response to pyridoxine-IV neither identifies nor excludes pyridoxine-dependent epilepsy. Epilepsia 51: 2406–2411.

Brocker, C., N. Lassen, T. Estey, A. Pappa, M. Cantore *et al.*, 2010 Aldehyde dehydrogenase 7A1 (ALDH7A1) is a novel enzyme involved in cellular defense against hyperosmotic stress. J. Biol. Chem. 285: 18452–18463.

Brocker, C., M. Cantore, P. Failli, and V. Vasiliou, 2011 Aldehyde dehydrogenase 7A1 (ALDH7A1) attenuates reactive aldehyde and oxidative stress induced cytotoxicity. Chem. Biol. Interact. 191: 269–277.

Chan, C.-L., J. W. Y. Wong, C.-P. Wong, M. K. L. Chan, and W.-P. Fong, 2011 Human antiquitin: structural and functional studies. Chem. Biol. Interact. 191: 165–170.

Clayton, P. T., 2006 B6-responsive disorders: a model of vitamin dependency. J. Inherit. Metab. Dis. 29: 317–326.

Coughlin, II, C. R., C. D. M. van Karnebeek, W. Al-Hertani, A. Y. Shuen, S. Jaggumantri *et al.*, 2015 Triple therapy with pyridoxine, arginine supplementation and dietary lysine restriction in pyridoxine-dependent epilepsy: neurodevelopmental outcome. Mol. Genet. Metab. 116: 35–43.

Coulter-Mackie, M. B., A. Li, Q. Lian, E. Struys, S. Stockler *et al.*, 2012 Overexpression of human antiquitin in E. coli: enzymatic characterization of twelve ALDH7A1 missense mutations associated with pyridoxine-dependent epilepsy. Mol. Genet. Metab. 106: 478–481.

Dalazen, G. R., M. Terra, C. E. D. Jacques, J. G. Coelho, R. Freitas *et al.*, 2014 Pipecolic acid induces oxidative stress in vitro in cerebral cortex of young rats and the protective role of lipoic acid. Metab. Brain Dis. 29: 175–183.

Darin, N., E. Reid, L. Prunetti, L. Samuelsson, R. A. Husain *et al.*, 2016 Mutations in PROSC disrupt cellular pyridoxal phosphate homeostasis and cause vitamin-B6-dependent epilepsy. Am. J. Hum. Genet. 99: 1325–1337.

Dragunow, M., and H. A. Robertson, 1987 Kindling stimulation induces c-fos protein(s) in granule cells of the rat dentate gyrus. Nature 329: 441–442.

Farrant, R. D., V. Walker, G. A. Mills, J. M. Mellor, and G. J. Langley, 2001 Pyridoxal phosphate de-activation by pyrroline-5-carboxylic acid. Increased risk of vitamin B6 deficiency and seizures in hyperprolinemia type II. J. Biol. Chem. 276: 15107–15116.

Fleming, A., H. Diekmann, and P. Goldsmith, 2013 Functional characterisation of the maturation of the blood-brain barrier in larval zebrafish. PLoS One 8: e77548.

Footitt, E. J., P. T. Clayton, K. Mills, S. J. Heales, V. Neergheen *et al.*, 2013 Measurement of plasma B6 vitamer profiles in children with inborn errors of vitamin B6 metabolism using an LC-MS/MS method. J. Inherit. Metab. Dis. 36: 139–145.

Gospe, S. M., 2017 Pyridoxine-dependent epilepsy. GeneReviews® [Internet]. Available at: https://www.ncbi.nlm.nih.gov/books/NBK1486/. Accessed July, 2017.

Gospe, S. M. J., K. L. Olin, and C. L. Keen, 1994 Reduced GABA synthesis in pyridoxine-dependent seizures. Lancet (London, England) 343: 1133–1134.

Goto, T., N. Matsuo, and T. Takahashi, 2001 CSF glutamate/GABA concentrations in pyridoxine-dependent seizures: etiology of pyridoxine-dependent seizures and the mechanisms of pyridoxine action in seizure control. Brain Dev. 23: 24–29.

Griffin, A., K. R. Hamling, K. Knupp, S. Hong, L. P. Lee *et al.*, 2017 Clemizole and modulators of serotonin signalling suppress seizures in Dravet syndrome. Brain 140: 669–683.

Grone, B. P., M. Marchese, K. R. Hamling, M. G. Kumar, C. S. Krasniak *et al.*, 2016 Epilepsy, behavioral abnormalities, and physiological comorbidities in syntaxin-binding protein 1 (STXBP1) mutant zebrafish. PLoS One 11: e0151148.

Hortopan, G. A., M. T. Dinday, and S. C. Baraban, 2010 Spontaneous seizures and altered gene expression in GABA signaling pathways in a mind bomb mutant zebrafish. J. Neurosci. 30: 13718–13728.

Hunt, A. D. J., J. J. Stokes, W. W. McCrory, and H. H. Stroud, 1954 Pyridoxine dependency: report of a case of intractable convulsions in an infant controlled by pyridoxine. Pediatrics 13: 140–145.

Hwang, W. Y., Y. Fu, D. Reyon, M. L. Maeder, S. Q. Tsai *et al.*, 2013 Efficient genome editing in zebrafish using a CRISPR-Cas system. Nat. Biotechnol. 31: 227–229.

Kiessling, M., and P. Gass, 1993 Immediate early gene expression in experimental epilepsy. Brain Pathol. 3: 381–393.

Kiyota, E., I. A. Pena, and P. Arruda, 2015 The saccharopine pathway in seed development and stress response of maize. Plant Cell Environ. 38: 2450–2461.

Kurlemann, G., R. Ziegler, M. Gruneberg, T. Bomelburg, K. Ullrich *et al.*, 1992 Disturbance of GABA metabolism in pyridoxine-dependent seizures. Neuropediatrics 23: 257–259.

Lee, G.-H., S.-Y. Sung, W.-N. Chang, T.-T. Kao, H.-C. Du *et al.*, 2012 Zebrafish larvae exposed to ginkgotoxin exhibit seizure-like behavior that is relieved by pyridoxal-5′-phosphate, GABA and anti-epileptic drugs. Dis. Model. Mech. 5: 785–795.

Lee, P., W. Kuhl, T. Gelbart, T. Kamimura, C. West *et al.*, 1994 Homology between a human protein and a protein of the green garden pea. Genomics 21: 371–378.

Lott, I. T., T. Coulombe, R. V. Di Paolo, E. P. J. Richardson, and H. L. Levy, 1978 Vitamin B6-dependent seizures: pathology and chemical findings in brain. Neurology 28: 47–54.

Mercimek-Mahmutoglu, S., D. Cordeiro, V. Cruz, K. Hyland, E. A. Struys *et al.*, 2014 Novel therapy for pyridoxine dependent epilepsy due to ALDH7A1 genetic defect: L-arginine supplementation alternative to lysine-restricted diet. Eur. J. Paediatr. Neurol. 18: 741–746.

Mikati, M. A., E. Trevathan, K. S. Krishnamoorthy, and C. T. Lombroso, 1991 Pyridoxine-dependent epilepsy: EEG investigations and long-term follow-up. Electroencephalogr. Clin. Neurophysiol. 78: 215–221.

Mills, P., E. Footitt, and P. T. Clayton, 2011 Vitamin B6 metabolism and inborn errors. *The Online Metabolic and Molecular Bases of Inherited Disease*. Available at: http://ommbid.mhmedical.com/content.aspx?bookid=971&sectionid=62646411. Accessed July, 2017.

Mills, P. B., R. A. H. Surtees, M. P. Champion, C. E. Beesley, N. Dalton *et al.*, 2005 Neonatal epileptic encephalopathy caused by mutations in the PNPO gene encoding pyridox(am)ine 5′-phosphate oxidase. Hum. Mol. Genet. 14: 1077–1086.

Mills, P. B., E. Struys, C. Jakobs, B. Plecko, P. Baxter *et al.*, 2006 Mutations in antiquitin in individuals with pyridoxine-dependent seizures. Nat. Med. 12: 307–309.

Mills, P. B., E. J. Footitt, K. A. Mills, K. Tuschl, S. Aylett *et al.*, 2010 Genotypic and phenotypic spectrum of pyridoxine-dependent epilepsy (ALDH7A1 deficiency). Brain 133: 2148–2159.

Mills, P. B., S. S. M. Camuzeaux, E. J. Footitt, K. A. Mills, P. Gissen *et al.*, 2014 Epilepsy due to PNPO mutations: genotype, environment and treatment affect presentation and outcome. Brain 137: 1350–1360.

Naasan, G., M. Yabroudi, A. Rahi, and M. A. Mikati, 2009 Electroencephalographic changes in pyridoxine-dependent epilepsy: new observations. Epileptic Disord. 11: 293–300.

Neshich, I. A. P., E. Kiyota, and P. Arruda, 2013 Genome-wide analysis of lysine catabolism in bacteria reveals new connections with osmotic stress resistance. ISME J. 7: 2400–2410.

Pena, I. A., A. MacKenzie, and C. D. M. Van Karnebeek, 2016 Current knowledge for pyridoxine-dependent epilepsy: a 2016 update. Expert Rev. Endocrinol. Metab. 12: 1–16.

Pena, I. A., L. A. Marques, A. B. A. Laranjeira, J. A. Yunes, M. N. Eberlin *et al.*, 2017 Mouse lysine catabolism to aminoadipate occurs primarily through the saccharopine pathway; implications for pyridoxine dependent epilepsy (PDE). Biochim. Biophys. Acta 1863: 121–128.

Percudani, R., and A. Peracchi, 2003 A genomic overview of pyridoxal-phosphate-dependent enzymes. EMBO Rep. 4: 850–854.

Plecko, B., C. Hikel, G. Korenke, B. Schmitt, M. Baumgartner *et al.*, 2005 Pipecolic acid as a diagnostic marker of pyridoxine-dependent epilepsy. Neuropediatrics 36: 200–205.

Plecko, B., K. Paul, E. Paschke, S. Stoeckler-Ipsiroglu, E. Struys *et al.*, 2007 Biochemical and molecular characterization of 18 patients with pyridoxine-dependent epilepsy and mutations of the antiquitin (ALDH7A1) gene. Hum. Mutat. 28: 19–26.

Sander, J. D., M. L. Maeder, D. Reyon, D. F. Voytas, J. K. Joung *et al.*, 2010 ZiFiT (Zinc Finger Targeter): an updated zinc finger engineering tool. Nucleic Acids Res. 38: W462–W468.

Schmitt, B., M. Baumgartner, P. B. Mills, P. T. Clayton, C. Jakobs *et al.*, 2010 Seizures and paroxysmal events: symptoms pointing to the diagnosis of pyridoxine-dependent epilepsy and pyridoxine phosphate oxidase deficiency. Dev. Med. Child Neurol. 52: e133–e142.

Sourbron, J., H. Schneider, A. Kecskes, Y. Liu, E. M. Buening *et al.*, 2016 Serotonergic modulation as effective treatment for Dravet syndrome in a zebrafish mutant model. ACS Chem. Neurosci. 7: 588–598.

Srivastava, A., K. Hamre, J. Stoss, R. Chakrabarti, and S. K. Tonheim, 2006 Protein content and amino acid composition of the live feed rotifer (Brachionus plicatilis): with emphasis on the water soluble fraction. Aquaculture 254: 534–543.

Stockler, S., B. Plecko, S. M. Gospe, M. Coulter-Mackie, M. Connolly *et al.*, 2011 Pyridoxine dependent epilepsy and antiquitin deficiency. Clinical and molecular characteristics and recommendations for diagnosis, treatment and follow-up. Mol. Genet. Metab. 104: 48–60.

Struys, E. A., and C. Jakobs, 2010 Metabolism of lysine in alpha-aminoadipic semialdehyde dehydrogenase-deficient fibroblasts: evidence for an alternative pathway of pipecolic acid formation. FEBS Lett. 584: 181–186.

Struys, E. A., L. A. Bok, D. Emal, S. Houterman, M. A. Willemsen *et al.*, 2012a The measurement of urinary Δ^1-piperideine-6-carboxylate, the alter ego of α-aminoadipic semialdehyde, in Antiquitin deficiency. J. Inherit. Metab. Dis. 35: 909–916.

Struys, E. A., B. Nota, A. Bakkali, S. Al Shahwan, G. S. Salomons *et al.*, 2012b Pyridoxine-dependent epilepsy with elevated urinary α-amino adipic semialdehyde in molybdenum cofactor deficiency. Pediatrics 130: e1716–e1719.

Teng, Y., X. Xie, S. Walker, G. Rempala, D. J. Kozlowski *et al.*, 2010 Knockdown of zebrafish Lgi1a results in abnormal development, brain defects and a seizure-like behavioral phenotype. Hum. Mol. Genet. 19: 4409–4420.

Teng, Y., X. Xie, S. Walker, M. Saxena, D. J. Kozlowski *et al.*, 2011 Loss of zebrafish lgi1b leads to hydrocephalus and sensitization to pentylenetetrazol induced seizure-like behavior. PLoS One 6: e24596.

Tóth, K., and Z. Maglóczky, 2014 The vulnerability of calretinin-containing hippocampal interneurons to temporal lobe epilepsy. Front. Neuroanat. 8: 1–12.

Tóth, K., L. Eross, J. Vajda, P. Halász, T. F. Freund *et al.*, 2010 Loss and reorganization of calretinin-containing interneurons in the epileptic human hippocampus. 133: 2763–2777.

Treiman, D. M., 2001 GABAergic mechanisms in epilepsy. Epilepsia 42: 8–12.

van der Ham, M., M. Albersen, T. J. de Koning, G. Visser, A. Middendorp *et al.*, 2012 Quantification of vitamin B6 vitamers in human cerebrospinal fluid by ultra performance liquid chromatography-tandem mass spectrometry. Anal. Chim. Acta 712: 108–114.

van Karnebeek, C. D. M., and S. Jaggumantri, 2015 Current treatment and management of pyridoxine-dependent epilepsy. Curr. Treat. Options Neurol. 17: 335.

van Karnebeek, C. D. M., H. Hartmann, S. Jaggumantri, L. A. Bok, B. Cheng *et al.*, 2012 Lysine restricted diet for pyridoxine-dependent epilepsy: first evidence and future trials. Mol. Genet. Metab. 107: 335–344.

van Karnebeek, C. D. M., S. A. Tiebout, J. Niermeijer, B. T. Poll-The, A. Ghani *et al.*, 2016 Pyridoxine-dependent epilepsy: an expanding clinical spectrum. Pediatr. Neurol. 59: 6–12.

Waterval, W. A. H., J. L. J. M. Scheijen, M. M. J. C. Ortmans-Ploemen, C. D. Habets-van der Poel, and J. Bierau, 2009 Quantitative UPLC-MS/MS analysis of underivatised amino acids in body fluids is a reliable tool for the diagnosis and follow-up of patients with inborn errors of metabolism. Clin. Chim. Acta 407: 36–42.

Waymire, K. G., J. D. Mahuren, J. M. Jaje, T. R. Guilarte, S. P. Coburn *et al.*, 1995 Mice lacking tissue non-specific alkaline phosphatase die from seizures due to defective metabolism of vitamin B-6. Nat. Genet. 11: 45–51.

Weiss, M. J., D. E. Cole, K. Ray, M. P. Whyte, M. A. Lafferty *et al.*, 1988 A missense mutation in the human liver/bone/kidney alkaline phosphatase gene causing a lethal form of hypophosphatasia. Proc. Natl. Acad. Sci. USA 85: 7666–7669.

Westerfield, M., 2000 *The Zebrafish Book. A guide for the Laboratory use of Zebrafish (Danio Rerio)*. University of Oregon Press, Eugene, OR.

Wilkinson, R. N., S. Elworthy, P. W. Ingham, and F. J. M. van Eeden, 2013 A method for high-throughput PCR-based genotyping of larval zebrafish tail biopsies. Biotechniques 55: 314–316.

Xia, J., and D. S. Wishart, 2002 Using MetaboAnalyst 3.0 for comprehensive metabolomics data analysis. *Curr. Protoc. Bioinformatics* 55: 14.10.1–14.10.91.

Xia, J., I. V. Sinelnikov, B. Han, and D. S. Wishart, 2015 MetaboAnalyst 3.0—making metabolomics more meaningful. Nucleic Acids Res. 43: W251–W257.

Yang, Z., X. Yang, Y. Wu, J. Wang, Y. Zhang *et al.*, 2014 Clinical diagnosis, treatment, and ALDH7A1 mutations in pyridoxine-dependent epilepsy in three Chinese infants. PLoS One 9: e92803.

Zhang, Y., A. Kecskés, D. Copmans, M. Langlois, A. D. Crawford *et al.*, 2015 Pharmacological characterization of an antisense knockdown zebrafish model of Dravet syndrome: inhibition of epileptic seizures by the serotonin agonist fenfluramine. PLoS One 10: e0125898.

Zhu, X., Y. Xu, S. Yu, L. Lu, M. Ding *et al.*, 2014 An efficient genotyping method for genome-modified animals and human cells generated with CRISPR/Cas9 system. Sci. Rep. 4: 6420.

Communicating editor: D. Greenstein

OXFORD UNIVERSITY PRESS | Brain

PLPHP deficiency: Clinical, genetic, biochemical, and mechanistic insights

Journal:	*Brain*
Manuscript ID	BRAIN-2018-00921
Manuscript Type:	Original Article
Date Submitted by the Author:	22-May-2018
Complete List of Authors:	Johnstone, Devon ; Children's Hospital of Eastern Ontario Research Institute; University of Ottawa, Biology Al-Shekaili, Hilal; University of British Columbia Department of Medical Genetics; BC Children's Hospital, Research Institute Tarailo-Graovac, Maja; University of British Colombia, Department of Medical Genetics; British Columbia Children's Hospital Research Institute; The University of Belgrade, Institute of Physiology and Biochemistry, Faculty of Biology; University of Calgary, Departments of Biochemistry, Molecular Biology, and Medical Genetics, Cumming School of Medicine Wolf, Nicole; VU University Medical Centre, Child Neurology Ivy, Autumn; Stanford University School of Medicine, Division of Child Neurology, Department of Neurology and Neurological Sciences Roussel, Yann; University of Ottawa, Biology Kernohan, Kristen; Children's Hospital of Eastern Ontario Research Institute van Roermund, Carlo; AMC, Department of Pediatrics and Clinical Chemistry, Laboratory Division, Laboratory Genetic Metabolic Diseases Kosuta, Ceres; Children's Hospital of Eastern Ontario Research Institute; University of Ottawa, Biology Ban, Kevin; Children's Hospital of Eastern Ontario Research Institute; University of Ottawa, Biology Al-Thihli, Khalid; Sultan Qaboos University Hospital, Genetic and Developmental Medicine Clinic Abdelrahim, Rana; Sultan Qaboos University Hospital, Department of Child Health Koul, Roshan; Sultan Qaboos University Hospital, Paediatric Neurology Unit, Child Health Department AlFutaisi, Amna; sultan qaboos university hospital, childhealth Haaxma, Charlotte; Radboud University Medical Center, Department of Neurology and Amalia Children's Hospital Olson, Heather; Boston Children's Hospital, Neurology Demarest, Scott; University of Colorado Denver School of Medicine, Departments of Pediatrics and Neurology Sigurdardottir, Laufey; Nemours Children's Clinic, Department of Neurology Arnold, Georgianne; Nemours Children's Clinic, Department of Genetics Gerkes, Erica; Universitair Medisch Centrum Groningen Thoraxcentrum, Department of Genetics Boon, M; Universitair Medisch Centrum Groningen Thoraxcentrum,

	Department of Genetics Heiner-Fokkema, M.; University of Groningen, University Medical Center Groningen, Department of Laboratory Medicine Noble, Sandra; University of Ottawa, Biology Bosma, Marjolein; University Medical Center Utrecht, Department of Genetics Ciapaite, Jolita; University Medical Center Utrecht, Department of Genetics Jans, Judith ; University Medical Center Utrecht, Department of Genetics Koolen, David; Radboud University Medical Center, Department of Human Genetics, Radboud Institute for Molecular Life Sciences and Donders Institute for Brain, Cognition and Behaviour Kamsteeg, Erik-Jan; Genome Diagnostics Nijmegen Drögemöller, Britt; British Columbia Children's Hospital Research Institute; University of British Columbia, Faculty of Pharmaceutical Sciences Ross, Colin; British Columbia Children's Hospital Research Institute; University of British Columbia, Faculty of Pharmaceutical Sciences Majewski, Jacek; McGill University and Genome Quebec Innovation Centre; McGill University, Department of Human Genetics Cho, Megan; GeneDx, Begtrup, Amber; GeneDx Wasserman, Wyeth; British Columbia Children's Hospital Research Institute Bui, Tuan; University of Ottawa, Biology Brimble, Elise; Stanford University School of Medicine, Department of Neurology and Neurological Sciences Houten, Sander; Icahn School of Medicine at Mount Sinai Department of Genetics and Genomic Sciences Violante, Sara; Icahn School of Medicine at Mount Sinai Department of Genetics and Genomic Sciences Wevers, Ron; Radboudumc, Laboratory of Genetic, Endocrine and Metabolic Diseases (LGEM), Department of Laboratory Medicine van Faassen, Martijn; University of Groningen, University Medical Center Groningen, Department of Laboratory Medicine Kema, Ido; University of Groningen, University Medical Center Groningen, Department of Laboratory Medicine Lepage, Nathalie; Children's Hospital of Eastern Ontario Research Institute Consortium, Care4Rare ; Children's Hospital of Eastern Ontario Research Institute Lines, Matthew; University of Ottawa Faculty of Medicine, Pediatrics Dyment, David; Children's Hospital of Eastern Ontario Research Institute Wanders, Ronald; AMC, Department of Pediatrics and Clinical Chemistry, Laboratory Division, Laboratory Genetic Metabolic Diseases Verhoeven-Duif, Nanda; University Medical Center (UMC) Utrecht, Department of Genetics Ekker, Marc; University of Ottawa, Biology Boycott, Kym; CHEO Research Institute, Friedman, Jan; University of British Columbia Department of Medical Genetics; British Columbia Children's Hospital Research Institute Pena, Izabella; Children's Hospital of Eastern Ontario Research Institute; University of Ottawa, Biology; Whitehead Institute for Biomedical Research van Karnebeek, Clara; AMC, Department of Pediatrics and Clinical Genetics; BC Children's Hospital, Research Institute; University of British Colombia, Department of Pediatrics
Subject category:	Genetics
To search keyword list, use whole or part words followed by an *:	Epilepsy: experimental models < EPILEPSY AND SLEEP, Genetics: epilepsy < GENETICS, Metabolic disease < GENETICS, Whole-exome sequencing < GENETICS, Epilepsy: other < EPILEPSY AND SLEEP

PLPHP deficiency: Clinical, genetic, biochemical, and mechanistic insights

Devon L. Johnstone,[1,2*] Hilal H. Al-Shekaili,[3,4]* Maja Tarailo-Graovac,[3,4,5,6] Nicole I. Wolf,[7] Autumn S. Ivy,[8] Yann Roussel,[2] Kristin D. Kernohan,[1] Carlo W.T. van Roermund,[9] Ceres Kosuta,[1,2] Kevin Ban,[1,2] Khalid Al-Thihli,[10] Rana A. Abdelrahim,[11] Roshan L. Koul,[12] Amna Al Futaisi,[12] Charlotte A. Haaxma,[13] Heather Olson,[14] Scott Demarest,[15] Laufey Yr. Sigurdardottir,[16] Georgianne L. Arnold,[17] Erica H. Gerkes,[18] M. Boon,[18] M. Rebecca Heiner-Fokkema,[19] Sandra Noble[2], Marjolein Bosma,[20] Jolita Ciapaite,[20] Judith Jans,[20] David A. Koolen,[21] Erik-Jan Kamsteeg,[22] Britt Drögemöller,[4,23] Colin J. Ross,[4,23] Jacek Majewski,[24,25] Megan T. Cho,[26] Amber Begtrup,[26] Wyeth W. Wasserman,[4] Tuan Bui,[2] Elise Brimble,[27] Sara Violante,[28] Sander M. Houten,[28] Ron Wevers,[29] Martijn van Faassen,[19] Ido P. Kema,[19] Nathalie Lepage,[1] Care4Rare Canada Consortium,[1] Matthew A. Lines,[1,30] David A. Dyment,[1,31] Ronald J.A. Wanders,[9] Nanda Verhoeven-Duif,[20] Marc Ekker,[2] Kym M. Boycott,[1,31] Jan M. Friedman,[3,4] Izabella A. Pena,[1,2**] Clara D.M. van Karnebeek[4,32,33**]

1 Children's Hospital of Eastern Ontario Research Institute, Ottawa, ON, Canada
2 Department of Biology, University of Ottawa, Ottawa, ON, Canada
3 Department of Medical Genetics, University of British Columbia, Vancouver, BC, Canada
4 British Columbia Children's Hospital Research Institute, Vancouver, BC, Canada
5 Institute of Physiology and Biochemistry, Faculty of Biology, The University of Belgrade, Belgrade, Serbia
6 Departments of Biochemistry, Molecular Biology, and Medical Genetics, Cumming School of Medicine, Alberta Children's Hospital Research Institute, University of Calgary, Calgary, AB, Canada
7 Department of Child Neurology, VU University Medical Center, and Amsterdam Neuroscience, Amsterdam, The Netherlands
8 Division of Child Neurology, Department of Neurology and Neurological Sciences, Stanford University School of Medicine, Stanford, CA, USA
9 Department of Pediatrics and Clinical Chemistry, Laboratory Division, Laboratory Genetic Metabolic Diseases, Academic Medical Center, Amsterdam, The Netherlands
10 Genetic and Developmental Medicine Clinic, Sultan Qaboos University Hospital, Muscat, Oman

11 Department of Child Health, Sultan Qaboos University Hospital, Muscat, Oman

12 Paediatric Neurology Unit, Child Health Department, Sultan Qaboos University Hospital, Muscat, Oman

13 Department of Neurology and Amalia Children's Hospital, Radboud University Medical Center, Nijmegen, The Netherlands

14 Department of Neurology, Division of Epilepsy and Clinical Neurophysiology, Boston Children's Hospital, Boston, MA, USA

15 Departments of Pediatrics and Neurology, University of Colorado School of Medicine, Children's Hospital Colorado, Aurora, CO, USA

16 Department of Neurology, University of Central Florida, Nemours Children's Hospital, Orlando, FL, USA

17 Department of Genetics, Nemours Children's Hospital, University of Pittsburgh Medical Center, Orlando, FL, USA

18 Department of Genetics, University Medical Centre Groningen, Groningen, The Netherlands

19 Department of Laboratory Medicine, University Medical Centre Groningen, The Netherlands

20 Department of Genetics, Center for Molecular Medicine, University Medical Center, Utrecht, The Netherlands

21 Department of Human Genetics, Radboud Institute for Molecular Life Sciences and Donders Institute for Brain, Cognition and Behaviour, Radboud University Medical Center, Nijmegen, The Netherlands

22 Genome Diagnostics Nijmegen, Nijmegen, The Netherlands

23 Faculty of Pharmaceutical Sciences, University of British Columbia, Vancouver, BC, Canada

24 McGill University and Genome Quebec Innovation Centre, Montreal, QC, Canada

25 Department of Human Genetics, McGill University, Montreal, QC, Canada

26 GeneDx Inc., Gaithersburg, MD, USA

27 Department of Neurology and Neurological Sciences, Stanford University School of Medicine, Stanford, CA, USA

28 Department of Genetics and Genomic Sciences and Icahn Institute for Genomics and Multiscale Biology, Icahn School of Medicine at Mount Sinai, New York, NY, USA

29 Translational Metabolic Laboratory, Department Laboratory Medicine, Radboud University Medical Center, Nijmegen, The Netherlands

30 Division of Metabolics and Newborn Screening, Children's Hospital of Eastern Ontario, Ottawa, ON, Canada

31 Department of Medical Genetics, Children's Hospital of Eastern Ontario, Ottawa, ON, Canada

32 Departments of Pediatrics and Clinical Genetics, Academic Medical Centre, Amsterdam, The Netherlands

33 Centre for Molecular Medicine and Therapeutics, Department of Pediatrics, University of British Columbia, Vancouver, Canada

Full postal and email address of the corresponding authors:
**CDMvK: Room H7-224, Meibergdreef 9, 1105 AZ Amsterdam, The Netherlands, c.d.vankarnebeek@amc.nl
**IAP: Children's Hospital of Eastern Ontario Research Institute, Ottawa, ON, K1H 8L1, Canada, ipena2@uottawa.ca
* these authors contributed equally as first authors
**these authors contributed equally as senior authors

Running title:

Insights into PLPHP deficiency

Abstract

Biallelic mutations in *PLPBP* (formerly *PROSC*) have recently been shown to cause a novel form of vitamin B6-dependent epilepsy, the pathophysiological basis of which is poorly understood. When left untreated, the disease can progress to status epilepticus and death in infancy. Here we present 12 previously undescribed patients and seven novel mutations in *PLPBP*. Provisional diagnoses prior to identification of *PLPBP* pathogenic variants included mitochondrial encephalopathy (two patients), folinic acid-responsive epilepsy (one patient) and a movement disorder compatible with AADC deficiency (one patient). The encoded protein, PLPHB is believed to be crucial for B6 homeostasis. We modelled the pathogenicity of the mutations and developed a clinical severity scoring system. The most severe phenotypes were

associated with mutations leading to loss of function of *PLPBP* or significantly affecting protein stability/PLP-binding. To further explore the pathophysiology of this disease, we developed the first zebrafish model of PLPHP deficiency using CRISPR/Cas9. Our model recapitulates the disease, with *plpbp*$^{-/-}$ larvae showing behavioral, biochemical, and electrophysiological signs of seizure activity by 10 days post-fertilization and early death by 16 days post-fertilization. Treatment with pyridoxine significantly improved the epileptic phenotype and extended lifespan in *plpbp*$^{-/-}$ animals. Larvae had disruptions in amino acid metabolism as well as GABA and catecholamine biosynthesis, indicating impairment of PLP-dependent enzymatic activities. Using mass spectrometry, we observed significant B6 vitamer level changes in *plpbp*$^{-/-}$ zebrafish, patient fibroblasts and PLPHP deficient HEK293 cells. Additional studies in HEK293 cells and yeast provide the first empirical evidence that PLPHP is localized in mitochondria and may play a role in mitochondrial metabolism. These models provide new insights into disease mechanisms and can serve as a platform for drug discovery.

Keywords:

PLPBP, *PROSC*, epilepsy, pyridoxine, vitamin B6-responsive epilepsy.

Abbreviations:

3MT = 3-methoxytyramine; 5-HIAA = 5-hydroxyindoleacetic acid; 5-HTP = 5-hydroxytrytpophan; AADC = Aromatic l-amino acid decarboxylase; ADR = adrenaline; AED = anti-epileptic drug; B6RD = (Vitamin) B6-responsive disorder; DOPE = discrete optimized protein energy; dpf = days post-fertilization; HMA-PAGE = heteroduplex melting assay polyacrylamide gel electrophoresis; LOF = loss of function; MR = magnetic resonance; NAD = nicotinamide adenine dinucleotide; PA = 4-pyridoxic acid; PL = pyridoxal; PLP = pyridoxal 5'-phosphate; *PLPBP* = PLP binding protein; PLPHP = PLP homeostasis protein; PM = pyridoxamine; PMP = pyridoxamine 5'-phosphate; PN = pyridoxine; PNP = pyridoxine 5'-phosphate; PTZ = pentylenetetrazol; TIM = typical triosephosphate isomerase; WT = wild type.

Introduction

The vitamin B6-responsive disorders (B6RDs) are a clinically and genetically heterogeneous group of rare, autosomal recessive conditions (Clayton, 2006) with the hallmark feature of seizures uniquely responsive to treatment by the B6 vitamers pyridoxine (PN) and/or pyridoxal-5'-phosphate (PLP) (Baumgartner-Sigl *et al.*, 2007; Basura *et al.*, 2009). PLP is a cofactor for over 140 enzymes, including some involved in glucose, lipid and amino acid metabolism (John, 1995; Percudani and Peracchi, 2003; Eliot and Kirsch, 2004), and for the synthesis of neurotransmitters, making it an essential vitamer for normal brain function (Surtees *et al.*, 2006).

The B6RDs are characterized by recurrent seizures in the prenatal, neonatal, or postnatal period and are resistant to anti-epileptic medication (Walker *et al.*, 2000; Mills *et al.*, 2005; Mills *et al.*, 2006; Baumgartner-Sigl *et al.*, 2007). Intellectual disability, behavioral abnormalities, psychiatric disturbances, as well as abnormalities in brain structure and myelination are frequently observed (Stockler *et al.*, 2011), and if untreated, B6RDs may lead to status epilepticus and death (Gospe, 2017). B6RDs have been attributed to a number of gene mutations disrupting B6 metabolism, including those leading to the accumulation of toxic metabolites that inactivate PLP (*ALDH7A1* (MIM#266100), *ALDH4A1,* (MIM#239510)), those interfering with the interconversion of B6 vitamers (*PNPO* (MIM#610090), *TNSALP* (MIM#171760) (Hamosh *et al.*, 2005; Mills *et al.*, 2005; Clayton, 2006; Mills *et al.*, 2006; Stockler *et al.*, 2011) and with PLP homeostasis ((*PLPBP* (encoding PLP homeostasis protein, PLPHP), MIM#604436, previously named "*PROSC"*) (Darin *et al.*, 2016; Plecko *et al.*, 2017).

In bacteria (YggS) and yeast (YBL036C), the PLPHP orthologous structures show PLP covalently bound to a lysine residue, phosphate-binding motifs and a typical triosephosphate isomerase (TIM)-barrel domain (Eswaramoorthy *et al.*, 2003; Ito *et al.*, 2013). The purified human PLPHP is also bound to PLP in the native state but still, little is known about the molecular function of this protein (Tremino *et al.*, 2018). Studies in YggS-deficient *Escherichia coli* revealed growth impairment and disrupted amino and keto acid homeostasis (Ito *et al.*, 2013; Prunetti *et al.*, 2016). In cyanobacteria, it has been suggested that the C-terminal helix may play a role in PLP exchange with apoenzymes (Tremino *et al.*, 2017). B6 vitamer levels were

significantly altered in human PLPHP loss-of-function (LOF), and it has been hypothesized this protein has a key role in B6 homeostasis (Darin *et al.*, 2016; Prunetti *et al.*, 2016), possibly acting as a PLP-carrier that prevents PLP from reacting with other molecules, supplying it to dependent enzymes and/or protecting from phosphatases.

PLPHP deficiency in humans is manifested by early-onset intractable seizures responsive to PN and/or PLP, developmental delay, and structural brain abnormalities, most notably simplified gyral pattern and cyst-like structures adjacent to the anterior horns (Darin *et al.*, 2016). The genotypic and phenotypic spectra of this disease are not yet fully delineated, and the mechanisms through which seizures and other symptoms manifest are not known. We undertook a comprehensive genetic and biochemical study of PLPHP deficiency in a cohort of 12 previously undescribed patients. To better characterize the pathophysiology of this neurometabolic disease, we generated knockout models in zebrafish (*Danio rerio*), yeast (*Saccharomyces cerevisiae*) and HEK293 cells which provided insights on the biochemical consequences of PLPHP deficiency.

Materials and methods

Patients

This study was approved by the clinical research ethics board of BC Children's and Women's Hospital, University of British Columbia (H12-00067), the Children's Hospital of Eastern Ontario Research Ethics Board, and local institutional review boards at the University of Colorado. Many of the patients were recruited through international collaboration as part of an ongoing TIDEX neurometabolic gene discovery project (Tarailo-Graovac *et al.*, 2016). After obtaining signed informed parental consent, referring clinicians provided detailed reports of clinical, MRI and EEG features of study patients.

Whole-exome sequencing, Sanger sequencing and *in silico* analysis

Detailed descriptions of whole-exome sequencing, bio-informatic analyses, Sanger sequencing and *in silico* analysis strategies are provided in the Supplementary Material. All exomes were aligned to the human reference genome, February 2009 assembly (GRCh37/hg19).

Structural model of human PLPHP

The 3D model of PLPHP protein (NP_009129.1) was obtained by homology modelling using MODELLER (Webb and Sali, 2014) and the yeast ortholog (YBL036C, PDB 1CT5, (Eswaramoorthy *et al.*, 2003), 41% identical, 57% similar) as template. DOPE (discrete optimized protein energy) score was used to select the best model for subsequent refinement using Coot (v0.8.6.1, (Emsley *et al.*, 2010)). Prosa-Web (Wiederstein and Sippl, 2007) and Coot's Ramachandran plot analysis module were used to validate model quality. PyMOL (Schrodinger, 2015) was used for structural superimposition of the human PLPHP model with yeast 1CT5, and the coordinates of the PLP co-crystalized with the yeast ortholog were transferred to the PLPHP model, covalently bound to p.Lys47. Images were prepared using PyMOL. Arpeggio was used to calculate contacts (Jubb *et al.*, 2017). DUET (Pires *et al.*, 2014) was used to calculate stability changes.

Clinical severity score

We assessed the clinical severity of patients within this study and previous studies (Darin *et al.*, 2016; Plecko *et al.*, 2017) based on published data. We adapted a scoring system of patients with B6RD due to mutations in *ALDH7A1* (Al Teneiji *et al.*, 2017). The following criteria were used: A) global and/or intellectual delay: 0=normal; 1=mild; 2=moderate; 3=severe; B) age of onset of seizures and/or movement disorder: 0=absent; 1=>1month; 2=≥7 days; 3=<7 days; C) therapeutic response: 0=full response on <200mg B6 (PN and/or PLP) total daily AND normalization of EEG (if available); 1=no clinical seizures or abnormal movements on higher dose, with or without electrographic normalization OR clinical response to lower dose but still with abnormal EEG; 2=no seizures with B6 (any dose) AND other medication, with or without EEG normalization; 3=breakthrough seizures and/or persistent movement disorder, no responsiveness. We calculated the sum of each clinical feature, and classified as mild (1-3), moderate (4-6) or severe (7-9)(Al Teneiji *et al.*, 2017).

PLPHP overexpression in HEK293 cells and sample preparation for immunofluorescence

HEK293 cells were seeded in 6-well plates containing coverslips and transfected with a plasmid encoding Myc-DDK-tagged *PLPBP* (Origene, RC200853, C-terminal) using Lipofectamine following manufacturer specifications (4µg DNA and 15µL Lipofectamine). Cells were fixed in

pre-warmed 2% paraformaldehyde in PBS/0.1% Triton X-100 at 37°C for 20 minutes. After washing with PBS, free aldehyde groups were blocked by incubating for 10 minutes in 0.1 M NH_4Cl in PBS. After washing with PBS, coverslips were blocked for 30 minutes with 1% BSA in PBS. Primary antibodies (mouse anti-DDK monoclonal (Origene, TA50011, 1:1000) and a rabbit polyclonal against human citrate synthase [N2C3] (GeneTex, GTX110624, 1:1000) were diluted in PBS containing 1% BSA and incubated for 45 minutes. Secondary antibodies (FITC-Goat anti-mouse IgG (Origene, TA130014, 1:60) and Texas Red-goat anti-rabbit IgG (H+L) (ThermoFisher, T-2767, 1:1000)) were diluted in PBS containing 1% BSA and incubated for 30 minutes.

Yeast strains and culture conditions

Saccharomyces cerevisiae BY4742 (MATα *his3Δ1 leu2Δ0 lys2Δ0 ura3Δ0*) was used as Wild Type (WT) strain along with the derivative strains: *fox1*::KAN, carrying a deletion of peroxisomal acyl-CoA oxidase and *ybl036C*::KAN mutant (Euroscaft). Yeast strains and transformants containing the expression plasmids p*PROSC1a* and p*PROSC2a* (human *PLPBP*) were selected and grown in minimal medium containing 6.7 g/L yeast nitrogen base without amino acids (YNB-WO), supplemented with 5 g/L glucose and amino acids (20 mg/L), and growth was measured. For the induction of peroxisome and mitochondrial proliferation, cells were shifted to ethanol (YPE) 20g/L, glycerol (YPG) 20g/L, or oleate (YPO) medium containing 5g/L potassium phosphate buffer, pH 6.0, 3g/liter yeast extract, 5g/L peptone. YPO media were supplemented with 1.2 g/L oleate, and 2g/L Tween-80. Prior to shifting to these media, the cells were grown in minimal medium with 5 g/L glucose for at least 24h.

Generation of mutant zebrafish lines

Zebrafish were maintained following standard protocols (Westerfield, 1993), and experiments were in accordance with the animal care guidelines of the Canadian Council on Animal Care and the University of Ottawa animal care committee (protocol BL-2678) and the ARRIVE guidelines (Kilkenny *et al.*, 2012). Handling, treatments, husbandry and nursery were performed as outlined

previously (Pena *et al.*, 2017). CRISPR/Cas9 was used to induce targeted indel mutations in the *plpbp* gene of zebrafish embryos as previously described (Hwang *et al.*, 2013), using ZiFit targeter (Sander *et al.*, 2010) to select CRISPR targets and design oligonucleotides (5' TAGGTGGAGCGGGTGAATCAAG 3' and 5' AAACCTTGATTCACCCGCTCCA 3') in the first exon. The target was chosen as having the fewest predicted off-targets (minimum three mismatches with any predicted off-target sequence). Generation of the sgRNA and CRISPR/Cas9 injection, as well as screening for mutants by PCR/HMA-PAGE, were performed as previously described (Zhu *et al.*, 2014; Pena *et al.*, 2017). Genotyping PCR was performed as described in (Kosuta *et al.*, in press) and in Supplementary Material. F0 larvae were raised to adulthood and backcrossed with WT to generate heterozygous F1 fish. These were again backcrossed with WT to minimize off-targets. Experimental animals were obtained by crossing F2 heterozygotes.

Behavioral phenotyping

Sixteen 11 days post-fertilization (dpf) larvae per group were dispensed (one per well) in 48-well flat-bottomed culture dishes (Corning) containing 500µL of system water. Behavior was monitored as previously described (Pena *et al.*, 2017) using a ZebraBox system (ViewPoint Behavior Technology). Videos were also analyzed blindly by two observers to classify seizure scores using the S0-S3 system (Baraban *et al.*, 2005).

Electrophysiology and *c-fos* expression

Electrophysiological local field potential recordings of activity in the optic tectum of five 11dpf larvae per group selected randomly were obtained as previously described (Pena *et al.*, 2017). Since *c-fos* expression can be used as a biomarker for increased neuronal activity and is known to increase with seizure activity (Baraban *et al.*, 2005), we measured *c-fos* mRNA expression in pools of five 11dpf larvae (mutants and WT) as well as in WT larvae treated with 15mM pentylenetetrazol (PTZ) as a positive control. RNA was extracted, reverse transcribed and quantified by qPCR as previously described (Pena *et al.*, 2017). Primers used were: *cfos*-F 5' AACTGTCACGGCGATCTCTT 3' and *cfos*-R 5' TCTTCTGGAGAAAGCTGTTC 3' with β-*actin* as internal control: *actin*-F 5' CATCCATCGTTCACAGGAAGTG 3' and *actin*-R 5' TGGTCGTTCGTTTGAATCTCAT 3').

Metabolite extraction and mass spectrometry

For analysis of B6 vitamers, three pools of six 10 dpf larvae (*plpbp*$^{-/-}$, WT) were analyzed as previously described (Pena *et al.*, 2017). Measurement of amino acid panels was performed using three pools of five larvae per group (*plpbp*$^{-/-}$, WT, heterozygotes) following established protocols (van der Ham *et al.*, 2012; Pena *et al.*, 2017), with the modification that 10 dpf larvae were fasted for 24 hours prior to collection with metabolite extraction at 11 dpf. Neurotransmitter analytes (5 pools of *plpbp*$^{-/-}$ and 4 pools of WT; 6 larvae per pool) were measured following established methods (van Vliet *et al.*, 2015).

Statistical analysis

All statistical analyses and graphing were performed using GraphPad Prism. Where appropriate, one-way ANOVA with Tukey's test, or Krustal-Wallis with Dunn's *post hoc* test was performed. Student's t-test was used for pairwise comparisons.

Data availability

Sequences, plasmids, cell and zebrafish lines are available upon request. All data necessary for confirming the conclusions are represented fully within the article.

Results

Phenotypic spectrum of patients with biallelic *PLPBP* mutations

The 12 patients reported here presented with encephalopathic phenotypes comprising neonatal-onset of refractory epilepsy (or a movement disorder in one case), with or without additional clinical features (Table 1, Supplementary Material). Of the 12 patients described in our cohort, 10 showed responsiveness and improvement of seizures or abnormal movements upon institution of vitamin B6. This cohort comprised six male and six female patients from six different ethnic backgrounds. For patients 1 and 6, the pregnancy history was notable for excessive fetal movements, possibly indicating seizures *in utero*. Three patients experienced respiratory insufficiency after birth, of which patient 3 had the most significant progressive respiratory failure. Epileptic seizures started within the first week of life in all affected infants except patient

7, who instead presented with infantile spasm-like episodes and a movement disorder at two months of age. Tonic-clonic seizures were the most frequent seizure type, and initial EEG showed various patterns of abnormal electrographic activity with burst suppression being most common (7/11 reported). Seizures were refractory to anti-convulsive treatment in all patients (Table 1, Supplementary Material). Vitamin B6 therapy was first trialed as PN in eight patients, PLP in one patient and a combination of both vitamers in another patient (Table 1). The incomplete response to PN or PLP in patient 1 prompted the clinicians to add folinic acid to his treatment, which produced a marked reduction in seizure frequency (only two brief episodes in a three-month period), and gain of milestones. In patient 3, PLP was initially started but failed to exert sufficient seizure control, and adjuvant AED treatment was necessary. A similar picture was seen for patient 11 on PN and adjuvant AED.

Patients 1 (Fig. 1), 6, 7, 8 and 9 had normal brain MR imaging studies (with the exception of mild T2-hyperintense white matter signal in the neonatal period for patient 1) (Supplementary Table 1). The remainder (6/11 in which brain imaging was done) had structural brain abnormalities (Fig. 1, Supplementary Table 1). Four patients (3, 4, 5 and 12) had simplified gyral pattern, suggesting prenatal onset of the disease and possible effect of PLPHP-deficiency on neuronal migration. In addition, these patients displayed large cysts adjacent to the anterior horns. In two patients, a lactate doublet was present in single voxel MR spectroscopy of the basal ganglia.

Clinical presentations deviating from previous descriptions of this disease were also reported. Patient 7, in addition to suspected infantile-spasms, showed a prominent movement disorder and biochemical picture resembling aromatic l-amino acid decarboxylase (AADC) deficiency (MIM#608643), with no suspicious variants in *DDC*. Patients 4 and 5 presented with signs and symptoms suggestive of severe mitochondrial disease with fatal epileptic encephalopathy, lactic acidosis and brain white matter lesions. Both patients deteriorated rapidly and died at two and eight weeks of age, respectively, due to uncontrolled seizures and respiratory failure. In neither case was the presentation deemed typical of pyridoxine-dependent epilepsy, nor were B6 vitamers administered.

Genotypic spectrum, variant effect prediction and clinical severity

Eight disease-causing variants in *PLPBP* were identified in our patient cohort, mostly novel missense variants (Fig. 2, Supplementary Table 2). The exceptions are a novel homozygous frameshift deletion (c.370_373del) leading to a premature stop codon in two patients (5, 12) and the splice site mutation (c.320-2A>G) previously reported by Darin *et al.* (Supplementary Table 2). To investigate potential genotype-phenotype correlations, we developed a clinical severity score to classify patients into three categories: mild, moderate and severe (Table 2). This score reflects the broad spectrum of clinical severity observed, ranging from B6-responsive epilepsy with normal developmental outcome, to perinatal lethality with lactic acidosis and structural brain malformations (e.g. patients 4 and 5). All truncating variants leading to complete LOF of PLPHP (c.207+1G>A, c.320-2A>G; p.Ser78Ter, p.Gln71Ter and p.Asp124Lysfs*2) are associated with the most severe forms of the disease (Table 2). In our cohort, this is evidenced in patients 5 (deceased) and 12, both affected by biallelic exon 5 frameshift (p.Asp124Lysfs*2) leading to absence of protein expression in patient fibroblasts (Supplementary Fig. 1).

To study the pathogenic effect of the missense mutations in our cohort on PLPHP function (here based on PLP-binding, folding or stability), we modeled the tridimensional structure of the human PLPHP protein (Fig. 2B-D). The model indicates that PLPHP folds in a typical (β/α)8-TIM barrel structure, with PLP covalently bound to Lys47 (Schiff base). As with several TIM barrel fold members, a structurally conserved "phosphate binding motif" exists; this is formed by the end of β-strands and loops, especially at the C-terminal (Nagano *et al.*, 2002). PLP interacts with R241, M225, S226, I242, G243, S244, V45, N68, I94 and M181 (Fig. 2C-D). Combining the novel and previously described variants (Darin *et al.*, 2016; Plecko *et al.*, 2017), 12 missense PLPHP mutations were reported so far in B6RD patients (Fig. 2A); seven in homozygosity (Table 2). Patients 3, 6, 10 and 11 from our cohort were classified as severe, with either p.Glu67Lys or p.Thr116Ile homozygous mutations identified. Both substitutions were computationally predicted as damaging (Table 2, Supplementary Table 2). Residues 67 and 116 are conserved (Supplementary Fig. 5) and adjacently located to the predicted PLP-binding site (Fig. 2B-D); mutations to Lys and Ile, respectively, likely lead to disruption of PLP-binding properties (Supplementary Table 2). Patients 4 and 2 were also classified as severe; patient 4 is compound heterozygous for the splice variant leading to LOF (c.320-2A>G) and the substitution of the invariant Gly224 (Supplementary Fig. 5) to Ala (Supplementary Table 2). Gly224Ala mutation likely impacts loop 15 structure and orientation of key PLP-binding residues, especially

364 due to alanine's reduced degree of freedom (φ and ψ angles). The last severe case, patient 1, is
365 compound heterozygous for p.Thr116Ile (discussed above) and p.His275Asp; the importance of
366 the C-terminal residues for ligand binding, stability and activity of proteins that fold as a TIM
367 barrel is well known (Wierenga, 2001; Dias-Lopes *et al.*, 2013), therefore it is expected that a
368 drastic chemical change (e.g. replacing a basic by a negatively charged amino acid at the C-
369 terminal) may negatively impact these functions.

370 Of the four mild cases reported here, three patients (2, 8 and 9) are homozygous for p.Arg41Gln.
371 Normal intellectual development, average-excellent school performance, seizures that are well
372 controlled with relatively low doses of pyridoxine, and normal brain structure on MRI were
373 reported. Arg41 is not an invariant residue (Supplementary Fig. 5) and is located in the distal
374 face of the TIM-Barrel structure, not directly involved in PLP-binding. The p.Pro40Leu mutant
375 (adjacent residue) seen in a previously reported mild case (Plecko *et al.*, 2017) still binds PLP
376 but has reduced stability (Tremino *et al.*, 2018); it is possible that Arg41Gln has similar impact.
377 Patient 7 was also classified as mild and is homozygous for a p.Ile94Phe mutation. This
378 substitution is predicted as damaging, destabilizing and likely inducing misplacement of PLP due
379 to the large size of Phe compared to Ile (Supplementary Table 2, Table 2). Although Phe has not
380 been observed at that position among known orthologues (Suppl. Fig 5), that p.Ile94Phe results
381 in a milder phenotype suggests that hydrophobic and aromatic residue can still be accommodated
382 within the PLP binding site.
383

384 **Biochemical, respiratory chain and vitamer profiles of PLPHP deficiency patients**
385 **and cells**

386 Biochemical investigations performed in patients prior to B6 treatment uncovered several
387 abnormal profiles. The most consistently observed alterations were hyperlactatemia (6 patients)
388 and hyperglycinemia (3 patients). Cultured skin fibroblasts from patient 5 showed an elevated
389 lactate-to-pyruvate ratio (41.65±7.13 SD; reference 9.57-26.49), which is consistent with NADH
390 accumulation. Activities of mitochondrial pyruvate dehydrogenase and respiratory complexes II-
391 IV were normal, as were mitochondrial morphology and inner membrane potential. Extracellular
392 flux testing showed an apparent reduction of carbonyl cyanide-*4*-
393 (trifluoromethoxy)phenylhydrazone (FCCP)-stimulated spare respiratory capacity.

Urine organic acids investigation in patient 7 revealed the presence of vanillactic acid, vanillpyruvic acid, and n-acetyl-vanilalanine, similar to what is seen in AADC deficiency. Minor elevations of urine lactic, malic, 2-ketoglutaric, and n-acetylaspartic acids were also observed. Pre-treatment CSF metabolomics analysis showed elevated 3-methoxytyrosine with normal 3-methoxytyramine levels.

B6 vitamer analysis in plasma from patient 4 (no B6 treatment), revealed low levels of PLP (1.1nM, reference >20.5nM) and elevation of 4-pyridoxic acid (PA) (130 nM, reference <84 nM). In a plasma sample from patient 3, collected during treatment with vitamin B6, accumulations of PLP (685 nM), PA (365 nM) and pyridoxal (PL) (276 nM) were observed (Supplementary Table 3). Analysis of B6 vitamers from patient 5 fibroblast lysates revealed significant decreases in PLP ($p<0.0001$), pyridoxamine 5'-phosphate (PMP) ($p=0.007$) and PN ($p=0.0018$), along with accumulation of pyridoxine 5'-phosphate (PNP) ($p<0.0001$) (ANOVA) in the patient cells compared to the controls, whereas PL, pyridoxamine (PM) and PA showed no difference (Supplementary Fig. 2). Similarly, in PLPHP-deficient HEK293 cells, PLP was significantly decreased ($p<0.0001$) and PNP ($p<0.0001$) accumulated significantly (Supplementary Fig. 3).

PLPHP mitochondrial localization and effects on energy metabolism

To further provide insights on PLPHP function, we investigated its subcellular localization in human cells. Some evidence suggests that PLPHP resides primarily in the cytoplasm (Ikegawa *et al.*, 1999; Uhlen *et al.*, 2015) (Human Protein Atlas available from www.proteinatlas.org). The MitoCarta 2.0 database however suggests a mitochondrial localization for human and mouse PLPHP (Pagliarini *et al.*, 2008; Calvo *et al.*, 2016). Furthermore, MitoMiner 4.0 rates the protein as "known mitochondrial" (Integrated Mitochondrial Protein Index score 0.991), based on mass-spectrometry evidence (Smith and Robinson, 2016). To test if PLPHP does localize to the mitochondria, we overexpressed *PLPBP* cDNA with a C-terminal Myc-DDK tag in HEK293 cells and performed immunofluorescence using anti-DDK antibody. The anti-DDK antibody labeled PLPHP overexpressing cells in a pattern that co-localizes with the mitochondrial protein citrate synthase (Fig. 3A).

To determine if PLPHP and its orthologs could play a role in energy metabolism, we performed growth experiments in yeast. Importantly, growth of YBL036CΔ yeast cells was completely normal on glucose medium but markedly reduced under conditions in which either glycerol, oleate, or ethanol was used as a carbon source (Fig. 3B-D). Since oxidation of the latter three substrates is fully dependent on the proper functioning of the mitochondrial citric acid cycle and oxidative phosphorylation system, whereas oxidation of glucose is not, these findings suggest that YBL036C (and likely PLPHP) can affect mitochondrial metabolism. Because PLP is a cofactor for more than 140 distinct enzyme activities (Percudani and Peracchi, 2003) including the glycine cleavage system and aspartate aminotransferase (AST) in the malate-aspartate shuttle, the metabolic pleiotropy of PLPHP deficiency is expected, although the mechanisms through which *PLPBP* mutations produce mitochondrial dysfunction remain to be elucidated in detail.

Loss of Plphp in zebrafish leads to spontaneous seizures and early death

We developed zebrafish lines carrying two different *plpbp* mutant alleles: a 4bp deletion (chr23:34037190-chr23:34037193) (*plpbp*^{ot101}) and the mutation CGG**GTGAATCA**A>CGG**TGG--TGG**A (chr23:34037185-34037192) (*plpbp*^{ot102}), the latter resulting in a 2bp frameshift, in the transcript (NM_001126409) (p.Asp23Trpfs*56) (Fig. 4A). We crossed the F2s from each heterozygous line (*plpbp*$^{+/ot101}$ x *plpbp*$^{+/ot102}$) to generate compound heterozygous *plpbp*$^{ot101/ot102}$ (henceforth referred to as *plpbp*$^{-/-}$). F3 homozygous mutants and/or compound-heterozygous *plpbp*$^{-/-}$ displayed LOF of Plphp as evidenced by Western blot analysis (Fig. 4B). There were no phenotypic differences between homozygous and compound heterozygous mutants (Supplementary Fig. 8), and the latter was used for experiments due to the relative ease of genotyping (Supplementary Material). In the F3 generation, there were no obvious morphological or behavioral differences between genotypes up until ~9 dpf. As early as 10 dpf, *plpbp*$^{-/-}$ larvae showed spontaneous seizure-like behavior, and all mutants died by 16 dpf (Fig. 4C).

Epilepsy in zebrafish can be characterized by episodes of excessive locomotion, sustained rhythmic jerking (clonus), stiffening (tonus) and/or tonic-clonic seizures (Baraban *et al.*, 2005; Hortopan *et al.*, 2010; Teng *et al.*, 2010; Baraban *et al.*, 2013). We measured the amount of high-speed movements as a correlate of hyperactivity and found that untreated *plpbp*$^{-/-}$ larvae spent

significantly more time ($p<0.01$) and moved a greater distance in high-speed movements ($p<0.01$) than WT or heterozygous siblings (Fig. 4D-E). 11dpf *plpbp*$^{-/-}$ larvae displayed increased *c-fos* mRNA expression (a biomarker of neuronal activity (Baraban *et al.*, 2005)) compared to WT larvae, though less than WT treated with 15mM PTZ (Fig. 4F). Finally, tectal field recordings of agar-immobilized 11 dpf larvae showed that mutant larvae (n=5) displayed spontaneous electrical discharges with high amplitude and duration, similar to ictal-like events previously reported in other zebrafish models, whereas WT siblings (n=5) showed only normal activity (Fig. 4G/5G). We conclude that *plpbp*$^{-/-}$ larvae recapitulate a seizure phenotype.

Vitamin B6 responsiveness and dependency in *plpbp*$^{-/-}$ larvae

We tested if seizures in *plpbp*-null zebrafish larvae show beneficial response to PLP and PN. Although we observed a PLP dose-dependent increase in the lifespan, all larvae died by 26 dpf, even at the highest dose (500 μM PLP) (Fig. 5A). Treatment with PN showed a more remarkable effect, with dose-dependent rescue of survival to nearly 100% until juvenile stages using 5 or 10 mM PN (Fig. 5B). Removal of PN daily treatments induced seizures and death within days, indicating B6-dependence, as previously reported for *aldh7a1*$^{-/-}$ larvae (Pena *et al.*, 2017).

In agreement with the B6-dependency and rescue, PN treatment significantly reduced the number of hyperactive movements as measured by the time spent ($p=0.0028$) and distance travelled in high-speed movements ($p<0.0001$) (Fig. 5D-E). Additionally, by classifying larval movements as little movement (S0), increased spontaneous swim bursts (S1), whirlpool-like swimming (S2) or whole-body convulsions with loss of posture (S3) (Baraban *et al.*, 2005) through blinded analysis, we observed that only untreated *plpbp*$^{-/-}$ larvae displayed S2 or S3 swimming behavior (Fig. 5F). Similarly, treatment with 5mM PN resulted in a 5-fold reduction of the number of high-amplitude spikes of electrographic activity in tectal field recordings ($p=0.0458$) (Fig. 5G). We conclude that *plpbp*$^{-/-}$ larvae have B6-responsive and dependent epilepsy.

Biochemical abnormalities in *plpbp*$^{-/-}$ zebrafish

B6 vitamer levels were quantified in untreated 10 dpf larval lysates. The *plpbp*$^{-/-}$ larvae displayed significant reductions in systemic concentrations of PLP and PL (1.4 and 5.5-fold reductions, $p=0.0026$ and $p=0.0003$, respectively) compared to WT siblings, together with non-significant

reductions in PMP and PN levels (Fig. 6A). PNP was not detectable. As PLP was markedly low in *plpbp*$^{-/-}$ larvae, we hypothesized that neurotransmitter and amino acid metabolism would be greatly affected since most transamination/decarboxylation reactions require PLP. Neurotransmitters were also analyzed in fasted 11 dpf larval lysates (Fig. 6B). We note a significant decrease in levels of adrenaline ($p<0.001$), as well as significant accumulations of 3-methoxytyramine (3-MT), normetanephrine and 5-hydroxyindoleacetic acid (5-HIAA) ($p<0.001$).

Analysis of amino acid levels by liquid chromatography-mass spectrometry in fasted larvae revealed 17 analytes significantly different between homozygous mutants and the heterozygous/WT siblings (Fig. 6C). Nine analytes were found reduced in *plpbp*$^{-/-}$ larval extracts: threonine, asparagine, glutamate, glutamine, proline, alanine, α-aminobutyric acid, γ-aminobutyric acid (GABA), and lysine (Tukey's post-hoc comparison: p= 0.0315, <0.0001, 0.0015, <0.0001, 0.0020, <0.0001, 0.0006, <0.0001, and 0.0068, respectively). Eight compounds were significantly elevated in *plpbp*$^{-/-}$ larvae compared to WT: methionine, cystathionine, isoleucine, tyrosine, ß-alanine, phenylalanine, aminoisobutyric acid and tryptophan (p=0.0147, <0.0001, <0.0001, 0.0005, <0.0001, <0.0001, <0.0001, 0.0013). Low GABA levels were also observed in *aldh7a1*$^{-/-}$ zebrafish and could constitute part of the pathophysiologic mechanism for seizure occurrence. We conclude that Plphp deficiency leads to significant disruptions in amino acid and neurotransmitter metabolism and likely other metabolic pathways that are dependent on PLP.

Discussion

Here we report a cohort of 12 patients, seven novel disease-causing variants in *PLPBP,* and experimental models to further elucidate the pathophysiology of this B6RD. We expand the phenotypic spectrum of the disease; one patient required folinic acid in addition to B6 for adequate seizure control, two patients had clinical features resembling a mitochondrial encephalopathy, and another patient presenting an AADC deficiency-phenocopy. (Darin *et al.*, 2016) described increased levels of AADC substrates in another PLPHP-deficient patient, and our zebrafish *plpbp*$^{-/-}$ model accumulated phenylalanine, tryptophan and tyrosine, in keeping with reduced AADC function. It is possible that reduction of AADC function may contribute to

the clinical picture in PLPHP-deficient patients, given it is a PLP-dependent enzyme important in the biosynthesis of serotonin, dopamine, epinephrine and norepinephrine (Brun *et al.*, 2010).

The severe clinical presentation of patients 4 and 5 with respiratory failure, permanent lactic acidosis, NADH accumulation, and periventricular cerebral cysts prompted us to investigate whether PLPHP could have a putative role in mitochondrial energy metabolism. *In silico* prediction tools and previous high-throughput mass spectrometry experiments suggested intracellular localization of PLPHP in the cytosol and mitochondria (Calvo *et al.*, 2016; Smith and Robinson, 2016). Indeed, our experiments suggest mitochondrial localization of PLPHP upon overexpression. Several PLP-dependent enzymes, such as serine hydroxymethyltransferase (Giardina *et al.*, 2015) and the glycine cleavage system (Kikuchi *et al.*, 2008) have mitochondrial localization. We observed that energy metabolism is affected in YBL036C deficient yeast. However, it is not yet clear if this is due to a direct effect or to indirect changes in key energy metabolism substrates. For example, it has recently been shown that mutations in *KYNU*, encoding a PLP-dependent enzyme, lead to deficiencies in the synthesis of NAD (Shi *et al.*, 2017). Tryptophan, the precursor for NAD in this pathway, accumulated in *plpbp*$^{-/-}$ zebrafish larvae, suggesting a block in this pathway; which includes several PLP-dependent enzymes (Rios-Avila *et al.*, 2013). No defects in the respiratory complexes II-IV were detected in fibroblast assays from a PLPHP-deficient patient, suggesting a direct role in this pathway is unlikely. The multitude of enzymatic functions of PLP may explain the complex biochemical array of phenotypes associated with B6RDs, suggestive of a key role of PLPHP in PLP homeostasis.

By adapting a clinical severity score used for another B6RD (Al Teneiji *et al.*, 2017), we observed that the patients with severe phenotypes (scores 7-9) and/or early mortality were usually associated with proven or predicted LOF mutations (Table 2). These included splicing defects, truncating variants as well as missense mutations predicted or experimentally proven (Tremino *et al.*, 2018) to negatively affect PLP binding. A missense mutation associated with a severe disease presentation (Darin *et al.*, 2016), Leu175Pro, was experimentally proven to induce PLPHP LOF due to protein misfolding (Tremino *et al.*, 2018). In contrast, it seems that missense mutations in residues not associated with the PLP-binding site are seen in patients with milder disease presentations (Table 2). When stability and folding are not drastically affected, it is possible that PLPHP is still able to bind PLP, as evidenced experimentally for p.Pro40Leu and

p.Arg205Gln (Tremino *et al.*, 2018). Residual PLP binding and PLPHP function may be associated with milder presentations of the disease. *In silico* molecular dynamics simulations or *in vitro* assessment of PLP binding, PLPHP folding and stability should be performed to further access these scenarios in the missense mutations reported here.

In both lysates derived from patient fibroblasts and PLPHP-deficient HEK293 cells, decreases in intracellular PLP were observed. Intracellular PLP was found to accumulate as reported by Darin *et al.*, thus further work may be necessary to resolve this discrepancy. A significant accumulation of PNP levels were found in PLPHP-deficient cells but our methods were not sensitive for the detection of PNP in plasma, CSF or whole zebrafish larvae. PNP accumulation, therefore, may be of limited use as a biomarker of the disease but it may help further unravel the functional role of PLPHP.

To enable analysis of the untreated biochemical status, improve our understanding of the pathophysiology of this disease and establish a platform for potential drug discovery, we successfully developed a *plpbp*-null zebrafish model. The *plpbp*$^{-/-}$ larvae recapitulated the disease, and seizure activity was detected as early as 10 dpf, with reduced lifespan and 100% mortality by 16 dpf. Treatment with PN fully reversed these phenotypes, and treated *plpbp*$^{-/-}$ larvae often survived to adulthood, but PLP was not very effective, similar to *aldh7a1*$^{-/-}$ larvae (Pena *et al.*, 2017). It is possible that low water solubility, instability, and light sensitivity of PLP play an important role. Larvae showed significant changes in the levels of B6 vitamers, particularly PLP and PL, which lend further support to the hypothesis that PLPHP is important for PLP homeostasis (Darin *et al.*, 2016; Prunetti *et al.*, 2016). By quantifying systemic amino acid levels, our results indicate disruption to the functions of many of the PLP-dependent enzymes. Furthermore, the reduction of GABA may provide a possible explanation for the increased neuronal activity of mutants, as has been previously reported in *aldh7a1*$^{-/-}$ zebrafish (Pena *et al.*, 2017). Another mechanism to consider as part of disease pathophysiology is altered biosynthesis of catecholamines (especially adrenaline), likely due to reduced availability of PLP for AADC activity (Fig. 6D). This is further evidenced in the mutant animals by the accumulation of phenylalanine, tryptophan and tyrosine (precursors to monoamine neurotransmitter synthesis). PLPHP-deficiency patients with AADC deficiency-like symptoms can provide support to this observation. Given that systemic dopamine levels were unchanged, a

reduction of metabolic flux towards AADC is likely taking place rather than a complete inactivation of this enzyme; alternatively, small amounts of dopamine may be formed via tyramine hydroxylation by renal CYP2D6, as suggested by (Wassenberg *et al.*, 2010). Our results illustrate the dynamic and complex nature of PLP binding to dependent enzymes and its turnover in the context of PLPHP deficiency.

In conclusion, we expanded the clinical and biochemical phenotypic spectrum of PLPHP deficiency and provided evidence of genotype-phenotype correlation. Given the broad phenotypic spectrum of B6RDs, PLPHP deficiency should be considered in neonatal/infantile epilepsy and possibly also in patients who present with a movement disorder and/or phenotype suggestive of mitochondrial epileptic encephalopathy. In the latter case, we note that patients with severe forms of this disease may show increased levels of glycine in combination with marked lactic acidosis, a finding not typical of similar presentations such as pyruvate dehydrogenase deficiency (Prasad *et al.*, 2011). When PLPHP deficiency is suspected, B6 therapy should be initiated. A lack of response to PN may not rule out this condition, and PLP should be trialed as well. Obtention of diagnostic samples prior to B6 treatment and screening for vitamer levels is recommended, with low PLP suggestive of this condition. We report the first model organism for PLPHP deficiency, which replicated the human epileptic disorder. Research using the zebrafish *plpbp*$^{-/-}$ has added insight into which PLP-dependent pathways are mostly affected and increased our understanding of systemic B6 vitamer levels. This model may be used to investigate other disease mechanisms and to search for biomarkers that may facilitate diagnosis. Finally, our zebrafish model provides a stepping stone for preclinical treatment trials, which are necessary, given the poor developmental outcomes and incomplete seizure control seen in many patients with this form of B6-dependent epilepsy.

Acknowledgements

We gratefully acknowledge the patients and families living with pyridoxine-dependent epilepsy for participating in this study; they give our work meaning. We also thank the Canadian Rare Disease Models and Mechanism Network for their support, as well as the clinicians and laboratory specialists involved in the management of these families, as well as the following individuals for their contributions: Xiaohua Han for Sanger sequencing; Evelyn Lomba and Dora Pak for research management support; Michelle Higginson for DNA extraction, sample

handling, and technical data; Lauren Muttumacoroe and Bryan Sayson for data management; Skye McBride for Seahorse assays; Dr. Wyatt Yue for critically reviewing the variant interpretation section; Vishal Saxena, Christine Archer and Bill Fletcher for the invaluable help to support the zebrafish protocols.

Funding

Funding support was provided by the B.C. Children's Hospital Foundation as "1st Collaborative Area of Innovation" (www.tidebc.org); Genome British Columbia (grant number SOF-195); BC Clinical Genomics Network (Michael Smith Foundation for Health Research grant #00032); the Canadian Institutes of Health Research (CIHR) (grant #301221); the Rare Diseases Foundation; a catalyst grant from the Canadian Rare Diseases Models and Mechanism Network; the Care4Rare Canada Consortium (funded by Genome Canada, CIHR, Ontario Genomics, Ontario Research Fund, and the CHEO Foundation); and informatics infrastructure supported by Genome British Columbia and Genome Canada (ABC4DE Project). The Zebrabox was funded by a Natural Sciences and Engineering Research Council RTI grant. DJ is supported by a Vanier Canada Graduate Scholarship. IAP is supported by a CIHR postdoctoral fellowship award. KMB's program is supported by a CIHR Foundation grant (# FDN-154279). HHAS is supported by doctoral scholarship from the Ministry of Higher Education, Oman, and Al Awael Overseas Company LLC, Oman. AD and RKO were supported by TUBİTAK from Turkey (grant #111S217). CDMvK is a recipient of the Michael Smith Foundation for Health Foundation Research Scholar Award and a Metakids Foundation salary award.

Supplementary material

Further methods and results as well as detailed clinical descriptions are available in Supplementary Material.

References

634 Al Teneiji A, Bruun TU, Cordeiro D, Patel J, Inbar-Feigenberg M, Weiss S*, et al.* Phenotype,
635 biochemical features, genotype and treatment outcome of pyridoxine-dependent epilepsy. Metab
636 Brain Dis 2017; 32(2): 443-51.

637 Baraban SC, Dinday MT, Hortopan GA. Drug screening in Scn1a zebrafish mutant identifies
638 clemizole as a potential Dravet syndrome treatment. Nat Commun 2013; 4: 2410.

639 Baraban SC, Taylor MR, Castro PA, Baier H. Pentylenetetrazole induced changes in zebrafish
640 behavior, neural activity and *c-fos* expression. Neuroscience 2005; 131(3): 759-68.

641 Basura GJ, Hagland SP, Wiltse AM, Gospe SM. Clinical features and the management of
642 pyridoxine-dependent and pyridoxine-responsive seizures: review of 63 North American cases
643 submitted to a patient registry. Eur J Pediatr 2009; 168(6): 697-704.

644 Baumgartner-Sigl S, Haberlandt E, Mumm S, Scholl-Bürgi S, Sergi C, Ryan L*, et al.* Pyridoxine-
645 responsive seizures as the first symptom of infantile hypophosphatasia caused by two novel
646 missense mutations (c.677T>C, p.M226T; c.1112C>T, p.T371I) of the tissue-nonspecific
647 alkaline phosphatase gene. Bone 2007; 40(6): 1655-61.

648 Brun L, Ngu LH, Keng WT, Ch'ng GS, Choy YS, Hwu WL*, et al.* Clinical and biochemical
649 features of aromatic L-amino acid decarboxylase deficiency. Neurology 2010; 75(1): 64-71.

650 Calvo SE, Clauser KR, Mootha VK. MitoCarta2.0: an updated inventory of mammalian
651 mitochondrial proteins. Nucleic Acids Res 2016; 44(D1): D1251-7.

652 Clayton PT. B6-responsive disorders: A model of vitamin dependency. Journal of Inherited
653 Metabolic Disease 2006; 29(2): 317-26.

654 Darin N, Reid E, Prunetti L, Samuelsson L, Husain RA, Wilson M*, et al.* Mutations in *PROSC*
655 Disrupt Cellular Pyridoxal Phosphate Homeostasis and Cause Vitamin-B6-Dependent Epilepsy.
656 Am J Hum Genet 2016; 99(6): 1325-37.

657 Dias-Lopes C, Neshich IA, Neshich G, Ortega JM, Granier C, Chavez-Olortegui C*, et al.*
658 Identification of new sphingomyelinases D in pathogenic fungi and other pathogenic organisms.
659 PLoS One 2013; 8(11): e79240.

660 Eliot AC, Kirsch JF. Pyridoxal phosphate enzymes: mechanistic, structural, and evolutionary
661 considerations. Annu Rev Biochem 2004; 73: 383-415.

662 Emsley P, Lohkamp B, Scott WG, Cowtan K. Features and development of Coot. Acta
663 Crystallogr D Biol Crystallogr 2010; 66(Pt 4): 486-501.

664 Eswaramoorthy S, Gerchman S, Graziano V, Kycia H, Studier FW, Swaminathan S. Structure of
665 a yeast hypothetical protein selected by a structural genomics approach. Acta Crystallogr D Biol
666 Crystallogr 2003; 59(Pt 1): 127-35.

667 Giardina G, Brunotti P, Fiascarelli A, Cicalini A, Costa MG, Buckle AM*, et al.* How pyridoxal
668 5'-phosphate differentially regulates human cytosolic and mitochondrial serine
669 hydroxymethyltransferase oligomeric state. FEBS J 2015; 282(7): 1225-41.

670 Gospe SJ. Pyridoxine-Dependent Epilepsy. GeneReviews® [Internet] 2017 2017 Apr 13 [cited
671 2017; Available from: https://www.ncbi.nlm.nih.gov/books/NBK1486/

672 Hamosh A, Scott AF, Amberger JS, Bocchini CA, McKusick VA. Online Mendelian Inheritance
673 in Man (OMIM), a knowledgebase of human genes and genetic disorders. Nucleic Acids Res
674 2005; 33(Database issue): D514-7.

675 Hortopan GA, Dinday MT, Baraban SC. Zebrafish as a model for studying genetic aspects of
676 epilepsy. Dis Model Mech 2010; 3(3-4): 144-8.

677 Hwang WY, Fu Y, Reyon D, Maeder ML, Tsai SQ, Sander JD*, et al.* Efficient genome editing in
678 zebrafish using a CRISPR-Cas system. Nat Biotechnol 2013; 31(3): 227-9.

679 Ikegawa S, Isomura M, Koshizuka Y, Nakamura Y. Cloning and characterization of human and
680 mouse PROSC (proline synthetase co-transcribed) genes. J Hum Genet 1999; 44(5): 337-42.

681 Ito T, Iimori J, Takayama S, Moriyama A, Yamauchi A, Hemmi H*, et al.* Conserved pyridoxal
682 protein that regulates Ile and Val metabolism. J Bacteriol 2013; 195(24): 5439-49.

683 John RA. Pyridoxal phosphate-dependent enzymes. Biochim Biophys Acta 1995; 1248(2): 81-
684 96.

685 Jubb HC, Higueruelo AP, Ochoa-Montano B, Pitt WR, Ascher DB, Blundell TL. Arpeggio: a
686 web server for calculating and visualising interatomic interactions in protein structures. J Mol
687 Biol 2017; 429(3): 365-71.

688 Kikuchi G, Motokawa Y, Yoshida T, Hiraga K. Glycine cleavage system: reaction mechanism,
689 physiological significance, and hyperglycinemia. Proc Jpn Acad Ser B Phys Biol Sci 2008;
690 84(7): 246-63.

691 Kilkenny C, Browne WJ, Cuthill IC, Emerson M, Altman DG. Improving bioscience research
692 reporting: the ARRIVE guidelines for reporting animal research. Osteoarthritis Cartilage 2012;
693 20(4): 256-60.

694 Kosuta C, Daniel K, Johnstone DL, Mongeon K, Ban K, LeBlanc S*, et al.* High-throughput DNA
695 extraction and genotyping of 3dpf zebrafish larvae by fin clipping. JoVE, in press.

696 Mills PB, Struys E, Jakobs C, Plecko B, Baxter P, Baumgartner M*, et al.* Mutations in antiquitin
697 in individuals with pyridoxine-dependent seizures. Nat Med 2006; 12(3): 307-9.

698 Mills PB, Surtees RA, Champion MP, Beesley CE, Dalton N, Scambler PJ*, et al.* Neonatal
699 epileptic encephalopathy caused by mutations in the PNPO gene encoding pyridox(am)ine 5'-
700 phosphate oxidase. Hum Mol Genet 2005; 14(8): 1077-86.

701 Nagano N, Orengo CA, Thornton JM. One fold with many functions: the evolutionary
702 relationships between TIM barrel families based on their sequences, structures and functions. J
703 Mol Biol 2002; 321(5): 741-65.

704 Pagliarini DJ, Calvo SE, Chang B, Sheth SA, Vafai SB, Ong SE*, et al.* A mitochondrial protein
705 compendium elucidates complex I disease biology. Cell 2008; 134(1): 112-23.

706 Pena IA, Roussel Y, Daniel K, Mongeon K, Johnstone D, Mendes HW*, et al.* Pyridoxine-
707 Dependent Epilepsy in Zebrafish Caused by Aldh7a1 Deficiency. Genetics 2017; 207(4): 1501-
708 18.

709 Percudani R, Peracchi A. A genomic overview of pyridoxal-phosphate-dependent enzymes.
710 EMBO Rep 2003; 4(9): 850-4.

711 Pires DE, Ascher DB, Blundell TL. DUET: a server for predicting effects of mutations on
712 protein stability using an integrated computational approach. Nucleic Acids Res 2014; 42(Web
713 Server issue): W314-9.

714 Plecko B, Zweier M, Begemann A, Mathis D, Schmitt B, Striano P*, et al.* Confirmation of
715 mutations in *PROSC* as a novel cause of vitamin B 6 -dependent epilepsy. J Medical Genet 2017;
716 54(12): 809-14.

717 Prasad C, Rupar T, Prasad AN. Pyruvate dehydrogenase deficiency and epilepsy. Brain Dev
718 2011; 33(10): 856-65.

719 Prunetti L, El Yacoubi B, Schiavon CR, Kirkpatrick E, Huang L, Bailly M*, et al.* Evidence That
720 COG0325 Proteins are involved in PLP Homeostasis. Microbiology 2016; 162: 694-706.

721 Rios-Avila L, Nijhout HF, Reed MC, Sitren HS, Gregory JF, 3rd. A mathematical model of
722 tryptophan metabolism via the kynurenine pathway provides insights into the effects of vitamin
723 B-6 deficiency, tryptophan loading, and induction of tryptophan 2,3-dioxygenase on tryptophan
724 metabolites. J Nutr 2013; 143(9): 1509-19.

725 Sander JD, Maeder ML, Reyon D, Voytas DF, Joung JK, Dobbs D. ZiFiT (Zinc Finger
726 Targeter): an updated zinc finger engineering tool. Nucleic Acids Res 2010; 38(Web Server
727 issue): W462-8.

728 Schrodinger, LLC. The PyMOL Molecular Graphics System, Version 1.8. 2015.

729 Shi H, Enriquez A, Rapadas M, Martin E, Wang R, Moreau J*, et al.* NAD Deficiency, Congenital
730 Malformations, and Niacin Supplementation. N Engl J Med 2017; 377(6): 544-52.

731 Smith AC, Robinson AJ. MitoMiner v3.1, an update on the mitochondrial proteomics database.
732 Nucleic Acids Res 2016; 44(D1): D1258-61.

733 Stockler S, Plecko B, Gospe SM, Jr., Coulter-Mackie M, Connolly M, van Karnebeek C*, et al.*
734 Pyridoxine dependent epilepsy and antiquitin deficiency: clinical and molecular characteristics
735 and recommendations for diagnosis, treatment and follow-up. Mol Genet Metab 2011; 104(1-2):
736 48-60.

737 Surtees R, Mills P, Clayton P. Inborn errors affecting vitamin B6 metabolism. Future Neurology
738 Future Neurology 2006; 1(5): 615-20.

739 Tarailo-Graovac M, Shyr C, Ross CJ, Horvath GA, Salvarinova R, Ye XC, *et al.* Exome
740 Sequencing and the Management of Neurometabolic Disorders. N Engl J Med 2016; 374(23):
741 2246-55.

742 Teng Y, Xie X, Walker S, Rempala G, Kozlowski DJ, Mumm JS, *et al.* Knockdown of zebrafish
743 Lgi1a results in abnormal development, brain defects and a seizure-like behavioral phenotype.
744 Hum Mol Genet 2010; 19(22): 4409-20.

745 Tremino L, Forcada-Nadal A, Contreras A, Rubio V. Studies on cyanobacterial protein PipY
746 shed light on structure, potential functions, and vitamin B6 -dependent epilepsy. FEBS Lett
747 2017; 591(20): 3431-42.

748 Tremino L, Forcada-Nadal A, Rubio V. Insight into vitamin B6 -dependent epilepsy due to
749 PLPBP (previously PROSC) missense mutations. Hum Mutat 2018.

750 Uhlen M, Fagerberg L, Hallstrom BM, Lindskog C, Oksvold P, Mardinoglu A, *et al.* Proteomics.
751 Tissue-based map of the human proteome. Science (New York, NY) 2015; 347(6220): 1260419.

752 van der Ham M, Albersen M, de Koning TJ, Visser G, Middendorp A, Bosma M, *et al.*
753 Quantification of vitamin B6 vitamers in human cerebrospinal fluid by ultra performance liquid
754 chromatography-tandem mass spectrometry. Anal Chim Acta 2012; 712: 108-14.

755 van Vliet D, Bruinenberg VM, Mazzola PN, van Faassen MH, de Blaauw P, Kema IP, *et al.*
756 Large Neutral Amino Acid Supplementation Exerts Its Effect through Three Synergistic
757 Mechanisms: Proof of Principle in Phenylketonuria Mice. PLoS One 2015; 10(12): e0143833.

758 Walker V, Mills GA, Peters SA, Merton WL. Fits, pyridoxine, and hyperprolinaemia type II.
759 Arch Dis Child 2000; 82(3): 236-7.

760 Wassenberg T, Willemsen MA, Geurtz PB, Lammens M, Verrijp K, Wilmer M, *et al.* Urinary
761 dopamine in aromatic L-amino acid decarboxylase deficiency: the unsolved paradox. Mol Genet
762 Metab 2010; 101(4): 349-56.

763 Webb B, Sali A. Comparative Protein Structure Modeling Using MODELLER. Curr Protoc
764 Bioinformatics 2014; 47: 5 6 1-32.

765 Westerfield M. The zebrafish book : a guide for the laboratory use of zebrafish (Brachydanio
766 rerio). Eugene, OR: M. Westerfield; 1993.

767 Wiederstein M, Sippl MJ. ProSA-web: interactive web service for the recognition of errors in
768 three-dimensional structures of proteins. Nucleic Acids Res 2007; 35(Web Server issue): W407-
769 10.

770 Wierenga RK. The TIM-barrel fold: a versatile framework for efficient enzymes. FEBS Lett
771 2001; 492(3): 193-8.

772 Zhu X, Xu Y, Yu S, Lu L, Ding M, Cheng J*, et al.* An efficient genotyping method for genome-
773 modified animals and human cells generated with CRISPR/Cas9 system. Sci Rep 2014; 4: 6420.

774

Figure and table legends:

Fig. 1: Axial T2 (first 3 columns) and sagittal (last column) T1-weighted images of patients 1, 3 and 4. At age 3 years, the MRI of patient 1 is normal. Patient 3 and 4 show a simplified gyral pattern, cyst-like structures connected to the anterior horns and a T2-hyperintense signal of the hilus of the dentate nuclei. White matter signal is T2 hyperintense and appears swollen. These abnormalities are more severe in patient 4 (who additionally has intraventricular blood) than in patient 3. The corpus callosum lacks the most posterior part.

Fig. 2: Pathogenic variants reported so far and their genetic location, predicted secondary structure and tridimensional structure in the PLPHP protein in the context of PLP-binding. (A) Human *PLPBP* gene structure, protein coding exons shown in dark blue and 5' and 3' UTR shown in light blue. Position of the variants reported previously by Darin *et al.* (2016) and Plecko *et al.* (2017) are shown in black, seven novel variants identified by this study are shown in red and a splicing variant reported previously but also observed in our cohort is shown in green. (B) 2D graphical representation of the PLPHP protein based on secondary structure prediction and the tridimensional model (shown in D). Blue cylinders represent the outer α-helices and pink arrows represent the inner β-strands that comprise the (β/α)8-TIM barrel structure. Residues observed mutated in PLPHP-deficiency are shown in circles, black for variants reported previously or red for novel variants reported here. Residues located within 6Å of the modeled PLP position are shown in blue, from which the residues that establish contacts with PLP shown in cyan. (C) Predicted PLP-binding pocket showing the key Lysine 47 predicted to form the PLP-Lys adduct, black dashed lines indicate hydrogen bonds and salt bridges, green solid line show hydrophobic interactions. (D) tridimensional structure of the human PLPHP model showing the PLP molecule in green and the positions of the residues found mutated in PLPHP-deficiency in black or red according to A.

Fig. 3: Evidence in HEK293 cells and yeast *ybl036cΔ* that PLPHP can localize to mitochondria and affects growth in several energy sources. (A) HEK293T cells overexpressing PLPHP with a C-terminal Myc-DDK tag shows co-localization of PLPHP with citrate synthase; (B) Growth curves of wild-type yeast cells and mutant strains on rich oleate

medium. The strains shown are: WT (BY4742) (blue), *fox1Δ* (green) and *ybl036cΔ* (purple). (C) Growth of wild-type cells and mutant cells on 2% ethanol medium. The strains shown are: WT (BY4742) (blue), *ybl036cΔ* + pPROSC1a (human PLPHP under catalase promoter (orange) or pPROSC2a (human PLPHP under Tef promoter) (red) and *ybl036cΔ* + empty vector (purple). (D) Growth of wild-type and mutant cells after 18 hours on 20g/L glucose and non-fermentable carbon sources: rich oleate, 2% ethanol and 2% glycerol medium. Values are expressed as % growth relative to WT. The strains shown are: WT (BY4742) (blue), *fox1Δ* (green) and *ybl036cΔ* (purple).

Fig. 4: Development of *plpbp*$^{-/-}$ zebrafish model by CRISPR/Cas9 and epileptic phenotypic analysis. A) Chromatograms of zebrafish larvae showing WT and the genotypes for homozygous mutants *plpbp*$^{ot101/ot101}$ *and plpbp*$^{ot102/ot102}$. Compound heterozygous mutant larvae (*plpbp*$^{ot101/ot102}$) (not shown) were used for most experiments with the same phenotype as the homozygotes. (B) Cropped WB (for clarity) showing that no Plphp protein was detected in mutant larvae. Total protein (Stain free blot) is shown underneath for standardization. Full blot available in Supplementary Material. (C) Survival curves showing reduced survival of mutant larvae compared to WT and the two heterozygous parental types (n=20 larvae per group). (D and E) Mutant larvae moved a greater total distance during fast speed (>20mm/s) movements and spent more time in fast movements, respectively (n=16 larvae per group). (F) Relative mRNA expression showing increased expression of *c-fos* in mutant larvae compared to WT larvae, PTZ treatment was used as a positive control. (G) Example electrophysiology recordings of mutant (top) and WT (bottom) larvae showing increased number of ictal-like events. Inset are zoomed-in examples (4 seconds) of ictal-like, interictal and WT recordings. Significance: ** ($p<0.01$), * ($p<0.05$).

Fig. 5: Vitamin B6-responsive epilepsy in *plpbp*$^{-/-}$ zebrafish larvae. Survival in mutants was moderately improved using PLP (A) but showed a better response that was clearly dose-dependent with pyridoxine (B). (C) 5-minute trace recordings of 11dpf zebrafish larvae showing increased hyperactivity in the mutants which was alleviated with 10mM pyridoxine treatment, as measured by (D) time spent in fast movements and (E) distance moved in fast movements. (F) Highest seizure-like behavior category identified by blinded observers. Only untreated mutant

larvae showed evidence of S2 or S3 seizure-like activity. (G) Electrographic activity in mutant larvae was normalized by treatment with 5mM pyridoxine. (H) Example electrophysiology recordings of untreated and treated mutant larvae. Significance: ** ($p<0.01$), * ($p<0.05$).

Fig. 6: Targeted mass spectrometry studies of *plpbp*$^{-/-}$ zebrafish larvae indicates changes in B6 vitamer, amino acid, and neurotransmitter profiles. (A) B6 vitamer profile of Mutant and WT 10 dpf larvae. (B) Amino acid and neurotransmitter profile of whole larval mutant, heterozygous and WT 11dpf larvae after 24 hours fasting. (C) Metabolic pathways for the synthesis and degradation of PLP. (D). Biosynthetic pathways of catecholamines and trace amines, highlighting (in blue) the role of AADC. (E) The serotonin biosynthesis pathway, highlighting the role of AADC. Abbreviations: 3-MT: 3-methoxytyramine, 5-HIAA: 5-hydroxyindoleacetic acid, 5-HTTP: 5-hydroxytrytpophan, AADC: aromatic-L-amino acid decarboxylase, AO: *aldehyde oxidase I*, DH: β-NAD dehydrogenase, PA: 4-pyridoxic acid, PK: pyridoxal kinase, PL: pyridoxal, PLP: Pyridoxal 5'-Phosphate, PM: pyridoxamine, PMP: pyridoxamine 5'-phosphate, PN: pyridoxine, PNP: pyridoxine 5'-phosphate, PNPO: PNP oxidase Significance: ****($p<0.0001$), ***($p<0.001$), ** ($p<0.01$), * ($p<0.05$).

Table 1: Clinical features of PLPHP-deficient patients. Abbreviations: GA: Gestational Age, NA: Not Available, HC: Head Circumference, AEDs: Anti-Epileptic Drugs, GTCs: Generalized Tonic-Clonic seizures, PN: Pyridoxine, PLP: Pyridoxal 5'-Phosphate, EEG: Electroencephalography, MRI: Magnetic Resonance Imaging, MRS: Magnetic Resonance Spectroscopy, wk(s): week(s), mo: month(s), yr: year(s), nb: nota bene.

Table 2: Clinical severity scores based on system adapted from (Al Teneiji *et al.*, 2017). Variants are organized by whether seen homozygously vs. compound heterozygous, then based on mutation type (missense, truncating, splicing). Note that truncating mutations are associated with the most severe phenotypes. NA[a], NA[b], NA[c], full clinical scores could not be calculated due to early death of these patients but assumed severe based on lethality. NA* full clinical score could not yet be calculated due to early age of patient, so GDD/ID cannot yet be assessed. [1]Variant reported by(Darin *et al.*, 2016). [2] Variant reported by (Plecko *et al.*, 2017). [3]Mutation experimentally studied by (Tremino *et al.*, 2018).

867

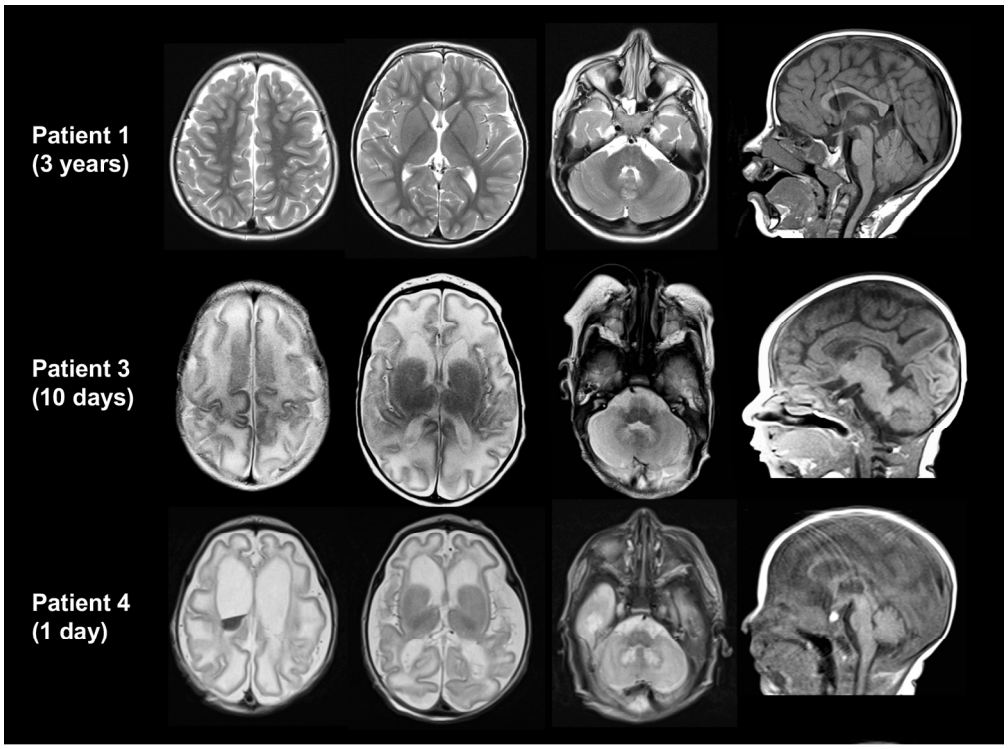

Fig. 1: Axial T2 (first 3 columns) and sagittal (last column) T1-weighted images of patients 1, 3 and 4.‼ ┼

155x115mm (300 x 300 DPI)

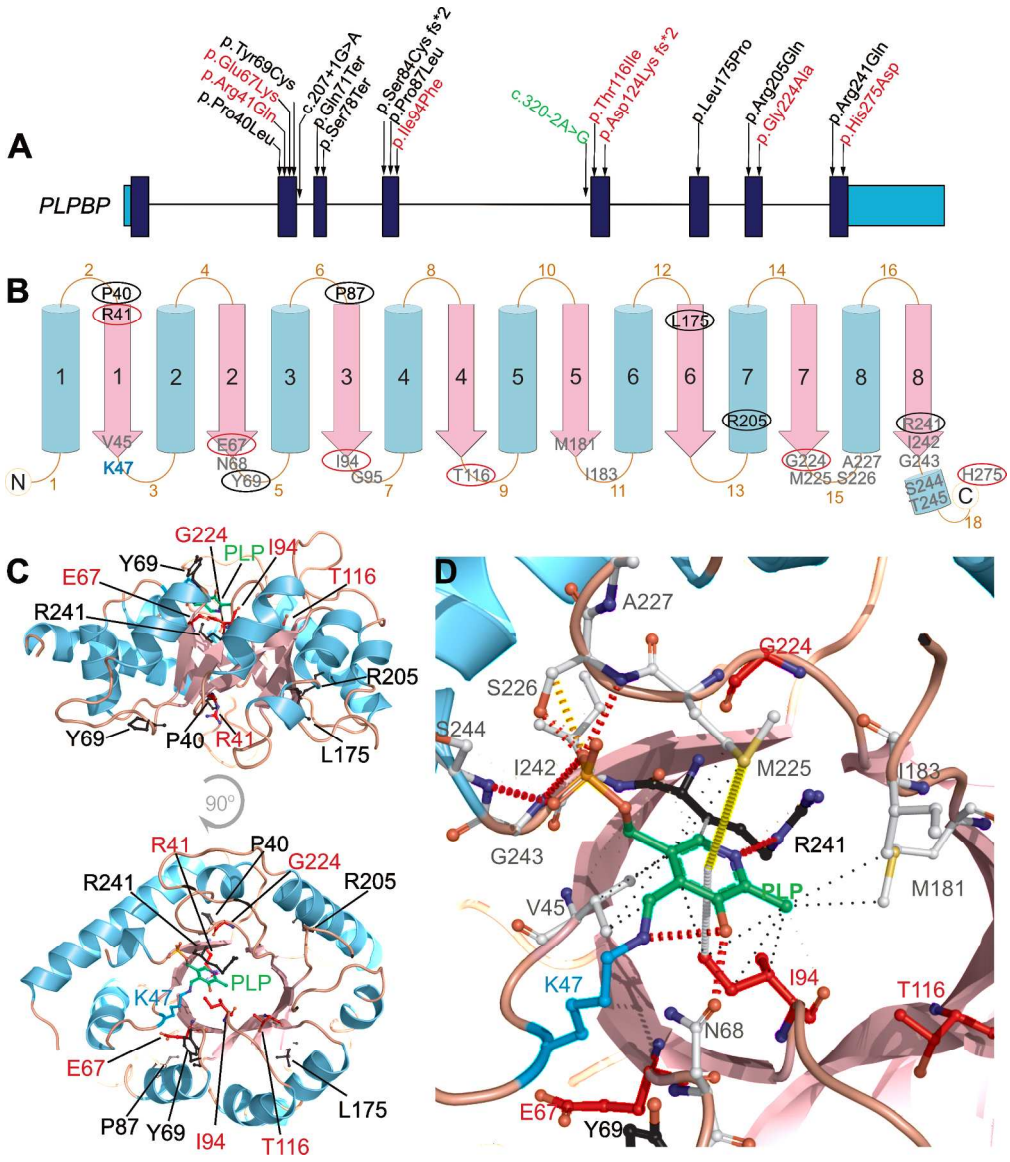

Fig. 2: Pathogenic variants reported so far and their genetic location, predicted secondary structure and tridimensional structure in the PLPHP protein in the context of PLP-binding.

209x239mm (300 x 300 DPI)

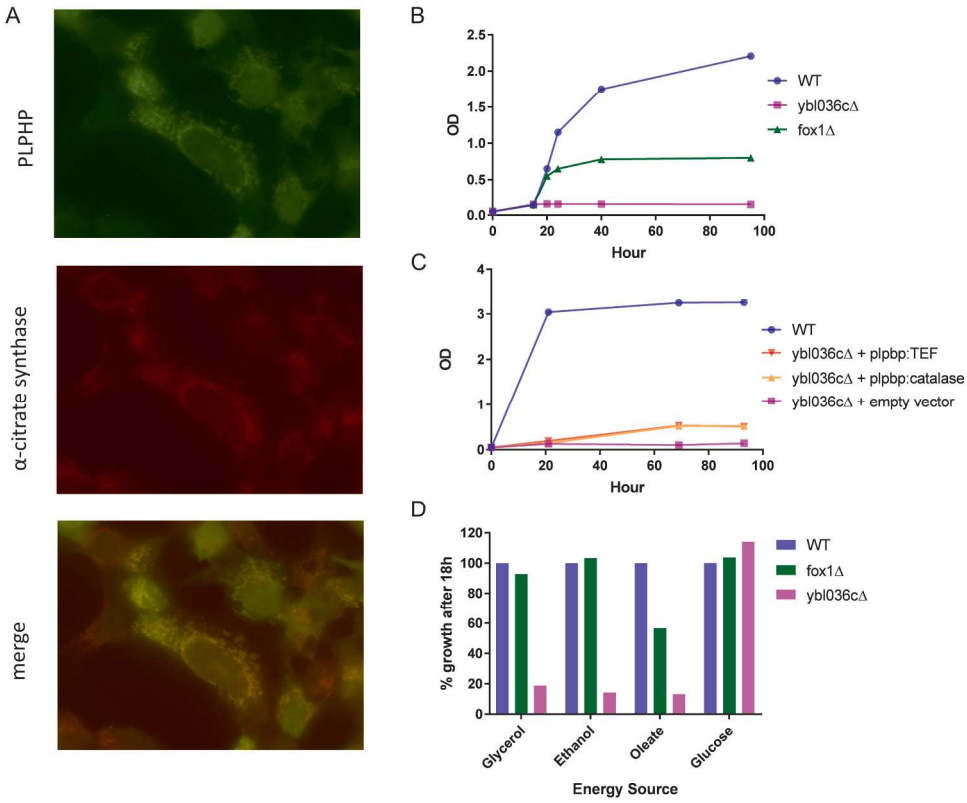

Fig. 3: Evidence in HEK293 cells and yeast ybl036cΔ that PLPHP can localize to mitochondria and affects growth in several energy sources.

242x199mm (300 x 300 DPI)

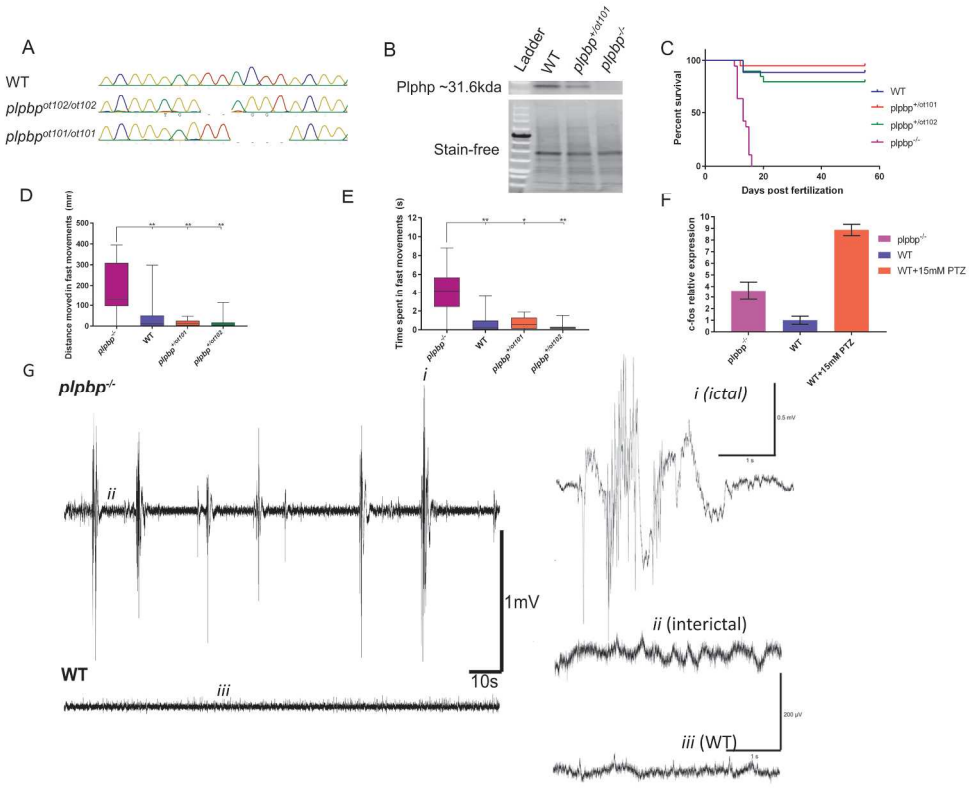

Fig. 4: Development of *plpbp*$^{-/-}$ zebrafish model by CRISPR/Cas9 and epileptic phenotypic analysis.

265x209mm (300 x 300 DPI)

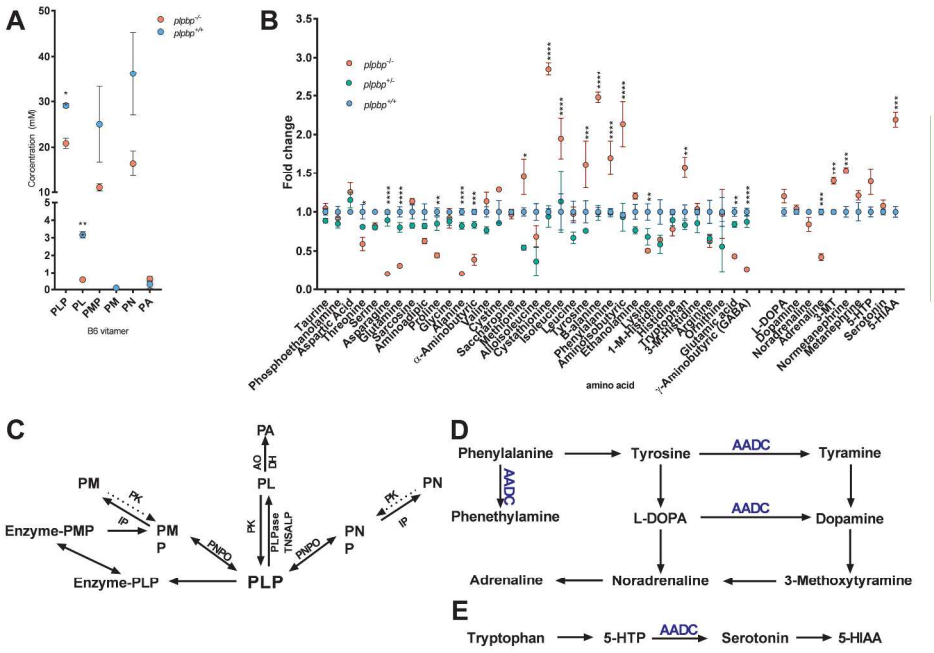

Fig. 6: Targeted mass spectrometry studies of *plpbp*$^{-/-}$ zebrafish larvae indicates changes in B6 vitamer, amino acid, and neurotransmitter profiles.

296x209mm (300 x 300 DPI)

Patient's ID (sex, current age)	**Patient 1** (Male, 3 11/12 yr)	**Patient 2** (Male, 14 yr)	**Patient 3** (Female, 5 2/12 yr)	**Patient 4** (Female, died at 2 wks)	**Patient 5** (Female, died at 8 wks)	**Patient 6** (Male, 4 3/12 yr)	**Patient 7** (Male, 23 mo)	**Patient 8** (Male, 8 1/12 yr)	**Patient 9** (Male, 14 mo)	**Patient 10** (Female, 10 6/12 yr) (sister of Patient 11)	**Patient 11** (Female, 6 10/12 y) (sister of Patient 10)	**Patient 12** (Female, 5 mo)
Ancestry (domicile)	Arab (Oman)	Arab (Oman)	Dutch (Netherlands)	Dutch (Netherlands)	Cree First Nation (Canada)	Arab (United Arab Emirates)	Hispanic (Guatemala)	Arab (Oman)	Arab (Oman)	Kurdish (USA)	Kurdish (USA)	African American (USA)
Consanguinity (degree)	+ (first cousin)	+ (first cousin)	-	-	+ (second cousin)	+ (second cousin)	-	+ (first cousin)	+ (first cousin)	+ (first cousins)	+ (first cousin)	1st degree relatives
***PLPBP* cDNA change (NM_007198)**	347C>T; 823C>G	122G>A (homozygous)	199G>A (homozygous)	320-2A>G; 671G>C	370_373del (homozygous)	347C>T (homozygous)	280A>T (homozygous)	122G>A (homozygous)	122G>A (homozygous)	199G>A (homozygous)	199G>A (homozygous)	370_373del (homozygous)
Protein change	Thr116Ile ; His275Asp	Arg41Gln	Glu67Lys	Splicing; Gly224Ala	Asp124Lysfs*2	Thr116Ile	Ile94Phe	Arg41Gln	Arg41Gln	Glu67Lys	Glu67Lys	Asp124Lysfs*2
Pregnancy / delivery complications	Increased fetal movements	-	Twin pregnancy with vanishing twin at GA 9 wks, Caesarean for fetal distress	DCDA-gemelli pregnancy, sib is healthy with normal development	Caesarean section for fetal distress	Two episodes of fast fetal movements late 3rd trimester	-	-	-	Caesarean (fetal decelerations and meconium stained amniotic fluid)	-	-
Postnatal Complications / death	-	-	Respiratory insufficiency with lactic acidosis	Initial presentation of perinatal asphyxia, followed by progressive respiratory and circulatory failure with fatal lactic acidosis, abnormal neurologic exam (strong motor unrest and dysautonomia) (patient passed away at age of 2 wks)	Progressive respiratory and circulatory failure with fatal lactic acidosis, neurologic abnormalities with hypertonia, hyperreflexia, persistent flexion and clenching of upper extremities (patient passed away at age of 8 wks)	-	Lactic acidosis	-	Transient tachypnea of the newborn	Irritability with a high-pitched cry, dysconjugate eye movements, and tonic posturing	Opisthotonos, irritability, and eye deviation (episodic, but up to 1 hour)	Lactic acidosis (blood and elevated lactic acid in MR spectroscopy), respiratory insufficiency
Birth HC percentile	66th centile	10th centile	<2nd centile	1st centile	82nd centile	10th centile at age 10 mo	12.5th centile	50th centile	50th centile	NA	2nd centile	22nd centile at birth, << 0.1st centile at 2 mo
Lactic acidosis	-	-	+	+	+	NA	+	- **	NA	- ***	NA	+
Seizure onset	Day 5	Day 7	Day 2	Day 1	Day 1	Day 4	2 months	1st week	Day 5	Day 1	Day 1	Day 1
Seizure type	Myoclonic, generalized tonic-clonic, uprolling of eyes and tonic-clonic	Staring and tonic-clonic	Tonic-clonic	Tonic spasms of the face, thorax and arms	Tonic posturing with occasional myoclonic jerks	Infantile spasms, clonic, generalized tonic-clonic	Infantile spasms (unclear if true seizures)	Myoclonic	Generalized tonic-clonic	Flexor spasms, eye deviation, segmental myoclonic jerks	Partial and generalized seizures	Focal seizures and myoclonic jerks followed by tonic posturing
EEG pattern (at age)	1st EEG (1 wk): Burst suppression pattern	NA	EEG (5 days): discontinuous pattern, and a tendency to	1st EEG (day 1): diffusely abnormal, excessively	EEG (age NA): Burst suppression	EEG (4 mo): multifocal epileptiform activity	EEG (2 mo): continuously disorganized background	1st EEG (3 wks): Burst suppression	1st EEG (10 days): Burst suppression	EEG after phenobarbital load (2 days): Discontinuous	EEG (age NA): discontinuous record with multifocal	EEG (age 2days-4weeks): Burst suppression

	Most recent EEG (5 mo): normal		burst suppression	discontinuous pattern, no correlation with clinical phenomena suggestive of seizures. 3rd EEG (day 7): progressively frequent rhythmic sharp activity (electrographic neonatal seizures) and BIRDS		EEG (7 mo): normal after B6 treatment EEG (10 mo): intermittent bilateral parasagittal slowing, poorly formed sleep elements EEG (2.5 yr): normal	with bursts of higher-amplitude activity, and several spike and slow wave complexes followed by electrodecrement EEG (9 mo): normal after B6 treatment	Last EEG (4 yr, 2 mo): normal after B6 treatment	EEG (10 mo): Normal	background rhythm EEG (4 days): near burst suppression pattern	sharps (bilateral frontal/central/temporal)	Last EEG (4.5 mo): normal after PLP treatment
AEDs (response)	Phenytoin, phenobarbitone & midazolam (no response) clonazepam and topiramate (initial reduction but later relapsed)	Mutiple AEDs (names NA) (No response)	NA	Phenobarbital, Levetiracetam Midazolam and Chloralhydrate (short & incomplete response <1 day)	Midazolam, prednisone (& 6 other AEDs) (short transient response)	Prednisolone (transient response), levetiracetam and vigabatrin (poor response, prior to B6) oxcarbazepine (partial response, with B6)	Initially poor response to prednisolone, no response to lorazepam, partial response to levetiracetam	Phenobarbitone, midazolam & levetiracetam: no response	Not tried	Mild response to phenobarbital for the first 2 days	No initial response to AEDs	Initial period of seizure freedom after phenobarbital loading but later relapsed No response to 9 other AEDs
Initial B6 treatment (age/ response)	PN (5 wks) PLP (2 yr, 6 mo) (incomplete control)	PN (< 1 mo) (complete control)	PLP (5 days) PN (3 yr, 10 mo) (incomplete control)	Not tried	Not tried	PN (6 mo/ complete control of spasms and clonic seizures, new GTCs with fever several months later)	PN and PLP (2.5 mo/ complete resolution of symptoms)	PN (25 days/ complete control)	PN (2nd week/ complete control)	PN (2nd week/ complete control)	PN (age NA/ incomplete control)	PN (age NA/ no repsonse) PLP (1 mo/ complete control)
B6 withdrawal (vitamer/ response)	-	-	+ (PLP/ seizure relapsed)	Not applicable	Not applicable	+ (PN/ seizure relapsed)	-	-	-	+ (PN/ seizure relapsed)	+ (PN/ increased seizures)	-
B6 vitamer switch (type/ response)	+ (PN→PLP/ no improvement)	-	+ (PLP→PN/ no improvement)	Not applicable	Not applicable	-	-	-	-	-	-	+ (PN→PLP/ complete response)
Current treatment	PLP 300 mg TID (58 mg/kg/day) Folinic acid 1 mg BID (2mg/kg/day)	PN 80 mg BID (5 mg/kg/day)	PN 200 mg BID (9 mg/kg/day) Midazolam (used during seizures only) Macrogol: 4g daily Omeprazol: 10mg BID	Not applicable	Not applicable	PN 100 mg BID (12.8 mg/kg/day) oxcarbazepine 420 mg BID (53.8 mg/kg/day)	PN 23 mg/kg/day div BID PLP 30 mg/kg/day div TID	PN 80 mg BID (6 mg/kg/day)	PN 20 mg BID (8.5 mg/kg/day)	PN 100 mg BID (4.7 mg/kg/day) Lamotrigine 50 mg BID (3.5 mg/kg/day) Clobazam 10 mg BID (0.75 mg/kg/day)	PN 100 mg BID (7.8 mg/kg/day) Lamotrigine 37.5 mg BID (4.5 mg/kg/day) Clobazam 10 mg BID (1.25mg/kg/day)	PLP 40 mg/kg/day Phenobarbital 9 mg/kg/day
Breakthrough	+	+	+ (seizure	Not applicable	Not applicable	+	-	+	-	+	+	-

seizures with fever			relapse on viral infections or sleep deprivation)									
Clinical neurologic exam (age)	Unremarkable (3 yr, 10 mo)	Unremarkable (age NA)	Hypertonia, stereotypic hand movements, unstable walking (3 yr, 8 mo)	NA	NA	Mild axial hypotonia, stereotypies, poor eye contact (6 mo)	Unremarkable (15 mo)	Unremarkable (age NA)	hyperreflexia of all limbs (age NA)	Hypotonia, mild dysmetria, coordination difficulties, wide based gait (age NA)	Hypotonia, mild dysmetria, wide based and ataxic gait. (age NA)	mild hypotonia (age 4 months)
Developmental delay / intellectual disability	+ (moderate-severe), Autism spectrum disorder	-	+ (severe)	Not applicable	Not applicable	+ (severe before B6 therapy, mild after), Autism spectrum disorder	-	-	-	+ (*Moderate-severe, has autistic features but no formal diagnosis*)	+ (*Moderate-severe, worse than sister, has autistic features but no formal diagnosis*)	- (at 5mo)
Speech delay	+	-	+	Not applicable	Not applicable	+	-	-	NA	+	+	Not applicable
School performance or IQ	NA	Average school performance	NA	Not applicable	Not applicable	DQ=70, 2nd percentile (Bayley-III Cognitive Composite score)	NA	Excellent school performance	NA	NA	NA	Not applicable
Dysmorphic features	-	-	- (slight upslant of the eyes and a slightly prominent forehead within normal spectrum)	-	-	-	+ (bilateral syndactyly of the third and fourth fingers)	-	-	+ (joint laxity)	-	-
Neuro-imaging (at age)	MRI (6 weeks): mild T2 hyperintense periventricular white matter changes MRI (age 9 months): mild communicating hydrocephalus. MRI (3.5 years): normal.	Not performed	MRI (day 10): Simplified gyral pattern, diffusely elevated T2 signal of the swollen white matter, large paraventricular (pseudo)-cysts alongside the anterior horns, lack of the most posterior part of the corpus callosum, T2-hyperintese signal of the hilus of the dentate nuclei. The PLIC is not myelinated.	MRI (day 1): Simplified gyral pattern, diffusely elevated T2 signal of the swollen white matter, large paraventricular (pseudo)-cysts alongside the anterior horns, lack of the most posterior part of the corpus callosum, T2-hyperintese signal of the hilus of the dentate nuclei. Some blood in the posterior horn of the	MRI (day 6): cystic leukencephalopathy with a 'vanishing' appearance of the cerebral white matter, and presence of a lactate doublet on MR spectroscopy	MRI (8 months): normal.	MRI (2 months): normal	MRI (4 weeks): normal	MRI (10 months): normal	MRI (2 days): underdeveloped frontal gyri. Subsequent MRI: thin posterior corpus callosum, little periventricular white matter volume, normal gyral pattern. Most recent MRI: underdevelopment of the occipitoparietal white matter with decreased volume and hence thin posterior corpus	Initial MRI: normal. Subsequent MRI: Slight asymmetry in height of the hippocampi, nonspecific T2 hyperintensity in the periatrial white matter extending to the subcortical white matter.	MRI (brain) at ages of 2 days and 3 weeks: Simplified gyral pattern, diffusely elevated T2 signal of the swollen white matter, mild dilatation of the lateral and third ventricles with multiple intraventricular septations. Small intraventricular haemorrhage. The PLIC is not myelinated.

				right lateral ventricle. The PLIC is not myelinated.						callosum		

** elevated lactate but normal pH, *** first measured after B6 treatment

Abbreviations: **AEDs:** Anti-Epileptic Drugs, **BIRDS**, brief ictal rhythmic discharges, **DQ:** developmental quotient, **EEG:** Electroencephalography, **GA:** Gestational Age, **HC:** Head Circumference, **mo:** month(s), **MRI:** Magnetic Resonance Imaging, **MRS:** Magnetic Resonance Spectroscopy, **NA:** Not Available, **PLIC**, posterior limb of the internal capsule, **PN:** Pyridoxine, **PLP:** Pyridoxal 5'-Phosphate, **wk(s):** week(s), **yr:** year(s), **nb:** nota bene.

Table 2: Clinical severity scores based on system adapted from (Al Teneiji *et al.*, 2017). Variants are organized by whether seen homozygously vs. compound heterozygous, then based on mutation type (missense, truncating, splicing). Note that truncating mutations are associated with the most severe phenotypes. NA[a], NA[b], NA[c], full clinical scores could not be calculated due to early death of these patients but assumed severe based on lethality. NA* full clinical score could not yet be calculated due to early age of patient, so GDD/ID cannot yet be assessed. [1]Variant reported by(Darin *et al.*, 2016). [2] Variant reported by (Plecko *et al.*, 2017). [3]Mutation experimentally studied by (Tremino *et al.*, 2018).

Patient ID	Type of mutation	Variant annotation	First seizure/ movement episode score	GDD / ID score	B6 response score	Severity score sum	Protein effect
Patients reported in this study							
1	Compound het.	Thr116Ile;	3	2	2	Severe (7)	Predicted LOF - mutation likely impacts PLP binding
		His275Asp					Predicted LOF - mutation likely impacts PLP binding
2	Homo. missense	Arg41Gln	2	0	0	Mild (2)	Predicted to still bind PLP, but stability is reduced
3	Homo. missense	Glu67Lys	3	3	2	Severe (8)	Predicted LOF - mutation likely impacts PLP binding
4	Compound het.	c.320-2A>G;	3	NA[a]	NA[a]	Deceased: Severe (9)	LOF - Truncated protein[1]
		Gly224Ala					Predicted LOF - Mutation likely disrupts loop 15 structure and orientation of several PLP binding residues
5	Homo. deletion	Asp124Lys fs*2	3	NA[b]	NA[b]	Deceased: Severe (9)	LOF - Truncated protein (band absent as in Supp. Fig 1)
6	Homo. missense	Thr116Ile	3	2	3	Severe (8)	Predicted LOF - mutation likely impacts PLP binding
7	Homo. missense	Ile94Phe	1	1	1	Mild (3)	Predicted LOF? Mutation likely impacts PLP binding, but it is possible Phe could still establish

							aromatic/hydrophobic contacts with PLP;
8	Homo. missense	Arg41Gln	3	0	0	Mild (3)	Predicted to still bind PLP, but stability is reduced
9	Homo. missense	Arg41Gln	3	0	0	Mild (3)	Predicted to still bind PLP, but stability is reduced
10	Homo. missense	Glu67Lys	3	2	2	Severe (7)	Predicted LOF - mutation likely impacts PLP binding
11	Homo. missense	Glu67Lys	3	2	2	Severe (7)	Predicted LOF - mutation likely impacts PLP binding
12	Homo. deletion	Asp124Lysfs*2	3	NA*	2	NA*	LOF - Truncated protein (band absent as in Supp. Fig 1)
Patients reported by (Darin *et al.*, 2016)							
1	Homo. nonsense	Ser78Ter	3	NA[c]	NA[c]	Deceased Severe (9)	LOF - Truncated protein[1]
2	Homo. nonsense	Ser78Ter	3	2	3	Severe (8)	LOF - Truncated protein[1]
3	Homo. nonsense	Ser78Ter	3	3	3	Severe (9)	LOF - Truncated protein[1]
4	Homo. missense	Leu175Pro	3	3	2	Severe (8)	LOF - Misfolded protein[1,3]
5	Compound het.	c.207+1G>A; c.320-2A>G;	3	3	2	Severe (8)	LOF - Truncated protein[1]; absent band in Western blot1
6	Homo. nonsense	Gln71Ter	3	2	3	Severe (8)	LOF - Truncated protein[1]
7	Compound het.	Pro87Leu;	1	1	1	Mild (3)	Lower solubility and some precipitated; Folded forms still binds to PLP [3]
		Arg241Gln					LOF - mutation abolishes PLP binding3, drastic reduction in stability (Tm shift - 14°C)[3]
Patients reported by (Plecko *et al.*, 2017 Dec)							
1	Compound het.	Pro40Leu;	2	0	1	Mild (3)	Reduced stability (Tm shift -6ºC); Still binds to PLP [3]
		Arg241Gln					LOF - mutation abolishes PLP binding, drastic reduction in stability (Tm shift - 14°C)[3]

2	Compound het.	Ser84Cysfs*21 ; Arg205Gln	2	1	1	Moderate (4)	LOF - Truncated protein [2] Reduced stability (Tm shift -7°C); Still binds to PLP 3
3	Homo. missense	Pro87Leu	3	3	1	Severe (7)	Lower solubility and some precipitated; Folded forms still binds to PLP [3];
4	Homo. missense	Tyr69Cys	2	0	2	Moderate (4)	Cys forms disulfide bridges that creates an artificial dimer that hides PLP. Decreased PLP binding in 30%[3]

Supplemental Appendix

Clinical Patient Descriptions

note: MRI findings detailed in Fig. 1 and Supplementary Table 1

Patient 1

This Omani boy, now 3 years and 10 months old, was born to a G3P3 mother. His parents are first cousins, who are healthy with normal learning abilities and there is a family history of similar disease in a younger newly born sibling. Antenatally, the mother experienced increased fetal movements. He was born at term, cried immediately and APGAR scores were 9 / 10. His birth weight was 2.95 kg (10^{th} percentile), length: 49 cm (50^{th} percentile) and HC: 35 cm (50^{th} percentile).

Seizures were first observed on the 5^{th} day of life, presenting with decreased consciousness, uprolling of the eyes and tonic-clonic movements of the body; each episode lasted 10-15 minutes and recurred every few minutes. He then developed myoclonic seizures. He was treated with phenytoin, phenobarbitone and midazolam infusion without clinical response; subsequently he was started on clonazepam and topiramate with initial reduction of seizures but subsequent relapse. His EEG showed burst suppression.

At 5 weeks of age, he was started on oral pyridoxine (25 mg BD) with immediate effect; he was sedated yet hemodynamically stable. All anti-epileptics were discontinued after the first dose of pyridoxine because of excessive sleepiness. He continued to be sleepy (remained sleepy for almost 72 hours) and therefore pyridoxine was withheld for 48 hours then restarted at 5 mg BD with gradual increment to 25 mg BD. EEG was repeated, and it showed marked improvement with no burst suppression on the lower pyridoxine dose. Generalized tonic-clonic seizures relapsed but were brief and infrequent and occurred during febrile illness. He was started on levetiracetam but there was no response, so it was tapered and discontinued.

At the age of 2 years and 4 months, the dose of pyridoxine was increased to 120 mg BD p.o. (= 24 mg/kg/d) that is increased to TID during febrile illness and his seizures were controlled for around 2 months but then he was admitted again with *status epilepticus*. Pyridoxine was thus substituted by PLP starting at a dose of 200 mg TID (= 42 mg/kg/d) which was then increased to PLP 300 mg

TID (=58mg/kg/day) with no notable improvement of his seizure control. Subsequently, folinic acid 15 mg BID (= 2mg/kg/day) was added to his PLP regimen, this combination resulted in the best seizure control during his entire course of treatment. He was last seen at the age of 3 years and 11 months in February 2018, where his parents reported marked reduction in the frequency of his seizures. They reported only 2 brief episodes in 3 months period, mainly fever provoked.

He suffered global developmental delay, of a moderate to severe degree: When he was assessed at 2.5 years of age, his developmental age was around 12-18 months. Speech and language developmental age is around 7-8 months of age (he had 4 syllable babbles, had 1 word (unspecific) – Mama-, could not do head shaking for "No," was not able to babble monologs, could know his own name). He is hyperactive and was diagnosed with autism spectrum disorder (ASD). After folinic acid supplementation, his development improved, and he started to gain some milestones. He is currently walking without support and steadily and is able to run and climb the stairs. He can say around 10 words with meaning, he obeys commands and can scribble. He has also become less hyperactive. Physical exam revealed no dysmorphic features with biometry on the 50th centile; systemic exam was also unremarkable without organomegaly. A normal neurological examination showed no focal deficits.

Biochemical investigation at the age of 15 months showed high-normal urinary α-aminoadipic semialdehyde (α-AASA, 0.19 μmol/l, reference range: 0-0.2 μmol/l) but plasma pipecolic acid was within the reference range. Antiquitin deficiency was subsequently ruled out by Sanger sequencing of *ALDH7A1*. Plasma amino acids were measured twice and were normal while blood lactate was high-normal (1.7 mmol/l, reference range: 0.5-2.2 mmol/l) (tests were done at the age of 6 weeks).

Patient 2

This boy of Omani descent currently aged 13 years and 10 months was born to consanguineous parents (first cousins) at term without antenatal or postnatal complications. There is family history of 2 siblings' deaths; both were due to intractable seizures (at the age of 2-4 months). He has 5 living siblings (3 males and 2 females) that are all healthy. His birth head circumference was at the 10th percentile.

At the age of 7 days, brief, frequent seizures were noted with staring and tonic-clonic movements of the body. He was tried on different AEDs but no response until pyridoxine was administered and subsequently seizures were controlled before the age of 1 month. Infrequent seizures occurred mainly during febrile illnesses, the most recent one at the age of 7-8 years. EEG reports are not available.

He is currently on pyridoxine 80 mg BID (= 5 mg/kg/day), increased during febrile illness to 80mg TID. Physical examination revealed no dysmorphic features, anthropometric measurements on the 10th centile, no systemic abnormalities and no organomegaly. Development in all domains and cognition are normal for age; he attends a regular grade 6 at school and has average school performance. His neurological exam was reported as normal. Biochemical screening revealed no detectable α-AASA in urine and Sanger sequencing of *ALDH7A1* was negative. Given the striking response to pyridoxine, no other investigations were carried.

Patient 3

This girl of Dutch descent, now 5 years and 2 months old, was born at 37+5 weeks of gestation after an emergency caesarian section because of fetal distress. She is the first and only living child of non-consanguineous parents (as far as known). The pregnancy was complicated by a vanishing twin at 9 weeks of gestation. APGAR scores were 8/9. There was meconium in the amniotic fluid. Umbilical cord blood gas had pH 7.00. Birth weight was 2422 grams (5-10th centile / -1,91 SD), birth length was 47 cm (25th centile/ -1.23SD) and head circumference was 30 cm (<2nd centile / -4,01 SD). Her fontanel was small. After birth, she needed CPAP for breathing difficulties and she had trouble keeping her temperature. She received antibiotics because of suspicion of a perinatal infection. Blood lactate was 13.2 mmol/L (reference range: <2.2 mmol/L); blood gas at day 0: pH 7.15 (normal range: 7.35-7.45); pCO_2 4.2 kPa (normal range: 4.7-6.4 kPa); pO2 7.5 kPa (normal range: 10.0-13.3 kPa); HCO_3 11 mmol/L (normal range: 22-29 mmol/L); and base excess -17.3 mmol/l (normal range: -3 - +3 mmol/L). Lactate was between 4.2 and 8.8 mmol/L on days 1-5 (normal range =<2.2 mmol/L). Blood glucose was normal, creatine kinase was 6593 U/L (normal range: <200 U/L) at day 1 and went down to 460 U/L at day 5.

On day 1, she had clinically evident tonic-clonic seizures and an abnormal cerebral function monitoring (CFM). Phenobarbital was started, with clonazepam, midazolam and lidocaine, with variable response. She was variable hypo- and hypertonic. EEG at day 5 was in keeping with

encephalopathy showing a discontinuous pattern, and a tendency to burst suppression with epileptic activity was seen during burst episodes. The liver projected two centimeters below the costal margins.

At day 5, PLP was started orally (40 mg 3 dd = 48mg/kg/d) after which the convulsions vanished, and blood lactate started to normalize after day 6 (between 1.6 and 2.9 mmol/L).

At 2.5 months of age there were no clinical signs of epileptic activity, the EEG was normal, and the head circumference had shown catch-up growth to -2.5 SD. The PLP dose was lowered to 20 mg 3dd (15mg/kg/d) because of vomiting. At six months of age the development was still normal. There was a short possibly epileptic episode after which the dose of PLP was adjusted to 40 mg 3dd (16mg/kg/d).

At 10 months of age, she had a 15-20 minutes lasting tonic-clonic insult shortly after stopping the PLP because *PNPO* Sanger analysis was normal as was urine concentration of α-AASA. The next days she had several epileptic insults and the EEG results were slower and less differentiated showing mild encephalopathic changes, but no overt epileptic phenomena. PLP was restarted (40 mg 3dd = 12 mg/kg/day) because of suspicion of a yet undetected pyridoxine/ PLP-responsive epilepsy, and again her clinical condition improved significantly. Levetiracetam was started at 20 mg/kg/day.

At 14 months of age she had an epileptic insult after sleep deprivation. The parents tried to reduce the PLP dose at 18 months of age, but she had another insult after that, so they restarted the medication. The girl has signs of pavor nocturnus from 20 months of age. She has had several epileptic insults that were mostly induced by viral infections/fever or sleep deprivation. At the age of 3 years and 10 months, her B6 therapy was switched to pyridoxine at 100 mg/day in one dose (= 5.9 mg/kg/day), because PN has less severe side effects on the long term. B6 vitamer conversion went smoothly and at the age of 4 years and 2 months, levetiracetam was gradually discontinued. This did not seem to affect frequency of seizures. She had a seizure about once every two months at this time, more severe than on the PLP regimen. Seizures occurred mostly during illness. At the same age (4 years and 2 months), her pyridoxine dose was leveled up to 150 mg/day (100 mg in the morning and 50 mg in the evening, = 8.8 mg/kg/day) and her seizures became less frequent. The dose was adjusted to 100 mg 2dd (= 9.0 mg/kg/day) at the age of 5 years. Midazolam is used during seizure attacks. In addition, she is also taking omeprazol (10mg BID) and macrogol (4g daily) to control her GE reflux and constipation, respectively.

Her development currently at age 5 years is profoundly delayed; she could walk independently at 35 months of age, and there is no speech at 3.9 years of age. Physical examination at 3.2 years of age showed no overt dysmorphism except a slight upslant of the eyes and a slightly prominent forehead. Length at the 25th centile and head circumference at 2.5th centile / -2 SD. Neurologically, at 3 years and 8 months she hardly makes eye contact, follows her own lead. She has some stereotypic hand movements. She walks somewhat unstable. The leg tonus seems slightly high, reflexes are vivid and no Babinski reflex.

Additional investigations included TORCH serology (negative). Metabolic screening of urine at day 3 before PLP therapy showed normal amino acid profile, a trace of sulfite, high lactate, and negative α-AASA. In blood, carnitines, acylcarnitines and methylmalonic acid levels were normal, and plasma amino acids showed elevated glycine 915 μmol/L (normal range 197-487 μmol/L) and ornithine (197 μmol/l, normal range 42-170 μmol/L).

Pre-treatment CSF screening at day 3 revealed normal total protein (670 mg/L, normal range: 450-1090 mg/L); high lactate 4.4 mmol/l (normal range: 1.1-2.4 mmol/L); high pyruvate (0.23 mmol/L, normal range: 0.03-0.15 mmol/L) and normal glucose (4.2 mmol/L, normal range: 2.2-4.4 mmol/L). Amino acids showed slightly high values of glycine (25 μmol/L; normal range: 3-17 μmol/L), threonine, glutamine, and ornithine. Neurotransmitters and pterins were normal.

Chromosome micro-array showed a paternal 5p15.2 duplication of 433 kb (genes in the duplication interval are *ANKRD33B*, *DAP* and *CTNND2*) and a maternal 12q24.33 duplication of 370 kb (genes in the duplication interval are: *GPR133* and *LOC116437*). Both variants are likely benign. Whole-exome sequencing of the proband and both parents was performed as described (Dyment *et al.*, 2013), identifying a homozygous missense variant in the *PLPBP* gene: Chr8(GRCh37):g.37623143G>A; NM_007198.3:c.199G>A; p.(Glu67Lys).

Patient 4

This girl of Dutch non-consanguineous origin, who died at 2 weeks of age, was the first of DCDA twins, born via spontaneous vaginal delivery at 36+6 weeks gestation (birth weight: 2215 g (10^{th} percentile), head circumference 30.7 cm (-2.5 SD corrected for gestational age) and APGAR 6/7/8). The family history was negative for epilepsy or developmental problems. Her twin sib is healthy with normal development. Directly postpartum, spontaneous breathing was insufficient, requiring assisted ventilation for 5 minutes followed by CPAP with oxygen. Spontaneous

ventilation was restored. Glucose was 4.5 mmol/L but rapidly decreased to <0.6 mmol/L one hour postpartum and remained between 0.8 and 1.8 for four hours despite extreme supplementation dosages; at 6 hours postpartum normoglycemia was first reached (6.6 mmol/L). Initial lactate was 19 mmol/L, CK 3137 U/L (normalized to 232 U/L at day 9). A brain ultrasound on postnatal day 1 showed a dilation of the ventricular system, intraventricular bulkheads, an abnormal gyral pattern and abnormal white matter.

Neurologically the girl showed strong motor unrest and progressive axial hyperextension upon light touch. Seizures probably started at day 1 postnatally (but could not be proven by EEG at that time) and escalated at day 3 (irritability, nystagmus, tonic spasms of the face, thorax and arms, later on also tachycardia, hypertension, apneas, and desaturations, followed by crying and grimacing). The first EEG (postnatal day 1) showed a diffusely abnormal and excessively discontinuous pattern. Upon external stimulation, there was sharp polymorphic and asynchronous activity in the central areas and sometimes more generalized. EEGs on day 4 and 7 displayed a similar background, progressively frequent BIRDS (brief ictal rhythmic discharges) and progressive episodes of rhythmic sharp activity compatible with electrographic neonatal seizures, sometimes without clinical correlate. Over the course of two weeks several AEDs were trialed, all leading to unsustained (minutes to one hour) and only partial seizure control. Because of the severe structural brain abnormalities on ultrasound and MRI, pyridoxine treatment was not considered. Phenobarbital loading doses up to 40 mg/kg were followed by 5 mg/kg/day. Levetiracetam was given twice daily (60 mg/kg) after 2 loading dosages of 20 mg/kg. Continuous intravenous midazolam (0.8 mg/kg/hour) with several additional loading doses had a similar effect. Finally, repeated doses of oral chloral hydrate (50 mg/kg) accomplished a good clinical response for several hours. However, seizures became intractable and on day 16, after elevating midazolam and adding morphine for comfort control the girl died of respiratory depression and bradycardia. Permission for restricted brain autopsy was granted by the parents (only one slice). Histopathological examination showed focal abnormalities, mainly of the white matter consistent with hypoxic-ischemic injury. WES open exome trio-analysis came back negative at first. However, re-analysis of open exome data revealed a compound heterozygous mutation in *PLPBP*.

Patient 5

This female neonate was the first child to consanguineous parents (second cousins) of Cree First Nation ancestry. The pregnancy was unremarkable, but a Caesarean delivery was performed at term due to a non-reassuring fetal heart rate. Her birthweight was 3470 g (76th percentile), head circumference was 35 cm (82nd percentile) and height was 47cm (14th percentile). The child briefly (10-15 seconds) received positive pressure ventilation for poor respiratory effort, being initially stable. Over the first hours of life, she developed progressive respiratory failure requiring intubation and transfer to a tertiary care NICU.

The admitting diagnosis was suspected birth asphyxia. Her neurological examination was notable for hypertonia, hyperreflexia, and abnormal movements (persistent flexion and clenching of her upper extremities). Clinical seizures were noted on the first day of life; EEG was markedly abnormal with a burst-suppression pattern, and she was given a neurological diagnosis of early infantile epileptic encephalopathy (Ohtahara syndrome). Routine lab studies were notable for a persistently increased lactate level in blood (range 1.5 - 11.2 mmol/L) and cerebrospinal fluid (5.6 mmol/L).

The patient was successfully extubated post-transport, however her seizures proved to be refractory. Seizures were managed, to the extent possible, with an intravenous midazolam infusion (150 μg/kg/hour), followed by an escalating series of up to six simultaneous anticonvulsant agents, and high-dose prednisone. Empiric therapy with biotin and thiamine produced no obvious benefit (pyridoxine was not tried). Seizures and apneic episodes persisted, becoming increasingly frequent despite these treatments. At eight weeks of age, she acutely deteriorated with recurrent apneas, acute renal failure, and hemodynamic compromise, and care was recognized to be futile, and withdrawn.

The patient's clinical presentation and imaging were considered most consistent with a mitochondrial disorder. Plasma amino acids were notable for hyperglycinemia (943-1010 μmol/L; reference interval 81-436) with corresponding high glycine in CSF (28 μmol/L; reference interval 3-23); of note, alanine and proline concentrations in blood and CSF were normal. Acylcarnitine profile was normal. Urine organic acids showed increased excretion of lactic, pyruvic, and 2-hydroxybutyric acids, consistent with lactic acidosis. Muscle biopsy was refused; cultured skin fibroblasts showed an elevated lactate-to-pyruvate ratio (41.7 +/- 7.13; reference interval 9.6-26.5),

normal activities of several enzymes (pyruvate dehydrogenase (PDH) native: 0.94±0.06nmoles/min/mg protein, ref 0.46-1.60; PDH: 1.32±0.06nmoles/min/mg protein, ref 0.87-2.33; pyruvate carboxylase: 0.51, ref 0.35-5.18; and respiratory complexes II-IV), and normal mitochondrial morphology and inner membrane potential. Extracellular flux testing showed an apparent reduction of carbonyl cyanide-*4*-(trifluoromethoxy)phenylhydrazone (FCCP)-stimulated spare respiratory capacity.

Genetic investigations which were normal or inconclusive in the patient included oligonucleotide microarray, mtDNA point mutation panel, and an NGS-based nuclear mitochondrial gene panel (Mitome200, Baylor College). She was enrolled into a local research program and an NGS-based panel of 4,813 genes associated with any clinical phenotype (Illumina TruSight One) was performed and negative. Whole-exome sequencing of the proband and both parents was performed as described (Beaulieu *et al*., 2014; Hamilton *et al*., 2016), identifying a homozygous frameshift mutation in NM_007198(*PLPBP*):c.370_373del (p.Asp124Lysfs*2). Absence of PLPHP protein expression was confirmed by immunoblot of fibroblast lysates from the patient and controls (Supplementary Fig. 1).

Patient 6

This boy, now 4 years and 3 months old, was born to consanguineous parents (second cousins) from the UAE after a pregnancy complicated by possible fetal seizures in the late third trimester consisting of rapid movements. There is a family history of similar epileptic encephalopathy with infantile spasms in a sibling who died from pneumonia while being treated with steroids. He was born at term with birth weight of 2.8 kg. His head circumference measured at the age of 10 months was at the 10th percentile (44 cm) and has remained normocephalic. Apgar scores were not available but there were no reports of complications or need for resuscitation after delivery. He had irritability from the first day with possible seizures and clear diagnosis of seizures by day 4 of life. Initial seizures types were infantile spasms and rapid clonic seizures. Results of first EEG at 2 months are unknown. An EEG at 4 months showed multifocal epileptiform activity predominantly in the frontal and parietal regions. He had transient response with 2 weeks seizure free on prednisolone then the effect waned. He had no response to levetiracetam or vigabatrin. Around 6 months of age, pyridoxine 50 mg BID (approximately 6 mg/kg/day) was given, then cutting back to 25 mg BID resulted in complete control of spasms and clonic seizures, and his

EEG normalized. Within 1-2 months, however, he developed new seizures, generalized tonic-clonic seizures with illness or fever, lasting up to 30 minutes in duration. The frequency is one every 1-3 months. He has had improvement in duration and frequency of seizures with oxcarbazepine and early treatment with diazepam. His longest seizure free interval was approximately 3 months. He had a brief withdrawal of PN for two days with recurrence of seizures and thus it was resumed at a dose of 50 mg BID. After PLPHP deficiency diagnosis was made, his PN dose was increased to 100 mg BID (12.8 mg/kg/day). He has been on this dose ongoing in addition to oxcarbazepine 420 mg BID (53.8 mg/kg/day).

Developmentally, he was severely delayed without achieving any milestones during the first 6 months prior to PN treatment; he was markedly hypotonic and made no eye contact. After treatment, he made excellent improvement in his development but still has mild motor delays and a diagnosis of ASD was made at 2 ½ years old. He sat independently by 12 months, walked by 2 years, and had a pincer on one hand by 2 ½ years. He repeats words but does not talk independently or communicate with gestures and his eye contact is limited. He has limited social reciprocity and joint attention. He has frequent stereotypies and self-stimulatory behaviors fitting the ASD.
At 2 years and 7 months of age, he was assessed on the Bayley Scales of Infant and Toddler Development, where his scores were: Cognitive Composite 70 (2^{nd} percentile), Language Composite 62 (1^{st} percentile), Motor Composite 85 (16^{th} percentile).

Patient 7

This boy, currently 23 months old, was born at term to non-consanguineous parents who originate from a small town in Guatemala. He was born with bilateral syndactyly of the third and fourth fingers. His birth weight was 3.317 kg (47.6th percentile, Z = -0.06), head circumference was 33 cm (12.5th percentile, Z = -1.15) and APGAR 9, 9. He initially presented to Neurology in an urgent clinic visit at 2 months of age for abnormal movements: flexor posturing with arm abduction, tonic posturing of his UE and LE with internal rotation of his arms, jerking of the left arm and upward eye deviation with each event. There were no recognized triggers of these events, and they clustered for minutes to over an hour. He did not present with clear epilepsy. His initial routine EEG was read as disorganized background and bursts of higher-amplitude activity, with several spike and slow wave complexes followed by electro-decrement with clinical correlate of subtle

twitch. Although this EEG did not meet criteria for hypsarrhythmia, there was high clinical suspicion for infantile spasms with emerging hypsarrhythmia on EEG; he was thus treated for infantile spasms with high dose prednisolone. CSF analysis of cell count, chemistry and culture were unremarkable.

His parents discontinued prednisolone on the 8th day of treatment due to side effects of irritability, diarrhea, persistence and worsening of his abnormal movements. An inpatient video EEG was repeated and captured opisthotonic-like events (back arching, sometimes twisting at the trunk, occasional arm stiffening) and oculogyric crises. These movements did not correlate with electrographic changes on the EEG suggestive of seizures or spasms. He would become extremely tachycardic with the events. Cardiac and GI workups were negative. His movements did not respond to lorazepam (0.1 mg/kg), though reduced in frequency during levetiracetam treatment (30 mg/kg twice daily), and parenteral hydration. Biochemical labs revealed a profile suggestive of aromatic L-amino acid decarboxylase (AADC) deficiency (see details below) and he was started on recommended treatment for this disorder: PN 50 mg BID, PLP 60 mg TID and Sinemet 0.4 mL TID (approximately 1 mg/kg/day based on levodopa component) at 2.5 months of age with complete resolution of symptoms on this regimen. Once *PLPBP* mutation was identified, Sinemet was later discontinued (at age of 8 months) and he is currently on a mixed regimen of PN (23 mg/kg/day div BID) and PLP (30 mg/kg/day div TID). Following initiation of treatment, all subsequent EEGs have been normal.

Early developmental milestones were achieved within the normal age range; more recently, asymmetric delays were identified. Clinical neurologic exam performed at the age of 20 months was normal: vision and hearing grossly intact; motor: normal bulk, full strength at all extremities at distal and proximal muscles in BUE and BLE, no hypotonia, sits, crawls, walks independently, stands flat footed; sensation: intact grossly at all extremities; coordination: no tremor, reaches for objects with both hands, transfers objects between hands, pincer grasp, using hands equally; reflexes: 2+ bilateral bicep and BR, symmetric brisk 2+ at patella, symmetric 2 at ankles, no clonus. At 23 months of age, significant delays were noted in expressive and receptive language skills with preservation of gross and fine motor development.

Biochemical investigations: Lactate remained normal when checked on hospital readmission (1.7 mM, reference range: <2.0 mM). However, during a third admission, he was confirmed to have

elevated lactate (8.46) and metabolic acidosis on VBG with elevated anion gap (23) as well as hyperglycemia (325) in the setting of repeated opisthotonic events. His UA showed 4+ glucose and 1+ ketones. His hyperglycemia and elevated lactate corrected quickly following a NS bolus. CRP and ammonia were normal.

Urine organic acids resulted positive for presence of vanillactic acid, vanilpyruvic acid, and n-acetyl-vanilalanine; also, minor elevations of lactic, malic, 2-ketoglutaric, and n-acetylaspartic acids. This profile is typical of aromatic AADC deficiency, an enzyme necessary for synthesis of neurotransmitters (DA, Epi, NE, 5HT). The rest of the metabolic workup (including plasma amino acids, acylcarnitine profiling) was negative. Confirmatory testing with AADC enzyme assay revealed partial enzymatic activity (18.84 pmol/min/mL), suspicious for carrier status of the condition but not complete AADC enzyme deficiency. Biochemical analysis of CSF at age of 2 months (before B6 treatment) showed normal levels of glucose (71 mg/dL, reference range: >40 mg/dL) but elevated protein concentration (75 mg/dL, reference range: <45 mg/dL) which normalized after B6 treatment (25 mg/dL at age of 2.5 months). Pre-B6 treatment CSF metabolomics (at age of 2 months) revealed several minor elevations of (Z score): 3-methoxytyrosine (4.2), palmitoyl-GPA 16:0 (3.7), alpha-ketoglutarate (3.2), adenosine (2.6), 2-aminooctanoate (2.6) and tryptophan (2.5).

Clinical whole-exome sequencing (WES) on the proband identified a homozygous variant in the *PLPBP* (c.280 A>T, p.Ile94Phe in exon 4). A homoplasmic variant in MT-ND1 was also described. A dopamine-related disorders gene panel identified a heterozygous pathogenic splice variant in *DBH* (c.339+2T>C). No variants were detected in *DDC*, the gene that encodes AADC. Sinemet (Levodopa/carbidopa) treatment was successfully discontinued after WES resulted, further supporting PLPHP dysfunction, rather than AADC deficiency, as disease-causing.

Patient 8

This boy of Arab descent, now 8 years and 1 month old, was born at term via spontaneous vaginal delivery to a primigravida mother with insulin dependent diabetes. The parents are consanguineous with a family history of pyridoxine-dependent epilepsy. The patient is 1st cousins with patient 9.

His APGAR scores were 7 & 9 at 1 & 5 minutes, respectively. At birth he weighed 2.98 kg (50th percentile), was 55 cm tall (90th percentile) and his head circumference was 35cm (50th percentile).

He was feeding well and active until the age of 1 week when he started to have episodes of myoclonic movements of the upper and lower limbs lasting for few seconds, but in clusters. He continued to have daily episodes. He was irritable and crying with disturbed sleep. The seizures became very frequent with time and at the age of 3 weeks he was admitted for the control of seizures. His initial EEG at the age of 3 weeks showed burst suppression. He was initially loaded with phenobarbitone but there was no response. He was then started on midazolam infusion and IV levetiracetam but he continued to have frequent seizures. At age of 25 days, a dose of 20 mg oral PN was tried and the seizures immediately stopped. He was sleepy for more than 10 hours for which he was shifted to PICU for observation. An EEG was repeated and it was normal. He was then gradually weaned off midazolam and levetiracetam. He was back to his normal activity. Phenobarbitone was also tapered and discontinued. He continued to be on PN only 40 mg BID with increasing the dose to TID during febrile illnesses. He remained seizure free since then except at the age of 5 years when he had a febrile illness and there was not enough PN at home to increase the dose. After that he had no more seizures. He is currently on pyridoxine 80 mg BD (6 mg/kg/day), increased during febrile illness to 80 mg TID = 8.8 mg/kg/day.

He achieved all his developmental milestones at an appropriate age. He is in grade 2 at school now with excellent performance. A physical examination found no dysmorphic features or neurocutaneous marks, no organomegally, and his clinical neurologic exam was normal (normal tone, power and DTR, planters are downgoing, normal cranial nerves examination, no cerebellar signs). His weight, height and head circumference are currently between the 50th and 75th percentiles.

Biochemical investigations found normal pipecolic acid levels and metabolic workup at the age of 3 weeks revealed raised blood lactate (4.5 & 3.4) but normal pH. Amino acids and acylcarnitines were unremarkable on tandem mass spectrometry in dried blood spots. Long-term EEG at the age of 4 years and 4 months resulted normal.

Patient 9

This boy of Arab descent, now 14 months old, was born at term by spontaneous vaginal delivery 37 weeks of gestation to a primigravida mother with no antenatal complications. The parents were consanguineous with a family history of pyridoxine-dependent epilepsy, the patient is the cousin of patient 8. His APGAR scores were 9 and 10 at 1 and 5 minutes, respectively. His birth weight

was 2.56kg (50th percentile), he was 49cm tall (50th percentile) and his head circumference was 33cm (50th percentile). He was admitted to the SCBU soon after delivery with the impression of TTN (transient tachypnea of the newborn). He was in SCBU for 5 days during which he was treated for presumed sepsis and jaundice. After discharge and at home on day 5 of life, the parents started to notice frequent episodes of generalized tonic-clonic seizures. The episodes were brief and lasting for seconds only. He continued to be active and was feeding well. His first EEG at the age of 10 days showed burst suppression. He was started on PN at home by his uncle (father of patient 8). At hospital, he received 40 mg once and he became very sleepy but had no more seizures. Within 24 hours he became active and was again feeding well. He was discharged on oral PN. He had no other symptoms. He is currently on 20 mg PN BID (8.5 mg/kg/day), increased during febrile illness to 80 mg TID (= 12.5 mg/kg/day).

Physical examination revealed no dysmorphic features or neurocutaneous marks and his weight, height and head circumference are all now in the 10th-50th percentile. He has normal tone, power and cranial nerves examination but noted to have hyperreflexia in all limbs. Urinary aminoadipic semialdehyde was mildly elevated at 0.35 mmol/mol Creatinine (reference, 0-0.19). Urinary pipecolic acid concentration was normal at 0.12 mmol/mol Creatinine (reference, 0.01-1.54). Piperidine-6 carboxylic acid was normal at 0.37 mmol/mol Creatinine (reference 0-1.62). Amino acids and acylcarnitines were unremarkable on tandem mass spectrometry in dried blood spots.

Repeat EEG at 10 months was normal.

Patient 10

This girl, currently at 10 years and 6 months of age, was born from consanguineous (first cousins) parents of Kurdish descent. There is a family history of similar disease in the younger sister (patient 11). She was born at 38 weeks gestation via C-section due to fetal decelerations and meconium stained amniotic fluid. Ultrasound examination performed at 20 weeks of gestation was remarkable for cysts in the head, but these were not seen on repeat ultrasound at 28 weeks. Her APGAR scores were 8 and 9. After birth, she was irritable with a high-pitched cry, dysconjugate eye movements, and tonic posturing was seen early on.

Within the first day of life, she presented with seizures characterized by flexor spasms and eye deviations; oxygen desaturations were seen. She continued to exhibit irritability and seizure

activity with segmental myoclonic jerks involving the upper trunk, eye deviation, crying, hiccupping and flexor spasms.

She was given a phenobarbital load during the first two days of life, with a mild response. An EEG after phenobarbital load showed discontinuous background rhythm with periods of quiescence, lasting up to 10 seconds, consistent with mild cerebral dysrhythmia. On day four of life, an overnight extended video EEG was pursued. At the beginning, near burst suppression pattern was seen, characterized by spike and slow wave and poly spike and slow wave complexes lasting up to 10 seconds. Relative periods of quiescence lasting up to 20 seconds were seen. During the burst of generalized paroxysmal discharges, she exhibited periodic episodes of high pitched cry, flexor spasms with arm extension, with and without hiccupping and with and without eye bobbing, lip smacking and emesis.

A 50 mg dose of PN was given twice over a short period of time. After 5 minutes, the periodic episodes of high pitched cry, flexor spasm, and hiccupping stopped and there was a significant improvement in the EEG background rhythm. During wakefulness, the background rhythm was continuous with fair synchrony and symmetry for age. Background rhythm appeared to be discontinuous during quiet sleep. A moderate number of sharp waves were seen over the left central temporal and right temporal region. Phenobarbital and phenytoin were discontinued, and the child remained without seizures. She was discharged home at 11 days of age, was breast feeding well and taking 75 mg PN per day. Doses were given in the evening since the child became very sleepy as a result. At the age of 8 years and 2 months, the family took her off PN treatment for two weeks which led to uncontrollable seizures and was taken to the ED where her seizures could not be stopped until she was put back on PN.

In terms of her language development, she began babbling at approximately 12 months of age. She started to say "mama" and "dada" at 3 years of age. She currently has several hundred words, which tend to be more representative of objects, and can sometimes be difficult to recognize. She will string four or five words together to communicate. She can follow one-step, very familiar commands or one-step commands with gestures. She does know her body parts including more minor body parts such as teeth and elbows. She does identify many of her letters. She is able to play with other children mostly her siblings. She points when she wants something and is fully potty-trained.

A neurological exam found that she has hypotonia with joint laxity, mild dysmetria and is unable to balance on each foot for 3 seconds. She has a wide based gait with poor coordination but is able to navigate an iPad. She can walk up and down stairs by herself, hops on each leg independently. She can kick and throw a ball and ride a tricycle. She needs some help with dressing but can pull up pants and underpants on her own and can take off her coat. She needs some help with putting on a coat. She can use a spoon and a fork well but makes a lot of mess. She holds a pen well. She does not yet write letters or numbers but can trace them or do so if her family is using hand over hand. She does not yet draw items that others recognize.

For her seizures she now takes 100 mg PN BID (4.7 mg/kg/day). She also requires lamotrigine 50 mg BID (3.5 mg/kg/day) and clobazam 10 mg BID (0.75 mg/kg/day) for optimal seizure control. During illness however, she can have breakthrough seizures.

Biochemical investigations included normal urine organic acids and purines; blood lactate, acylcarnitines, amino acids (both after PN therapy); and a normal CSF amino acids (except for a slight increase in alanine (43 nmol/ml)), folate/5MTHF, lactate, protein, glucose, BH4, neopterin, PLP, and neurotransmitter metabolites (5HIAA, HVA, 3-OMD).

Genetic investigations included normal 500Kb array CGH microarray, Prader-Willi/Angelman methylation studies, and Sanger analysis of *ALDH7A1* (heterozygous for non-pathogenic variant p.K411Q), and deletion/duplication analysis (negative), *CDKL5, SCN1A, SCN1B, GABRG2,* and *PCDH19* sequencing (all negative).

Patient 11

This girl, who is now 6 years and 10 months old, is the sister of patient 10. She was delivered via C-section after an unremarkable pregnancy. Her head circumference was in the 2nd percentile. On the first day of life, she had ophisthotonus, irritability, and eye deviation throughout the day (episodic, but up to 1 hour). This was not diagnosed as seizures until an EEG was performed at a few days of life. The EEG showed a discontinuous record with multifocal sharp waves (bilateral frontal/central/temporal). She was admitted to the NICA for two weeks due to meconium aspiration and seizures.

She was noted to have partial seizures (hemibody clonic activity with lateral eye deviation either left or right) lasting 7 seconds to 5 minutes (average 2 minutes, 2-3 times a week), or generalized convulsions with whole body stiffening with some neck extension, lasting more than 2 minutes, about twice a month. Her seizures typically occurred at night.

She had no initial response to AEDs. With initial PN administration, the EEG report describes persistence of sharp waves at moderate frequency, and her seizures did persist over several weeks and thus levetiracetam was added to her treatment. Subsequent additions of clobazam and lamotrigine have been helpful, but she still has seizures with fever. At the age of 4 years and 10 months, her PN dose was reduced to 50 mg BID and she suffered increase in frequency of seizures. She is currently on following medications: 100 mg PN BID (7.8 mg/kg/day), lamotrigine 37.5 mg BID (4.5 mg/kg/day) and clobazam 10 mg BID (1.25mg/kg/day).

Her neurological examination revealed mild dysmetria, and a wide based and ataxic gait. She is very hypotonic in the trunk, making mobility much more difficult. She continues to progress in gross and fine motor skills. Still cannot climb up or down stairs. She has separation anxiety and severe stranger anxiety. She knows a lot more words now than previously. She is interested in others, points at what she wants, but cries if approached by other children.

Biochemical investigations: A comprehensive metabolic panel (sodium, potassium, chloride, calcium, bicarbonates, glucose, BUN, creatinine, total protein, albumin, A/G ratio, total bilirubin, alkaline phosphatase, GOT/AST, GPT/ALT) was screened four times (first one at age of 15 months) and resulted normal profiles in all.

Genetic investigations: GeneDx Infantile Epilepsy Panel (all negative): sequencing and deletion/duplication analysis of the following genes: *ADSL, ALDH7A1, ARX, ATP6AP2, CDKL5, CLN3, CLN5, CLN6, CLN8, CNTNAP2, CTSD, FOXG1, GABRG2, GAMT, KCNQ2, KCNQ3, MECP2, MFSD8, NRXN1, PCDH19, PNKP, PNPO, POLG, PPT1, SCN1A, SCN2A, SCN1B, SLC25A22, SLC2A1, SLC9A6, SPTAN1, STXBP1, TCF4, TPP1, TSC1, TSC2, UBE3A* and *ZEB2*.

Clinical whole exome sequencing ultimately discovered the *PLPBP* variant in patients 10 and 11 after reanalysis as the original analysis did not classify the "*PROSC*" gene that had not yet been described.

Patient 12

This African American girl, now 5 months old, was born via spontaneous vaginal delivery at 35 weeks of gestation to a 17-year-old G1 P0 female after an uncomplicated pregnancy. The parents were consanguineous. Her APGAR scores were 7 at 1 minute and 9 at 5 minutes and birth head circumference was 31 cm which is at 22nd percentile. She presented shortly after birth with neonatal seizures. She started having repeated stereotyped episodes of extremity jerking and irregular respirations within the first few hours of life and evolved into super refractory neonatal seizures.

She did have initial period of seizure freedom after phenobarbital loading but relapsed within the first week of life. Her seizures failed multiple antiepileptic medications, including phenobarbital, phenytoin, topiramate, levetiracetam, clonazepam, vigabatrin, midazolam, lorazepam, leucovorin, and a single dose of PN (100 mg IV) given early in the course. The VEEG background had no noted improvement after the first PN dose. She had focal seizures and myoclonic jerks followed by tonic posturing and initial EEG showed a burst suppression pattern followed by very frequent focal and independent right and left sided seizures and bilateral synchronous tonic seizures and/or myoclonic startle like seizures with generalized epileptiform activity. After failing multiple conventional anticonvulsants, dextromethorphan was tried without success. She was placed on a 3:1 ketogenic diet and serine supplementation for low CSF serine. PLP was started at one month of age resulting in seizure freedom, significant improvement in EEG background activity and improvement in her neurologic exam. EEG background became continuous and no electrographic or clinical seizures were after PLP was started. Focal interictal epileptiform activity continued to be present but overall there was much improvement after initiation of PLP.

For seizure control, she is now taking 40 mg/kg/day of PLP divided q12h and 9 mg/kg/day of phenobarbital. She has been weaned from the ketogenic diet. On exam at age 2 months, she was microcephalic (z score -4.4), non-dysmorphic and was feeding well by mouth. She had conjugate eye movements and emerging visual fixation. She had normal axial tone and localized pain to extremity. Her deep tendon reflexes were 3+. No myoclonus was seen. Upon most recent check at age of 4.5 months, her EEG has 4-4.5 Hz background of normal voltage with no epileptiform activity. She is developing relatively well, has mild hypotonia but intact visual fixation and is a good oral feeder. Mother reports possible rare brief seizures but none noted in 24 hour EEG.

Her laboratory work-up revealed normal CBC, normal CMP, negative CRP, normal ammonia, initial elevated serum lactic acid which normalized within first 2 days, negative HSV PCR, negative TORCH titers, normal CSF lactic acid, normal CSF pyruvic acid, normal CSF glucose and normal CSF protein. Low CSF serine (30 nmol/mL, normal range: 44 - 136 nmol/mL) was noted, but other CSF amino acids were normal. Plasma amino acids checked at age of 6 days revealed elevated glycine (575 nmol/mL, reference range: 111 - 426 nmol/mL). Repeat plasma amino acids at 9 days of life showed normal glycine levels (370 nmol/mL). CSF glycine was normal at 3 weeks of age 23 nmol/ml (reference range: 5 - 115 nmol/mL). Acylcarnitine, urine organic acids and uric acid were all within reference intervals. Lymphocyte choriomeningitis AB IgG and IgM was negative. Pipecolic acid was 0.4 nmol/mL (normal range <6 nmol/mL). Urinary S-sulfocysteine was within limits. CSF neurotransmitters (5-hydroxyindoleacetic acid, HVA, 3-Omethyldopa) were all normal.

A microarray showed vast areas of homozygosity, totaling 20% of the genome. GeneDX Xome DxSlice on the proband revealed a pathogenic mutation in the gene *PLPBP* which results in pyridoxine-dependent seizures, in addition to 3 additional homozygous mutations of uncertain significance (c.1421G>A in *CYP27A1*, c.1429A>G in *DENND5A* and c.997C>T in *VPS53*, all typically associated with recessive disorders and here without second variants identified).

Supplemental methods

Whole-exome and Sanger sequencing and *in silico* analysis

Patients 1 and 2

Whole exome sequencing (WES) was performed on patients 1 and 2 using the SureSelectXT Library Prep Kit and Illumina HiSeq 4000 (Macrogen, Korea). The data was analyzed using a semi-automated bioinformatics pipeline (Tarailo-Graovac *et al*., 2016). Illumina sequencing reads were aligned to the human reference genome version hg19 using Bowtie2 aligner (Langmead and Salzberg, 2012) and local realignment was performed using Genome Analysis Toolkit (McKenna *et al*., 2010), achieving mean coverage of 24x for both patients 1 and 2. Variants were called using SAMtools (Li *et al*., 2009) and annotated using SnpEff (Cingolani *et al*., 2012). Rare variants were identified using public databases, such as exome variant server (EVS), dbSNP v138 (Sherry *et al*.,

2001) and the Exome Aggregation Consortium (ExAC) database (Lek *et al*., 2016), as well as our in-house database of more than 400 exomes and 40 genomes (UBC) and against an in-house database of 817 Saudi Arab exomes at Alfaisal University (Dr. Fowzan Alkuraya, personal communication). Manual inspection on variant quality was carried out with Integrative Genomics Viewer (IGV) (Robinson *et al*., 2011).

Patient 3

Clinical child-parents whole-exome sequencing (trio-WES) was performed at the Department of Human Genetics at the Radboudumc (Nijmegen, The Netherlands), with examination of all known genes according to previously described WES methods (de Ligt *et al*., 2012; Lelieveld *et al*., 2016).

Patient 4

Whole-exome sequencing of the proband and both parents was performed as described (Dyment *et al*., 2013).

Patient 5

Trio WES was performed using SureSelect Human All Exon Kit version 4 (Agilent) for target enrichment. The library was sequenced with 100bp paired-end reads on a HiSeq 2000 platform (Illumina), and bioinformatics analysis was carried out as described previously (Dyment *et al*., 2013). Sanger sequencing showed the affected individual was homozygous for this variant, parents heterozygous.

Patients 6, 7, 10, 11 and 12

Using genomic DNA from the proband and parents if available, the exonic regions and flanking splice junctions of the genome were captured using the SureSelect Human All Exon V4 (50 Mb), the Clinical Research Exome kit (Agilent) or the IDT xGen Exome Research Panel v1.0. Massively parallel (NextGen) sequencing was done on an Illumina system with 100bp or greater paired-end reads. Reads were aligned to human genome build GRCh37/UCSC hg19 and analyzed for sequence variants using a custom-developed analysis tool. Additional sequencing technology and variant interpretation protocol has been previously described (Tanaka *et al*., 2015). The general assertion criteria for variant classification are publicly available on the GeneDx ClinVar

submission page (http://www.ncbi.nlm.nih.gov/clinvar/submitters/26957/). Given patient 11 is a sibling of patient 10, the variants were diagnosed through targeted Sanger sequencing.

Patients 8 and 9

The *PLPBP* mutation in these cousin patients was identified by targeted Sanger sequencing.

In silico assessment of variants

In silico variant effect predictions and scores from the 6 prediction algorithms (SIFT, Polyphen2 HDIV, MutationTaster, MutationAssessor, FATHMM MKL and PROVEAN) for all *PLPBP* single-nucleotide variants (SNVs) were retrieved from GenomeBrowse 2.1.2 (Golden Helix, USA) using its data track "dbNSFP Functional Predictions and Scores 3.0". The track curates and visualizes functional predictions and scores that are originally obtained from the dbNSFP database (Liu *et al*., 2011, 2013). Only one tool (MutationTaster (Schwarz *et al*., 2014)) provided prediction for the 4bp deletion mutation in patients 5 and 12 (obtained manually from http://www.mutationtaster.org). CADD scores (Kircher *et al*., 2014) were queried individually.

Primary skin fibroblast culture

For patient 5, a skin biopsy was taken from which a fibroblast cell line was established at the Centre for Applied Genomics (Toronto, Canada) and maintained in HyClone DMEM media (GE Healthcare Life Sciences) supplemented with 10% FBS, Penicillin-Streptomycin (SV30010, GE Healthcare Life Sciences) and 2mm L-glutamine (SH3003401, Thermo Scientific).

Patient fibroblast protein analysis

Total protein from the patient and three control lines was extracted in RIPA buffer containing protease inhibitors (Sigma) and was run on SDS-PAGE (20μg) following standard protocols. Antibodies used were rabbit anti-PROSC (Proteintech, 25151-1-AP, 1:5000); anti-β-tubulin (Abcam, ab6046, 1:20 000) and anti-GAPDH (ImmunoChemical, 200-901-BJ4, 1:10 000) were used as loading controls. HRP-linked anti-rabbit or anti-mouse IgG (1:2000) was used as secondary, and the Clarity ECL WB Substrate kit (BioRad) was used for protein detection using a ChemiDoc Touch Imaging System (BioRad).

Analysis of mitochondrial function in fibroblasts

A sample of the patient 5 fibroblast line was sent to the Mitochondrial Disease Laboratory (SickKids, Toronto). Measurements performed were pyruvate dehydrogenase (PDH) in its native and dichloroacetate activated forms, pyruvate carboxylase (PC), cytochrome oxidase, succinate cytochrome c reductase, and the cellular lactate/pyruvate ratio.

Oxygen consumption rate (OCR) was measured in patient and control fibroblasts using a Seahorse XF-24 Extracellular Flux Analyzer and V7 PS cell culture microplates (Agilent). Cells were seeded 50 000/well 24 hours before the assay, which followed the standard protocols of the XF Cell Mito Stress Test (Agilent). Data were normalized to protein concentration.

PLPBP targeting in HEK293 cells

Two guide RNAs were designed in exon 2 of *PLPBP* (NM_007198) targeting the region downstream of the start codon using the CRISPR design website (http://crispr.mit.edu/). The guide RNA sequences were TTGCTGACCGCCACTAGCCG (Guide 1 on reverse strand; primers 1F 5' CACCGTTGCTGACCGCCACTAGCCG 3' and 1R 5' AAACCGGCTAGTGGCGGTCAGCAAC 3') and CATCCAGCCCCGGCTAGTGG (Guide 2 on forward strand; primers 2F 5' CACCGCATCCAGCCCCGGCTAGTGG 3' and 2R 5' AAACCCACTAGCCGGGGCTGGATG C 3'). Oligonucleotide guide sequences were cloned into the pSpCas9(BB)-2A-GFP plasmid (Addgene Plasmid 48138). The resulting plasmids were transfected into HEK293 cells and GFP positive cells were sorted two days after transfection. These cells were used for obtaining clonal cell lines. We obtained two clonal cell lines with predicted biallelic disease-causing mutations; Guide 1_B, homozygous for c.124_127delCTAG (L42Wfs*12) and Guide 2_C, homozygous for c.128_129ins131bp (A44Gfs*55).

Quantification of B6 vitamers in plasma, leucocytes and cultured cells

Plasma samples from patient 4 (prior to treatment with any form of vitamin B6) and patient 3 (during treatment with PLP) were collected, shed from light and stored at -80°C. B6 vitamers PLP, pyridoxal (PL), PN, pyridoxamine (PM) and the degradation product 4-pyridoxic acid (PA) were quantified by LC-MSMS as previously described (van der Ham *et al*., 2012; Mathis *et al*.,

2016). Pyridoxine-5'-phosphate (PNP) was not quantified due to plasma-related technical limitations of the method (ion suppression) and pyridoxamine-5'-phosphate (PMP) was not quantified as it is known to be highly unstable in plasma.

Fibroblasts from patient 5 and four controls, and HEK293 cells were cultured in DMEM GlutaMAX-I (Gibco, cat # 31966) containing 10% fetal bovine serum and 1% penicillin-streptomycin. B6 vitamers were extracted with tricholracetic acid (50g/L) and quantified with UPLC-MS/MS in biological triplicates as described by (van der Ham *et al*., 2012).

Zebrafish genotyping

F1s were raised to adulthood and were fin-clipped for genotyping by HMA-PAGE. Fish with candidate variants causing frameshift mutations were backcrossed to WT fish to further reduce the chance of off-target effects, generating F2 heterozygotes. F3 larvae from the crossing of F2 heterozygotes were genotyped by extracting DNA from 3-4 days post-fertilization (dpf) larval fins and HMA-PAGE was used following previously described protocols (Pena *et al*., 2017; Kosuta *et al*., in press). Primers used: *plpbp-F 5'* GCACTCTGGCTATGTGGAGA 3'; *plpbp*-R 5' AGCTGTCACTCATCCCTCGT 3'. Because differentiating homozygous mutants and homozygous WT genotypes requires two rounds of HMA-PAGE, and since no suitable primers could be identified for a reliable multiplex PCR strategy that would clearly identify homozygous mutants, two separate F2 mutant lines were crossed to generate compound heterozygous F3 offspring which facilitated genotyping by HMA-PAGE in a high-throughput manner (Supplementary Figs. 4 and 5). A pilot study was performed to show no difference in phenotype or survival between the compound heterozygous and homozygous mutant lines (Supplementary Fig. 6).

Western blotting for zebrafish larvae

Pools of 4 larvae were collected at 11dpf and total soluble proteins were extracted following previously established protocols (Pena *et al*., 2017). 40μg of protein from each sample was separated by SDS-PAGE using BioRad 4-20% pre-cast stain-free gels and blotted on low fluorescence PVDF (BioRad). Antibodies used were rabbit Anti-PROSC (Proteintech, 25151-1-AP, 1:5000) and HRP-linked anti-rabbit IgG (1:2000) was used as secondary. The Clarity ECL

’s

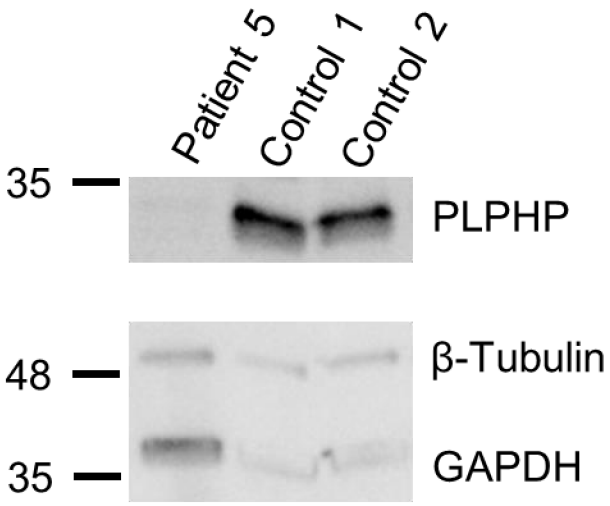

Patient 5's fibroblasts show an altered B6 vitamer profile

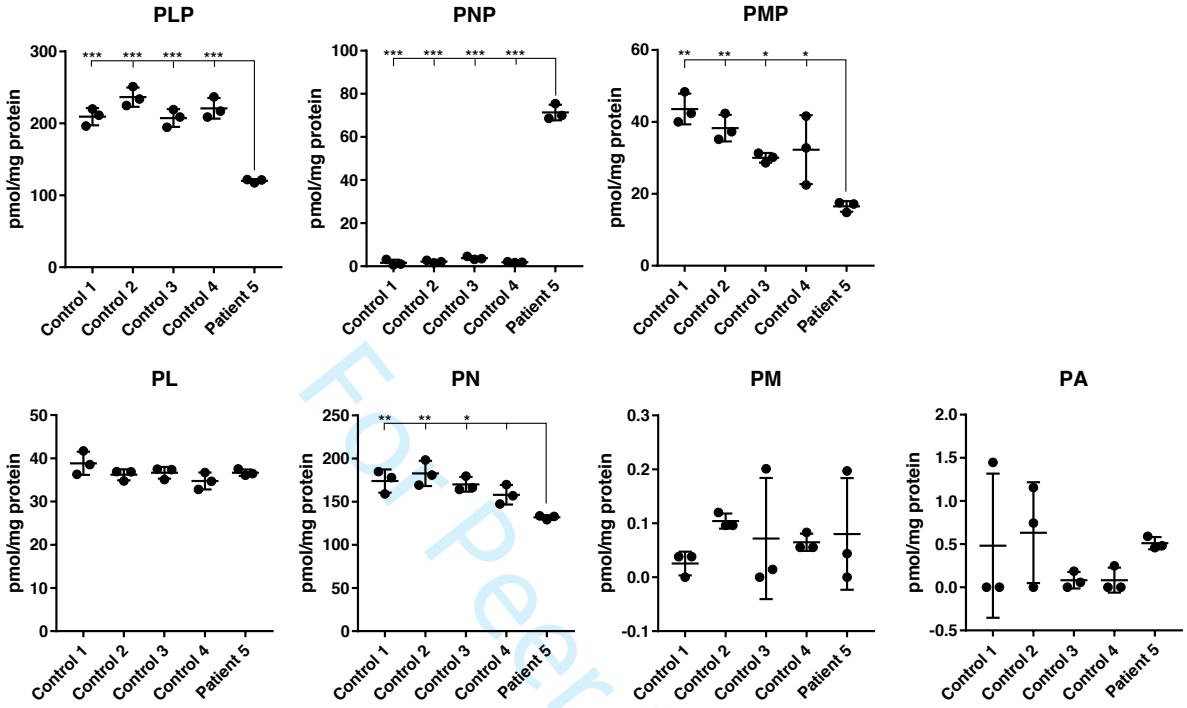

Supplementary Figure 2: B6 vitamer profiles in cultured fibroblasts from four control subjects and patient 5. Data are n=3 biological replicates per group. PA, pyridoxic acid; PL, pyridoxal; PLP, pyridoxal 5'-phosphate; PM, pyridoxamine; PMP, pyridoxamine 5'-phosphate; PN, pyridoxine; PNP, pyridoxine 5'-phosphate. ANOVA ***p<0.001, **p<0.01, *p<0.05.

HEK293 cells deficient for PLPHP show altered B6 vitamer profiles

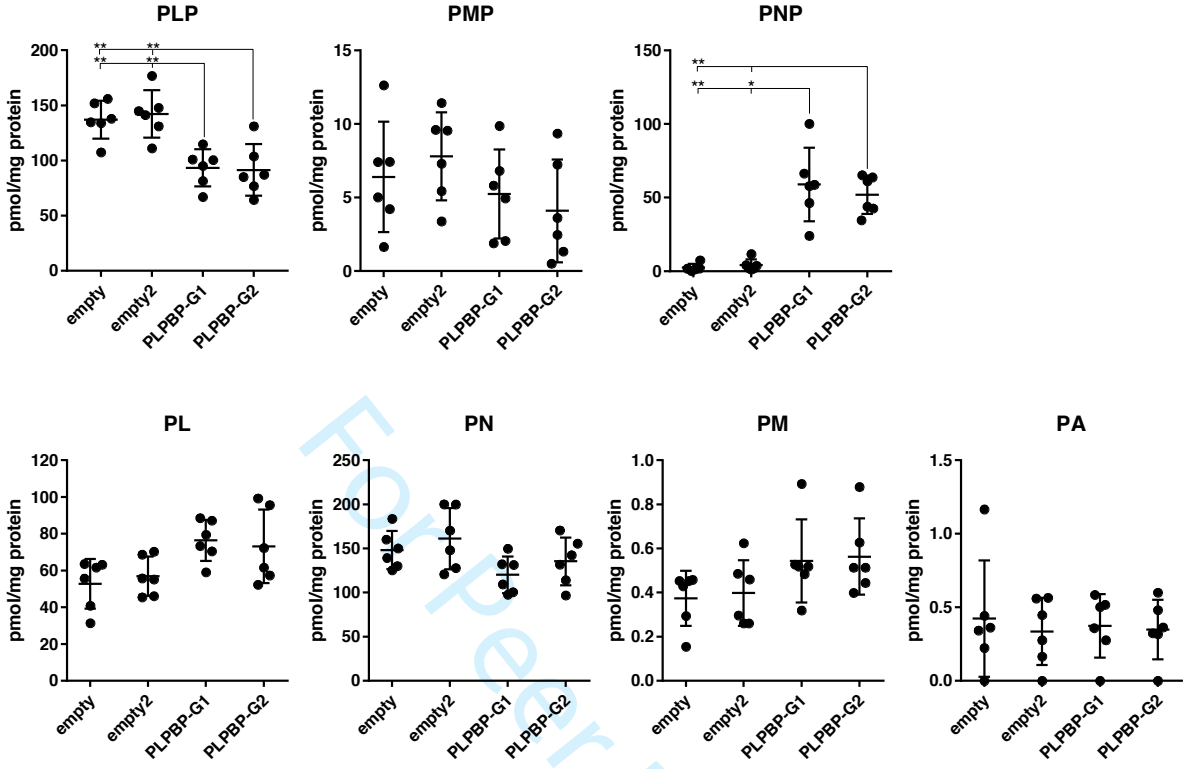

Supplementary Figure 3: B6 vitamer profiles in control (WT+empty vector) and PLPHP-deficient HEK293 cells (PLPHP-KO: PLPBP-G1 and PLPBP-G2). Data are from n=6 independent experiments (each consisting of 3 biological replicates per group), ±SD. Abbreviations: PN, pyridoxine; PL, pyridoxal; PM, pyridoxamine; PNP, pyridoxamine 5'-phosphate; PLP, pyridoxal 5'-phosphate; PMP, pyridoxamine 5'-phosphate; PA, pyridoxic acid. **p<0.01, *p<0.05.

Supplementary Table 1: Detailed MRI findings

Patient ID	Patient 1	Patient 2	Patient 3	Patient 4	Patient 5	Patient 6	Patient 7	Patient 8	Patient 9	Patient 10	Patient 11	Patient 12
MRI age	6 weeks, 8.5 months, 3.5 y	Not performed	10 days	1 day	6 days	8 months	12 weeks, 3.5 months,	MRI not available for review	MRI not available for review	6 years	2 years	MRI not available for review
WM abnormalities	Very mild T2-hyperintense and T1-hypointense changes in periventricular WM at age 6 weeks		Yes, T2 hyperintense and T1 hypointense, swollen aspect	Yes, T2 hyperintense and T1 hypointense, swollen aspect, subcortical cystic degeneration	Yes, T2 hyperintense and T1 hypointense, swollen aspect, subcortical cystic degeneration	No	no			Mild T2-hyperintensity in the posterior periventricular white matter	Faint T2-hyperintensity in the posterior periventricular white matter	
Cortex abnormalities	no		Simplified gyral pattern	Simplified gyral pattern	Simplified gyral pattern	no	no			no	no	
Basal ganglia abnormalities	no		no	no	no	no	no			no	no	
Thalamus abnormalities	no		no	no	no	no	no			no	no	
Cerebellar involvement	no		no	T2-hyperintense signal of the hilus of the dentate nucleus	no	no	no			no	no	
Cysts anterior horn	no		++	++	+ (L>R)	no	no			no	no	
CC abnormalities	no		Thin CC	Thin CC		no	no			Pronounced isthmus	no	
Other abnormalities	Age 8 months: mild communicating hydrocephalus with prominent external CSF spaces. Age 3.5 y: normal MRI			Lactate doublet at MR spectroscopy (basal ganglia)	Cavum septi pellucidi; small lactate doublet at MR spectroscopy (basal ganglia)	MRI normal	MRI normal	MRI at age 4 weeks reported as normal.	MRI at age 10 months reported as normal.			MRI at ages of 2 days and 3 weeks: Diffuse broadening of the gyri in both cerebral hemispheres, mild dilatation of the lateral and third ventricles with multiple intraventricular septations. There are blood products in the left lateral ventricule.

Supplementary Table 2: List of *PLPBP* variants found in our cohort of 12 patients. All variants are expressed as found in PLPHP (NP_009129.1). Variant effect is predicted is based on 7 *in silico* prediction tools (SIFT, Polyphen2 HDIV, MutationTaster, MutationAssessor, FATHMM MKL, PROVEAN and CADD). DUET uses as input the structural model developed for the human PLPHP to predict if a given amino acid change is stabilizing or destabilizing (ΔΔG). * Not modelled due to lack of this residue in yeast model used as template. NA: not available; NR: not reported.

Variant annotation			**Detailed *in silico* predictions [predicted effect (score)]**							
Genomic (GRCh37)	**cDNA and protein**	**Variant frequency (gnomAD)**	**DUET Predicted Stability Change (ΔΔG):**	**SIFT**	**Polyphen 2 HDIV**	**MutationTaster**	**MutationAssessor**	**FATHMM MKL**	**PROVEAN**	**CADD score**
chr8: g.37630300 C>T	NM_007198: c.347C>T; p.Thr116Ile	NR	0.123 Kcal/mol (Stabilizing)	Damaging (0.003)	Probably damaging (1)	Damaging (1)	Functional (high) (3.855)	Damaging (0.98019)	Damaging (-5.56)	29.20
chr8: g.37635617 C>G	NM_007198: c.823C>G; p.His275Asp	NR	Not modeled*;	Damaging (0.017)	Benign (0.361)	Damaging (0.918861)	Non-functional (low) (1.1)	Damaging (0.96396)	Neutral (-0.71)	23.3
chr8: g.37623066 G>A	NM_007198: c.122G>A; p.Arg41Gln	$4.06*10^{-6}$	-0.265 Kcal/mol (Destabilizing)	Damaging (0.04)	Probably damaging (0.978)	Damaging (1)	Non-functional (low) (1.795)	Damaging (0.99714)	Damaging (-2.73)	28.7
Chr8: g.37623143 G>A	NM_007198.3: c.199G>A; p.Glu67Lys	$4.06*10^{-6}$	-2.127 Kcal/mol (Destabilizing)	Damaging (0)	Probably damaging (1)	Damaging (1)	Functional (high) (4.1)	Damaging (0.99824)	Damaging (-3.96)	35
Chr8: g.37630271 A>G	NM_007198.3: c.320-2A>G splicing	$1.08*10^{-5}$	-	NA	NA	Damaging (1)	NA	Damaging (0.99207)	NA	24.7
Chr8: g.37633509 G>C	NM_007198.3: c.671G>C; p.Gly224Ala	NR	-0.966 Kcal/mol (Destabilizing)	Damaging (0)	Probably damaging (0.999)	Damaging (1)	Functional (high) (4.07)	Damaging (0.99191)	Damaging (-5.69)	27.7
Chr8: g.37630323_37630326del	NM_007198: c.370_373del; (p.Asp124Lysfs*2)	NR	-	NA	NA	Damaging (1)	NA	NA	NA	NA
chr8: g.37623834 A>T	NM_007198: c.280A>T; p.Ile94Phe	NR	-1.398 Kcal/mol (Destabilizing)	Damaging (0.001)	Probably damaging (1)	Damaging (1)	Functional (high) (4.43)	Damaging (0.99692)	Damaging (-3.96)	29.6

Supplementary Table 3: concentrations of B6 vitamers in plasma from 2 patients affected with PLPHP deficiency. Concentrations are expressed in nM.

	PL	PM	PN	PA	PLP
Patient 4	39	<2.7	0,1	130	1,1
Patient 3, treated	276	<2.7	0,1	365	685
Reference interval, untreated (Mathis *et al.*, 2016)	6.6-54	<2.7	<1	6.7-84	16-269

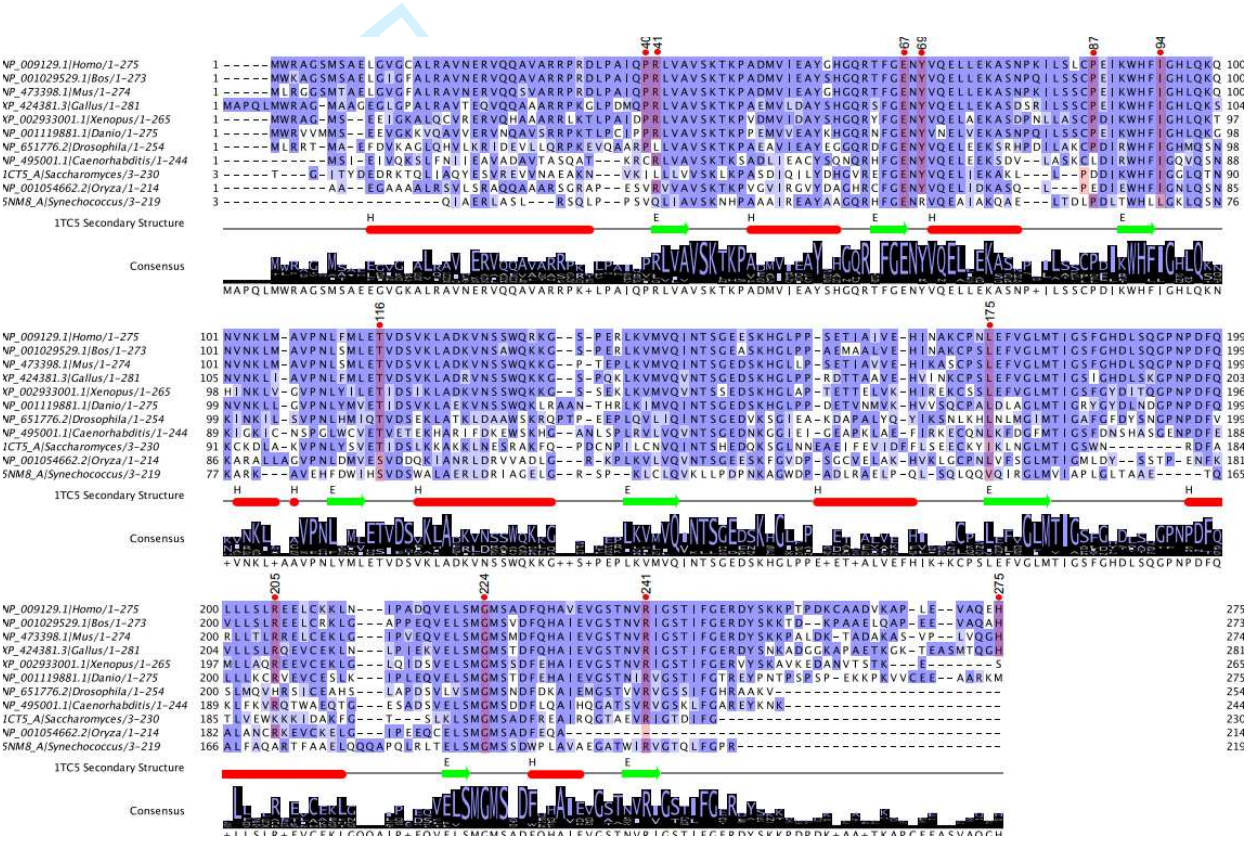

Supplementary Figure 5: Protein sequence alignment of PLPHP orthologues from several species (RefSeq identifiers shown in the sequence labels). Residues found mutated in patients are highlighted in red (missense mutations). Secondary structure as in the yeast orthologue (PDB 1CT5) is shown under the alignment. Consensus sequence is also shown. Image produced using Jalview (Waterhouse *et al.*, 2009) .

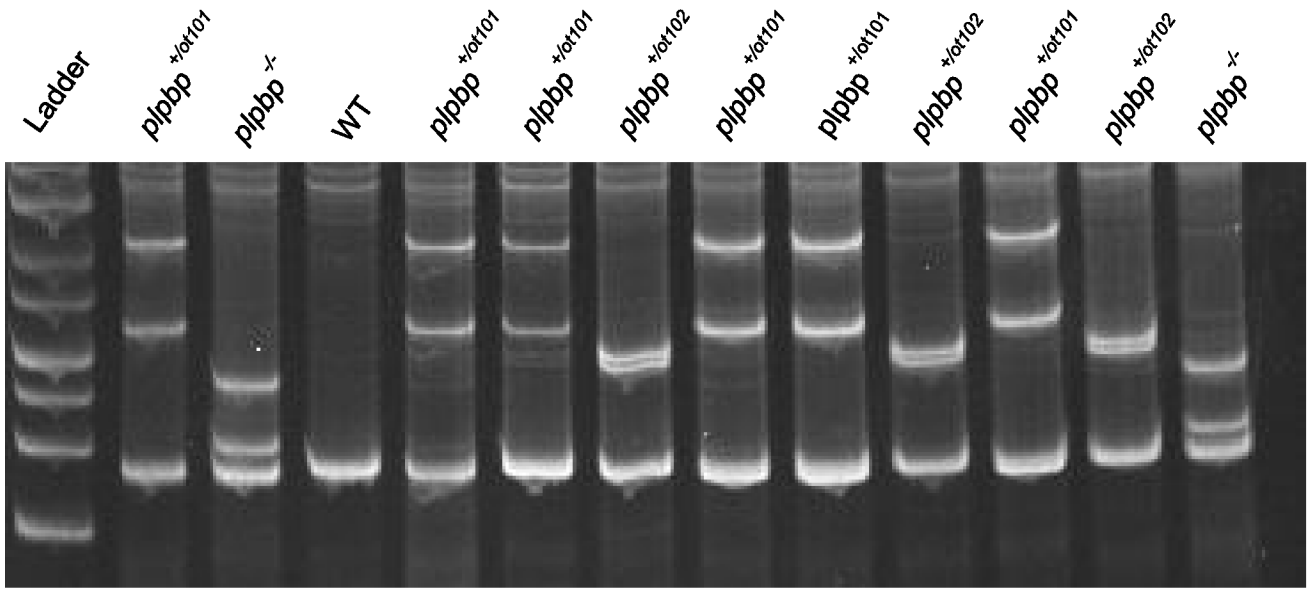

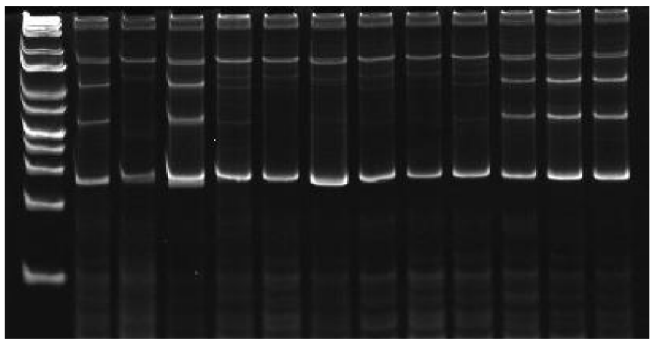

Gel 1

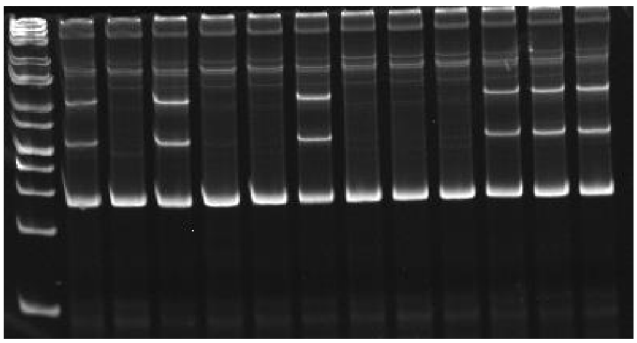

Gel 2: PCR product mixed with WT

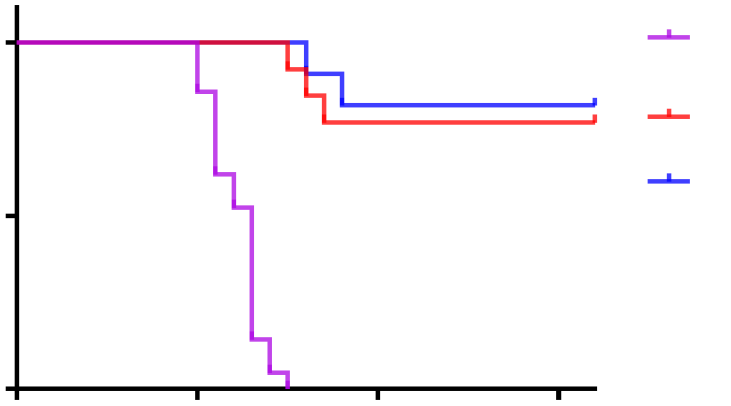

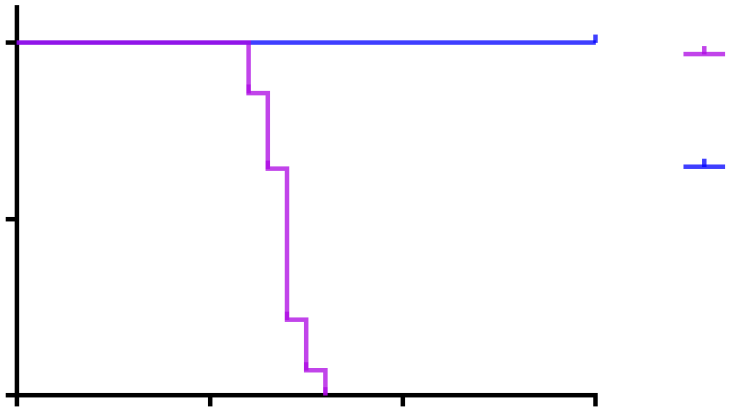

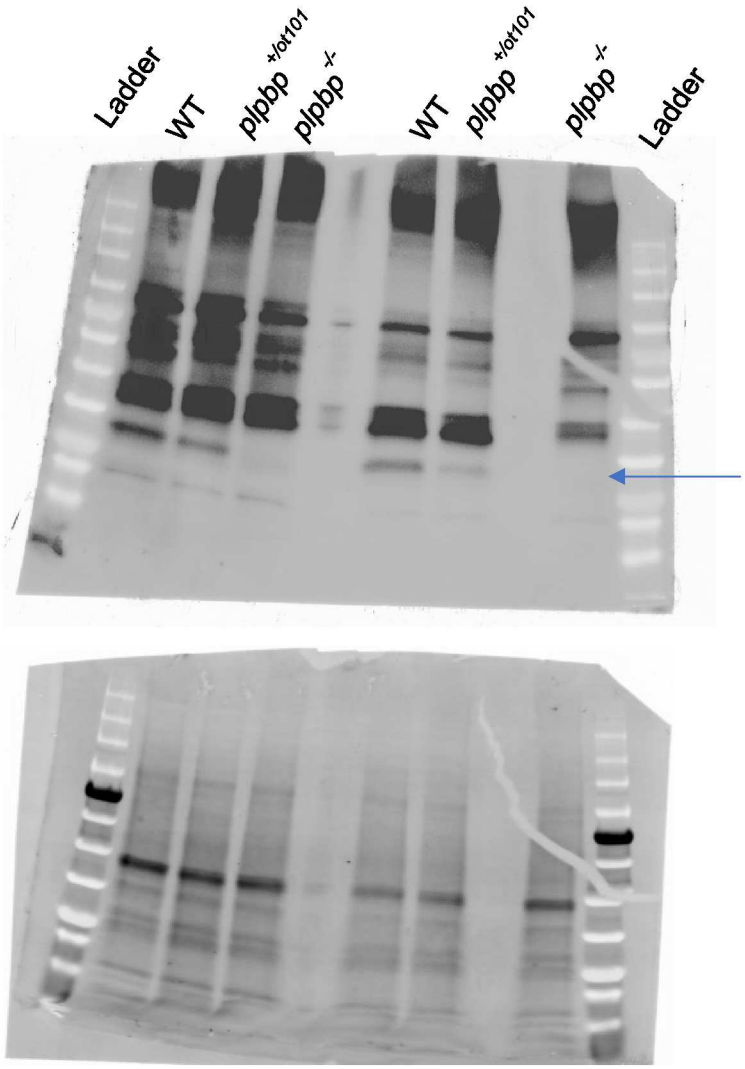
Ladder
WT
Plpbp +/ot101
Plpbp -/-
WT
Plpbp +/ot101
Plpbp -/-
Ladder

Supplemental References

Al Teneiji A, Bruun TU, Cordeiro D, Patel J, Inbar-Feigenberg M, Weiss S, *et al*. Phenotype, biochemical features, genotype and treatment outcome of pyridoxine-dependent epilepsy. Metab Brain Dis 2017; 32(2): 443-51.

Beaulieu CL, Majewski J, Schwartzentruber J, Samuels ME, Fernandez BA, Bernier FP, *et al*. FORGE Canada Consortium: outcomes of a 2-year national rare-disease gene-discovery project. Am J Hum Genet 2014; 94(6): 809-17.

Cingolani P, Platts A, Wang le L, Coon M, Nguyen T, Wang L, *et al*. A program for annotating and predicting the effects of single nucleotide polymorphisms, SnpEff: SNPs in the genome of Drosophila melanogaster strain w1118; iso-2; iso-3. Fly (Austin) 2012; 6(2): 80-92.

Darin N, Reid E, Prunetti L, Samuelsson L, Husain RA, Wilson M, *et al*. Mutations in PROSC Disrupt Cellular Pyridoxal Phosphate Homeostasis and Cause Vitamin-B6-Dependent Epilepsy. Am J Hum Genet 2016; 99(6): 1325-37.

de Ligt J, Willemsen MH, van Bon BW, Kleefstra T, Yntema HG, Kroes T, *et al*. Diagnostic exome sequencing in persons with severe intellectual disability. N Engl J Med 2012; 367(20): 1921-9.

Dyment DA, Smith AC, Alcantara D, Schwartzentruber JA, Basel-Vanagaite L, Curry CJ, *et al*. Mutations in PIK3R1 cause SHORT syndrome. Am J Hum Genet 2013; 93(1): 158-66.

Hamilton A, Tetreault M, Dyment DA, Zou R, Kernohan K, Geraghty MT, *et al*. Concordance between whole-exome sequencing and clinical Sanger sequencing: implications for patient care. Mol Genet Genomic Med 2016; 4(5): 504-12.

Kircher M, Witten DM, Jain P, O'Roak BJ, Cooper GM, Shendure J. A general framework for estimating the relative pathogenicity of human genetic variants. Nat Genet 2014; 46(3): 310-5.

Kosuta C, Daniel K, Johnstone DL, Mongeon K, Ban K, LeBlanc S, *et al*. High-throughput DNA extraction and genotyping of 3dpf zebrafish larvae by fin clipping. JoVE in press.

Langmead B, Salzberg SL. Fast gapped-read alignment with Bowtie 2. Nat Methods 2012; 9(4): 357-9.

Lek M, Karczewski KJ, Minikel EV, Samocha KE, Banks E, Fennell T, *et al*. Analysis of protein-coding genetic variation in 60,706 humans. Nature 2016; 536(7616): 285-91.

Lelieveld SH, Reijnders MR, Pfundt R, Yntema HG, Kamsteeg EJ, de Vries P, *et al*. Meta-analysis of 2,104 trios provides support for 10 new genes for intellectual disability. Nat Neurosci 2016; 19(9): 1194-6.

Li H, Handsaker B, Wysoker A, Fennell T, Ruan J, Homer N, *et al*. The Sequence Alignment/Map format and SAMtools. Bioinformatics 2009; 25(16): 2078-9.

Liu X, Jian X, Boerwinkle E. dbNSFP: a lightweight database of human nonsynonymous SNPs and their functional predictions. Hum Mutat 2011; 32(8): 894-9.

Liu X, Jian X, Boerwinkle E. dbNSFP v2.0: a database of human non-synonymous SNVs and their functional predictions and annotations. Hum Mutat 2013; 34(9): E2393-402.

Mathis D, Abela L, Albersen M, Burer C, Crowther L, Beese K, *et al*. The value of plasma vitamin B6 profiles in early onset epileptic encephalopathies. J Inherit Metab Dis 2016; 39(5): 733-41.

McKenna A, Hanna M, Banks E, Sivachenko A, Cibulskis K, Kernytsky A, *et al*. The Genome Analysis Toolkit: a MapReduce framework for analyzing next-generation DNA sequencing data. Genome Res 2010; 20(9): 1297-303.

Pena IA, Roussel Y, Daniel K, Mongeon K, Johnstone D, Mendes HW, *et al*. Pyridoxine-Dependent Epilepsy in Zebrafish Caused by Aldh7a1 Deficiency. Genetics 2017; 207(4):1501-1518.

Plecko B, Zweier M, Begemann A, Mathis D, Schmitt B, Striano P, *et al*. Confirmation of mutations in PROSC as a novel cause of vitamin B 6 -dependent epilepsy. J Med Genet 2017 Dec; 54(12): 809-14.

Robinson JT, Thorvaldsdottir H, Winckler W, Guttman M, Lander ES, Getz G, *et al*. Integrative genomics viewer. Nat Biotechnol 2011; 29(1): 24-6.

Schwarz JM, Cooper DN, Schuelke M, Seelow D. MutationTaster2: mutation prediction for the deep-sequencing age. Nat Methods 2014; 11(4): 361-2.

Sherry ST, Ward MH, Kholodov M, Baker J, Phan L, Smigielski EM, *et al*. dbSNP: the NCBI database of genetic variation. Nucleic Acids Res 2001; 29(1): 308-11.

Tanaka AJ, Cho MT, Millan F, Juusola J, Retterer K, Joshi C, *et al*. Mutations in SPATA5 Are Associated with Microcephaly, Intellectual Disability, Seizures, and Hearing Loss. Am J Hum Genet 2015; 97(3): 457-64.

Tarailo-Graovac M, Shyr C, Ross CJ, Horvath GA, Salvarinova R, Ye XC, *et al*. Exome Sequencing and the Management of Neurometabolic Disorders. N Engl J Med 2016; 374(23): 2246-55.

Tremino L, Forcada-Nadal A, Rubio V. Insight into vitamin B6 -dependent epilepsy due to PLPBP (previously PROSC) missense mutations. Hum Mutat 2018.

van der Ham M, Albersen M, de Koning TJ, Visser G, Middendorp A, Bosma M, *et al*. Quantification of vitamin B6 vitamers in human cerebrospinal fluid by ultra performance liquid chromatography-tandem mass spectrometry. Anal Chim Acta 2012; 712: 108-14.

Waterhouse AM, Procter JB, Martin DM, Clamp M, Barton GJ. Jalview Version 2--a multiple sequence alignment editor and analysis workbench. Bioinformatics 2009; 25(9): 1189-91.

ARRIVE

The ARRIVE Guidelines Checklist

Animal Research: Reporting In Vivo Experiments

Carol Kilkenny[1], William J Browne[2], Innes C Cuthill[3], Michael Emerson[4] and Douglas G Altman[5]

[1]The National Centre for the Replacement, Refinement and Reduction of Animals in Research, London, UK, [2]School of Veterinary Science, University of Bristol, Bristol, UK, [3]School of Biological Sciences, University of Bristol, Bristol, UK, [4]National Heart and Lung Institute, Imperial College London, UK, [5]Centre for Statistics in Medicine, University of Oxford, Oxford, UK.

	ITEM	RECOMMENDATION	Section/ Paragraph
Title	1	Provide as accurate and concise a description of the content of the article as possible.	Line 1
Abstract	2	Provide an accurate summary of the background, research objectives, including details of the species or strain of animal used, key methods, principal findings and conclusions of the study.	Lines 81-103
INTRODUCTION			
Background	3	a. Include sufficient scientific background (including relevant references to previous work) to understand the motivation and context for the study, and explain the experimental approach and rationale. b. Explain how and why the animal species and model being used can address the scientific objectives and, where appropriate, the study's relevance to human biology.	Lines 122-164
Objectives	4	Clearly describe the primary and any secondary objectives of the study, or specific hypotheses being tested.	Lines 158-164
METHODS			
Ethical statement	5	Indicate the nature of the ethical review permissions, relevant licences (e.g. Animal [Scientific Procedures] Act 1986), and national or institutional guidelines for the care and use of animals, that cover the research.	Lines 236-240
Study design	6	For each experiment, give brief details of the study design including: a. The number of experimental and control groups. b. Any steps taken to minimise the effects of subjective bias when allocating animals to treatment (e.g. randomisation procedure) and when assessing results (e.g. if done, describe who was blinded and when). c. The experimental unit (e.g. a single animal, group or cage of animals). A time-line diagram or flow chart can be useful to illustrate how complex study designs were carried out.	Lines 252-257 Lines 259-265 Lines 270-277 Fig. 4 Fig .5 Lines 797-833
Experimental procedures	7	For each experiment and each experimental group, including controls, provide precise details of all procedures carried out. For example: a. How (e.g. drug formulation and dose, site and route of administration, anaesthesia and analgesia used [including monitoring], surgical procedure, method of euthanasia). Provide details of any specialist equipment used, including supplier(s). b. When (e.g. time of day). c. Where (e.g. home cage, laboratory, water maze). d. Why (e.g. rationale for choice of specific anaesthetic, route of administration, drug dose used).	Lines 239-240
Experimental animals	8	a. Provide details of the animals used, including species, strain, sex, developmental stage (e.g. mean or median age plus age range) and weight (e.g. mean or median weight plus weight range). b. Provide further relevant information such as the source of animals, international strain nomenclature, genetic modification status (e.g. knock-out or transgenic), genotype, health/immune status, drug or test naïve, previous procedures, etc.	Lines 235-240

The ARRIVE guidelines. Originally published in *PLoS Biology*, June 2010[1]

Housing and husbandry	9	Provide details of: a. Housing (type of facility e.g. specific pathogen free [SPF]; type of cage or housing; bedding material; number of cage companions; tank shape and material etc. for fish). b. Husbandry conditions (e.g. breeding programme, light/dark cycle, temperature, quality of water etc for fish, type of food, access to food and water, environmental enrichment). c. Welfare-related assessments and interventions that were carried out prior to, during, or after the experiment.	Lines 236-240
Sample size	10	a. Specify the total number of animals used in each experiment, and the number of animals in each experimental group. b. Explain how the number of animals was arrived at. Provide details of any sample size calculation used. c. Indicate the number of independent replications of each experiment, if relevant.	Line 253 Lines 260-265 Lines 271-277 Lines 805-807
Allocating animals to experimental groups	11	a. Give full details of how animals were allocated to experimental groups, including randomisation or matching if done. b. Describe the order in which the animals in the different experimental groups were treated and assessed.	Lines 239-240 Line 250 Lines 253-256 Lines 260-261
Experimental outcomes	12	Clearly define the primary and secondary experimental outcomes assessed (e.g. cell death, molecular markers, behavioural changes).	Lines 236-278
Statistical methods	13	a. Provide details of the statistical methods used for each analysis. b. Specify the unit of analysis for each dataset (e.g. single animal, group of animals, single neuron). c. Describe any methods used to assess whether the data met the assumptions of the statistical approach.	Lines 280-283 Fig. 4 Fig. 5 Fig. 6 Lines 799-835
RESULTS			
Baseline data	14	For each experimental group, report relevant characteristics and health status of animals (e.g. weight, microbiological status, and drug or test naïve) prior to treatment or testing. (This information can often be tabulated).	Lines 429-453 Fig. 4
Numbers analysed	15	a. Report the number of animals in each group included in each analysis. Report absolute numbers (e.g. 10/20, not 50%[2]). b. If any animals or data were not included in the analysis, explain why.	Lines 450-453 Figs. 4-6, 799-835
Outcomes and estimation	16	Report the results for each analysis carried out, with a measure of precision (e.g. standard error or confidence interval).	462-494, Fig 4-6, 799-835
Adverse events	17	a. Give details of all important adverse events in each experimental group. b. Describe any modifications to the experimental protocols made to reduce adverse events.	Lines 239-240
DISCUSSION			
Interpretation/ scientific implications	18	a. Interpret the results, taking into account the study objectives and hypotheses, current theory and other relevant studies in the literature. b. Comment on the study limitations including any potential sources of bias, any limitations of the animal model, and the imprecision associated with the results[2]. c. Describe any implications of your experimental methods or findings for the replacement, refinement or reduction (the 3Rs) of the use of animals in research.	Lines 501-506 Lines 546-569
Generalisability/ translation	19	Comment on whether, and how, the findings of this study are likely to translate to other species or systems, including any relevance to human biology.	Lines 580-587
Funding	20	List all funding sources (including grant number) and the role of the funder(s) in the study.	Lines 600-615

References:
1. Kilkenny C, Browne WJ, Cuthill IC, Emerson M, Altman DG (2010) Improving Bioscience Research Reporting: The ARRIVE Guidelines for Reporting Animal Research. *PLoS Biol* 8(6): e1000412. doi:10.1371/journal.pbio.1000412
2. Schulz KF, Altman DG, Moher D, the CONSORT Group (2010) CONSORT 2010 Statement: updated guidelines for reporting parallel group randomised trials. *BMJ* 340:c332.